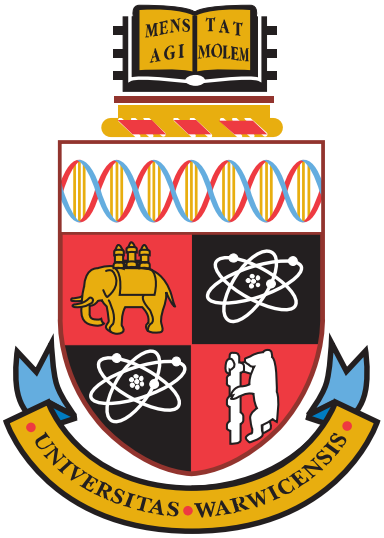

Probing the dynamic response of dense matter with x-ray Thomson scattering

by

David Alan Chapman

Thesis

Submitted to the University of Warwick

for the degree of

Doctor of Philosophy

Department of Physics

December 2015

THE UNIVERSITY OF WARWICK

Contents

Declarations

I declare that the work presented in this thesis is my own except where stated explicitly otherwise, and was carried out at the University of Warwick under the supervision of Dr D. O. Gericke. The work has not been submitted in this or any other academic institution for admission to a higher degree.

Some parts of the work presented herein have been published in peer reviewed journals:

- *Analysis of Thomson scattering from nonequilibrium plasmas*,
  D. A. Chapman and D. O. Gericke,
  Phys. Rev. Lett. **107**, 165004 (2011).

- *Analysis of Thomson scattering data from strongly-driven hydrogen*,
  D. A. Chapman, J. Vorberger, K. Wünsch and D. O. Gericke,
  High Energy Density Phys. **8**, 175 (2012).

- *Modelling Thomson scattering for systems with non-equilibrium electron distributions*,
  D. A. Chapman, J. Vorberger, K. Wünsch and D. O. Gericke,
  Eur. Phys. J. Web Conf. **59**, 13009 (2013).

- *Reduced coupled-mode approach to electron-ion energy relaxation*,
  D. A. Chapman, J. Vorberger and D. O. Gericke,
  Phys. Rev. E **88**, 013102 (2013).

- *X-ray Thomson scattering measurements of temperature and density from multi-shocked CH capsules*,
  L. B. Fletcher, A. L. Kritcher, A. Pak, T. Ma, T. Döppner, C. Fortmann, L. Divol, O. L. Landen, J. Vorberger, **D. A. Chapman**, D. O. Gericke, R. W. Falcone and S. H. Glenzer,
  Phys. Plasmas **20**, 056316 (2013).

- *Probing matter at Gbar pressures at the NIF*,
  A. L. Kritcher, T. Döppner, D. Swift, J. A. Hawreliak, G. W. Collins, J. Nilsen, B. Bachmann, E. Dewald, D. Strozzi, S. Felker, O. L. Landen, O. S. Jones, C. Thomas, J. Hammer, C. Keane, H. J. Lee, S. H. Glenzer, S. D. Rothman, **D. A. Chapman**, D. Kraus, P. Neumayer, R. W. Falcone,
  High Energy Density Phys. **10**, 27 (2014).

- *Observation of continuum depression in warm dense matter with x-ray Thomson scattering*,
  L. B. Fletcher, A. L. Kritcher, A. Pak, T. Ma, C. Fortmann, L. Divol, O. S. Jones, O. L. Landen, H. A. Scott, J. Vorberger, **D. A. Chapman**, D. O. Gericke, B. A Mattern, G. T. Seidler, G. Gregori, R. W. Falcone and S. H. Glenzer
  Phys. Rev. Lett. **112**, 145004 (2014).

- *Observations of strong ion-ion correlations in dense plasmas*,
  T. Ma, L. B. Fletcher, A. Pak, **D. A. Chapman**, R. W. Falcone, C. Fortmann, E. Galtier, D. O. Gericke, G. Gregori, J. Hastings, O. L. Landen, S. Le Pape, H. J. Lee, B. Nagler, P. Neumayer, D. Turnbull, J. Vorberger, T. G. White, K. Wünsch, U. Zastrau, S. H. Glenzer and T. Döppner,
  Phys. Plasmas **21**, 056302 (2014).

- *Simulating x-ray Thomson scattering signals from high-density, millimetre-scale plasmas at the National Ignition Facility*,
  D. A. Chapman, D. Kraus, A. L. Kritcher, B. Bachmann, G. W. Collins, R. W. Falcone, J. A. Gaffney, D. O. Gericke, S. H. Glenzer, T. M. Guymer, J. A. Hawreliak, O. L. Landen, S. Le Pape, T. Ma, P. Neumayer, J. Nilsen, A. Pak, R. Redmer, D. C. Swift, J. Vorberger and T. Döppner,
  Phys. Plasmas **21**, 082709 (2014).

- *X-ray continuum emission spectroscopy from hot dense matter at Gbar pressures*,
  D. Kraus, T. Döppner, A. L. Kritcher, B. Bachmann, **D. A. Chapman**, G. W. Collins, S. H. Glenzer, J. A. Hawreliak, O. L. Landen, T. Ma, S. Le Pape, P. Neumayer, D. C. Swift and R. W. Falcone,
  Rev. Sci. Instrum. **85**, 11D606 (2014).

- *Observations of finite-wavelength screening in high-energy-density matter*,
  D. A. Chapman, J. Vorberger, L. B. Fletcher, R. A. Baggott, L. Divol, T. Döppner, R. W. Falcone, S. H. Glenzer, G. Gregori, T. M. Guymer, A. L. Kritcher, O. L. Landen, T. Ma, A. E. Pak and D. O. Gericke,
  Nat. Commun. **6**, 6839 (2015).

- *Ultra-bright x-ray laser scattering for dynamic warm dense matter physics*,
  L. B. Fletcher, H. J. Lee, T. Döppner, E. Galtier, B. Nagler, P. Heimann, C. Fortmann, S. Le Pape, T. Ma, M. A. Millot, A. Pak, D. Turnbull, **D. A. Chapman**, D. O. Gericke, J. Vorberger, T. White, G. Gregori, M. Wei, B. Barbrel, R. W. Falcone, C.-C. Kao, H. Nuhn, J. Welch, U. Zastrau, P. Neumayer, J. B. Hastings and S. H. Glenzer,
  Nat. Photon. **9**, 274 (2015).

Acknowledgments

Suffice to say that listing everyone who has helped me get to where I am today would itself require a thesis-length document and, given that anyone about to embark on reading this thesis is about to have to wade through more than 200 pages of physics, I'll therefore try to be concise.

First and foremost, I'd like to thank my supervisor, Dr Dirk Gericke, for his guidance during my studies. His positive attitude in feeding my curiosity toward physics has played no small part in my academic development over the last five years. I'm especially thankful for his encouragement in making me write up and publish my work throughout. I must also express a profound gratitude to Dr Jan Vorberger for his unending patience in dutifully answering every frantic barrage of questions, sent at all hours of the day and night. Thanks also go to past and present members of the dense matter group at the Centre for Fusion, Space and Astrophysics (University of Warwick) for inspiring discussions and for sharing ideas and code which have assisted with various aspects of this work. Special mentions go to Dr Kathrin Wünsch, Dr Don Edie and Rory Baggott. Good luck to you all.

As for the people I've been fortunate enough to work with at AWE, my heart-felt thanks goes to you too: Dr Mike Rubery, Andy Hodgson, Dr Rich Britton, Dr Damon Swatton, Dr Matt Hill, Dr Peter Allan, Dr Colin Brown, Steve James, Tom Guymer, Dr Andrew Simons, Steve Gales... the list goes on. Your support, friendship, words of (not always deliberately condescending) advice, encouragement and continual ribbing have made coming to work every day marginally less unbearable! Most importantly, having a hot, steaming and super-strong (you have a serious problem, Colin) coffee waiting for me every morning has got me through more than a few long and eye-meltingly dull days of writing up. I also gratefully acknowledge funding from the Plasma Physics Department at AWE and the support of my line management chain, most prominently Warren Garbett, Mark Stevenson and Pete Thompson.

Furthermore, the support and warm hospitality of my colleagues from the USA and Europe is gratefully recognised. Special thanks go to Dr Tilo Döppner, Dr Siegfried Glenzer, Dr Andrea Kritcher, Dr Dominik Kraus, Dr Luke Fletcher and Dr Jim Gaffney amongst a great many more. The presentation of experimental data obtained at the Omega laser facility, the National Ignition Facility, and the Linac Coherent Light Source in this thesis would not have been possible without these valued collaborations. It is my fond hope that we'll be able to continue working together for many years to come.

Finally, the biggest thanks of all goes to the diverse collection of characters and surnames that make up my wonderful family, most importantly my beautiful girls Alex and Georgie, for their continuous support, love, encouragement and patience. Your collective unwavering and steely resolve to feign interest in my science-based ramblings for the past five years (and more) will never be forgotten. I thank you all from the bottom of my heart and I love you all more than words can express. You'll all be glad to know that you'll never have to listen to me bang on about any of it, ever again!

List of Figures

Abstract

This thesis describes the development of a comprehensive and detailed theoretical framework for modelling x-ray Thomson scattering (XRTS) diagnostics for investigating dense plasmas. Throughout, the well-known description ubiquitously used for modelling XRTS experiments is modified in a novel way in order to meet the challenges arising from the latest experiments in the thriving fields of warm dense matter (WDM), high-energy-density (HED) plasmas and inertial confinement fusion (ICF) energy research. In particular, plasmas in which the electrons and ions are in non-equilibrium states are considered, relating to both momentum and energy relaxation and also spatial inhomogeneity.

The theoretical basis for describing the spectrum of scattered radiation is given by a quantum statistical approach in order to be applicable to dense, strongly coupled and partially ionized plasmas. The correlation and response properties of the electrons and ions are treated using the techniques of non-equilibrium Green's functions, such that the different contributions to the total scattering are generalised to experiments conducive to strongly non-equilibrium electron distributions. Of particular interest is the dynamic structure of the free electrons, especially in the collective scattering regime, where the mode spectrum provides a sensitive measurement of the properties of the electron gas. The non-equilibrium model is used to analyse recent data from the FLASH free-electron laser, and it is shown that a robust understanding of the data is only possible within this new framework.

The model developed is also used to study and design experiments in which other forms of non-equilibrium may be present. Simplified simulations of temperature relaxation of isochorically heated targets are presented and coupled the bespoke XRTS analysis code developed in this work; the *multicomponent scattering simulation* (MCSS) model. The results show that spectrally- and angularly-resolved XRTS could potentially be used to perform such measurements and, moreover, assess the validity of electron-ion transfer models under challenging conditions. Furthermore, the code is also coupled to radiation hydrodynamics simulations of experiments in large-scale targets currently being developed for the National Ignition Facility. In this case, the strongly inhomogeneous state of the target, combined with other three-dimensional effects, requires a significant development of the standard approach to modelling XRTS.

Finally, the MCSS code is use to analyse data from recent experiments using shock-compressed plastic. Here, the target is small enough and evolves sufficiently slowly for the well-understood equilibrium-based XRTS theories to be robust. Detailed statistical analysis of the data supports the breakdown of the well-known Debye-Hückel description of the screening properties of dense matter. Instead, a more general approach studied in this work is shown to provide a better fit. This result constitutes the first such experimental observation in dense plasmas, and is of significant interest to a wide range of fields in which charge screening is important.

Abbreviations

Acronyms

BAM	Beam acoustic mode
BE	Bose-Einstein [distribution function]
BMA	Born-Mermin approximation
BOHT	Bump-on-hot-tail [distribution function]
C	Coulomb [interaction potential]
CH	Carbon-hydrogen [simple plastic]
CM	Coupled modes [energy relaxation model]
CSD	Charge-switching Debye [interaction potential]
DFT	Density functional theory
DFT-MD	Density functional theory [coupled to] molecular dynamics
D	Debye [interaction potential]
DH	Debye-Hückel [screening model/limit]
DLFC	Dynamic local field correction
DPA	Diagonalised polarisation approximation
DSF	Dynamic structure factor
EM	Electromagnetic [radiation]
FD	Fermi-Dirac [distribution function]
FDT	Fluctuation-dissipation theorem
FEL	Free-electron laser
FFA	Form factor approximation
FFT	Fast Fourier transform
FGR	Fermi golden rule [energy-relaxation model]
FLASH	Free-electron laser in Hamburg
FWHM	Full-width at half-maximum
FWS	Finite-wavelength screening
HED	High-energy-density [matter/plasma]
HNC	Hypernetted-chain [approximation]
KBA	Kadanoff-Baym ansatz
KMS	Kubo-Martin-Schwinger [condition]
LS	Landau-Spitzer [energy relaxation model]
LFC	Local field correction
IA	Impulse approximation

ICF	Inertial confinement fusion
MB	Maxwell-Boltzmann [distribution function]
MC	Monte Carlo [simulation]
MCSS	Multicomponent scattering simulation
MD	Molecular dynamics [simulation]
NIF	National Ignition Facility
OCP	One-component plasma
OTS	Optical Thomson scattering
PDF	Probability density function
PIC	Particle-in-cell [simulation]
RCM	Reduced coupled modes [energy relaxation model]
RFGR	Reduced Fermi golden rule [energy relaxation model]
RPA	Random phase approximation
SFF	Static structure factor
SLFC	Static local field correction
SP	Stewart-Pyatt [continuum lowering model]
SRR	Short range repulsion [interaction potential]
TS	Thomson scattering
TT	Two-temperature [distribution function]
VIXEN	Volume-integrated x-ray scattering for experiments in non-uniform plasmas
WDM	Warm dense matter
XRTS	X-ray Thomson scattering

Indices

'$a, b, \ldots$'	General particle species labels
'e, i'	Particle species labels for electrons and ions
'i'	Incident quantity
's'	Scattered quantity

Fundamental constants in SI units (with experimental uncertainty)

$a_\mathrm{B} = 5.2917721092(17) \times 10^{-11}\,\mathrm{m}$	Bohr radius
$c = 2.99792458 \times 10^{8}\,\mathrm{m\,s^{-1}}$	Speed of light in free space
$e = 1.602176565(35) \times 10^{-19}\,\mathrm{C}$	Fundamental unit of charge
$\hbar = 1.054571726(47) \times 10^{-34}\,\mathrm{J\,s}$	Dirac's constant
$k_\mathrm{B} = 1.3806488(13) \times 10^{-23}\,\mathrm{J\,K^{-1}}$	Boltzmann's constant
$m_e = 9.10938215(45) \times 10^{-31}\,\mathrm{kg}$	Mass of an electron
$m_u = 1.660538921(73) \times 10^{-27}\,\mathrm{kg}$	Unified atomic mass of nucleons
$r_e = 2.8179403267(27) \times 10^{-15}\,\mathrm{m}$	Classical radius of an electron
$\varepsilon_0 = 8.854187817\ldots \times 10^{-12}\,\mathrm{F\,m^{-1}}$	Permittivity of free space
$\mu_0 = 4\pi \times 10^{-7}\,\mathrm{H\,m^{-1}}$	Permeability of free space

Important physical quantities

$1 = \{\mathbf{r}_1, t_1, \sigma\}$	Position-time-spin basis
$a^\dagger(\nu)$, $a(\nu)$	Construction operators [operating on states with basis ν]
$C_{ab} = \partial U_a / \partial T_b$	Heat capacity
$C_{ei} = \nu_{ei}(0)/\omega_{\mathrm{p}e}$	Collision parameter
$d_{aa} = (\pi n_a/6)^{-1/3}$	Mean inter-particle separation
$D_a = n_a \Lambda_a^3/(2\sigma_a + 1)$	Equilibrium degeneracy parameter
$\tilde{D}_a = \max(f_a(\mathbf{p}))$	Non-equilibrium degeneracy parameter
E	Energy
$E_a(\mathbf{p}) = p^2/2m_a$	Free-particle kinetic energy
$E_{\mathrm{F}a} = p_{\mathrm{F}a}^2/2m_a$	Fermi energy
$E_{n,l}^{\mathrm{bind}}$	Binding energy for state n, l
$f_a(\mathbf{k})$, $f_a(k)$	Ionic form factor
$f_a(\mathbf{p})$	Distribution function [in momentum space]
$g_{ab}(\mathbf{r})$, $g_{ab}(r)$	Classical [radial] pair distribution/correlation function
$G_{a\ldots n}(1\ldots N, 1'\ldots N')$	Many-particle correlation/Green's function
$G_a(1,1')$, $G_a(\mathbf{k},\omega)$	Single-particle correlation/Green's functions
$G_a^0(1,1')$, $G_a^0(\mathbf{k},\omega)$	Free-particle correlation/Green's function
$G_{aa}(\mathbf{k})$, $G_{aa}(k)$	Static local field correction
$G_{aa}(\mathbf{k},\omega)$	Dynamic local field correction
I	Intensity [of radiation]
$J_{n,l}(\mathbf{k},\omega)$	Dimensionless Compton profile for state n, l
$\mathbf{k}$	Wave vector
k	Wave vector magnitude/wave number
$\langle K_a \rangle$	Mean kinetic energy
$L_{ab}(1,1')$, $L_{ab}(\mathbf{k},\omega)$	Density response/fluctuation correlation function
n_a	Mean particle number density
$n_{\mathrm{B}a}(\omega) = (e^{\beta_a \hbar\omega} - 1)^{-1}$	Bose function
N_a	Total number of particles
$p = \hbar k$	Momentum magnitude
$\mathbf{p} = \hbar\mathbf{k}$	Momentum vector
$p_a = (m_a/\beta_a)^{1/2}$	Thermal momentum
$p_{\mathrm{F}a} = \hbar(6\pi n_a/(2\sigma_a+1))^{1/3}$	Fermi momentum
P	Power
$q_a(\mathbf{k})$, $q_a(k)$	Screening cloud
$\mathbf{Q}_a$	Heat flux
Q_a	Charge
$\mathbf{r}$	Position vector/microscopic Wigner position
$\mathbf{R}$	Macroscopic Wigner position
$S_{ab}(\mathbf{k})$, $S_{ab}(k)$	Static structure factor
$S_{ab}(\mathbf{k},\omega)$	Dynamic structure factor

$S_a^0(\mathbf{k},\omega)$	Non-interacting dynamic structure factor
t	Time/macroscopic Wigner time
T_a	Temperature
U_a	Mean internal energy
v	Velocity magnitude/speed
$\mathbf{v}$	Velocity vector
$v_a = (m_a\beta_a)^{-1/2}$	Thermal speed
$\mathcal{V}$	Volume
$\langle V_{aa}\rangle = Q_a^2/4\pi\varepsilon_0 d_{aa}$	Mean Coulomb potential energy
$V_{ab}(1,1')$, $V_{aa}(\mathbf{r})$	Pair interaction potential energy
$V_{ab}(k) = Q_aQ_b/\varepsilon_0 k^2$	Fourier transform of Coulomb potential
$w_a = \omega/\sqrt{2}kv_a$	Dimensionless frequency shift
$W_{ab}(1,1')$	Screened potential energy
$W_{\mathrm{C}}(\mathbf{k},\omega)$	Total inelastic scattering/Compton profile
$W_{\mathrm{R}}(\mathbf{k})$, $W_{\mathrm{R}}(k)$	Elastic scattering/Rayleigh amplitude/weight
$\mathcal{W}(\mathbf{R})$	Total three-dimensional weighting function
$x_a = n_a/\sum_a n_a$	Partial number density
Z_a^{A}	Atomic number of atom
Z_a^{b}	Number of bound electrons per atom
Z_a^{f}	Number of free electrons per atom
Z_a, Z_a^*, $\bar{Z}_a^{\mathrm{f}}$	Mean ionic charge [in units of e]
$Z_{n,l}^{\mathrm{eff}}$	Effective nuclear charge seen by an electron in state n, l
$\mathcal{Z}_{ab}$	Energy exchange rate per unit volume
$\alpha = \kappa_e/k$	Salpeter scattering/collectivity parameter
$\beta_a = (k_{\mathrm{B}}T_a)^{-1}$	Inverse temperature [in units of energy]
$\Gamma_{aa} = \langle V_{aa}\rangle/\langle K_a\rangle$	Coupling parameter
$\delta\varrho_a = n_a - \langle n_a\rangle$	Density fluctuation
Δ	Full-width half-maximum [of a distribution]
ΔE	Ionization potential depression
$\varepsilon(1,1')$, $\varepsilon(\mathbf{k},\omega)$	Total dielectric screening function
$\eta_a = \beta_a\mu_a$	Dimensionless chemical potential
θ	Scattering angle/declination angle [in spherical coordinates]
$\Theta_a = (\beta_a E_{\mathrm{F}a})^{-1}$	Alternative degeneracy parameter
κ_a	Screening wave number
$\kappa_{\mathrm{D}a} = (Q_a^2 n_a\beta_a/\varepsilon_0)^{1/2}$	Debye screening wave number
$\kappa_{\mathrm{TF}a} = (3Q_a^2 n_a/2\varepsilon_0 E_{\mathrm{F}a})^{1/2}$	Thomas-Fermi screening wave number
$\varkappa_a = \hbar k/\sqrt{8}p_a$	Dimensionless Compton shift
$\Lambda_a = \sqrt{2\pi}\hbar/p_a$	Thermal de Broglie wavelength
μ_a	Chemical potential
$\nu_{ei}(\omega)$	Dynamic electron-ion collision frequency
$\Pi_{ab}(1,1')$, $\Pi_{ab}(\mathbf{k},\omega)$	Polarisation function
ρ	Mass density

$\hat{\rho}$	Statistical operator
σ_a	Spin (intrinsic angular momentum)
$\sigma_\mathrm{T} = 8\pi r_e^2/3$	Thomson cross section
$\Sigma(\omega)$	X-ray source function
$\bar{\Sigma}_a(1,1')$	Screened self energy function
τ	Microscopic Wigner time
χ^2	Statistical measure of mean square deviation
$\psi^\dagger(1)$, $\psi(1)$	Field operators (construction operators in position basis)
ω	Frequency/frequency shift
$\omega_{\mathrm{C}a} = \hbar k^2/2m_a$	Compton frequency
$\omega_{\mathrm{p}a} = (Q_a^2 n_a/\varepsilon_0 m_a)^{1/2}$	Plasma frequency
$\mathrm{d}\Omega = \sin\theta\,\mathrm{d}\theta\,\mathrm{d}\phi$	Solid angle element

Mathematical functions and symbols

$[A,B]^\pm = AB \mp BA$	Symmetrised commutator between quantites A and B
$\langle A \rangle$	Ensemble average of operator A over the many-particle system
$\mathrm{Tr}(A)$	Trace of operator A
$\Gamma(x)$	Complete Gamma function
$\nabla_\mathbf{r}$	*Nabla* or *Del* gradient operator [with respect to $\mathbf{r}$]
$\delta(x)$	Dirac delta distribution
δ_{ab}	Kronecker delta symbol
$\mathcal{D}(x)$	Dawson function of the first kind
$\mathrm{erf}(x)$	Error function
$\mathcal{F}\{A\}$, $\mathcal{F}^{-1}\{A\}$	Fourier transform/inverse transform of a function A
$\mathcal{F}_j(x)$	Complete Fermi integral function of order j
$\Theta(x)$	Heaviside unit step function
$\mathcal{P}$	Cauchy principal value of an integral
ϵ	Real infinitesimal quantity
r, k, p, etc.	Scalar quantities
$\mathbf{r}$, $\mathbf{k}$, $\mathbf{p}$, etc.	Vector quantities
$\lvert\psi\rangle$	Ket vector for state ψ
$\langle\psi\rvert$	Bra vector for state ψ (adjoint of $\lvert\psi\rangle$)
$\partial f(x)/\partial x$	Partial derivative of function $f(x,y,\dots)$ with respect to variable x
$\delta f(x)/\delta g(x')$	Functional derivative of function $f(x)$ with respect to function $g(x')$
$\mathrm{Re}A$, $\mathrm{Im}A$	Real and imaginary parts of complex quantity A

Chapter 1

Introduction

Within the last few decades, significant advances in laser technology, pulsed-power machines, versatile and powerful diagnostic techniques and high-performance computing have enabled large strides to be taken in the field of high-energy-density (HED) physics. The latest generation of experimental facilities combine the power of high-energy, high-intensity and ultra-short duration drivers for heating and compressing matter to extreme conditions with cutting-edge diagnostic capabilities. Such extreme states of matter are of fundamental interest to a diverse range of active fields, including laboratory astrophysics and planetary physics, inertial confinement fusion (ICF) research and materials science, on both microscopic and macroscopic scales. Moreover, in the age of the comprehensive test ban treaty, producing and understanding HED matter is of crucial importance to underwriting a fully predictive capability for certifying existing stockpiles.

The rapid rate of progress made in these fields is exemplified by the achievements of the National Ignition Facility (NIF) at Lawrence Livermore National Laboratory (LLNL), USA [Moses and Wuest, 2005]. Following the completion of the facility in 2009, records in the pressure, temperature, implosion symmetry and neutron yield produced in indirectly-driven implosions have been consistently set and subsequently broken [Landen et al., 2011; Mackinnon et al., 2012; Robey et al., 2012; Glenzer et al., 2012]. Indeed, the recently reported and much publicised milestone of *scientific break even* [Hurricane et al., 2014] has demonstrated that self-sustaining nuclear fusion may soon be in reach. However, the set backs and difficulties encountered during the National Ignition Campaign have served to highlight the scale of the challenges that remain and, in particular, the crucial role of advanced theoretical and computational tools for platform design, modelling and optimisation, and in supporting data analysis [Dittrich et al., 2014].

In addition to large-scale facilities such as the NIF, a new generation of medium-scale high-power lasers incorporating both long-pulse and short-pulse technology provide highly flexible platforms for HED physics research. Important examples are the Omega laser at the Laboratory for Laser Energetics in Rochester, USA [Boehly et al., 1997], the Vulcan laser at the Rutherford Appleton Laboratory [Danson et al., 1998] and the newly commissioned Orion laser at AWE's Aldermaston site [Hopps et al., 2015], both in the UK, as well as many others around the world. Combining high-energy long-pulse drivers

with short-pulse laser-driven heating sources such as energetic charged particles allows for hot, dense plasmas to be produced on sufficiently short time scales for complexities such as hydrodynamic motion and instabilities to be effectively mitigated [Roth et al., 2009; Pelka et al., 2010; Brown et al., 2011].

Another exciting area of current development is in the use of x-ray free-electron lasers (FELs) such as the free-electron laser in Hamburg (FLASH) at DESY, Germany [Ackermann et al., 2007], and the Linac Coherent Light Source (LCLS) at Stanford University, USA [Arthur, 2002]. These machines can produce ultra-bright, coherent x-rays with narrow bandwidths and in ultra-short pulses over time scales of direct relevance to atomic processes [Gaffney and Chapman, 2007]. Furthermore, by combining FELs with optical laser systems [Nagler et al., 2015], measurements of hot, dense plasmas are made possible with unparalleled signal-to-noise ratio and repeatability. LCLS in particular has enabled the development of novel diagnostic techniques [Wang et al., 2012], as well as vastly improving the x-ray probes used for scattering measurements [Brown et al., 2014; Gauthier et al., 2014; Gamboa et al., 2015; Fletcher et al., 2015].

Of particular interest to this work is the warm dense matter (WDM) regime. This occurs as a transient state in all laser-matter interactions in which the target is initially at near-solid density and, furthermore, is thought to exist in the cores of giant planets [Guillot, 1999] and massive compact objects, such as white dwarfs and the crusts of neutron stars [Dufour et al., 2007]. Here, theoretical descriptions are made exceptionally challenging by the need for a fully quantum mechanical description, which goes beyond simple *ideal* models. Important examples of properties affected by uncertainties due to these considerations are the equation of state (EOS) [Hoarty et al., 2012; Morales et al., 2012; Vorberger et al., 2006; 2013], energy and temperature equilibration [Ng et al., 1995; Dharma-wardana and Perrot, 1998; Vorberger et al., 2010; White et al., 2014], transport properties [Perrot and Dharma-wardana, 1987; Gericke and Schlanges, 1999; Gericke et al., 2002b; Zylstra et al., 2015] and dynamic phenomena such as charge screening and the dielectric response [see, e.g., Fortmann et al., 2010; Plagemann et al., 2012; Chapman et al., 2015].

Another complication arises in the analysis of experimental data, which can be undermined by insufficiently detailed modelling methodologies as well as shortcomings in theoretical understanding. In the case of WDM, the preparation of the state of interest may lead to significant spatial inhomogeneities in the target, i.e. gradients in temperature, density, etc., or strongly time-dependent non-equilibrium effects with respect to both momentum and energy relaxation over the duration of the measurement. Indeed, such considerations are well-known to constitute significant sources of uncertainty in the interpretation of experimental data.

1.1 Characterisation of dense matter

In general, the experimentally observable properties of dense matter vary strongly depending on the importance of quantum effects, the influence of inter-particle coupling,

relativistic effects and the roles of collective and non-collective behaviour. Since a statistical picture is ubiquitously necessary for interpreting experimental data and constructing theoretical models, it is natural to base the characterisation of a particular system on the properties of the distribution function $f_a(\mathbf{p})$.

For the important case of systems in thermal equilibrium the relevant description is given by either the Fermi-Dirac (FD) [Fermi, 1926; Dirac, 1926] or Bose-Einstein (BE) [Bose, 1924; Einstein, 1924] distributions

$$f_a(\mathbf{p}) = \left[\exp\left(\frac{p^2}{2p_a^2} - \eta_a\right) \pm 1\right]^{-1}, \tag{1.1}$$

for fermions (+) or bosons (−), respectively. For plasmas, the constituent particles (electrons, protons and ions) are fermions and, thus, the properties of the FD distribution are of interest. In Eq. (1.1), $p_a = (m_a/\beta_a)^{1/2}$ is the thermal momentum, $\eta_a = \beta\mu_a$ is the dimensionless chemical potential and $\beta = (k_\mathrm{B}T)^{-1}$.

Taking the limit $\eta_a \to -\infty$ yields the classical Maxwell-Boltzmann (MB) distribution, whereas in the opposite limit $\eta_a \to +\infty$ one obtains the fully degenerate Fermi distribution

$$f_a(\mathbf{p}) = \begin{cases} \exp\left(\eta_a - \frac{p^2}{2p_a^2}\right) & : \eta_a \to -\infty \\ \\ \Theta(p_{\mathrm{F}a} - p) & : \eta_a \to +\infty \end{cases}. \tag{1.2}$$

Here, $\Theta(p_{\mathrm{F}a} - p)$ is the Heaviside function and $p_{\mathrm{F}a} = (2m_a\mu_a)^{1/2}$ is the Fermi momentum. The fact that one obtains these two distinct limits highlights the importance of temperature on the properties of the system, due in particular to the importance of the spin statistics postulate [Pauli, 1925; 1940] under conditions where random thermal motion is too weak to mask the quantum nature of the particles. The difference is fundamentally determined by the chemical potential η_a, which can be obtained from the normalisation condition

$$n_a = \sum_{\sigma_a} \int \frac{\mathrm{d}\mathbf{p}}{(2\pi\hbar)^3}\, f_a(\mathbf{p}). \tag{1.3}$$

Here, n_a is the total mean number density of particles of species a. For fermions the sum over the particle spins σ_a is $\sum_{\sigma_a} = 2\sigma_a + 1$. Applying Eqs. (1.1) and (1.2) one has

$$\eta_a = \mathcal{F}_{1/2}^{-1}(D_a) = \begin{cases} \ln(D_a) & : \eta_a \to -\infty \\ \\ \beta E_{\mathrm{F}a} = \left(\dfrac{3D_a}{4\sqrt{\pi}}\right)^{2/3} & : \eta_a \to +\infty \end{cases}. \tag{1.4}$$

where, $\mathcal{F}_j^{-1}(x)$ is the inverse of the Fermi integral of order j [Kremp et al., 2005]

$$\mathcal{F}_j(x) = \frac{1}{\Gamma(j+1)} \int_0^\infty \mathrm{d}t\, t^j \left[e^{t-x} + 1\right]^{-1}, \quad \Gamma(j+1) = \int_0^\infty \mathrm{d}t\, t^j e^{-t}. \tag{1.5}$$

From Eq. (1.4), the importance of quantum statistics in determining the properties of the system is governed by the *degeneracy parameter*

$$D_a = \frac{n_a \Lambda_a^3}{2\sigma_a + 1} \equiv \mathcal{F}_{1/2}(\eta_a). \tag{1.6}$$

Eq. (1.6) compares the mean number density to the volume associated with the mean spatial extent of the wavefunction of an individual particle, i.e. the thermal (de Broglie) wavelength $\Lambda_a = \sqrt{2\pi}\hbar/p_a$, and, thus, measures the overlapping of the wavefunctions of individual particles. One has $D_a \ll 1$ for non-degenerate states, since particles are effectively localised and may be treated classically, and $D_a \gg 1$ in degenerate matter.

For systems out of thermal equilibrium, Eq. (1.6) is not suitable as the concept of temperature is not well-defined. One might alternatively give a more general definition in terms of the maximum occupation of the distribution

$$\tilde{D}_a = \max(f_a(\mathbf{p})), \tag{1.7}$$

such that non-degenerate states again have $\tilde{D}_a \ll 1$, whilst degeneracy is important for distributions in which a given momentum state is highly occupied. For example, $\tilde{D}_a \to 1$ for particles with $\sigma_a = 1/2$. Note that under equilibrium conditions in the non-degenerate limit the MB distribution returns $\tilde{D}_a \equiv D_a$. This definition may be important for states which are strongly driven around high energies, e.g. rapidly photoionized solids, which produce highly non-equilibrium distribution functions [see, e.g., Ziaja and Medvedev, 2012; Medvedev et al., 2013; Abdallah Jr et al., 2013].

Another important factor is the effect of inter-particle correlations. This can be estimated by a generalised *coupling parameter* [Brush et al., 1966]

$$\Gamma_{aa} = \frac{\langle V_{aa} \rangle}{\langle K_a \rangle}, \tag{1.8}$$

which compares the mean kinetic energy of free (non-interacting) particles with the mean energy due to interactions. For charged-particles systems one has

$$\langle V_{aa} \rangle = \frac{Q_a^2}{4\pi\varepsilon_0 d_{aa}}, \tag{1.9}$$

$$\langle K_a \rangle = \frac{2\sigma_a + 1}{n_a} \int \frac{\mathrm{d}\mathbf{p}}{(2\pi\hbar)^3} \frac{p^2}{2m_a} f_a(\mathbf{p}), \tag{1.10}$$

in which $d_{aa} = (6/\pi n_a)^{1/3}$ is the mean inter-particle separation. In equilibrium the mean kinetic energy has the expected limits [Kremp et al., 2005]

$$\langle K_a \rangle \overset{\text{equil.}}{=} \frac{3}{2} k_\mathrm{B} T \frac{\mathcal{F}_{3/2}(\eta_a)}{D_a} = \begin{cases} \frac{3}{2} k_\mathrm{B} T & : \eta_a \to -\infty \\ \frac{3}{5} E_{\mathrm{F}a} & : \eta_a \to +\infty \end{cases}. \tag{1.11}$$

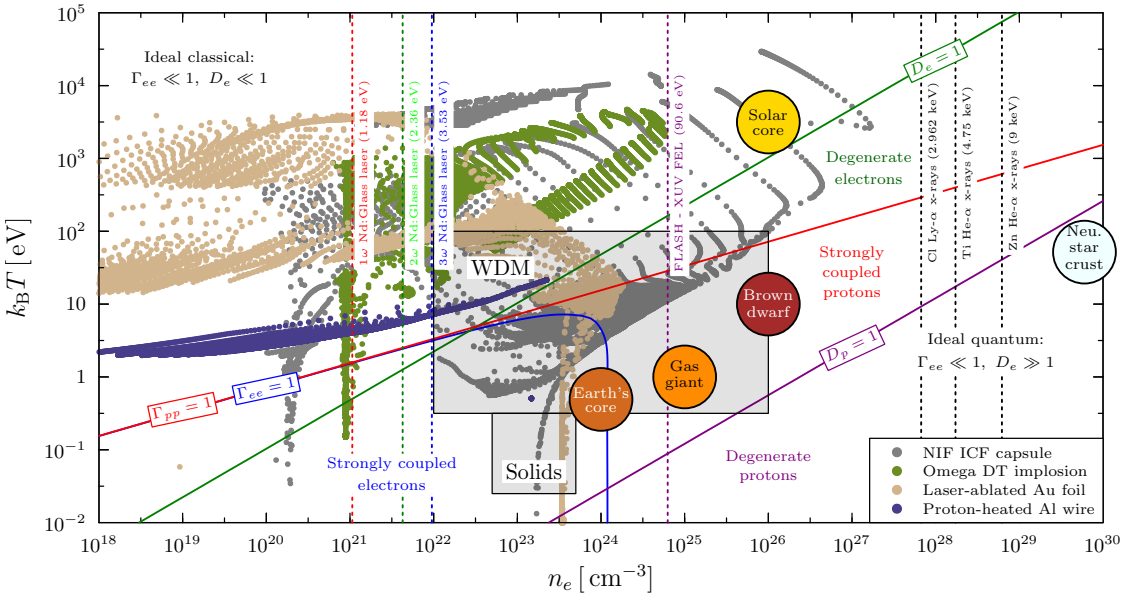

Figure 1.1: Phase space plot for a hydrogen plasma in the density-temperature plane showing the contours separating degenerate and strongly coupled states. The conditions related to various astrophysical objects are shown for comparison. Furthermore, cell trajectories from radiation-hydrodynamics simulations of laser-driven plasmas relevant to this work (courtesy of W. Garbett, J. Morton and T. Guymer) are also plotted: an ICF ignition shot for the NIF, a directly-driven capsule implosion at Omega, a laser-ablated gold foil target and a proton-heated aluminium wire target. The important WDM regime may loosely be defined to occupy the region marked by the black box near the centre of the figure.

For $\Gamma_{aa} \ll 1$ the random motions of the particles dominate over correlations mediated via interactions and the system is *weakly coupled*, whereas for $\Gamma_{aa} \gg 1$ the interactions dominate and the system is said to be *strongly coupled*. In the intermediate regime, $\Gamma_{aa} \sim 1$, simple approximations break down and detailed theoretical descriptions and numerical simulations are generally required; these are appropriately described as *non-ideal*. Note that for non-equilibrium systems, the structural and dynamical behaviour may be dominated by non-thermal depletion or enhancement of the number of high-energy particles. This has important connotations for transport properties such as the electrical and thermal conductivity [Atzeni and Meyer-ter-Vehn, 2004].

The importance of different regimes of quantum and non-ideal effects may be visually depicted on the density-temperature plane, as shown in Fig. 1.1. The upper-left quadrant of the plane corresponds to weakly coupled and non-degenerate (classical) states. These are important to understand for problems such as laser propagation through plasma filled hohlraums [Glenzer et al., 2002; Froula et al., 2007], and in the long-time hydrodynamics of the post-ignition and decompression phases of ICF-relevant implosions [Atzeni and Meyer-ter-Vehn, 2004]. States in the lower-right quadrant are weakly coupled by virtue having a high Fermi energy but must be treated with quantum statistics. Massive-compact stellar objects such as the outer crustal envelopes of neutron stars lie in this region, which can be

studied using the methods of condensed matter physics [Ichimaru, 1994a;b].

The WDM regime may loosely be defined by the conditions bounded by the central shaded box, where the densities range from $0.1\rho_0 \lesssim \rho \lesssim 1000\rho_0$ (ρ_0 is the ambient density of typical solids) and the temperatures range from $0.1\,\mathrm{eV}(\sim T_{\mathrm{melt}}) \lesssim T \lesssim 100\,\mathrm{eV}$. In this region, an accurate theoretical picture of matter is made challenging by the confluence of strong correlations in both the electrons and ions, partial ionization, quantum effects, non-equilibrium considerations and phase transitions. Note that all systems of interest to this work lie in the region of phase space in which ions may be treated using classical MB statistics, and that relativistic effects are also always negligible.

1.2 X-ray Thomson scattering as a dense plasma diagnostic

Given the theoretical uncertainties associated with modelling these properties, especially in the WDM regime, experimental verification is essential. In particular, the benchmarking of advanced analytic models and numerical simulations [Mancic et al., 2010; Pelka et al., 2010; Kraus et al., 2013] constitutes one of the grand challenges of contemporary physics [Graziani et al., 2014a]. The most critical aspect which underpins the success of such investigations is the reliability with which the diagnostics used are able to determine the precise conditions achieved in the experiment.

Broadly speaking, dense plasma diagnostics can be separated into radiation-based and particle-based diagnostics, of which the former are of interest to this work. For example, spectroscopy [Brown et al., 2011; Hoarty et al., 2013a], x-ray radiography [Kritcher et al., 2014], calorimetry [Bourgade et al., 2001], velocimetry [Celliers et al., 204] and novel x-ray imaging methods [Bachmann et al., 2014], as well as combinations of such techniques [Falk et al., 2014], have all been used to investigate dense matter.

Another powerful technique which has been extensively developed in recent years is x-ray Thomson scattering (XRTS) [Glenzer and Redmer, 2009]. In contrast to many of the aforementioned techniques, XRTS enables information on the interiors of dense targets to be obtained. Moreover, it is nominally non-perturbative and is based on first principles. Another attractive quality of XRTS is that it is less susceptible to issues such as detailed understanding of the atomic physics of the material; the latter is of crucial importance to spectroscopic measurements. Having control over the energy of the probe allows a particular experimental platform to be optimised by tuning the x-ray energy away from strong absorption features in the target's opacity [Hill and Rose, 2012], and also the energy range dominated by Bremsstrahlung [Fortmann et al., 2006].

1.2.1 Historical context

The earliest studies on the scattering of electromagnetic (EM) radiation date back to the mid-19th century with the empirical investigations of Tyndall [Tyndall, 1870] on the colour of the sky. The theoretical grounds for Tyndall's observations were given by Strutt

(Lord Rayleigh) [Strutt, 1881]. Therein, the origin of the blue colour was shown to result from the scattering of sunlight by fine atmospheric particulates, with the strength of the scattering scaling strongly and inversely on the frequency of the light. However, Rayleigh's theory was found to be insufficient to describe scattering from charged particle systems, as demonstrated by Thomson [Thomson, 1906] during experiments investigating the nature and properties of cathode rays (electrons).

The physical mechanism of Thomson scattering is based on the classical theory of electromagnetism. Ignoring relativistic effects [Palastro et al., 2010; Ross et al., 2010], free electrons are accelerated by the time-varying electric field of the incident wave, producing oscillating dipoles which re-radiate into a characteristic toroidal angular distribution [see, e.g., Jackson, 1962; Sheffield et al., 2011]. The frequency distribution of this scattered radiation is Doppler broadened due to the random distribution of electron velocities. Within this classical picture, the scattering process is considered to be elastic as the states of the scattering electrons are not affected by the radiation. This picture was subsequently overturned in the early 1920s by the discovery of the Compton effect [Compton, 1923]. At this point, the discussion of scattering as an experimental diagnostic technique necessarily diverges; experiments using low-energy EM radiation, such as optical-wavelength and infrared light, microwaves and radio waves, evolved along a separate, largely independent trajectory to those making use of high-energy ionizing radiation, including extreme-ultraviolet (XUV) light and x-rays.

The first measurements of the properties of plasmas using scattering techniques relate to backscattering of radio waves from the ionosphere [Bowles, 1958]. This revealed some of the first evidence in support of the collective behaviour of electrons in plasmas [Bohm and Gross, 1949; Klimontovich and Silin, 1952; Salpeter, 1960]. Subsequently, the use of optical-wavelength Thomson scattering (OTS) using lasers from low-density laboratory plasmas was proposed by Fünfer et al. [Fünfer et al., 1963] and Kunze et al. [Kunze et al., 1963]. This early work was developed theoretically by Evans and Katzenstein [Evans and Katzenstein, 1969], and applied to magnetically confined Tokamak plasmas as an accurate temperature diagnostic [Peacock et al., 1969]. Following the rapid development of high-power laser facilities in the 1970s and 1980s, constructed primarily to investigate ICF and other related high-energy-density physics, OTS became an established and indispensable diagnostic tool [see, e.g., Landen and Winfield, 1985; La Fontaine et al., 1994; Glenzer et al., 1997; 1999a; Froula et al., 2006b;a].

During this period, enormous progress in understanding the detailed microscopic structure of cold solids at ambient density had been made using x-ray diffraction and crystallography. This is fundamentally distinct from OTS not only in the need for a quantum mechanical treatment of the scattering process, but also in the information obtained from the sample. Specifically, x-ray diffraction is angularly resolved and spectrally integrated, yielding information on the static structure via the Bragg condition. On the other hand, OTS is spectrally resolved and, thus, is primarily sensitive to the dynamic response of the

sample to the probe. Use of thermal line emission from laser-irradiated targets was then developed as a spectrally resolved diagnostic for cold matter in the early 1970s. Observations of the excitation spectrum of cold Be by Miliotis [Miliotis, 1971] gave the first experimental verification of predictions of solid state theory concerning the collective behaviour of electrons in the conduction band of metals, known as plasmons. These early results gave rise to the possibility of simultaneously heating, compressing and probing dense matter using high-energy lasers. The first suggestions of combining the diagnostic power of OTS with the penetrative capability provided by x-rays, so-called x-ray Thomson scattering (XRTS), at such facilities were given by Riley et al. [Riley et al., 2000] and Landen et al. [Landen et al., 2001].

1.2.2 Basic concepts

In order for EM radiation to propagate through a plasma its frequency must exceed the plasma frequency

$$\omega_\mathrm{p}^2 = \sum_a \omega_{\mathrm{p}a}^2 = \sum_a \frac{Q_a^2 n_a}{\varepsilon_0 m_a}. \tag{1.12}$$

This quantity is dominated by the electrons due to their small mass, i.e. $\omega_\mathrm{p} = \omega_{\mathrm{p}e}$. The dispersion relation in the material relating the wave number k_i and frequency ω_i is then changed from the usual *in vacuo* relation $\omega_\mathrm{i} = ck_\mathrm{i}$ according to

$$k_\mathrm{i}^2 = \frac{\omega_\mathrm{i}^2}{c^2}\left(1 - \frac{\omega_{\mathrm{p}e}^2}{\omega_\mathrm{i}^2}\right) = \frac{\omega_\mathrm{i}^2}{c^2}\left(1 - \frac{n_e}{n_\mathrm{crit}}\right) = \frac{\omega_\mathrm{i}^2 \mu^2}{c^2}. \tag{1.13}$$

For radiation with frequencies below the plasma frequency, one has $\mu^2 < 0$ and the wave suffers strong damping and reflection [Kruer, 1992]. Setting $\mu = 0$, on finds that radiation of a given energy can only freely propagate up to a critical electron density

$$n_\mathrm{crit} = \frac{\varepsilon_0 m_e \omega_\mathrm{i}^2}{e^2} \approx 7642 \times 10^{23} E_\mathrm{keV}^2 \,\mathrm{cm}^{-3}, \tag{1.14}$$

where E_keV is the x-ray energy in units of keV. The use of OTS is therefore clearly restricted to electron densities several orders of magnitude less than those present in the dense plasmas of interest (see the vertical colour-coded lines in Fig. 1.1). On the other hand, high-energy x-rays with $0.1 \lesssim \hbar\omega_\mathrm{i} \lesssim 10\,\mathrm{keV}$ are easily capable of penetrating such dense states of matter.

The probability that the radiation will be scattered in any direction is given by the low-energy limit of the Klein-Nishina cross section [Klein and Nishina, 1929]

$$\sigma_\mathrm{KN} = \sigma_\mathrm{T}\left[1 - 2\frac{\hbar\omega_\mathrm{i}}{m_e c^2} + \frac{26}{5}\left(\frac{\hbar\omega_\mathrm{i}}{m_e c^2}\right)^2 + \ldots\right]. \tag{1.15}$$

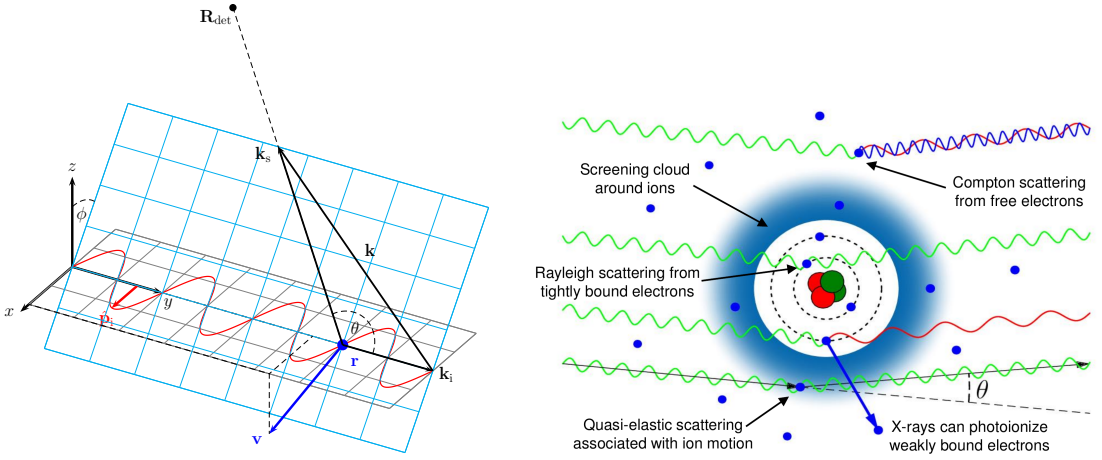

(a) Geometry of scattering experiments. (b) Sources of scattering in partially-ionized plasmas.

Figure 1.2: (a): Diagrammatic representation of the scattering geometry for which the incident probe with wave vector $\mathbf{k}_{\rm i}$ is scattered by an electron at $\mathbf{r}$ with initial velocity $\mathbf{v}$ into a detector instrument located at $\mathbf{R}_{\rm det}$ through an angle θ. Wave vector of the scattered radiation is $\mathbf{k}_{\rm s}$, giving a shift of $\mathbf{k}$ from the incident probe. The angle ϕ denotes the rotation of the scattering plane (cyan) relative to the plane defined by polarisation vector of the incident EM wave $\hat{\mathbf{p}}_{\rm i}$ (grey). (b): Cartoon illustration of the different sources of scattering from a partially-ionized plasma showing elastic, inelastic free-free, and inelastic bound-free contributions.

Here, $\sigma_{\rm T} = 6.65 \times 10^{-29}\,{\rm m}^2$ is the famous Thomson cross section. Corrections beyond the leading order are negligible for $\hbar\omega_{\rm i} \lesssim 10\,{\rm keV}$. In addition to having sufficiently high energies to penetrate the target, the small value of $\sigma_{\rm T}$ requires that the probe pulse contains a sufficiently large number of photons if a useful scattering signal is to be observed.

The development of high-intensity, high-energy x-ray sources suitable for XRTS have progressed significantly since early platforms were proposed. For *long* ($\sim$ ns) duration sources, the thermal line emission from laser-heated foils can be used. These have steadily advanced in both x-ray energy and peak intensity from Ly-α radiation at $\sim 3\,{\rm keV}$ from thin Cl-doped plastic targets [Glenzer et al., 2003; Urry et al., 2006; García Saiz et al., 2008] to He-α radiation between $\sim$5–18 keV from metal foils, such as Ti, Mn, Zn and Mo [Gregori et al., 2004; Lee et al., 2009; Kritcher et al., 2011b; Ma et al., 2013]. Furthermore, *short* ($\sim$ ps) duration measurements have been made using short-pulse laser-driven K-α fluorescence [see, e.g., Kritcher et al., 2009; Barbrel et al., 2009; Le Pape et al., 2010; Neumayer et al., 2010].

More recently, use of FELs has realised the possibility of probing matter on ultra-short $\sim 10\,{\rm fs}$ time scales, which is relevant to atomic processes [Gaffney and Chapman, 2007; Ziaja and Medvedev, 2012] and the dynamics associated with energy absorption and thermalisation [Medvedev et al., 2011] and phase transitions [Medvedev et al., 2013]. The theoretical descriptions of matter probed with FELs may be significantly more complex

than those required to describe laser-produced sources as the probe is often sufficiently intense to strongly drive the system under study. Accordingly, an evolving, strongly time-dependent non-equilibrium state may be produced, which must be rigorously accounted for when modelling the observed scattering spectrum [see, e.g., Chapman and Gericke, 2011].

A schematic representation of the geometry for scattering from a single moving electron is shown in Fig. 1.2(a). The incident radiation is incoming from the left with wave vector $\mathbf{k}_\mathrm{i}$ and frequency ω_i. The radiation is then scattered through an angle θ towards a distant detector instrument located at $\mathbf{R}_\mathrm{det}$, with a wave vector $\mathbf{k}_\mathrm{s}$ and frequency ω_s. The observed shifts in the wave vector and frequency are given by

$$\mathbf{k} = \mathbf{k}_\mathrm{i} - \mathbf{k}_\mathrm{s}, \tag{1.16}$$

$$\omega = \omega_\mathrm{i} - \omega_\mathrm{s} \approx \mathbf{k}\cdot\mathbf{v} + \omega_{\mathrm{C}e}, \tag{1.17}$$

respectively. The shift in frequency originates from the Doppler shift induced by the particle motion, $\mathbf{k}\cdot\mathbf{v}$, and the Compton shift $\omega_{\mathrm{C}e} = \hbar k^2/2m_e$ resulting from momentum transfer from the probe to the electron. From Eq. (1.17), the spectrum of frequency shifts observed by a spectrally-resolving detector yields a direct measurement of the momentum distribution of the electrons in the target. Moreover, information on the dynamic correlations between electrons can also be accessed.

1.2.3 Spectral features

In dense, partially-ionized plasmas the measured power spectrum typically contains three distinct features, which arise due to interaction of the probe with the different states of the electrons in the target (see Fig. 1.2(b)). Firstly, the electrons that are kinematically free from the ions are able to respond to the probe over a wide frequency range on the order of the electron plasma frequency $\omega_{\mathrm{p}e}$. The nature of this contribution can be either coherent or incoherent, depending on whether the probe samples the correlated or uncorrelated motion of the free electrons, respectively.

Incoherent scattering is observed when the spatial scale length probed by the x-rays is significantly larger than the characteristic scale length over which interactions between free electrons are effectively screened. The probe is then scattered by a thermal ensemble of uncorrelated individual electrons and the spectrum directly reflects the shape of the distribution function along the scattering vector [Sheffield et al., 2011]. For plasmas in thermal equilibrium the width of the distribution provides an accurate measurement of the mean kinetic energy (1.11). Information on the electron (plasma) temperature is therefore obtained under non-degenerate conditions, whereas under strongly degenerate conditions information on the electron density may be obtained via the Fermi energy [Glenzer and Redmer, 2009].

If the probe samples scale lengths within the screening radius the x-rays are scattered by the collective response of the free electrons. The spectrum then exhibits resonances

at the characteristic frequency of the microscopic wave-like fluctuations in the electron density. These are known as *electron plasma waves*, *Langmuir waves* or *plasmons* [Tonks and Langmuir, 1929]. Here, information on the electron density and kinetic energy may be inferred simultaneously from the dispersion (resonance location) and damping (amplitude and width) of the plasmons [Glenzer et al., 2007; Theile et al., 2008; Neumayer et al., 2010].

The scale length accessed by the probe is given by the wave number shift $k = |\mathbf{k}|$

$$k^2 = k_\mathrm{i}^2 + k_\mathrm{s}^2 - 2k_\mathrm{i}k_\mathrm{s}\cos\theta \overset{k_\mathrm{i}\approx k_\mathrm{s}}{\rightarrow} k = 2k_\mathrm{i}\sin(\theta/2). \tag{1.18}$$

Note that the second step tends to be reasonably well-fulfilled for high-energy x-rays only [Glenzer et al., 2000]. The importance of collective behaviour may then be characterised by the *scattering parameter* [Salpeter, 1960]

$$\alpha = \frac{1}{k\lambda_\mathrm{scr}}, \tag{1.19}$$

where λ_scr is the characteristic scale length for charge screening.

In general, the screening of interactions between particles is determined by the dielectric response of the fully coupled system and depends on both the frequency and wave number studied. A simple figure of merit may be given by comparing the scale length probed to the static, long-wavelength result for the screening length taken in the weakly coupled limit. For an arbitrary non-equilibrium isotropic distribution function one finds [Gericke et al., 2010]

$$\kappa_e^2 = \lambda_\mathrm{scr}^{-2} = \frac{e^2 m_e}{\pi^2\hbar^3\varepsilon_0}\int_0^\infty \mathrm{d}p\, f_e(p), \tag{1.20}$$

such that in thermal equilibrium

$$\kappa_e^2 = \lambda_\mathrm{scr}^{-2} \overset{\text{equil.}}{=} \frac{e^2 n_e \beta}{\varepsilon_0}\frac{\mathcal{F}_{-1/2}(\eta_e)}{D_e} = \begin{cases} \kappa_{\mathrm{D}e}^2 = \frac{e^2 n_e \beta}{\varepsilon_0} & : \eta_e \to -\infty \\ \kappa_\mathrm{TF}^2 = \frac{3e^2 n_e}{2\varepsilon_0 E_\mathrm{F}} & : \eta_e \to +\infty \end{cases}. \tag{1.21}$$

As expected, the non-degenerate result $\kappa_{\mathrm{D}e}$ gives the inverse of the Debye-Hückel screening length [Debye and Hückel, 1923] and the degenerate result κ_TF gives the inverse of the Thomas-Fermi screening length [Thomas, 1927; Fermi, 1928]. Collective scattering therefore corresponds to $\alpha \gg 1$, whereas one has $\alpha \ll 1$ for non-collective scattering. From Eq. (1.18), it is clear that the collective regime is most readily accessed for small-angle (forward) scattering, whilst the non-collective regime is accessed by large-angle (backward) scattering.

The second important contribution to the spectrum results from interactions of the probe with electrons which are closely associated with the ions, i.e. electrons in tightly bound states or in the screening cloud surrounding an ion. The frequency range over

which this contribution is significant is dictated by the distribution function of the ions. Accordingly, this feature is negligible for frequencies larger than the ion plasma frequency $\omega_{\mathrm{p}i}$, but is substantially brighter than the free electron contribution for $\omega \lesssim \omega_{\mathrm{p}i}$.

The screening cloud in particular is of interest to OTS experiments as collective excitations of the ions (*ion acoustic waves*) may be accessed [Glenzer et al., 1999a; Froula et al., 2002; 2006b]. In XRTS experiments, however, the bandwidths of present x-ray sources is too large to resolve such low-frequency structure [Gregori and Gericke, 2009]. Moreover, the purely elastic Rayleigh scattering from bound electrons, which is not present in OTS experiments due to the low energy of the probe beam, typically dominates over the screening contribution. In addition to detailed information the electronic screening [Chapman et al., 2015], the elastic feature is generally strongly sensitive to static correlations between the ions and, thus, provides estimates on the ion temperature and mean charge state [Riley et al., 2002; Barbrel et al., 2009; Wünsch, 2011].

The third distinct contribution to the scattering spectrum results from Raman-like transitions into the continuum [Raman and Krishnan, 1928]. Since such transitions are energetically improbable for photon energies less than the excitation thresholds of the bound states, the resulting features appears only for frequency shifts above the various edge features, e.g. the K- and L-edges. It is the dominant contribution for cold or weakly-ionized targets, and has been investigated extensively, principally using synchrotrons where it is referred to as non-resonant inelastic x-ray scattering, since the inception of x-ray scattering [see, e.g., Mattern and Seidler, 2013]. In dense plasmas, the shape of the bound-free feature is typically relatively insensitive to the plasma conditions, but does provides detailed information on the ionization equilibrium of the target. Indeed, the balance between free-free and bound-free scattering has recently been used to perform novel investigation of continuum lowering [Fletcher et al., 2014].

1.3 Scattered power spectrum and dynamic structure factor

The form of the scattered power spectrum can be derived within a relativistic, fully quantum mechanical framework by considering the behaviour of an interacting ensemble of electrons and ions subjected to the time-dependent scalar and vectors potentials associated with the incident x-ray photons [Crowley and Gregori, 2013; 2014]. However, a qualitative understanding of the expected properties of the power spectrum can be achieved using classical electrodynamics [Jackson, 1962; Sheffield et al., 2011].

For simplicity, consider a homogeneous volume of plasma $\mathcal{V}$ containing a number of charged particles $N_a = \mathcal{V} n_a$. The x-ray probe is modelled as an incident plane wave

$$\mathbf{E}_{\mathrm{i}} = E_{\mathrm{i}} e^{i(\mathbf{k}_{\mathrm{i}}\cdot\mathbf{r} - \omega_{\mathrm{i}} t)} \hat{\mathbf{p}}_{\mathrm{i}}, \tag{1.22}$$

where $\hat{\mathbf{p}}_{\mathrm{i}}$ denotes the unit vector in the direction of the electric field polarisation (see

Fig. 1.2). The relevant quantity is the time-averaged scattered power per unit solid angle observed by a detector instrument located at $\mathbf{R}_{\rm det}$, which depends on the distance from the source to the detector and the energy flux scattered in its direction

$$\frac{\partial P_{\rm s}(\mathbf{R}_{\rm det},t)}{\partial\Omega} = R_{\rm det}^2\,\mathbf{S}_{\rm s}\cdot\hat{\mathbf{e}}_{\rm s} = R_{\rm det}^2\varepsilon_0 c\,|\mathbf{E}_{\rm s}(\mathbf{R}_{\rm det},t)|^2\,. \tag{1.23}$$

Here, $\mathbf{S}_{\rm s}=\varepsilon_0 c^2\,\mathbf{E}_{\rm s}\times\mathbf{B}_{\rm s}$ is the Poynting vector of the scattered wave. The time averaging is performed over the period of the radiation T, which is assumed to be large compared to the characteristic life time of inter-particle correlations

$$\frac{\partial P_{\rm s}(\mathbf{R}_{\rm det})}{\partial\Omega} = \overline{\frac{\partial P_{\rm s}(\mathbf{R}_{\rm det},t)}{\partial\Omega}} = R_{\rm det}^2\varepsilon_0 c\lim_{T\to\infty}\frac{1}{T}\int_{-\infty}^{\infty}{\rm d}t\,|\mathbf{E}_{\rm s}(\mathbf{R}_{\rm det},t)|^2\,. \tag{1.24}$$

The electric field emitted from a single moving (non-relativistic) charge in the system (labelled j) can be found by solving the Ampere-Maxwell equation [Jackson, 1962]

$$\mathbf{E}_{\rm s}^j(\mathbf{R}_{\rm det},t) = \frac{Q_a}{4\pi\varepsilon_0 c^2 R_{\rm det}}\left[\hat{\mathbf{e}}_{\rm s}\times(\hat{\mathbf{e}}_{\rm s}\times\dot{\mathbf{v}}_j)\right]_{\rm ret}\,, \tag{1.25}$$

where $\dot{\mathbf{v}}_j$ denotes the acceleration of the particle induced by the E-field of the incident wave. The quantity in square brackets must be evaluated at the *retarded* time $t'\approx t-(R_{\rm det}-\mathbf{r}_j(t')\cdot\hat{\mathbf{e}}_{\rm s})/c$ to account for the time delay related to observations of the state of the particle made at the distant detector. The acceleration is given by the equation of motion under the action of the incident EM wave

$$\dot{\mathbf{v}}_j = \hat{\mathbf{p}}_{\rm i}\frac{Q_a E_{\rm i}}{m_a}e^{i(\mathbf{k}_{\rm i}\cdot\mathbf{r}_j(t')-\omega_{\rm i}t')}, \tag{1.26}$$

where $\mathbf{r}_j(t')$ describes the time-dependent trajectory of the charge as seen from the perspective of the detector instrument.

Since the time-dependent trajectories of all the particles are correlated due to their mutual interactions, the total scattered field cannot be obtained by simply scaling Eq. (1.25) by the number of scatterers. Instead, the scattered field samples a distribution function containing the statistical information on the many-particle system [Klimontovich, 1975]

$$F_a(\mathbf{r},\mathbf{v},t) = \sum_{j=1}^{N_a}\delta(\mathbf{r}-\mathbf{r}_j(t))\,\delta(\mathbf{v}-\mathbf{v}_j(t)). \tag{1.27}$$

The evolution of the distribution function obeys the Boltzmann equation [Hansen and McDonald, 1990] and, thus, encodes the information on the inter-particle correlations. The total scattered electric field is then given by averaging over all possible configurations

$$\mathbf{E}_{\rm s}(\mathbf{R}_{\rm det},t) = \frac{r_e E_i}{R_{\rm det}}\int{\rm d}\mathbf{r}\,n_a(\mathbf{r},t')\left[\hat{\mathbf{e}}_{\rm s}\times(\hat{\mathbf{e}}_{\rm s}\times\hat{\mathbf{p}}_{\rm i})\right]e^{i(\mathbf{k}_{\rm i}\cdot\mathbf{r}-\omega_{\rm i}t')}. \tag{1.28}$$

In Eq. (1.28), the velocity integral has been performed to give the density distribution

$$n_a(\mathbf{r},t') = \int \mathrm{d}\mathbf{v}\, F_a(\mathbf{r},\mathbf{v},t') = \int \frac{\mathrm{d}\mathbf{k}}{(2\pi)^3} \int_{-\infty}^{\infty} \frac{\mathrm{d}\omega}{2\pi}\, e^{i(\mathbf{k}\cdot\mathbf{r}-\omega t')}\, n_a(\mathbf{k},\omega). \tag{1.29}$$

For frequency-discriminating detectors such as spectrometers, the spectral information of the intensity of the scattered field is naturally of principal interest. Appealing to Parseval's theorem [Riley et al., 1998], the average of the intensity in the time domain is equivalent to averaging the intensity of the Fourier transform over scattered frequencies. Thus, by introducing the Fourier transform of the scattered field one may include the frequency dependence of the time-averaged signal Eq. (1.24). Subsequently, the scattered power spectrum at the detector is defined as

$$\frac{\partial^2 P_\mathrm{s}(\mathbf{R}_\mathrm{det},\omega_\mathrm{s})}{\partial\Omega\partial\omega_\mathrm{s}} = R_\mathrm{det}^2 \varepsilon_0 c \lim_{T\to\infty} \frac{1}{\pi T} \left| \int_0^{\infty} \mathrm{d}t\, e^{i\omega_\mathrm{s} t}\, \mathbf{E}_\mathrm{s}(\mathbf{R}_\mathrm{det},t) \right|^2 . \tag{1.30}$$

The factor of $1/\pi$ stems from the fact that the integration range over scattered frequencies is halved since only positive values are sampled.

Substituting Eqs. (1.28) and (1.29) into Eq. (1.30) and writing the time at the source in terms of the retarded time, i.e. $t \approx t' + R/c - \mathbf{r}\cdot\hat{\mathbf{e}}_\mathrm{s}$, the various phase factors may be collected to yield δ-functions which act to select the possible wave vectors and frequencies of $n_a(\mathbf{k},\omega)$ that can be interrogated. The result is

$$\frac{\partial^2 P_\mathrm{s}(\mathbf{R}_\mathrm{det},\omega_\mathrm{s})}{\partial\Omega\partial\omega_\mathrm{s}} = \frac{Z_a^4 m_e^2}{m_a^2} \frac{3\sigma_\mathrm{T}}{2\pi} I_i\, \mathcal{P}(\theta,\phi) \lim_{T\to\infty} \frac{1}{2\pi\mathcal{V}T}\, \left| n_a(\mathbf{k}_\mathrm{s}-\mathbf{k}_\mathrm{i}, \omega_\mathrm{s}-\omega_\mathrm{i}) \right|^2 . \tag{1.31}$$

Here, $I_\mathrm{i} = \frac{1}{2} c\varepsilon_0 E_\mathrm{i}^2$ is the intensity of the incident x-rays and $\mathcal{P}(\theta,\phi) = |\hat{\mathbf{e}}_\mathrm{s} \times (\hat{\mathbf{e}}_\mathrm{s} \times \hat{\mathbf{p}}_\mathrm{i})|^2 = 1-(\hat{\mathbf{e}}_\mathrm{s}\cdot\hat{\mathbf{p}}_\mathrm{i})^2$. The result Eq. (1.31) highlights the dominance of the scattering due to electrons over ions since the ratio is $Z_a^4(m_e/m_a)^2 \ll 1$ for all elements. Furthermore, it demonstrates that the magnitude of the scattered power detected depends on the polarisation of the probing radiation [Sheffield et al., 2011]

$$\mathcal{P}(\theta,\phi) = \begin{cases} 1-\sin^2\theta\,\cos^2\phi & : \text{linearly polarised} \\ 1-\frac{1}{2}\sin^2\theta = \frac{1}{2}(1+\cos^2\theta) & : \text{unpolarised} \end{cases} . \tag{1.32}$$

The optimum configuration is given for linearly-polarised x-rays with $\phi = 90°$, which may be achieved using FELs [Höll et al., 2007]. In comparison, using unpolarised x-rays, e.g. produced by thermal line emission from laser-heated foil backlighters, the amplitude of the signal is sensitive to the scattering geometry only.

It is important to note that a statistically significant number of random fluctuations will be sampled by the probe in the scattering volume. The measured power spectrum

therefore reflects the ensemble average of the spectral electron density

$$\frac{\partial^2 P_{\rm s}(\mathbf{R}_{\rm det},\omega_{\rm s})}{\partial\Omega\partial\omega_{\rm s}} = \frac{3\sigma_{\rm T}}{2\pi} I_i\, \mathcal{P}(\theta,\phi) \left(\frac{\omega_{\rm s}}{\omega_{\rm i}}\right)^2 N_e\, S_{ee}(\mathbf{k},\omega), \tag{1.33}$$

$$S_{ee}(\mathbf{k},\omega) \equiv \lim_{\mathcal{V},T\to\infty} \frac{1}{\mathcal{V}T} \frac{\langle \delta n_e(\mathbf{k},\omega)\delta n_e(-\mathbf{k},-\omega)\rangle}{2\pi n_e}, \tag{1.34}$$

in which the angular brackets $\langle \dots \rangle$ denotes the ensemble average. The quantity $S_{ee}(\mathbf{k},\omega)$ is the autocorrelation function of the density fluctuations and is known as the *dynamic structure factor* (DSF); the ensemble average over the density $n_e(\mathbf{k},\omega)$ and density fluctuations $\delta n_e(\mathbf{k},\omega) = n_e(\mathbf{k},\omega) - \langle n_e(\mathbf{k},\omega)\rangle$ are interchangeable since $\langle n_e(\mathbf{k},\omega) n_e(-\mathbf{k},-\omega)\rangle = \langle \delta n_e(\mathbf{k},\omega)\delta n_e(-\mathbf{k},-\omega)\rangle$. The DSF contains all the information on microscopic spatio-temporal correlations between density fluctuations, and therefore gives rise to spectral features associated with collective excitations such as plasmons. It is the principal quantity of interest to the study of dense matter using scattering diagnostics and will be examined extensively in this thesis. Note that the factor $(\omega_{\rm s}/\omega_{\rm i})^2$ appears due to momentum conservation in a fully quantum mechanical treatment [Crowley and Gregori, 2013].

The form of the power spectrum (1.33) assumes that the incident radiation is monochromatic. In reality, however, sources of probe x-rays have a finite bandwidth. If a distribution of incident frequencies interacts with the electrons in the target the scattered power spectrum becomes convolved with the source shape

$$\frac{\partial^2 P_{\rm s}^{\rm obs}(\mathbf{R},\omega_{\rm s})}{\partial\Omega\partial\omega_{\rm s}} \equiv \Sigma(\omega) * \frac{\partial^2 P_{\rm s}(\mathbf{R},\omega_{\rm s})}{\partial\Omega\partial\omega_{\rm s}} = \int_{-\infty}^{\infty} {\rm d}\omega'\, \Sigma(\omega-\omega') \frac{\partial^2 P_{\rm s}(\mathbf{R},\omega')}{\partial\Omega\partial\omega'} \tag{1.35}$$

where $\omega' = \omega_{\rm s}' - \omega_{\rm i}$. Best practice for modelling XRTS experiments requires that the source be well-characterised or actively monitored during the experiment, although it often suffices to use a simple model of the source function. Commonly used examples are Gaussian- or Lorentzian-shaped profiles [Glenzer and Redmer, 2009]. One may also consider combinations of functional forms, results of detailed atomic physics modelling from codes such as FLY/FLYCHK [Lee and Larsen, 1996; Chung et al., 2005] and SPECT3D [MacFarlane et al., 2007], and even experimentally characterised x-ray source data. In general, the source function must be normalised according to

$$\int_{-\infty}^{\infty} {\rm d}\omega\, \Sigma(\omega) = 1. \tag{1.36}$$

Furthermore, the response of the detector as a function of frequency also contributes to the broadening of the spectrum. This is typically characterised prior to an experimental campaign and modelled with a Gaussian function. For XRTS experiments the instrument response is typically a small contribution compared to the bandwidth of the source itself.

Further modelling considerations include source broadening, the angular divergence of the source (k-blurring), the effect of plasma gradients and temporal blurring of the

spectrum over the measurement time and the influence of non-equilibrium distribution functions. These will each be addressed throughout the course of this thesis.

1.4 Structure and scope of this thesis

The initial goal of this thesis is to develop a theoretical tool for modelling XRTS experiments conducted in dense matter. The framework of this capability is based on well-known physics models. In order to provide the first robust numerical capability for analysing scattering data currently being taken from current state-of-the-art facilities like FELs, the model is extended to systems out of thermal equilibrium. The second aim is to use this tool to design and analyse XRTS data from ongoing experiments.

In Chapter 2, an overview is given of the quantum statistical description of dense matter. This provides the theoretical foundation of the work presented in this thesis. The concept of real-time Green's functions is introduced to provide a rigorous framework enabling both equilibrium and non-equilibrium conditions to be considered. The Kadanoff-Baym equations that fully describe the evolution of interacting charged-particle systems are subsequently derived. A detailed account is then given of the density response of the system to probing x-rays via the polarisation functions.

Chapter 3 focusses on the DSF as the quantity of central relevance to modelling XRTS. As a quantum statistical treatment of strongly coupled particles is currently infeasible, this is presented in the well-known chemical picture of Chihara [Chihara, 2000]. Here, the density fluctuations are decomposed into distinct bound- and free-electron features, which give rise to separable contributions from elastic and inelastic scattering as described in the previous section. The general structure of the Chihara approach is shown to be valid for non-equilibrium systems. The various terms of the DSF are then evaluated in the context of a simple equilibrium plasma to demonstrate the typical behaviours of the various terms and important features expected to arise in XRTS spectra. The product of this effort is a novel and highly adaptable code capable of comprehensively modelling XRTS from dense matter. This code is known as MCSS (Multicomponent Scattering Simulation) and forms the core numerical capability which enables much of the original research undertaken in the remainder of this thesis.

Motivated by recent experiments using high-brightness x-rays produced by free-electron lasers (FELs), Chapter 4 considers the effect of non-equilibrium electron distributions on the high-frequency component of the spectrum. In this original work, model distribution functions which yield semi-analytic results for the DSF are used to explore the impact of high-energy, non-thermal electrons on the interpretation of XRTS from strongly-driven systems. The framework of this non-equilibrium model is then compared to recent experimental scattering data from liquid hydrogen. It is shown that non-equilibrium considerations are important for fully understanding the transient dynamic properties of such states. Finally, a fully numerical capability for arbitrary distribution functions is demonstrated

by coupling to kinetic simulations of FEL-driven solid aluminium.

In Chapter 5, the diagnostic potential of XRTS for temperature equilibration experiments is evaluated. The MCSS code is coupled to calculations of temperature relaxation under WDM conditions. In particular, the energy transfer and heat capacity contributions are evaluated within a suitably general framework to account for degeneracy effects in the electrons and contributions from strong correlations in the ions. A hypothetical XRTS experiment is proposed which considers simultaneous spectrally- and angularly-resolved scattering. It is shown that XRTS could in principle be used to diagnose the temperature evolution and also differentiate between energy equilibration models, although significant challenges exist if such measurements are to be realised.

In Chapter 6, the detailed modelling of currently ongoing experiments at the NIF are presented. In this case, the large size of the target necessitates the development of the MCSS code to account for the strongly inhomogeneous state created in the implosion. Furthermore, the transport of the x-ray probe through the opacity profile of the target is considered. It is shown that the scattering is insensitive to the ultra-high pressure states created in the compressed core of the target, but is instead dominated by the partially degenerate ablator material. Statistical analysis of synthetic spectra based on the full three-dimensional calculations demonstrate that a simple fit using the MCSS code yields conditions which are in close agreement with the density-weighted averages predicted by simulations. Conversely, measurements of the ionization are shown to be subject to significant uncertainty due plasma gradients and opacity effects.

The final chapter uses the full range of capabilities developed throughout the previous chapters to analyse recent XRTS data obtained at the Omega laser. Here, the configuration of the experimental platform is ideal for probing the screening cloud around the ions in a regime of relative uncertainty. Detailed statistical analysis of the inelastic and elastic scattering signals is used to self-consistently constrain both the plasma conditions and description of the screening cloud. The results of this study constitute the first observation of the breakdown of the well-known Debye-Hückel screening model in high-energy-density matter using XRTS.

Chapter 2

Quantum statistical description of dense plasmas

In order to provide a robust description of the thermodynamic and response properties of dense matter, a statistical treatment which accurately incorporates strong correlations and quantum effects is essential. The most natural basis for such a description appeals to the formalism of second quantisation [Dirac, 1930]. In this framework, interacting many-particle states are constructed using field operators in the occupation number representation, allowing strong correlations and quantum effects, e.g. diffraction, degeneracy of states and the symmetry postulate, to be fully included.

As the focus of this thesis is the provision of a suitably general description of XRTS, the main quantities explored in this chapter are the correlation functions related to density fluctuations, and the response of coupled systems to external perturbations. The latter are treated using the general framework of real-time Green's functions in order to apply to both equilibrium and non-equilibrium states alike. Specifically, the development of the Kadanoff-Baym equations that govern the evolution of the system allows a general representation of the dynamic processes underpinning the response of dense matter to x-rays to be given. It is shown that the fundamental objects of interest to the theory of XRTS are the polarisation functions, which characterise the response of the electrons and ions to the total effective potential including the self-consistent mean Coulomb field. For the electrons, perturbation expansion of the Bethe-Salpeter equation in terms of the interaction enables the fully dynamic properties of dense matter to be explored, which go beyond the well-known weak coupling limit. The theory developed in this chapter provides the basis for the models used throughout the remainder of this thesis.

2.1 Quantum statistics in second quantisation

A complete description of an interacting many-particle system may be obtained, in principle, by solving the Schrödinger equation for an appropriately symmetrised N-particle wavefunction Ψ. All the observable properties of the system may then be calculated. The wavefunction includes all information on the response of the constituent particles to an external potential and also their mutual interactions. Naturally, for systems with realistic numbers of particles such an exact approach is currently impossible. Fortunately, such precise knowledge on the exact quantum microstate of a many-particle system is not needed. Instead, information on the average macroscopic properties, e.g. the temperature and density, are typically measured.

The connection between the microscopic and macroscopic properties of many-particle systems is achieved by applying the methods of statistical physics. In particular, the most natural framework within which to treat such systems is the *second quantisation* formulation of quantum mechanics [Dirac, 1927]. In this framework, the *pure* microstate of an N-particle system is described by a state vector [Bruus and Flensberg, 2004; Kremp et al., 2005]

$$|\Psi_N\rangle = |\nu_1, \ldots, \nu_N\rangle^{\pm}. \tag{2.1}$$

ν_i represents a complete set of mutually observable properties of a single particle, e.g. the position and spin $\nu_i = \{\mathbf{r}_i, \sigma_i\}$, or the momentum and spin $\nu_i = \{\mathbf{p}_i, \sigma_i\}$. Since the constituent particles are indistinguishable, the state must satisfy the spin statistics postulate; states composed of bosons $(+)$ are symmetric upon particle interchange, whereas states composed of fermions $(-)$ are antisymmetric.

The state vector Eq. (2.1) exists in a symmetrised N-particle Hilbert space $\mathcal{H}_N^{\pm}$, which itself exists in a larger symmetrised Fock space $\mathcal{F}^{\pm}$ composed from the direct sum of all realisable many-particle Hilbert spaces $\mathcal{F}^{\pm} = \bigoplus_{i=0}^{N} \mathcal{H}_i^{\pm}$. State vectors also form the basis of this Fock space, as expressed by the completeness relation

$$\hat{I} = \sum\!\!\!\!\!\!\int \mathrm{d}(\nu_1 \ldots \nu_N) |\nu_1, \ldots, \nu_N\rangle^{\pm\pm}\langle \nu_1, \ldots, \nu_N| = \prod_{i=1}^{N} \sum\!\!\!\!\!\!\int \mathrm{d}\nu_i |\nu_i\rangle\langle\nu_i|, \tag{2.2}$$

where $\hat{I}$ stands for the identity operator. Furthermore, the state vectors are orthogonal

$${}^{\pm}\langle \nu_{1'}, \ldots, \nu_{N'} | \nu_1, \ldots, \nu_N\rangle^{\pm} = \delta(\nu_{1'} - \nu_1) \ldots \delta(\nu_{N'} - \nu_N) = \prod_{i=1}^{N} \delta(\nu_{i'} - \nu_i). \tag{2.3}$$

The notation $\sum\!\!\!\!\!\!\int \mathrm{d}\nu_i$ refers to integration or summation over continuous or discrete basis variables, respectively. The δ-functions refer to the usual Dirac δ-function for continuous basis variables and to the Kronecker symbol for discrete basis variables.

The state vector Eq. (2.1) is composed from the direct product of N single-particle states, i.e. $|\nu_1 \dots \nu_N\rangle^{\pm} = \bigotimes_{i=1}^{N} |\nu_i\rangle$. Each single-particle state is then constructed from a conceptual *vacuum* state containing no particles $|\mathbf{0}\rangle$ by the application of the *creation* operator $a_i^\dagger \equiv a^\dagger(\nu_i)$ acting in the Fock space, which increases the occupation of the state with basis ν_i by unity. One may therefore construct an N-particle state according to

$$|n_1, \dots, n_N\rangle^{\pm} = \frac{1}{\sqrt{N!}} \frac{1}{\sqrt{n_1!}} \left(a_1^\dagger\right)^{n_1} \dots \frac{1}{\sqrt{n_N!}} \left(a_N^\dagger\right)^{n_N} |\mathbf{0}\rangle, \tag{2.4}$$

where $n_i \equiv n(\nu_i)$ denotes the occupation. Note that the pre-factors associated with each operator arise from the normalisation of the resultant state [Bruus and Flensberg, 2004]. For bosons the occupation of a distinct state can be any natural number, $n_i \in \mathbb{N} = \{0, 1, 2, \dots\}$, whilst for fermions only $n_i \in \{0, 1\}$ is allowed. In contrast, application of the adjoint of the creation operator $a_i = (a_i^\dagger)^\dagger$, known as the *annihilation* operator, reduces the occupation of the state of interest by unity

$$a_i^\dagger |n_1, \dots, n_i, \dots, n_N\rangle = (-1)^{2\sigma\lambda_i} \sqrt{n_i + 1}\, |n_1, \dots, n_i + 1, \dots, n_N\rangle, \tag{2.5}$$

$$a_i |n_1, \dots, n_i, \dots, n_N\rangle = (-1)^{2\sigma\lambda_i} \sqrt{n_i}\, |n_1, \dots, n_i - 1, \dots, n_N\rangle. \tag{2.6}$$

Here, σ is the spin of the particles and $\lambda_i = \sum_{j=1}^{i-1} n_j$ changes the sign in line with the antisymmetry condition. For an N-particle system, it is given by the number of permutations needed to move the newly populated/depopulated state to its appropriate position in the ordered state. Application of a_i to an unpopulated single-particle state yields zero $a_i|n_1, \dots, 0, \dots, n_N\rangle = 0$, whilst, for fermions, the same result follows from application of the creation operator to an occupied state.

Using Eqs. (2.5) and (2.6), it is straightforward to show that

$$a_i^\dagger a_i |n_1, \dots, n_i, \dots, n_N\rangle = n_i\, |n_1, \dots, n_i, \dots, n_N\rangle, \tag{2.7}$$

returning the number of particles in the state with basis ν_i. Accordingly, one may define the occupation number operator as $\hat{n}_i = a_i^\dagger a_i$. In contrast to the action of $\hat{n}_i$, it is straightforward to demonstrate that $a_i a_i^\dagger |n_1, \dots, n_N\rangle = (n_i + 1)|n_1, \dots, n_N\rangle$ and, thus, that the construction operators do not commute. The commutation rules for $a_i^\dagger$ and a_i are

$$[a(\nu_i), a^\dagger(\nu_j)]^{\pm} = \delta(\nu_i - \nu_j), \quad [a(\nu_i), a(\nu_j)]^{\pm} = [a^\dagger(\nu_i), a^\dagger(\nu_j)]^{\pm} = 0, \tag{2.8}$$

where $[A, B]^+ = AB - BA$ applies to bosons and $[A, B]^- = AB + BA$ to fermions.

2.1.1 Representation of operators and ensemble averages

Using the construction operators, it is possible to represent any operator corresponding to an observable of the system which obeys particle conservation. Firstly, any operator $\hat{A}_N$ can be multiplied by the identity operator an arbitrary number of times on both sides,

i.e. $\hat{A}_N = \hat{I}\hat{A}_N\hat{I}$. Using the completeness relation (2.2) one finds

$$\hat{A}_N = \frac{1}{N!}\sum\!\!\!\!\!\!\int \mathrm{d}(\alpha_1 \ldots \alpha_N)\mathrm{d}(\beta_1 \ldots \beta_N)\, {}^{\pm}\langle \alpha_1, \ldots, \alpha_N|\hat{A}_N|\beta_N, \ldots, \beta_1\rangle^{\pm} \times a^\dagger(\alpha_N)\ldots a^\dagger(\alpha_1)\, a(\beta_1)\ldots a(\beta_N), \tag{2.9}$$

in which the completeness of the vacuum state $|\mathbf{0}\rangle\langle\mathbf{0}| = \hat{I}$ has been assumed. Since most operators have a unary (single-particle) or binary (two-particle) character, significant simplifications can be made to Eq. (2.9).

An important example relevant to the study of dense matter is the Hamiltonian $\hat{H}_a = \hat{K}_a + \hat{U}_a + \sum_b \hat{V}_{ab}$. Here, $\hat{K}_a$ and $\hat{U}_a$ are unary operators for a particle of species a describing the kinetic energy and potential energy due to an external source, respectively. $\hat{V}_{ab}$ is a binary operator describing the potential energy due to interactions between a pair of particles of species a and b. Choosing the position representation, $|\alpha\rangle \to |\mathbf{r}\rangle$ and $|\beta\rangle \to |\mathbf{r}'\rangle$, one finds the total Hamiltonian to be [Kremp et al., 2005]

$$\hat{H}(t) = \sum_a \int \mathrm{d}\mathbf{r}_1 \left[-\frac{\hbar^2}{2m_a}\nabla^2_{\mathbf{r}_1} + U_a(\mathbf{r}_1)\right] \psi_a^\dagger(\mathbf{r}_1, t)\psi_a(\mathbf{r}_1, t) + \frac{1}{2}\sum_{a,b}\int \mathrm{d}\mathbf{r}_1\mathrm{d}\mathbf{r}_2\, V_{ab}(\mathbf{r}_1 - \mathbf{r}_2)\, \psi_a^\dagger(\mathbf{r}_1, t)\psi_b^\dagger(\mathbf{r}_2, t)\psi_b(\mathbf{r}_2, t)\psi_a(\mathbf{r}_1, t). \tag{2.10}$$

In Eq. (2.10) the *field* operators are defined as $\psi^\dagger(\mathbf{r}) \equiv a^\dagger(\mathbf{r})$ and $\psi(\mathbf{r}) \equiv a(\mathbf{r})$. These are special cases of the construction operators in the position representation.

Due to the enormous number of single-particle states present in realistic systems, the properties of the *pure* quantum microstate can never be directly interrogated in practice. Instead, the coupling of states due to interactions between the particles results in a quantum statistical *mixed* state, representing a weighted average of all realisable microstates. The weighting of each pure state is contained in the density operator

$$\hat{\rho} = \sum\!\!\!\!\!\!\int \mathrm{d}\nu P_\nu |\nu\rangle\langle\nu|, \tag{2.11}$$

where P_ν is the probability of the system being found in the pure state $|\nu\rangle$. Taking the trace of this operator is equivalent to the probability that the system exists in one of all the possible states, which must clearly be unity, i.e. $\mathrm{Tr}\{\hat{\rho}\} = 1$. Moreover, for a pure state one has $\mathrm{Tr}\{\hat{\rho}^2\} = 1$, whereas for a mixed state $\mathrm{Tr}\{\hat{\rho}^2\} < 1$.

Measurement of an observable property of a system in a mixed state corresponds to taking an ensemble average of the corresponding operator. The statistical information of the system contained in $\hat{\rho}$ is included by taking $\mathrm{Tr}\{\hat{\rho}\hat{A}\}$. In the general case given by Eq. (2.9), one therefore has

$$\langle A_N\rangle = \frac{1}{N!}\sum\!\!\!\!\!\!\int \mathrm{d}(\alpha_1 \ldots \alpha_N)\mathrm{d}(\beta_1 \ldots \beta_N)\, {}^{\pm}\langle \alpha_1, \ldots, \alpha_N|\hat{A}_N|\beta_N, \ldots, \beta_1\rangle^{\pm}$$

$$\times\, n^{N\pm}\langle\beta_1,\ldots,\beta_N|\hat{F}_N|\alpha_N,\ldots,\alpha_1\rangle^{\pm}, \tag{2.12}$$

where the N-particle density matrix is defined as

$$\begin{aligned} n^{N\pm}\langle\beta_1,\ldots,\beta_N|\hat{F}_N|\alpha_N,\ldots,\alpha_1\rangle^{\pm} &= \mathrm{Tr}\left\{\hat{\rho}\, a^\dagger(\alpha_N)\ldots a^\dagger(\alpha_1)\, a(\beta_1)\ldots a(\beta_N)\right\} \\ &= \left\langle a^\dagger(\alpha_N)\ldots a^\dagger(\alpha_1)\, a(\beta_1)\ldots a(\beta_N)\right\rangle . \end{aligned} \tag{2.13}$$

Here, $\langle\ldots\rangle$ denotes the ensemble average. Thus, mean values of operators are determined by density matrices corresponding to averages of products of construction operators. For example, considering the single-particle density matrix in the position representation, $n_a\langle\mathbf{r}|F_a^1|\mathbf{r}\rangle = \mathrm{Tr}\{\hat{\rho}\psi_a^\dagger(\mathbf{r})\psi_a(\mathbf{r})\} = \langle\psi_a^\dagger(\mathbf{r})\psi_a(\mathbf{r})\rangle = \langle n_a(\mathbf{r})\rangle = n_a$, determines the local mean particle density at the point $\mathbf{r}$.

For systems in thermal equilibrium the density operator has the known form $\hat{\rho} \propto \exp(-\beta(\hat{H} - \mu\hat{N}))$. For systems out of thermal equilibrium, however, no such simple representation of $\hat{\rho}$ exists in general. Instead, the full dynamical evolution of the system from a precise set of initial conditions becomes important. Several formulations exist for treating the time evolution of systems in second quantisation. Firstly, in the Schrödinger picture the states and density matrix are considered as dynamic (time-dependent) quantities whilst operators are static (time-independent). The opposite case is known as the Heisenberg picture, where states and density matrix are static and operators are dynamic. A third case, known as the Dirac (or *interaction*) picture, combines elements of both approaches with all quantities being fully time-dependent.

In the Schrödinger picture, the statistical operator obeys the von-Neumann equation

$$i\hbar\frac{\partial\hat{\rho}}{\partial t} = -[\hat{\rho},\hat{H}], \tag{2.14}$$

whilst in the Heisenberg picture, the construction operators obey the Heisenberg equation

$$i\hbar\frac{\partial}{\partial t}a(\nu,t) = [a(\nu,t),\hat{H}]. \tag{2.15}$$

In the position representation the equation of motion for the field operators in a many-particle system follows from Eq. (2.10) and (2.15) as

$$\left[i\hbar\frac{\partial}{\partial t} + \frac{\hbar^2}{2m_a}\nabla_{\mathbf{r}}^2 - U_a(\mathbf{r})\right]\psi_a(\mathbf{r},t) = \sum_b\int \mathrm{d}\mathbf{r}' V_{ab}(\mathbf{r}-\mathbf{r}')\psi_b^\dagger(\mathbf{r}',t)\psi_b(\mathbf{r}',t)\psi_a(\mathbf{r},t). \tag{2.16}$$

A similar adjoint equation can also be found for the evolution of the creation operator $\psi_a^\dagger(\mathbf{r},t)$. In Eq. (2.16), the commutation relations (2.8) have been used. This expression forms the basis for understanding the dynamic evolution of many-particles states in terms of macroscopic processes such as thermodynamic equilibration and microscopic processes such as collective excitations.

2.2 Real-time non-equilibrium Green's functions

A straightforward generalisation of the N-particle density matrix is given by treating the time coordinate as an additional component of the basis corresponding to each particle. One may then define the multi-time N-particle correlation function

$$(\pm i\hbar)^N G_a^<(1\dots N, 1'\dots N') = \left\langle \psi_a^\dagger(1')\dots\psi_a^\dagger(N')\,\psi_a(N)\dots\psi_a(1)\right\rangle, \tag{2.17}$$

for bosons (+) and fermions (−). In Eq. (2.17), the notation $\psi(1)$, etc. has been adopted to refer to a field operator acting on a basis which labels both space and time in addition to the spin $1 = \{\mathbf{r}_1, t_1, \sigma\}$, such that $\int\!\!\!\!\!\!\int \mathrm{d}1 = \sum_\sigma \int \mathrm{d}\mathbf{r}_1 \int \mathrm{d}t_1$. Since the N-particle density matrix is recovered for $t_1 = \dots = t_N \equiv t \equiv t_{N'} = \dots = t_{1'}$, the physical meaning of Eq. (2.17) is clearly that of a generalised density operator. For the case of different times this function contains all dynamic and statistical information of the many-particle systems. In addition to the *lesser* correlation function Eq. (2.17), the *greater* correlation function is defined as

$$(i\hbar)^N G_a^>(1\dots N, 1'\dots N') = \left\langle \psi_a(1)\dots\psi_a(N)\,\psi_a^\dagger(N')\dots\psi_a^\dagger(1')\right\rangle. \tag{2.18}$$

Due to the symmetry postulate, the ordering of the field operators is of crucial importance for fermions and, thus, the time ordering ultimately controls the properties of the resulting many-particle state. The range of possible orderings of the construction operators in the greater and lesser correlation functions results in $(2N)!$ distinct states. These can be compactly represented in a single expression using Wick's chronological operator $\hat{\mathcal{T}}$

$$(i\hbar)^N G_a^{\mathrm{c}}(1\dots N, 1'\dots N') = \left\langle \hat{\mathcal{T}}\left\{\psi_a(1)\dots\psi_a(N)\,\psi_a^\dagger(N')\dots\psi_a^\dagger(1')\right\}\right\rangle, \tag{2.19}$$

which is known as the *causal* function. The action of the chronological operator is simply to order the field operators according to their temporal arguments; the field operator with the earliest time appears on the right and that with the latest time on the left. Furthermore, the *anti-causal* correlation function $G_a^{\mathrm{a}}(1\dots N, 1'\dots N')$ is defined to have the opposite time ordering to the causal function.

Often, only the dynamics of single particles are necessary to describe phenomena in many-particle systems. In this case one has

$$\pm i\hbar\, G_a^<(1,1') = \left\langle \psi_a^\dagger(1')\,\psi_a(1)\right\rangle, \tag{2.20}$$

$$i\hbar\, G_a^>(1,1') = \left\langle \psi_a(1)\,\psi_a^\dagger(1')\right\rangle. \tag{2.21}$$

These functions describe the motion of a particle of species a embedded in a fully interacting system between two separate points in space and time, e.g. from $\{\mathbf{r}_1, t_1\}$ to $\{\mathbf{r}_1', t_1'\}$. They are two-point generalisations of the density matrices for single-particle states.

Similarly, generalisations for the ensemble-averaged density fluctuations can be defined via the density fluctuation correlation functions

$$i\hbar L_{ab}^{<}(12,1'2') = \left\langle \delta\hat{\varrho}_a(2,2')\delta\hat{\varrho}_b(1,1') \right\rangle, \tag{2.22}$$

$$i\hbar L_{ab}^{>}(12,1'2') = \left\langle \delta\hat{\varrho}_a(1,1')\delta\hat{\varrho}_b(2,2') \right\rangle, \tag{2.23}$$

where the density fluctuation operators are given by

$$\delta\hat{\varrho}_a(1,1') = \psi_a^\dagger(1')\psi_a(1) - \left\langle \psi_a^\dagger(1')\psi_a(1) \right\rangle. \tag{2.24}$$

Note that Eqs. (2.22) and (2.23) are four-point functions in general, although often only the two-point versions $L_{ab}^{\gtrless}(1,2) \equiv L_{ab}^{\gtrless}(1=1',2=2')$ are of interest.

In the simple case of single-particle states, the causal and anti-causal functions related to Eqs. (2.20) and (2.21) become

$$G_a^{\mathrm{c}}(1,1') = \Theta(t_1-t_2)G_a^{>}(1,1') + \Theta(t_2-t_1)G_a^{<}(1,1'), \tag{2.25}$$

$$G_a^{\mathrm{a}}(1,1') = \Theta(t_1-t_1')G_a^{<}(1,1') + \Theta(t_2-t_1)G_a^{>}(1,1'), \tag{2.26}$$

where $\Theta(t_1-t_1')$ is the Heaviside function. In addition to the greater/lesser and causal/anti-causal functions, it is also useful to define the *retarded* and *advanced* functions

$$G_a^{\mathrm{R/A}}(1,1') = \pm\,\Theta(\pm(t_1-t_1'))\left[G_a^{>}(1,1') - G_a^{<}(1,1')\right], \tag{2.27}$$

which are the Green's functions (in the strict mathematical sense) associated with the Heisenberg equation of motion for the correlation functions, i.e. $G_a^{\gtrless}(1,1')$. Thus, Eq. (2.27) defines the kernel functions for propagating the state of a single particle forward or backward in time, respectively, and are accordingly referred to as *propagators*. The correlation functions, (anti)causal functions and propagators are generally collectively known as many-particle *Green's functions*.

In expressions involving the six types of single-particle Green's functions, especially involving integrals over time, the issue of the time ordering can introduce significant complications for non-equilibrium systems. For example, the quasi-periodic behaviour of functions on the imaginary time interval $\tau \in \{0, i\hbar\beta\}$, which is exploited in the method of Matsubara [Matsubara, 1955], does not apply since β is well-defined in equilibrium only. Generalisation to non-equilibrium systems was first discussed by Schwinger and Keldysh [Schwinger, 1961; Keldysh, 1965] using diagrammatic techniques based on a double-branched (anti-causal and causal) contour on the real time axis (denoted here as $\mathcal{K}$). This allows the functions $G_a^{\gtrless}$ and $G_a^{\mathrm{c/a}}$ to be represented as elements of a single matrix quantity G_a. The retarded and advanced functions follow from the simple relationships $G_a^{\mathrm{R/A}} = G_a^{\mathrm{c}} - G_a^{\lessgtr} = G_a^{\gtrless} - G_a^{\mathrm{a}}$. The rules governing the time-ordering in the context of products and integrals of two-time functions were detailed by Langreth and Wilkins [Langreth and Wilkins, 1972].

2.2.1 Spectral representation of single-particle Green's functions

For application of the techniques of many-particle Green's functions to problems in condensed matter and plasma physics [see, e.g., Martin, 1967; Jauho, 1989], often the spectral (Fourier space) representation is more useful than the position representation. In particular, the Wigner (relative and centre-of-mass) coordinates

$$\mathbf{r} = \mathbf{r}_1 - \mathbf{r}_1', \quad \tau = t_1 - t_1', \tag{2.28}$$

$$\mathbf{R} = \frac{1}{2}(\mathbf{r}_1 + \mathbf{r}_1'), \quad t = \frac{1}{2}(t_1 + t_1'), \tag{2.29}$$

are of principal importance for discussing two-point functions such as in Eqs. (2.20 - 2.27). Correlations between particles occur on spatio-temporal scales determined by the microscopic coordinates $\{\mathbf{r}, \tau\}$, whereas large-scale phenomena such as hydrodynamic evolution relate to the macroscopic coordinates $\{\mathbf{R}, t\}$.

In thermal equilibrium the system evolves neither in space nor time on the macroscopic scale, whereas under non-equilibrium conditions such considerations are generally important. Taking the Fourier transform with respect to the microscopic coordinates, the spectral representations of the Green's functions are defined as

$$G_a^{\mathrm{X}}(\mathbf{k}, \omega; \mathbf{R}, t) = \int \mathrm{d}\mathbf{r} \int_{-\infty}^{\infty} \mathrm{d}\tau \, e^{-i(\mathbf{k}\cdot\mathbf{r} - \omega\tau)} G_a^{\mathrm{X}}(\mathbf{r}, \tau; \mathbf{R}, t), \tag{2.30}$$

$$G_a^{\mathrm{X}}(\mathbf{r}, \tau; \mathbf{R}, t) = \int \frac{\mathrm{d}\mathbf{k}}{(2\pi)^3} \int_{-\infty}^{\infty} \frac{\mathrm{d}\omega}{2\pi} \, e^{i(\mathbf{k}\cdot\mathbf{r} - \omega\tau)} G_a^{\mathrm{X}}(\mathbf{k}, \omega; \mathbf{R}, t), \tag{2.31}$$

where X stands for $\gtrless$, c/a or R/A. These conventions are observed throughout this thesis.

In the case of the lesser correlation function the spectral representation allows for a clear connection to the usual classical kinetic theory to be established. Since the mean particle density is given by $n_a = \pm i\hbar G_a^<(1, 1')|_{1=1'}$, one finds from Eq. (2.31) the familiar normalisation condition discussed previously Eq. (1.3)

$$n_a(\mathbf{R}, t) = \int \frac{\mathrm{d}\mathbf{p}}{(2\pi\hbar)^3} \, f_a(\mathbf{p}; \mathbf{R}, t), \tag{2.32}$$

in which the Wigner distribution is defined as

$$f_a(\mathbf{p}; \mathbf{R}, t) = \pm \, i\hbar \int_{-\infty}^{\infty} \frac{\mathrm{d}\omega}{2\pi} \, G_a^<(\hbar\mathbf{k}, \omega; \mathbf{R}, t). \tag{2.33}$$

This definition may be interpreted as a quantum analogue of the classical phase space distribution function.

From the definitions Eq. (2.27), the important retarded/advanced quantities are

$$G_a^{\mathrm{R/A}}(\mathbf{k}, \omega; \mathbf{R}, t) = \int_{-\infty}^{\infty} \frac{\mathrm{d}\omega'}{2\pi} \frac{A_a(\mathbf{k}, \omega'; \mathbf{R}, t)}{\omega \pm i\epsilon - \omega'}, \tag{2.34}$$

where $\epsilon \to 0^+$ is a real, positive infinitesimal and the spectral function describing the dispersion relation between the energy and momentum of the single-particle state is

$$A_a(\mathbf{k},\omega;\mathbf{R},t) = i\left[G_a^{>}(\mathbf{k},\omega;\mathbf{R},t) - G_a^{<}(\mathbf{k},\omega;\mathbf{R},t)\right]. \tag{2.35}$$

The + root of Eq. (2.34) relates the retarded function whilst the − root relates to the advanced function. Applying Dirac's identity

$$\frac{1}{x \pm i\epsilon} \overset{\epsilon\to 0}{=} \mathcal{P}\left(\frac{1}{x}\right) \mp i\pi\delta(x), \tag{2.36}$$

to Eq. (2.34), one finds a Kramers-Kronig (KK) dispersion relation

$$\mathrm{Re}\, G_a^{\mathrm{R/A}}(\mathbf{k},\omega;\mathbf{R},t) = \pm\,\mathcal{P}\int_{-\infty}^{\infty}\frac{\mathrm{d}\omega'}{\pi}\frac{\mathrm{Im}\, G_a^{\mathrm{R/A}}(\mathbf{k},\omega';\mathbf{R},t)}{\omega'-\omega}, \tag{2.37}$$

$$\mathrm{Im}\, G_a^{\mathrm{R/A}}(\mathbf{k},\omega;\mathbf{R},t) = \mp\,\frac{1}{2}A_a(\mathbf{k},\omega;\mathbf{R},t). \tag{2.38}$$

This demonstrates that the imaginary parts of the retarded and advanced functions differ only in sign and, thus, are related by complex conjugation in Fourier space.

In general, the spectral representation of the correlation functions is determined by projecting the momentum/frequency basis onto the position/time basis and evaluating the trace over eigenstates for the energy and momentum operators. Using the equilibrium form of the density operator, one can show that the lesser and greater correlation functions are related in Fourier space by the Kubo-Martin-Schwinger (KMS) condition [Zubarev, 1960]

$$\pm G_a^{<}(\mathbf{k},\omega) \overset{\text{equil.}}{=} e^{-(\beta\hbar\omega-\eta_a)}\, G_a^{>}(\mathbf{k},\omega). \tag{2.39}$$

Using Eq. (2.39) in conjunction with the definition Eq. (2.35), one finds the general form of the equilibrium correlation functions in Fourier space

$$\pm iG_a^{<}(\mathbf{k},\omega) \overset{\text{equil.}}{=} A_a(\mathbf{k},\omega) f_a(\hbar\omega), \tag{2.40}$$

$$iG_a^{>}(\mathbf{k},\omega) \overset{\text{equil.}}{=} A_a(\mathbf{k},\omega)\left[1 \pm f_a(\hbar\omega)\right], \tag{2.41}$$

where $f_a(\hbar\omega) = \left[\exp\left(\beta\hbar\omega - \eta_a\right) \mp 1\right]^{-1}$. The form of the spectral function is restricted by the sum rule

$$\hbar\int_{-\infty}^{\infty}\frac{\mathrm{d}\omega}{2\pi}A_a(\mathbf{k},\omega) = 1. \tag{2.42}$$

For non-interacting (free) particles the solution is a simple delta-like dispersion relation

$$A_a(\mathbf{k},\omega) = 2\pi\delta(\hbar\omega - E_a^0(\hbar\mathbf{k})), \tag{2.43}$$

where $E_a^0(\hbar\mathbf{k}) = \hbar^2k^2/2m_a$ is the usual kinetic energy. It is straightforward to obtain the

expected normalisation condition for an equilibrium system of non-interacting particles by substituting this result into Eqs. (2.40) and (2.33). The shape of Eq. (2.43) assigns a unique energy to an excitation with a given momentum, independent of time, and therefore describes a stable *quasi-particle* picture.

If interactions are included in the system, the time-dependence of the single-particle states allows for the energy and momentum of a specific particle to become coupled to the wider system, resulting in a broadened dispersion relation with a quasi-Lorentzian shape

$$A_a(\mathbf{k},\omega) = \frac{\Gamma_a(\mathbf{k},\omega)}{\left[\hbar\omega - E_a(\mathbf{k},\omega)\right]^2 + \left[\Gamma_a(\mathbf{k},\omega)/2\right]^2}. \tag{2.44}$$

The lifetime of a given single-particle state is related to the damping rate $\Gamma_a(\mathbf{k},\omega)$ which is strongly dependent on the inter-particle coupling. The location of the resonance, i.e. the most likely energy for an excitation with a given momentum, are the eigenvalues of the fully-coupled, time-dependent single-particle Hamiltonian $E_a(\mathbf{k},\omega)$.

The KMS condition (2.39) does not hold for non-equilibrium states and, such that equivalent expressions for Eqs. (2.40) and (2.41) cannot be derived. In general, the functions $G_a^{\gtrless}$ are independent and must be determined from their respective equations of motion. A simple approach is given by the Kadanoff-Baym ansatz (KBA), which states that equivalent representations are reasonable despite not being derived on a rigorous basis [Kremp et al., 2005]. For the non-equilibrium case, however, the occupation (distribution) function of the particles is non-local in space and time and is described in terms of the momentum transfer instead of the energy transfer, i.e.

$$\pm iG_a^{<}(\mathbf{k},\omega;\mathbf{R},t) = A_a(\mathbf{k},\omega;\mathbf{R},t) f_a(\hbar\mathbf{k};\mathbf{R},t), \tag{2.45}$$

$$iG_a^{>}(\mathbf{k},\omega;\mathbf{R},t) = A_a(\mathbf{k},\omega;\mathbf{R},t)\left[1 \pm f_a(\hbar\mathbf{k};\mathbf{R},t)\right]. \tag{2.46}$$

Density conservation is enforced by spectral functions identical in form to Eqs. (2.43) and (2.44) which explicitly include the macroscopic variables. A more general basis has been discussed by Lipavský [Lipavský et al., 1968], although this approach is beyond the scope of the present work.

2.2.2 Self energy and the Dyson equation

The evolution of the Green's functions are governed by equations of motion with similar forms to Eq. (2.15). If all quantities are defined on the Keldysh time contour $\mathcal{K}$ then a general description can be given for all the time-ordered versions of these functions which is valid under non-equilibrium conditions

$$\left[i\hbar\frac{\partial}{\partial t_1} + \frac{\hbar^2}{2m_a}\nabla_1^2\right] G_a(1,1') = \delta(1-1') + \int_{\mathcal{K}} \mathrm{d}2\, U_a(1,2) G_a(2,1') \pm i\hbar \sum_b \int_{\mathcal{K}} \mathrm{d}2\, V_{ab}(1,2) G_{ab}(12,1'2^+), \tag{2.47}$$

where $V_{ab}(1,2) \equiv V_{ab}(\mathbf{r}_1 - \mathbf{r}_2)\delta(t_1 - t_2)$ is the pair interaction potential and $U_a(1,1') = U_a(\mathbf{r}_1, \mathbf{r}_1')\delta(t_1 - t_1')$ is a generalisation of the external potential to be non-local in space. The Green's function appearing in the interaction term, $G_{ab}(12,1'2^+)$, is a two-particle (four-point) function describing the behaviour of a pair of particles (a and b) within the N-particle system. The meaning of the notation 2^+ used in this function is that the time t_2^+ occurs infinitesimally later than t_2, i.e. $t_2^+ = \lim_{\epsilon\to 0^+}(t_2 + \epsilon)$.

In the simple case of free, non-interacting particles one has

$$\left[i\hbar\frac{\partial}{\partial t_1} + \frac{\hbar^2}{2m_a}\nabla_1^2\right] G_a^0(1,1') = \delta(1-1'). \tag{2.48}$$

The δ-function can be produced from the product of any matrix quantity $A(1,1')$ and its inverse $A^{-1}(1,1')$ and integrating over all internal coordinates, i.e.

$$\delta(1-1') = \int \mathrm{d}2\, A(1,2)A^{-1}(2,1'), \tag{2.49}$$

which makes it possible to define the inverse of the free-particle Green's function

$$G_a^{0\,-1}(1,1') = \left[i\hbar\frac{\partial}{\partial t_1} + \frac{\hbar^2}{2m_a}\nabla_1^2\right]\delta(1-1'), \tag{2.50}$$

and, thus, rewrite Eq. (2.49) as

$$\begin{aligned}\int_{\mathcal{K}} \mathrm{d}2\, G_a^{0\,-1}(1,2)G_a(2,1') = \delta(1-1') + \int_{\mathcal{K}} \mathrm{d}2\, U_a(1,2)G_a(2,1') \\ \pm i\hbar\sum_b \int_{\mathcal{K}} \mathrm{d}2\, V_{ab}(1,2)G_{ab}(12,1'2^+).\end{aligned} \tag{2.51}$$

Eq. (2.47) is not a closed expression since the evolution of $G_a(1,1')$ is coupled to the higher-order function $G_{ab}(12,1'2^+)$ via the interaction term. The equivalent equation of motion for $G_{ab}(12,1'2^+)$ in turn demands knowledge of a three-particle function $G_{abc}(123,1'2'3^+)$ and so on, eventually requiring the full N-particle function. The resulting system of coupled equations is known as the *Martin-Schwinger* hierarchy [Martin and Schwinger, 1959]. It is the quantum analogue of the BBGKY hierarchy for the classical reduced density operators [Hansen and McDonald, 1990].

The Martin-Schwinger hierarchy may be formally decoupled by introducing the two-point *self energy* function $\Sigma_a(1,1')$ according to

$$\int_{\mathcal{K}} \mathrm{d}2\, \Sigma_a(1,2)G_a(2,1') = \pm i\hbar\sum_b \int_{\mathcal{K}} \mathrm{d}2\, V_{ab}(1,2)G_{ab}(12,1'2^+), \tag{2.52}$$

which closes Eq. (2.51) with respect to $G_a(1,1')$ and transfers the unknown element of the problem to the determination of the self energy. By considering the evolution of $G_a(1,1')$ in the interaction picture, a functional dependence on $U_a(1,1')$ is introduced. It is then

possible to consider the functional derivative of the two-particle Green's function with respect to the applied potential, with the result [Kremp et al., 2005]

$$G_{ab}(12,1'2') = G_a(1,1')G_b(2,2') \pm \frac{\delta G_a(1,1')}{\delta U_b(2',2)}. \tag{2.53}$$

The first term represents the contribution without correlations between the pair of particles whilst the second relates to their interactions, e.g. via binary collisions or through the formation of bound states. Substituting Eq. (2.53) into Eq. (2.52) and Eq. (2.51), one finds

$$\int_{\mathcal{K}} \mathrm{d}2\, G_a^{0\,-1}(1,2)G_a(2,1') = \delta(1-1') + \int_{\mathcal{K}} \mathrm{d}2\, \left[U_a^{\mathrm{eff}}(1,2) + \bar{\Sigma}_a(1,2)\right] G_a(2,1'), \tag{2.54}$$

where the first term in square brackets on the right-hand side

$$U_a^{\mathrm{eff}}(1,1') = U_a(1,1') \pm i\hbar\,\delta(1-1') \sum_b \int_{\mathcal{K}} \mathrm{d}2\, V_{ab}(1,2)G_b(2,2^+), \tag{2.55}$$

is the effective mean potential including the self-consistent *Hartree* field created by the microfields of all the particles. Furthermore, the second term

$$\bar{\Sigma}_a(1,1') = i\hbar \sum_b \int_{\mathcal{K}} \mathrm{d}2\mathrm{d}2'\, V_{ab}(1,2) \frac{\delta G_a(1,2')}{\delta U_b(2^+,2)} G_a^{-1}(2',1'), \tag{2.56}$$

defines the pure correlation contribution to the self energy. The total self energy is the sum of these contributions $\Sigma_a(1,1') = \Sigma_a^{\mathrm{H}}(1,1') + \bar{\Sigma}_a(1,1')$.

Returning to Eq. (2.54), multiplying by the free-particle Green's function $G_a^0(2',1)$ and then integrating over $\int_{\mathcal{K}} \mathrm{d}1$ yields δ-functions according to Eq. (2.49) which collapse upon performing the remaining integration. After suitable changes of coordinate labels, one finds the well-known *Dyson equation* for the dressed particle propagator[1]

$$G_a(1,1') = G_a^0(1,1') + \int_{\mathcal{K}} \mathrm{d}2\mathrm{d}2'\, G_a^0(1,2)\Xi_a(2,2')G_a(2',1'),$$

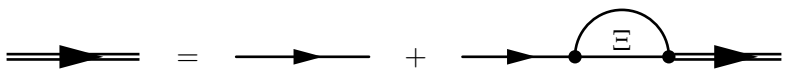

(2.57)

in which $\Xi_a(1,1') = U_a^{\mathrm{eff}}(1,1') + \bar{\Sigma}_a(1,1') = U_a(1,1') + \Sigma_a(1,1')$. This expression constitutes the exact solution to the equation of motion Eq. (2.47). Recursively substituting the left-hand side into the right-hand side generates a perturbation series

$$\begin{aligned} G_a(1,1') = {} & G_a^0(1,1') + \int_{\mathcal{K}} \mathrm{d}2\mathrm{d}2'\, G_a^0(1,2)\Xi_a(2,2')G_a^0(2',1') \\ & + \int \mathrm{d}2\mathrm{d}2'\mathrm{d}3\mathrm{d}3'\, G_a^0(1,2)\Xi_a(2,2')G_a^0(2',3)\Xi_a(3,3')G_a^0(3',1') + \ldots, \end{aligned} \tag{2.58}$$

[1] The Feynman diagram representation [Mattuck, 1992] of Eq. (2.57) is shown below the algebraic form here and other important governing equations.

which converges for systems with a weak total potential $\Xi_a(1,1')$, i.e. weakly driven and weakly interacting systems. Such an approach is clearly of limited use for practical calculations of all but near-ideal systems since the number of integrals which must be evaluated increases rapidly in the higher order terms.

An alternative and useful representation of Eq. (2.57) can be found by applying an obvious extension of the definition Eq. (2.49)

$$A(1,1') = \int \mathrm{d}2\mathrm{d}2' A(1,2)B^{-1}(2,2')B(2',1') = \int \mathrm{d}2\mathrm{d}2' B(1,2)B^{-1}(2,2')A(2',1'), \quad (2.59)$$

whereupon one may readily derive an *inverse* form of the Dyson equation

$$G_a^{-1}(1,1') = G_a^{0\,-1}(1,1') - \Xi_a(1,1'), \quad (2.60)$$

which enables the correlation part of the self energy to be further simplified by removing the dependence on $G_a^{-1}(1,1')$. Changing the functional derivative in Eq. (2.56) to one depending on the inverse Green's function and using Eq. (2.60) gives the *self energy equation*

$$\bar{\Sigma}_a(1,1') = \Sigma_a^{\mathrm{HF}}(1,1') + i\hbar \sum_b \int_{\mathcal{K}} \mathrm{d}2\mathrm{d}2'\, V_{ab}(1,2)G_a(1,2')\frac{\delta\Sigma_a(2',1')}{\delta U_b(2^+,2)}, \quad (2.61)$$

$$\Sigma_a^{\mathrm{HF}}(1,1') = i\hbar\, G_a(1,1')V_{aa}(1,1'). \quad (2.62)$$

The first term is known as the *Hartree-Fock* self energy.

The Dyson equation and the self energy equation are self-consistent and, thus, if $U_a(1,1')$ is either known or negligible then Eqs. (2.57) and (2.56) fully describe the interacting system. However, by themselves these coupled equations are not suitable to be applied to charge-particle systems such as plasmas since the long-ranged Coulomb potential

$$V_{ab}^{\mathrm{C}}(1,1') = \delta(t_1 - t_1')\frac{Z_a Z_b e^2}{4\pi\varepsilon_0 \left|\mathbf{r}_1 - \mathbf{r}_1'\right|}, \quad (2.63)$$

leads to divergent contributions to the self energy, even at relatively low order.

2.3 Extension to Coulomb systems

In practice, the divergent behaviour of the self energy is removed in Coulomb systems by virtue of the fundamental characteristic of screening. Screening of the Coulomb potential occurs as charged particles are coupled over long ranges, i.e. beyond nearest neighbour scale lengths, such that the response of a particular particle to the presence of a test charge also includes the dynamic mutual interactions between every other possible particle pair. The result is the formation of a cloud of particles responding to the test charge which acts to shield the full strength of its potential. Furthermore, the interactions between particles in the screening cloud also influence the formation of the self-consistent effective interaction.

The dynamic character of the screened potential underpins the development of collective phenomena such as longitudinal excitations in the particle density such as Langmuir waves (plasmons) and ion acoustic waves (or phonons in solids).

The most natural way to introduce screening in the Green's function formalism is to consider the response to the effective potential $U_a^{\text{eff}}(1,1')$, thereby explicitly including the self-consistent mean field created by the particles. Firstly, the density response to the externally applied potential is given by the functional derivative introduced in Eq. (2.53), which is simply a generalisation of the well-known definition from basic electrodynamics. This can be transformed to focus on the effective potential using the chain rule

$$L_{ab}(12,1'2') = \pm i\hbar \frac{\delta G_a(1,1')}{\delta U_b(2',2)}, \tag{2.64}$$

$$= \sum_c \int_{\mathcal{K}} \mathrm{d}3\mathrm{d}3'\, \Pi_{ac}(13,1'3') K_{cb}(23',2'3). \tag{2.65}$$

where the polarisation function and specific dielectric response have been defined as

$$\Pi_{ab}(12,1'2') = \pm i\hbar \frac{\delta G_a(1,1')}{\delta U_b^{\text{eff}}(2',2)}, \tag{2.66}$$

and

$$K_{ab}(12,1'2') = \frac{\delta U_b^{\text{eff}}(2,2')}{\delta U_a(1',1)}, \tag{2.67}$$

respectively. The physical meaning of these quantities is clear; the polarisation function determines the density excitation produced by a change in the self-consistent mean field created by the ensemble of particles, whilst the dielectric response is a measure of how the mean field changes due to a change in the applied potential altering the configuration of the particles.

2.3.1 Dynamically screened potential

Substituting Eq. (2.55) into Eq. (2.67) gives the dielectric response in terms of the bare Coulomb potential

$$K_{ab}(12,1'2') = \delta_{ab}\delta(1-2)\delta(1'-2') + \delta(2-2') \sum_c \int_{\mathcal{K}} \mathrm{d}3\, V_{ac}(2,3) L_{cb}(31,3^+1'). \tag{2.68}$$

This result can be used in Eq. (2.65) to explicitly relate the density responses to the applied and effective fields

$$L_{ab}(12,1'2') = \Pi_{ab}(12,1'2') + \sum_{c,d} \int_{\mathcal{K}} \mathrm{d}3\mathrm{d}4\, \Pi_{ac}(13,1'3^+) V_{cd}(3,4) L_{db}(42,4^+2'). \tag{2.69}$$

From the definition of the density response function Eq. (2.64), the correlation part of the self energy Eq. (2.56) contains the bare Coulomb interaction and the density response to the applied potential. Since the screening properties of the system are fully contained in the polarisation function, one may form an alternative definition in terms of a new dynamically screened potential

$$\pm\sum_b \int_{\mathcal{K}} \mathrm{d}2\, V_{ab}(1,2) L_{ab}(12,1',2^+) = \pm\sum_b \int_{\mathcal{K}} \mathrm{d}2\, W_{ab}(1,2)\Pi_{ab}(12,1',2^+), \tag{2.70}$$

from which one may derive the *screened self energy equation*

$$\begin{aligned}\bar{\Sigma}_a(1,1') = {} & i\hbar\, G_a(1,1') W_{aa}(1,1') \\ & \pm i\hbar \sum_b \int_{\mathcal{K}} \mathrm{d}2\mathrm{d}2'\mathrm{d}3\mathrm{d}3'\, W_{ab}(1,2) G_a(1,2') \frac{\delta\bar{\Sigma}_a(2',1')}{\delta G_a(3',3)} \Pi_{ab}(3'2,32^+).\end{aligned}$$

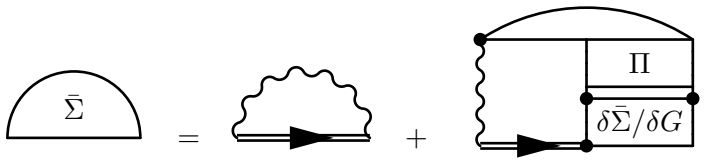

(2.71)

Substituting the relationship (2.65) for $L_{ab}(12,1'2^+)$, it can be shown that

$$W_{ab}(1,2) = \sum_c \int_{\mathcal{K}} \mathrm{d}3\, V_{ac}(1,3) K_{cb}(3,2), \tag{2.72}$$

in which the two-point generalised dielectric function $K_{ab}(12,1^+2') = K_{ab}(1,2)\delta(2-2')$ has been introduced. The screened potential therefore contains contributions from the specific dielectric response functions of all the species in the system, coupled together by the density responses to their mutual Coulomb interactions.

More generally, the bare Coulomb interaction between a pair of particles is modified by the inverse dielectric screening function of the total system

$$W_{ab}(1,2) = \int_{\mathcal{K}} \mathrm{d}3\, V_{ab}(1,3)\varepsilon^{-1}(3,2). \tag{2.73}$$

The latter obeys the following important relationships

$$\varepsilon^{-1}(1,2) = \delta(1-2) + \sum_{a,b} \int_{\mathcal{K}} \mathrm{d}3\, L_{ab}(13,1^+3^+) V_{ba}(3,1), \tag{2.74}$$

and

$$\varepsilon(1,2) = \delta(1-2) - \sum_{a,b} \int_{\mathcal{K}} \mathrm{d}3\, \Pi_{ab}(13,1^+3^+) V_{ba}(3,1). \tag{2.75}$$

It is subsequently straightforward to derive the *screening equation*

$$W_{ab}(1,2) = V_{ab}(1,2) + \sum_{c,d} \int_{\mathcal{K}} \mathrm{d}3\mathrm{d}4\, V_{ac}(1,3)\Pi_{cd}(34,3^+4^+)W_{db}(4,2).$$

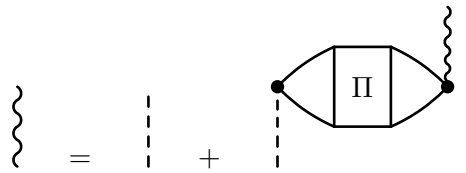

(2.76)

Note that, unlike the Coulomb potential (2.63), the screened potential is a dynamic quantity due to the time dependence of the density response.

2.3.2 Properties of the dielectric function

From the definition of the screened potential (2.73), the dielectric function controls the screening properties of the system. In particular, the Fourier transform of the retarded function $\varepsilon^{\mathrm{R}}(\mathbf{k},\omega)$ is responsible for determining the density excitation spectrum which is of interest to XRTS. The latter obeys a number of important relationships and sum rules obtained independently of the density response or polarisation functions. In a local approximation [Kremp et al., 2005], the complex retarded dielectric function obey Kramers-Kronig dispersion relations

$$\mathrm{Re}\,\varepsilon^{\mathrm{R}^{\pm 1}}(\mathbf{k},\omega;\mathbf{R},t) = 1 + \mathcal{P}\int_{-\infty}^{\infty} \frac{\mathrm{d}\omega'}{\pi} \frac{\mathrm{Im}\,\varepsilon^{\mathrm{R}^{\pm 1}}(\mathbf{k},\omega';\mathbf{R},t)}{\omega' - \omega}, \tag{2.77}$$

$$\mathrm{Im}\,\varepsilon^{\mathrm{R}^{\pm 1}}(\mathbf{k},\omega;\mathbf{R},t) = -\mathcal{P}\int_{-\infty}^{\infty} \frac{\mathrm{d}\omega'}{\pi} \frac{\mathrm{Re}\,\varepsilon^{\mathrm{R}^{\pm 1}}(\mathbf{k},\omega';\mathbf{R},t) - 1}{\omega' - \omega}. \tag{2.78}$$

From the definitions (2.74) and (2.75), these functions are related to the Fourier transforms of the retarded density response and polarisation functions

$$\varepsilon^{\mathrm{R}^{-1}}(\mathbf{k},\omega;\mathbf{R},t) = 1 + \sum_{a,b} L^{\mathrm{R}}_{ab}(\mathbf{k},\omega;\mathbf{R},t)V_{ab}(k), \tag{2.79}$$

$$\varepsilon^{\mathrm{R}}(\mathbf{k},\omega;\mathbf{R},t) = 1 - \sum_{a,b} \Pi^{\mathrm{R}}_{ab}(\mathbf{k},\omega;\mathbf{R},t)V_{ab}(k). \tag{2.80}$$

By taking frequency moments of these functions one may constrain numerous observable properties of the system, thus providing important benchmarks for modelling and simulations of experimental data. Of particular relevance to this work are those related to one-component systems such as the electron gas, i.e. $\varepsilon(\mathbf{k},\omega) = 1 - \Pi_{aa}(\mathbf{k},\omega)V_{aa}(k)$. Firstly, the *f-sum rule*

$$\int_{-\infty}^{\infty} \frac{\mathrm{d}\omega}{\pi}\, \omega\, \mathrm{Im}\,\varepsilon^{\mathrm{R}^{\pm 1}}(\mathbf{k},\omega) = \pm\omega_{\mathrm{p}}^2, \tag{2.81}$$

where ω_p is the plasma frequency (1.12), is a statement of particle density conservation. The second is the *perfect screening rule*

$$\lim_{k\to 0}\int_{-\infty}^{\infty}\frac{\mathrm{d}\omega}{\pi}\,\omega^{-1}\,\mathrm{Im}\,\varepsilon^{\mathrm{R}^{-1}}(\mathbf{k},\omega)=1, \tag{2.82}$$

which determines the limiting behaviour of the static screening cloud over large ranges. Finally, one has the *compressibility sum rule*

$$\lim_{k\to 0}\int_{-\infty}^{\infty}\frac{\mathrm{d}\omega}{\pi}\,\omega^{-1}\,\mathrm{Im}\,\varepsilon^{\mathrm{R}}(\mathbf{k},\omega)=V_{aa}(k)n_a^2\varkappa_{\mathrm{T}a}, \tag{2.83}$$

in which $\varkappa_{\mathrm{T}a}$ is the isothermal compressibility. The latter provides important information on the macroscopic properties of the bulk material. These general expressions hold for equilibrium and non-equilibrium states and for arbitrarily strongly coupled conditions. Higher order moments and multicomponent generalisations of the rules presented here are possible [Puff, 1965; Mihara and Puff, 1968] but are not of direct relevance to this work.

2.4 Polarisation function

By introducing a screened potential $W_{ab}(1,2)$ as the interaction of interest for plasmas, the self energy has been reformulated such that the bare Coulomb potential is removed from the description of the system. Naturally, an additional expression is now required to close the set of governing equations as the screened potential depends on the polarisation function. An equation of motion for the polarisation function can be straightforwardly derived by changing the definition (2.66) to depend on the inverse Green's function and once again using Eq. (2.60)

$$\Pi_{ab}(12,1'2')=\pm i\hbar\left[G_a(1,2')G_a(2,1')\delta_{ab}+\int_{\mathcal{K}}\mathrm{d}3\mathrm{d}3'\,G_a(1,3)\frac{\delta\bar{\Sigma}_a(3,3')}{\delta U_b^{\mathrm{eff}}(2',2)}G_a(3',1')\right]. \tag{2.84}$$

Using the chain rule to change the derivative the above yields a *Bethe-Salpeter equation* for the polarisation function

$$\begin{aligned}\Pi_{ab}(12,1'2')=&\pm i\hbar\,G_a(1,2')G_a(2,1')\delta_{ab}\\&+\sum_c\int_{\mathcal{K}}\mathrm{d}3\mathrm{d}3'\mathrm{d}4\mathrm{d}4'\,G_a(1,3')G_a(3,1')\frac{\delta\bar{\Sigma}_a(3',3)}{\delta G_c(4,4')}\Pi_{cb}(42,4'2').\end{aligned}$$

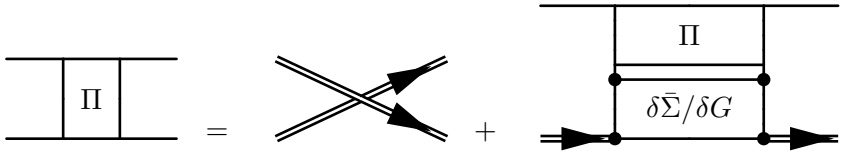

(2.85)

Together with the Dyson equation (2.57), the screened potential (2.76) and the corresponding screened self energy (2.61), the Bethe-Salpeter equation (2.85) completes the description of the dynamical evolution of an interacting Coulomb system. These four coupled equations are known collectively as the *Kadanoff-Baym quantum kinetic equations*. Note that since no restrictions are placed on the strength of the interactions this framework is applicable to strongly coupled systems.

2.4.1 Closed-form truncated GW approximation

The difficulty in evaluating the polarisation function lies in the functional derivative in Eq. (2.85). A simple way in which interactions can be included whilst avoiding such complexities is to neglect the second term of the screened self energy, which is the *GW approximation* [Aryasetiawan and Gunnarsson, 1998]

$$\bar{\Sigma}_a(1,1') \overset{\mathrm{GW}}{=} i\hbar\, G_a(1,1')W_{aa}(1,1'). \tag{2.86}$$

The functional derivative in the Bethe-Salpeter equation is then

$$\frac{\delta\bar{\Sigma}_a(3',3)}{\delta G_b(4,4')} \overset{\mathrm{GW}}{=} i\hbar\left[\delta_{ab}\delta(3'-4)\delta(3-4')W_{aa}(3',3) + G_a(3',3)\frac{\delta W_{aa}(3',3)}{\delta G_b(4,4')}\right], \tag{2.87}$$

$$\begin{aligned}\frac{\delta W_{aa}(3',3)}{\delta G_b(4,4')} &= \sum_{d,e}\int_{\mathcal{K}} \mathrm{d}5\mathrm{d}6\, V_{ad}(3',5)\frac{\delta\Pi_{de}(56,5^+6^+)}{\delta G_b(4,4')}W_{ea}(6,3) \\ &\quad + \sum_{d,e}\int_{\mathcal{K}} \mathrm{d}5\mathrm{d}6\, V_{ad}(3',5)\Pi_{de}(56,5^+,6^+)\frac{\delta W_{ea}(6,3)}{\delta G_b(4,4')},\end{aligned} \tag{2.88}$$

where the screening equation (2.76) has been used. If the polarisation function and screened potential appearing in Eq. (2.88) are truncated at their leading order terms, then

$$\begin{aligned}\frac{\delta\bar{\Sigma}_a(3',3)}{\delta G_b(4,4')} &\approx i\hbar\,\delta_{ab}\delta(3'-4)\delta(3-4')W_{aa}(3',3) \\ &\quad \pm (i\hbar)^2\, G_a(3',3)V_{ab}(3',4)G_b(4',4)W_{ba}(4',3) \\ &\quad \pm (i\hbar)^2\, G_a(3',3)V_{ab}(3',4')G_b(4',4)W_{ba}(4,3).\end{aligned} \tag{2.89}$$

Approximating the polarisation terms appearing on the right-hand side of Eq. (2.85) by the leading order term, i.e. $\Pi_{cb}(42,4',2') \approx \pm i\hbar\, G_c(4,2')G_c(2,4')\delta_{cb}$, one obtains a closed-form approximation which includes interactions between the particles on the level of the screened Hartree-Fock approximation. Moreover, the limits $1' \to 1^+$ and $2' \to 2^+$ must be taken for the application of calculating the two-point density fluctuation correlation function. The result is

$$\Pi_{ab}(1,2) \overset{\mathrm{GW}}{=} \pm i\hbar\,\delta_{ab}G_a(1,2)G_a(2,1)$$

$$
\begin{aligned}
&\pm (i\hbar)^2 \delta_{ab} \int_{\mathcal{K}} \mathrm{d}3\mathrm{d}4\, G_a(1,3) G_a(4,1) W_{aa}(3,4) G_b(3,2) G_b(2,4) \\
&+ (i\hbar)^3 \int_{\mathcal{K}} \mathrm{d}3\mathrm{d}3'\mathrm{d}4\mathrm{d}4'\, G_a(1,3) G_a(3,3') G_a(3',1) \\
&\times V_{ab}(3,4') W_{ba}(4,3') G_b(2,4) G_b(4,4') G_b(4',2) \\
&+ (i\hbar)^3 \int_{\mathcal{K}} \mathrm{d}3\mathrm{d}3'\mathrm{d}4\mathrm{d}4'\, G_a(1,3) G_a(3,3') G_a(3',1) \\
&\times V_{ab}(3,4) W_{ba}(4',3') G_b(2,4) G_b(4,4') G_b(4',2).
\end{aligned}
$$

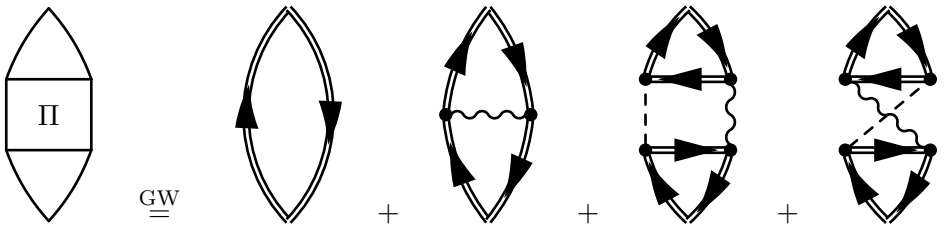

(2.90)

The three distinct contributions to Eq. (2.90) are worth briefly discussing. The first term is the well-known *random phase approximation* (RPA). It contains interactions by virtue of the self energy corrections to the Green's functions (double lines with arrows in the diagram), but no direct exchange. The first-order exchange correction enters in the second term via the screened potential (wavy line in the diagram), which is known as a *vertex correction*. The third and fourth terms are variants on the *fluctuation corrections*. The latter are distinct from the RPA and vertex terms as these are the lowest order contributions which couple together fluctuations in the density fields of different particle species. This is made especially clear from the shape of the diagrams, where two disconnected loops (each representing potentially different species) are coupled by interactions. Furthermore, the fluctuation terms are of second order in the interaction and, thus, are expected to be significantly smaller contributions to the overall polarisation function.

2.4.2 G_0W approximation - first-order corrections

In order to evaluate the truncated GW approximation, the interacting Green's functions must be estimated. This is made difficult by the self-consistent structure of both the Dyson and self energy equations, which themselves contain interactions via the screened potential and polarisation contributions. The most simple approximation is given by taking the perturbation expansion (2.58) with the self energy given by the HF approximation (2.86). In this way, a perturbation series in terms of the (screened) interaction strength can be established for the polarisation function. With the free-particle Green's function G_a^0 one has up to first order in W_{aa}

$$\begin{aligned}\Pi_{ab}(1,2) \overset{\mathrm{G_0W}}{=} \pm i\hbar\,\delta_{ab}\Big\{ & G_a^0(1,2)G_a^0(2,1) \\ & + i\hbar\left[\int_{\mathcal{K}} \mathrm{d3d4}\, G_a^0(1,3)G_a^0(3,4)W_{aa}(3,4)G_a^0(4,2)\right]G_a^0(2,1) \\ & + i\hbar\, G_a^0(1,2)\left[\int_{\mathcal{K}} \mathrm{d3d4}\, G_a^0(2,3)G_a^0(3,4)W_{aa}(3,4)G_a^0(4,1)\right] \\ & + i\hbar\int_{\mathcal{K}} \mathrm{d3d4}\, G_a^0(1,3)G_a^0(4,1)W_{aa}(3,4)G_b^0(3,2)G_b^0(2,4)\Big\}.\end{aligned}$$

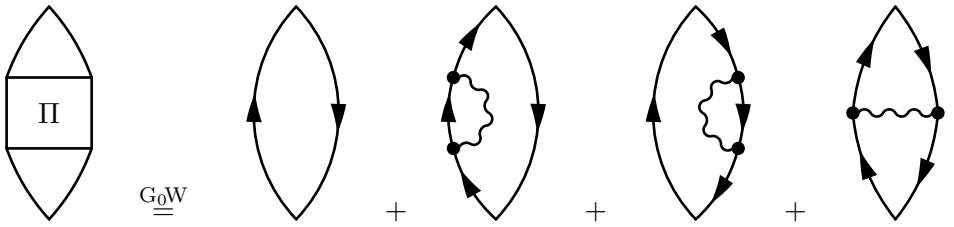

(2.91)

The above expressions have been previously derived in studies of the correlated one-component electron gas [Holas et al., 1979; Aravind et al., 1982; Engel and Vosko, 1990; Richardson and Ashcroft, 1994; De Witt et al., 1995]. The first term is the zeroth-order RPA (often this is simply referred to as the RPA), which was first discussed by Bohm and Pines [Pines and Bohm, 1952; Bohm and Pines, 1953]. It represents the lowest order at which dynamic screening and collective effects can be considered. The second and third terms arise from the first-order self-energy corrections to the free-particle Green's functions in the zeroth-order RPA term. The fourth term is the lowest-order vertex correction accounting for exchange in the screening of the inter-particle interactions.

By expanding the screened potential in a similar way to the Dyson equation, the leading order contributions yield bare Coulomb interactions in each term. Here, one simply replaces all wavy lines in the diagrammatic form of Eq. (2.91) with dashed lines. This is reasonable for the first-order corrections shown here, but leads to divergent contributions from the fluctuation diagrams. If the screened potential is taken in RPA these first-order contributions are extremely challenging and expensive to evaluate numerically. On the other hand, if only static screening is considered, one may obtain results for arbitrary non-equilibrium conditions. Since the conditions of interest here are mainly weakly coupled, only the RPA term will be considered in detail. Evaluation of the first-order corrections will be undertaken as part of the future development of the work presented in this thesis.

2.4.3 Random phase approximation

Due to its simple structure in the space/time domain, the correlation functions for the RPA term are simple to obtain from the Langreth-Wilkins rules

$$\Pi_{ab}^{\gtrless}(1,2) \overset{\mathrm{RPA}}{=} \pm i\hbar\,\delta_{ab}\, G_a^{\gtrless 0}(1,2)G_a^{\lessgtr 0}(2,1). \tag{2.92}$$

In Fourier space one subsequently finds

$$\Pi_{aa}^{\gtrless}(\mathbf{k},\omega;\mathbf{R},t) \overset{\text{RPA}}{=} \pm i\hbar \int \frac{\mathrm{d}\mathbf{k}'}{(2\pi)^3} \int_{-\infty}^{\infty} \frac{\mathrm{d}\omega'}{2\pi} G_a^{\gtrless 0}(\mathbf{k}'+\mathbf{k},\omega'+\omega;\mathbf{R},t) G_a^{\lessgtr 0}(\mathbf{k}',\omega';\mathbf{R},t). \quad (2.93)$$

Using the Kadanoff-Baym ansatz to relate $G_a^{\gtrless}(\mathbf{k},\omega)$ to $f_a(\mathbf{p})$, the straightforward result for the non-interacting spectral function given by Eqs. (2.43) and (2.45) is

$$\begin{aligned} i\Pi_{aa}^{\gtrless}(\mathbf{k},\omega;\mathbf{R},t) \overset{\text{RPA}}{=}\ & 2\pi \int \frac{\mathrm{d}\mathbf{p}}{(2\pi\hbar)^3}\, \delta\left(\hbar\omega - E_a^0(\mathbf{p}+\mathbf{q}) + E_a^0(\mathbf{p})\right) \\ & \times f_a^{\gtrless}(\mathbf{p}+\hbar\mathbf{k};\mathbf{R},t) f_a^{\lessgtr}(\mathbf{p};\mathbf{R},t), \end{aligned} \quad (2.94)$$

where the notation $f_a^{<} \equiv f_a$ and $f_a^{>} = 1 - f_a$ has been introduced.

For the Fourier transform of the two-point polarisation function $\Pi_{ab}(\mathbf{k},\omega;\mathbf{R},t)$, one may use the established relationships for the single-particle Green's functions to give similar general rules which hold for arbitrarily strongly coupled systems. Firstly, in thermal equilibrium a Kubo-Martin-Schwinger condition is obeyed

$$\Pi_{ab}^{<}(\mathbf{k},\omega) \overset{\text{equil.}}{=} e^{-\beta\hbar\omega}\, \Pi_{ab}^{>}(\mathbf{k},\omega), \quad (2.95)$$

such that $\Pi_{ab}^{\gtrless}(\mathbf{k},\omega) \overset{\text{equil.}}{=} \Pi_{ab}^{\lessgtr}(\mathbf{k},-\omega)$. Once again, this relationship is not generally true for non-equilibrium conditions. The real and imaginary parts of the retarded/advanced functions also satisfy a Kramers-Kronig relationship

$$\mathrm{Re}\Pi_{ab}^{\mathrm{R/A}}(\mathbf{k},\omega;\mathbf{R},t) = \pm\, \mathcal{P} \int_{-\infty}^{\infty} \frac{\mathrm{d}\omega'}{\pi} \frac{\mathrm{Im}\Pi_{ab}^{\mathrm{R/A}}(\mathbf{k},\omega';\mathbf{R},t)}{\omega'-\omega}, \quad (2.96)$$

$$\mathrm{Im}\Pi_{ab}^{\mathrm{R/A}}(\mathbf{k},\omega;\mathbf{R},t) = \mp\, \frac{1}{2}\left[i\Pi_{ab}^{>}(\mathbf{k},\omega;\mathbf{R},t) - i\Pi_{ab}^{<}(\mathbf{k},\omega;\mathbf{R},t)\right]. \quad (2.97)$$

Combining the KMS condition with the above yields the important general relationship, which is valid in equilibrium

$$\begin{aligned} \mathrm{Im}\Pi_{ab}^{\mathrm{R/A}}(\mathbf{k},\omega) &\overset{\text{equil.}}{=} \mp\, \frac{i}{2} \frac{1}{1-e^{-\beta\hbar\omega}}\, \Pi_{ab}^{>}(\mathbf{k},\omega) \\ &= \pm\, \frac{i}{2} \frac{1}{1-e^{\beta\hbar\omega}}\, \Pi_{ab}^{<}(\mathbf{k},\omega). \end{aligned} \quad (2.98)$$

By inserting the correlation functions (2.94) into Eq. (2.96), the familiar expression for the retarded/advanced RPA polarisation follows

$$\Pi_{aa}^{\mathrm{R/A}}(\mathbf{k},\omega;\mathbf{R},t) \overset{\text{RPA}}{=} \int \frac{\mathrm{d}\mathbf{p}}{(2\pi\hbar)^3} \frac{f_a(\mathbf{p}+\hbar\mathbf{k};\mathbf{R},t) - f_a(\mathbf{p};\mathbf{R},t)}{E_a^0(\mathbf{p}+\hbar\mathbf{k}) - E_a^0(\mathbf{p}) - \hbar(\omega \pm i\epsilon)}. \quad (2.99)$$

If the distribution functions are isotropic with respect to the momentum space, i.e. $f_a(\mathbf{p}) \to f_a(p)$, Eqs. (2.94) and (2.99) can be simplified by integrating over angular coordinates. The

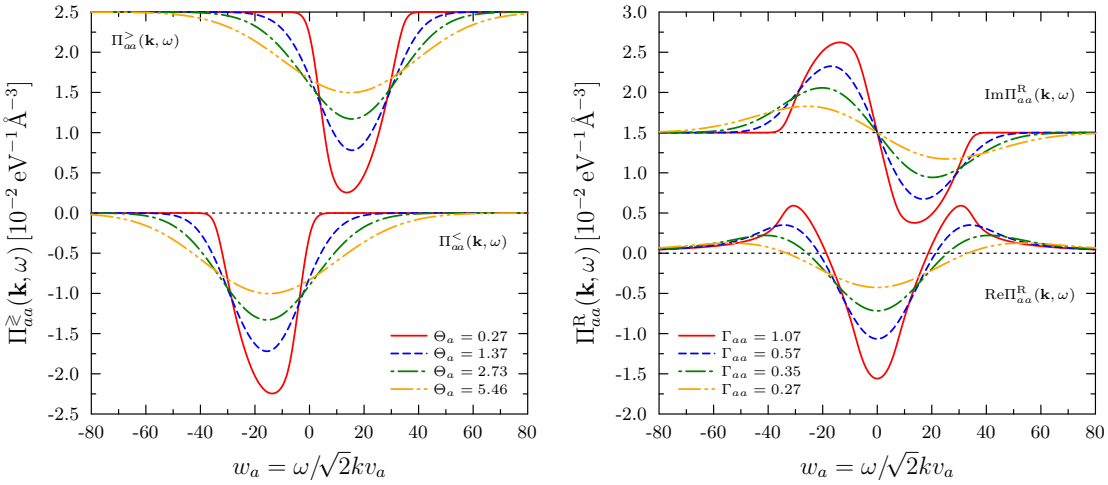

(a) Correlation functions. (b) Components of retarded function.

Figure 2.1: (a): Temperature dependence of equilibrium correlation functions in RPA for the polarisation function $\Pi^{\gtrless}_{aa}$ at near-solid density $n_a = 10^{23}\,\mathrm{cm}^{-3}$ and at atomic scale lengths $k = 1\,\mathrm{Å}^{-1}$. (b): Real and imaginary components of the retarded function Π^{R}_{aa}. The degeneracy is compared using the ratio of the thermal and Fermi energies $\Theta_a = k_{\mathrm{B}}T_a/E_{\mathrm{F}a}$. In both panels, one set of curves is artificially offset on the y-axis for clarity.

result for the correlation functions is

$$i\Pi^{\gtrless}_{aa}(\mathbf{k},\omega;\mathbf{R},t) \overset{\mathrm{RPA}}{=} \frac{2\pi^2 k}{(2\pi\hbar)^3\omega_{\mathrm{C}a}} \int_{\frac{m_a}{k}|\omega+\omega_{\mathrm{C}a}|}^{\infty} \mathrm{d}p\, p\, f^{\gtrless}_a(p;\mathbf{R},t) f^{\lessgtr}_a(\bar{p};\mathbf{R},t), \tag{2.100}$$

where $\bar{p}^2 = p^2 - 2m_a\hbar\omega$ and $\omega_{\mathrm{C}a} = \hbar k^2/2m_a$ is the Compton frequency of species a. The imaginary part of the retarded/advanced functions immediately follows from Eq. (2.97)

$$\mathrm{Im}\Pi^{\mathrm{R/A}}_{aa}(\mathbf{k},\omega;\mathbf{R},t) \overset{\mathrm{RPA}}{=} \pm \frac{\pi^2 k}{(2\pi\hbar)^3\omega_{\mathrm{C}a}} \int_{\frac{m_a}{k}|\omega+\omega_{\mathrm{C}a}|}^{\frac{m_a}{k}|\omega-\omega_{\mathrm{C}a}|} \mathrm{d}p\, p\, f_a(p;\mathbf{R},t), \tag{2.101}$$

and the real part is subsequently found using Eq. (2.96). From the frequency dependence of the above, it is clear that the imaginary part is an odd function of the frequency ω at fixed wave number k under non-equilibrium conditions and, accordingly, the real part is an even function of ω. These properties are independent of the shapes of the correlation functions, which may not have any clear relationship in general.

Under non-equilibrium conditions, the RPA expressions must be evaluated numerically. In thermal equilibrium, e.g. for a Fermi-Dirac distribution (1.1), the integration over the scalar momentum p can be performed analytically, yielding

$$i\Pi^{\gtrless}_{aa}(\mathbf{k},\omega) \overset{\mathrm{equil.}}{=} \pm \frac{1}{1-e^{\mp\beta\hbar\omega}} \frac{\sqrt{\pi} n_a \beta}{4\varkappa_a D_a} \mathcal{L}(w_a,\varkappa_a,\eta_a), \tag{2.102}$$

$$\mathcal{L}(w_a, \varkappa_a, \eta_a) = \ln\left[\frac{1 + e^{\eta_a - (w_a + \varkappa_a)^2}}{1 + e^{\eta_a - (w_a - \varkappa_a)^2}}\right] \tag{2.103}$$

for the correlation functions and

$$\Pi_{aa}^{\mathrm{R/A}}(\mathbf{k}, \omega) \overset{\text{equil.}}{=} \frac{n_a \beta}{8\sqrt{\pi}\varkappa_a D_a}\left\{\mathcal{P}\int_{-\infty}^{\infty}\frac{\mathrm{d}w}{w - w_a}\mathcal{L}(w, \varkappa_a, \eta_a) \pm i\pi\mathcal{L}(w_a, \varkappa_a, \eta_a)\right\}, \tag{2.104}$$

for the retarded/advanced functions. These results are clearly in agreement with the definition of the imaginary part of the retarded/advanced functions and the KMS condition. In Eqs. (2.102) and (2.104), the normalised frequency $w_a = \omega/\sqrt{2}kv_a$ and Compton shift $\varkappa_a = \hbar k/\sqrt{8}p_a$ are defined in addition to the equilibrium degeneracy parameter $D_a = n_a\Lambda_a^3/(2\sigma_a + 1)$. These important variables and parameters will be used extensively throughout the remainder of this thesis in the context of equilibrium and quasi-equilibrium systems. The real part of the retarded function must be evaluated numerically for arbitrarily degenerate conditions [Arista and Brandt, 1984], although accurate parameterisations have been obtained by Dandrea et al. [Dandrea et al., 1986] which make implementation of the RPA computationally inexpensive.

An example of the behaviour of the correlation functions and retarded function are shown in Fig. 2.1 for near-solid density conditions over a range of temperatures of interest. As expected, higher temperatures lead to broadened features in all the functions. This occurs as the number of particles with sufficiently high velocities that can respond to high frequency fluctuations increases with the mean kinetic energy, i.e. temperature. For non-degenerate conditions, the functions are self-similar with respect to the dimensionless frequency w_a, and simply scale linearly in amplitude with increasing particle density. Under partially degenerate conditions, however, the shape of the curves changes significantly to reflect the increasing importance of quantum effects, i.e. as Pauli blocking which dominate at high density.

Chapter 3

Theoretical model for the dynamic structure factor

The principal quantity investigated by the scattering of photons is the response of the target under study to the probing radiation, characterised by the power spectrum of the microscopic fluctuations in electron density. The latter is described by the dynamic structure factor (DSF), which is defined as the Fourier transform of the density-density autocorrelation function. In this chapter, a generalised description of the DSF of dense matter is given. Firstly, the density correlation function which underpins the DSF is formulated in terms of non-equilibrium Green's functions for a two-component plasma. The semi-classical model of Chihara [Chihara, 2000] is then adopted due to the failure of the perturbation approach to the Green's functions in the strongly coupled regime. The suitability of this framework to non-equilibrium systems is briefly discussed, and it is demonstrated that Chihara formula holds in a linear response approximation.

In the remainder of the chapter, the main terms of the Chihara model are discussed and evaluated. For each term, a suitably general description allowing for non-equilibrium conditions is given where possible. The typical sensitivities of the terms to the plasma conditions are considered under the restriction of equilibrium for simplicity. In particular, the bound and free electron contributions to the elastic and inelastic scattering are considered for a number of models suitable for the application of XRTS. For all conditions of interest the ions are considered as a classical equilibrium fluid. The ultimate aim of this part of the chapter is to develop and demonstrate the workings of a *multicomponent scattering simulation* (MCSS) code which can be used to analyse XRTS signals from dense plasmas.

3.1 Definition of the dynamic structure factor

The dynamic structure factor for interactions between two particle species a and b is defined as the Fourier transform of the ensemble average of the correlation function of density fluctuations

$$2\pi\sqrt{n_a(\mathbf{R},t)n_b(\mathbf{R},t)}S_{ab}(\mathbf{k},\omega;\mathbf{R},t) = \int \mathrm{d}\mathbf{r} \int_{-\infty}^{\infty} \mathrm{d}\tau\, e^{-i(\mathbf{k}\cdot\mathbf{r}-\omega\tau)} \left\langle \delta\hat{\varrho}_a(1)\, \delta\hat{\varrho}_b(2) \right\rangle, \quad (3.1)$$

with respect to the Wigner coordinates (2.28). Thus, the DSF encodes the microstate of the fluctuating, fully coupled system and contains all the information on dynamic screening, strong interactions and quantum statistics. The correlation functions of density fluctuations between different points in space and time were defined in Eqs. (2.22) and (2.23), from which straightforward comparison to Eq. (3.1) shows

$$S_{ab}(\mathbf{k},\omega;\mathbf{R},t) = \frac{i\hbar L_{ab}^{>}(\mathbf{k},\omega;\mathbf{R},t)}{2\pi\sqrt{n_a(\mathbf{R},t)n_b(\mathbf{R},t)}}. \quad (3.2)$$

This expression represents a general form of the *fluctuation-dissipation theorem* (FDT), which is also valid for non-equilibrium systems [Kremp et al., 2005].

The dependence of the DSF on the macroscopic spatial and temporal coordinates reflects the variation of the density response throughout an inhomogeneous target. Gradient expansion of the interconnection between macroscopic and microscopic coordinates can be performed [Kremp et al., 2005] for rapidly evolving or strongly inhomogeneous systems. Fortunately, for the experiments of interest, the targets tend to be relatively uniformly heated over time scales far longer than the correlation time of density fluctuations which scatter the x-ray probe. Only the local contributions are considered in this work.

3.1.1 Density correlation functions for two-component plasmas

The equation of motion governing the density fluctuation correlation functions $L_{ab}^{\gtrless}(1,2)$ was given in Section 2.3.1. In the general case of a plasma composed of electrons and arbitrarily many species of ions, all possible interactions between the different species of particles must be accounted for. In real space/time this leads to a complicated system of coupled integral equations, which are defined on the Keldysh contour $\mathcal{K}$ to correctly describe the time-ordering.

For the important case of a two-component plasma of electrons and a single species of ions, all interacting via the Coulomb potential (2.63), the required expressions are (in Fourier space)

$$\begin{aligned} L_{ee}(\mathbf{k},\omega) = {} & \Pi_{ee}(\mathbf{k},\omega) + \Big[\Pi_{ee}(\mathbf{k},\omega)V_{ee}(k) + \Pi_{ei}(\mathbf{k},\omega)V_{ie}(k)\Big] L_{ee}(\mathbf{k},\omega) \\ & + \Big[\Pi_{ee}(\mathbf{k},\omega)V_{ei}(k) + \Pi_{ei}(\mathbf{k},\omega)V_{ii}(k)\Big] L_{ie}(\mathbf{k},\omega), \end{aligned} \quad (3.3)$$

$$L_{ie}(\mathbf{k},\omega) = \Pi_{ie}(\mathbf{k},\omega) + \Big[\Pi_{ie}(\mathbf{k},\omega)V_{ee}(k) + \Pi_{ii}(\mathbf{k},\omega)V_{ie}(k)\Big]L_{ee}(\mathbf{k},\omega) + \Big[\Pi_{ie}(\mathbf{k},\omega)V_{ei}(k) + \Pi_{ii}(\mathbf{k},\omega)V_{ii}(k)\Big]L_{ie}(\mathbf{k},\omega). \tag{3.4}$$

The dependence on the macroscopic spatial and temporal coordinates $\{\mathbf{R}, t\}$ has been suppressed for brevity, here and throughout the remainder of this chapter. Note that the equivalent quantities for ion-ion and electron-ion correlations can be obtained from Eqs. (3.3) and (3.4) under label interchange ($e \Leftrightarrow i$), respectively.

Substituting Eq. (3.4) into Eq. (3.3) gives after lengthy rearrangement

$$L_{ee}(\mathbf{k},\omega) = \mathcal{L}_{ee}(\mathbf{k},\omega) + \mathcal{R}_{ee}(\mathbf{k},\omega) + \big[\mathcal{R}_{ee}(\mathbf{k},\omega)V_{ee}(k) + \mathcal{R}_{ei}(\mathbf{k},\omega)V_{ie}(k)\big]L_{ee}(\mathbf{k},\omega), \tag{3.5}$$

where the intermediate coupling functions and auxiliary density response functions are

$$\begin{aligned}
\mathcal{R}_{ea}(\mathbf{k},\omega) &\equiv \mathcal{P}_{ea}(\mathbf{k},\omega) + \mathcal{Q}_{ea}(\mathbf{k},\omega) \\
&= \big[\mathcal{L}_{ee}(\mathbf{k},\omega)V_{ei}(k) + \mathcal{L}_{ei}(\mathbf{k},\omega)V_{ii}(k)\big]\mathcal{L}_{ia}(\mathbf{k},\omega), && (3.6)\\
\mathcal{L}_{ea}(\mathbf{k},\omega) &= \Pi_{ea}(\mathbf{k},\omega) + \big[\Pi_{ee}(\mathbf{k},\omega)V_{ee}(k) + \Pi_{ei}(\mathbf{k},\omega)V_{ie}(k)\big]\mathcal{L}_{ea}(\mathbf{k},\omega), && (3.7)\\
\mathcal{L}_{ia}(\mathbf{k},\omega) &= \Pi_{ia}(\mathbf{k},\omega) + \big[\Pi_{ii}(\mathbf{k},\omega)V_{ii}(k) + \Pi_{ie}(\mathbf{k},\omega)V_{ei}(k)\big]\mathcal{L}_{ia}(\mathbf{k},\omega), && (3.8)
\end{aligned}$$

for combinations of labels $a = e, i$. Obtaining structures involving products of such functions as given above enables the Langreth-Wilkins rules to be used to determine the correct time-ordering of the quantities of interest.

It is possible to construct a very general expression for the electron-electron correlation function [Vorberger et al., 2010]

$$\begin{aligned}
L^{>}_{ee}(\mathbf{k},\omega) = &\frac{\big[\mathcal{L}^{>}_{ee}(\mathbf{k},\omega) + \mathcal{R}^{>}_{ee}(\mathbf{k},\omega)\big]\big[1 - \mathcal{R}^{\mathrm{A}}_{ee}(\mathbf{k},\omega)V_{ee}(k) - \mathcal{R}^{\mathrm{A}}_{ei}(\mathbf{k},\omega)V_{ie}(k)\big]}{\big|1 - \mathcal{R}^{\mathrm{R}}_{ee}(\mathbf{k},\omega)V_{ee}(k) - \mathcal{R}^{\mathrm{R}}_{ei}(\mathbf{k},\omega)V_{ie}(k)\big|^2} \\
&+ \frac{\big[\mathcal{R}^{>}_{ee}(\mathbf{k},\omega)V_{ee}(k) + \mathcal{R}^{>}_{ei}(\mathbf{k},\omega)V_{ie}(k)\big]\big[\mathcal{L}^{\mathrm{A}}_{ee}(\mathbf{k},\omega) + \mathcal{R}^{\mathrm{A}}_{ee}(\mathbf{k},\omega)\big]}{\big|1 - \mathcal{R}^{\mathrm{R}}_{ee}(\mathbf{k},\omega)V_{ee}(k) - \mathcal{R}^{\mathrm{R}}_{ei}(\mathbf{k},\omega)V_{ie}(k)\big|^2}.
\end{aligned} \tag{3.9}$$

Eq. (3.9) contains all orders of the interactions, requiring the direct contributions of non-vanishing polarisation functions relating to different species. If the latter are restricted to diagonal terms only ($\Pi_{ab} = \delta_{ab}\Pi_{aa}$) one immediately finds $\mathcal{L}_{ei} = \mathcal{L}_{ie} = \mathcal{R}_{ee} = 0$, $\mathcal{R}_{ei} = \mathcal{P}_{ei} = \mathcal{L}_{ee}V_{ei}\mathcal{L}_{ii}$ and $\mathcal{L}_{aa} = \Pi_{aa} + \Pi_{aa}V_{aa}\mathcal{L}_{aa}$. In this diagonalised polarisation approximation (DPA) the correlation function becomes

$$L^{>}_{ee}(\mathbf{k},\omega) \overset{\mathrm{DPA}}{=} \frac{\mathcal{L}^{>}_{ee}(\mathbf{k},\omega) + V_{ie}(k)\left|\mathcal{L}^{\mathrm{R}}_{ee}(\mathbf{k},\omega)\right|^2 V_{ei}(k)\mathcal{L}^{>}_{ii}(\mathbf{k},\omega)}{\left|1 - \mathcal{L}^{\mathrm{R}}_{ee}(\mathbf{k},\omega)V_{ei}(k)\mathcal{L}^{\mathrm{R}}_{ii}(\mathbf{k},\omega)V_{ie}(k)\right|^2}, \tag{3.10}$$

where the definitions of the greater- and retarded/advanced coupling functions

$$\mathcal{P}^{>}_{ei}(\mathbf{k},\omega) = \mathcal{L}^{>}_{ee}(\mathbf{k},\omega)V_{ei}(k)\mathcal{L}^{\mathrm{A}}_{ii}(\mathbf{k},\omega) + \mathcal{L}^{\mathrm{R}}_{ee}(\mathbf{k},\omega)V_{ei}(k)\mathcal{L}^{>}_{ii}(\mathbf{k},\omega), \tag{3.11}$$

$$\mathcal{P}_{ei}^{\mathrm{R/A}}(\mathbf{k},\omega) = \mathcal{L}_{ee}^{\mathrm{R/A}}(\mathbf{k},\omega)V_{ei}(k)\mathcal{L}_{ii}^{\mathrm{R/A}}(\mathbf{k},\omega), \tag{3.12}$$

have been used. Eq. (3.11) is the complementary function to that found by Vorberger et al. in the context of electron-ion energy relaxation.

Substituting Eq. (3.10) into Eq. (3.2), and using both the definitions of $\mathcal{L}_{aa}$ and the symmetry of the Coulomb interaction $V_{ei} = V_{ie}$, one finds for the DSF

$$S_{ee}(\mathbf{k},\omega) \overset{\mathrm{DPA}}{=} \left|\frac{1-\Pi_{ii}^{\mathrm{R}}(\mathbf{k},\omega)V_{ii}(k)}{\varepsilon(\mathbf{k},\omega)}\right|^2 \frac{i\hbar\Pi_{ee}^{>}(\mathbf{k},\omega)}{2\pi n_e} + \frac{n_i}{n_e}\left|\frac{\Pi_{ee}^{\mathrm{R}}(\mathbf{k},\omega)V_{ei}(k)}{\varepsilon(\mathbf{k},\omega)}\right|^2 \frac{i\hbar\Pi_{ii}^{>}(\mathbf{k},\omega)}{2\pi n_i}, \tag{3.13}$$

where the screening in (3.13) is provided by the retarded dielectric function $\varepsilon(\mathbf{k},\omega)$ (2.80). Clearly, the fundamental quantities underpinning the description of XRTS in dense matter are the polarisation functions.

It is important to clarify the restrictions on the strength of correlations imposed by the expressions that have been derived. Firstly, Eq. (3.9) is completely general with respect to the interaction strength as it includes all possible bound and scattering states, transitions, correlations and exchange contributions in the fully-coupled system; the only approximation made in its derivation is the local approximation, which is expected to be well-fulfilled in WDM. Neglecting off-diagonal contributions to Π_{ab} in Eq. (3.10) removes the direct coupling of the electron and ion systems and, thus, can be interpreted as a linear response approximation.

Although the interaction between the electron and ion subsystems is limited to the indirect influence of screening, this is of critical importance to describing the dynamic collective behaviour of two-component plasmas, such as the development of the ion acoustic mode [Vorberger and Gericke, 2009; Vorberger et al., 2010]. However, it does not imply that correlations between electrons and ions within their respective subsystems must themselves be weak; under strongly coupled conditions the excitation spectra of the electron and ion modes may be substantially modified. As discussed in the previous chapter, evaluation of terms beyond the DPA (such as the fluctuation contributions) is presently beyond the scope of this work.

3.2 Modelling the dynamic structure of dense matter

3.2.1 Weakly coupled limit

The most simple description of the DSF is given by the (zeroth-order) RPA. In this case, the polarisation functions are given by $\Pi_{aa}^{>} \to \Pi_{aa}^{>0}$ and $\Pi_{aa}^{\mathrm{R}} \to \Pi_{aa}^{\mathrm{R0}}$, as per Eqs. (2.94) and (2.99). These functions depends solely on the distribution function and contain no information of interactions between the particles. Thus, the correlation functions relating to the mean and applied fields are identical, such that $\Pi_{aa}^{>0} \equiv L_{aa}^{>0}$. One can therefore

define the DSF of the non-interacting system as

$$S_a^0(\mathbf{k},\omega) = \frac{i\hbar L_{aa}^{>0}(\mathbf{k},\omega)}{2\pi n_a} \equiv \frac{i\hbar \Pi_{aa}^{>0}(\mathbf{k},\omega)}{2\pi n_a} = \frac{2}{n_a}\int \frac{\mathrm{d}\mathbf{p}}{(2\pi\hbar)^3}\,\delta\big(\omega - \mathbf{k}\cdot\mathbf{p}/m_a - \omega_{Ca}\big) f_a(\mathbf{p})\left[1 - f_a(\mathbf{p}+\hbar\mathbf{k})\right], \tag{3.14}$$

where $\omega_{Ca} = \hbar k^2/2m_a$ is the frequency associated with the Compton shift for species a. The form of Eq. (3.14) can be interpreted as the power spectrum of s-wave Compton scattering from a system of free particles [Chapman and Gericke, 2011]. The DSF of the interacting system follows as

$$S_{ee}(\mathbf{k},\omega) \overset{\text{RPA}}{=} \left|\frac{1-\Pi_{ii}^{\text{R0}}(\mathbf{k},\omega)V_{ii}(k)}{\varepsilon^0(\mathbf{k},\omega)}\right|^2 S_e^0(\mathbf{k},\omega) + \frac{n_e}{n_i}\left|\frac{\Pi_{ee}^{\text{R0}}(\mathbf{k},\omega)V_{ei}(k)}{\varepsilon^0(\mathbf{k},\omega)}\right|^2 S_i^0(\mathbf{k},\omega). \tag{3.15}$$

Note the similarity of Eq. (3.15) with the famous result derived by Evans and Katzenstein [Evans and Katzenstein, 1969] for non-degenerate conditions under the restriction of thermal equilibrium.

3.2.2 Semi-classical approach for strongly coupled plasmas

Although treating the DSF within the formalism of non-equilibrium Green's functions enables a robust description of correlation effects and quantum statistics in dense systems, its utility is limited in practice due the complexities of fully accounting for strong interactions. In particular, robust description of the density response related to the ions, which tend to be strongly coupled, is extremely challenging. The use of single-particle Green's functions also makes the treatment of scattering from bound electrons difficult.

A theoretical framework for the scattering of x-rays from dense, partially ionized matter was first given by Chihara to describe liquid metals [Chihara, 1987; 2000]. Following early pioneering work [Nardi, 1991; Landen et al., 2001; Gregori et al., 2003], this formalism has become the cornerstone for the theory which enables XRTS to be used as a dense plasma diagnostic. The core idea of Chihara's approach is an artificial decomposition of total electron density into bound and free electron contributions

$$n_e^{\text{tot}}(\mathbf{k},t) = \sum_{j=1}^{N_e} \exp[-\mathbf{k}\cdot\mathbf{r}_j(t)] = n_e^{\text{b}}(\mathbf{k},t) + n_e^{\text{f}}(\mathbf{k},t), \tag{3.16}$$

known as the *chemical picture*. This enables a clear distinction between sources of coherent and incoherent scattering to be made. Such a decomposition is, of course, purely artificial since no such distinction exists for quantum mechanical particles; in reality electrons in *bound* and *free* states obey the same equation of motion, but experience significantly different potentials depending on their energies/momenta. Moreover, the derivation is based on the classical statistical picture of scattering [Hansen and McDonald, 1990] in which the

electrons and ions are described by Klimontovich distributions. Nevertheless, the resulting form of the DSF is sufficiently useful for it to provide a basis for modelling XRTS.

Chihara's result has been derived in detail by many authors [see, e.g., Wünsch, 2011] and is only briefly summarised here. To begin, insertion of Eq. (3.16) into Eq. (3.1) yields correlation functions between bound and free density fluctuations which are expressed via an intermediate scattering function

$$\begin{aligned} I(\mathbf{k},t) &\equiv \int \mathrm{d}\mathbf{r}\, e^{-i\mathbf{k}\cdot\mathbf{r}} \left\langle \delta\varrho_e(1)\delta\varrho_e(2)\right\rangle \\ &= \left\langle \left[\delta\varrho_e^{\mathrm{b}}(\mathbf{k},\tau)+\delta\varrho_e^{\mathrm{f}}(\mathbf{k},\tau)\right]\left[\delta\varrho_e^{\mathrm{b}}(-\mathbf{k},0)+\delta\varrho_e^{\mathrm{f}}(-\mathbf{k},0)\right]\right\rangle, \\ &= \left\langle \delta\varrho_e^{\mathrm{b}}(\mathbf{k},\tau)\delta\varrho_e^{\mathrm{b}}(-\mathbf{k},0)\right\rangle + \left\langle \delta\varrho_e^{\mathrm{f}}(\mathbf{k},\tau)\delta\varrho_e^{\mathrm{f}}(-\mathbf{k},0)\right\rangle + 2\left\langle \delta\varrho_e^{\mathrm{b}}(\mathbf{k},\tau)\delta\varrho_e^{\mathrm{f}}(-\mathbf{k},0)\right\rangle . \end{aligned} \tag{3.17}$$

For the bound electrons the orbits in the Klimontovich distribution are rewritten relative to the positions of the ions. The Born-Oppenheimer approximation is then applied to separate the electron and ion motions on the basis of the large mass ratio $m_i/m_e \gg 1$, such that $\delta\varrho_e^{\mathrm{b}}(\mathbf{k},t)$ may be expressed via the usual atomic/ionic form factor $f_i(\mathbf{k})$ modulated by the ensemble average of the ion correlations.

Next, considerations accounting for the self-motion of the ions related to both coherent and incoherent scattering are made [Hansen and McDonald, 1990], which further decomposes the bound-bound term. The free-free and bound-free correlation terms are left as definitions, allowing appropriate models to be used; this is what makes the framework *semi-classical*. With these manipulations, Fourier transformation of Eq. (3.17) with respect to the time difference τ directly yields the total DSF to be [Chihara, 2000]

$$\begin{aligned} Z_i^{\mathrm{A}} S_{ee}^{\mathrm{tot}}(\mathbf{k},\omega) = f_i^2(\mathbf{k}) S_{ii}(\mathbf{k},\omega) + Z_i^{\mathrm{f}} S_{ee}(\mathbf{k},\omega) + 2\sqrt{Z_i^{\mathrm{f}}} f_i(\mathbf{k}) S_{ei}(\mathbf{k},\omega) \\ + \tilde{S}_{ei}^{\mathrm{core}}(\mathbf{k},\omega) * S_{ii}^{\mathrm{self}}(\mathbf{k},\omega). \end{aligned} \tag{3.18}$$

Here, $f_i(\mathbf{k})$ is the ionic form factor which describes the mean bound electron distribution around the ions. In Eq. (3.18), the symbol $*$ denotes convolution in the frequency domain. Furthermore, the number of bound and free electrons per ion are defined as Z_i^{b} and Z_i^{f} with the total number of electrons per ion being the atomic number $Z_i^{\mathrm{A}} = Z_i^{\mathrm{b}} + Z_i^{\mathrm{f}}$.

3.2.3 Separation of electronic contributions

In its current form, Eq. (3.18) is of limited use since the second term accounts for all free electron correlations, including those related to the screening cloud which follows the low-frequency fluctuations of the ions. To separate this behaviour from the high-frequency fluctuations, which are essentially independent of the ionic properties, it is convenient to consider the structure of Eq. (3.13) for the free electrons only. Noting that the responses of the electrons and ions decay over significantly different frequency scales since $(m_i/m_e)^{1/2} \gg 1$ suggests a natural partitioning of contributions in the two terms.

The first term relates to the high-frequency behaviour of the free electrons, such that the ionic terms can be taken in the limit $\omega \to \infty$, where $\Pi_{ii} \to 0$. The second term is concerned with the low-frequency behaviour of the ions. Here, the electronic terms can be taken in the static limit $\omega \to 0$. The DSF may then be expressed in terms of effective one-component plasma contributions

$$\begin{aligned} Z_i^{\mathrm{f}} S_{ee}^{\mathrm{tot}}(\mathbf{k},\omega) &= Z_i^{\mathrm{f}} \frac{i\hbar}{2\pi n_e^{\mathrm{f}}} \frac{\Pi_{ee}^{>}(\mathbf{k},\omega)}{\left|\varepsilon_{ee}(\mathbf{k},\omega)\right|^2} + \left[\frac{\Pi_{ee}^{\mathrm{R}}(\mathbf{k},0) V_{ei}(k)}{\varepsilon_{ee}(\mathbf{k},0)}\right]^2 \frac{i\hbar}{2\pi n_i} \frac{\Pi_{ii}^{>}(\mathbf{k},\omega)}{\left|\varepsilon_{ii}^{\mathrm{scr}}(\mathbf{k},\omega)\right|^2} \\ &= Z_i^{\mathrm{f}} S_{ee}(\mathbf{k},\omega) + q_i^2(\mathbf{k})\, S_{ii}(\mathbf{k},\omega). \end{aligned} \tag{3.19}$$

The screening in the ion term is due to a modified ionic dielectric function in which the ion-ion interaction is the statically screened pseudo-potential $V_{ii}^{\mathrm{scr}}(\mathbf{k}) = V_{ii}(k)/\varepsilon_{ee}(\mathbf{k},0)$.

Similarly, the electron-ion term $S_{ei}(\mathbf{k},\omega)$ can be tackled by considering the complementary density response functions to Eqs. (3.3) and (3.4). In DPA, the term of interest can be shown to be [Vorberger et al., 2010]

$$\begin{aligned} L_{ei}^{>}(\mathbf{k},\omega) &\overset{\mathrm{DPA}}{=} \frac{\mathcal{L}_{ee}^{>}(\mathbf{k},\omega) V_{ei}(k) \mathcal{L}_{ii}^{\mathrm{A}}(\mathbf{k},\omega) + \mathcal{L}_{ee}^{\mathrm{R}}(\mathbf{k},\omega) V_{ei}(k) \mathcal{L}_{ii}^{>}(\mathbf{k},\omega)}{\left|1 - \mathcal{L}_{ee}^{\mathrm{R}}(\mathbf{k},\omega) V_{ei}(k) \mathcal{L}_{ii}^{\mathrm{R}}(\mathbf{k},\omega) V_{ie}(k)\right|^2} \\ &= \frac{V_{ei}(k) \Pi_{ii}^{\mathrm{A}}(\mathbf{k},\omega)[1 - \Pi_{ii}^{\mathrm{R}}(\mathbf{k},\omega) V_{ii}(k)]}{\left|1 - \Pi_{ee}^{\mathrm{R}}(\mathbf{k},\omega) V_{ee}(k) - \Pi_{ii}^{\mathrm{R}}(\mathbf{k},\omega) V_{ii}(k)\right|^2} \Pi_{ee}^{>}(\mathbf{k},\omega) \\ &\quad + \frac{V_{ei}(k) \Pi_{ee}^{\mathrm{R}}(\mathbf{k},\omega)[1 - \Pi_{ee}^{\mathrm{A}}(\mathbf{k},\omega) V_{ee}(k)]}{\left|1 - \Pi_{ee}^{\mathrm{R}}(\mathbf{k},\omega) V_{ee}(k) - \Pi_{ii}^{\mathrm{R}}(\mathbf{k},\omega) V_{ii}(k)\right|^2} \Pi_{ii}^{>}(\mathbf{k},\omega). \end{aligned} \tag{3.20}$$

Once more appealing to the idea of frequency separation, the first term can be neglected altogether, and the second yields the result

$$\begin{aligned} \sqrt{Z_i^{\mathrm{f}}} S_{ei}(\mathbf{k},\omega) &= \left[\frac{\Pi_{ee}^{\mathrm{R}}(\mathbf{k},0) V_{ei}(k)}{\varepsilon_{ee}(\mathbf{k},0)}\right] \frac{i\hbar}{2\pi n_i} \frac{\Pi_{ii}^{>}(\mathbf{k},\omega)}{\left|\varepsilon_{ii}^{\mathrm{scr}}(\mathbf{k},\omega)\right|^2}. \\ &= q_i(\mathbf{k})\, S_{ii}(\mathbf{k},\omega). \end{aligned} \tag{3.21}$$

Taking Eqs. (3.19) and (3.21) allows the desired separation of the electron contributions in Eq. (3.18) and, subsequently, Chihara's well-known expression emerges

$$\begin{aligned} Z_a^{\mathrm{A}} S_{ee}^{\mathrm{tot}}(\mathbf{k},\omega) &= f_i^2(\mathbf{k}) S_{ii}(\mathbf{k},\omega) + 2 f_i(\mathbf{k}) q_i(\mathbf{k}) S_{ii}(\mathbf{k},\omega) + q_i^2(\mathbf{k})\, S_{ii}(\mathbf{k},\omega) \\ &\quad + Z_i^{\mathrm{f}} S_{ee}(\mathbf{k},\omega) + \tilde{S}_{ei}^{\mathrm{core}}(\mathbf{k},\omega) * S_{ii}^{\mathrm{self}}(\mathbf{k},\omega) \\ &= \left[f_i(\mathbf{k}) + q_i(\mathbf{k})\right]^2 S_{ii}(\mathbf{k},\omega) + Z_i^{\mathrm{f}} S_{ee}(\mathbf{k},\omega) + \tilde{S}_{ei}^{\mathrm{core}}(\mathbf{k},\omega) * S_{ii}^{\mathrm{self}}(\mathbf{k},\omega). \end{aligned} \tag{3.22}$$

An important restriction of this derivation in the general non-equilibrium case is that the decomposition of the electronic contributions explicitly identifies the ion-ion DSF as that of a screened system. Conversely, the term originating directly from the density correlations (first term in Eq. (3.18)) is not similarly restricted and, thus, the form of Eq. (3.22) holds only if screening is treated consistently in the electron and ion subsystems.

3.2.4 Static approximation for ions

A further simplification of Eq. (3.22) is possible by treating the ions as static

$$S_{ii}(\mathbf{k},\omega) \approx S_{ii}(\mathbf{k})\delta(\omega), \tag{3.23}$$

where the ion-ion static structure factor (SSF) is defined as

$$S_{ii}(\mathbf{k}) = \int_{-\infty}^{\infty} \mathrm{d}\omega\, S_{ii}(\mathbf{k},\omega). \tag{3.24}$$

This assumption has been well-justified throughout the development of XRTS [Gregori et al., 2003] since the dynamical behaviour of the ions cannot be resolved using the high-energy x-ray sources present at laser facilities capable of producing dense plasmas, including advanced FELs such as LCLS. Principally, this limitation is due to the typically wide bandwidths of x-ray sources, especially for thermal line emission backlighters, but is also partly due to the energy resolution of crystal-based spectrometers.

In future, ultra-high brilliance and narrow bandwidth x-ray sources comparable to 3rd generation synchrotrons will enable routine access to the dynamic structure of the ions under high-energy density conditions [Sinn et al., 1997; Scopigno and Ruocco, 2005]. The current theoretical framework will then require modification to accurately represent the acoustic mode spectrum at high coupling strengths [Gregori and Gericke, 2009; Vorberger et al., 2012]. In this work, the static approximation is assumed to be reasonable for all ion species, whereupon Eq. (3.22) becomes

$$Z_i^{\mathrm{A}} S_{ee}^{\mathrm{tot}}(\mathbf{k},\omega) = W_{\mathrm{R}}(\mathbf{k})\delta(\omega) + Z_i^{\mathrm{f}} S_{ee}(\mathbf{k},\omega) + \tilde{S}_{ei}^{\mathrm{core}}(\mathbf{k},\omega). \tag{3.25}$$

The term $W_{\mathrm{R}}(\mathbf{k}) = [f_i(\mathbf{k}) + q_i(\mathbf{k})]^2\, S_{ii}(\mathbf{k})$ is known as the *Rayleigh amplitude* since low-frequency collective behaviour has been ignored, i.e. scattering on the time scales of the ions is assumed to be elastic.

3.2.5 Extension to multicomponent systems

The study of dense matter often necessitates the use of complex targets composed of different elements. The Rayleigh amplitude in particular reflects the contributions of potentially many different species of ions whose mutual interactions determine the density distribution of bound and screening electrons. Moreover, for high-temperature, high-Z targets a broad distribution of ionization states may exist for each atomic species.

The generalisation of the DSF to multiple ionic contributions was motivated by the study ionization balance in plastic (CH) targets [Gregori et al., 2006a]. Therein, the approximate decomposition of the SSF of the ions is based on an ansatz that is exact in RPA. However, it has been shown that the latter approach fails in the small k limit, resulting in unphysical negative Rayleigh amplitudes [Wünsch et al., 2011] for more strongly coupled

systems. A more rigorous derivation which fully accounts for correlations between electrons bound to different species of ions has been developed [Wünsch et al., 2008]. The resulting generalised form of Eq. (3.25) can be written as

$$Z_a^{\mathrm{A}} S_{ee}^{\mathrm{tot}}(\mathbf{k},\omega) = W_{\mathrm{R}}(\mathbf{k})\delta(\omega) + \sum_a x_a Z_a^{\mathrm{f}} S_{ee}(\mathbf{k},\omega) + \sum_a x_a \tilde{S}_{ea}^{\mathrm{core}}(\mathbf{k},\omega), \tag{3.26}$$

$$W_{\mathrm{R}}(\mathbf{k}) = \sum_{a,b} \sqrt{x_a x_b}\left[f_a(\mathbf{k}) + q_a(\mathbf{k})\right]\left[f_b(\mathbf{k}) + q_b(\mathbf{k})\right] S_{ab}(\mathbf{k}), \tag{3.27}$$

in which the summation runs over all distinct (by mass and/or charge) ion species present. The relative contributions of the different ion species are determined by the number fractions $x_a = n_a / \sum_a n_a$, with $\sum_a x_a = 1$.

Having appropriately decomposed the DSF into components suitable for modelling the interaction for x-rays with dense matter, it remains to give descriptions of each of the distinct terms in Eqs. (3.26) and (3.27). The resulting model forms the core capability of the code used for simulating, designing and analysing XRTS data throughout this thesis; it is referred to as the *multicomponent scattering simulation* (MCSS) code.

3.3 Ionic form factor

The first term to address in the Rayleigh amplitude $W_{\mathrm{R}}(\mathbf{k})$ is the ionic form factor $f_i(\mathbf{k})$, which describes the density distribution of the electrons in tightly bound states around the ions. It is the principal contribution to the signal detected from x-ray scattering from cold solids [Hubbell et al., 1975] and also typically dominates the total elastic scattering under weakly-ionized WDM conditions [White et al., 2013].

Accurate results for this term may be obtained using the Hartree-Fock method [see, e.g., Fehske et al., 2008] or density functional theory (DFT) [Kohn and Sham, 1965]. These approaches reduce the description of the interacting many-particle system into a reduced single-particle problem by introducing effective interaction potentials which depend on the (bound) electron density. Self-consistent solution for the wavefunction and electron density then yields the ionic form factor from the Fourier transform of $\langle \delta\varrho_e^{\mathrm{b}}(\mathbf{r}) \rangle$. Despite being relatively inexpensive for low-Z or highly-ionized targets, first-principles calculations quickly become prohibitively computational expensive for mid- and high-Z elements.

An alternative to accurate but expensive approaches is given by the screened hydrogenic model first discussed by Pauling and Sherman [Pauling and Sherman, 1932]. For hydrogenic states, the Schrödinger equation can be solved analytically, and the ionic form factor can be constructed from the sum of contributions from all occupied subshells

$$f_i(\mathbf{k}) = \sum_{n,l} f_{n,l}(\mathbf{k}) \equiv \sum_{n,l} \int \mathrm{d}\mathbf{r}\, e^{-i\mathbf{k}\cdot\mathbf{r}} \langle n,l|\mathbf{r}\rangle\langle\mathbf{r}|n,l\rangle, \tag{3.28}$$

where $|n,l\rangle$ represents the hydrogenic state with principal quantum number n and orbital

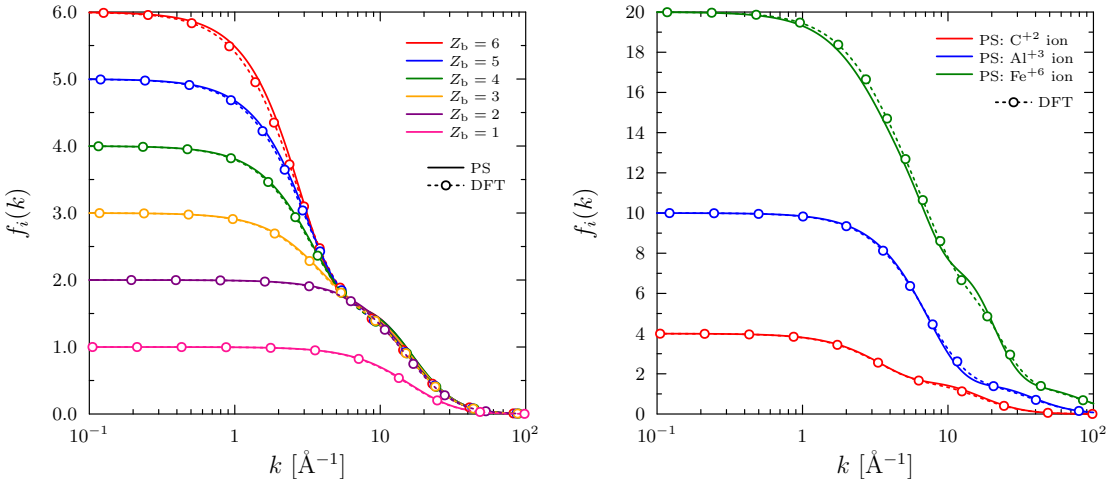

(a) Subshell contributions varying $Z^{\mathrm{f}}_{\mathrm{C}}$.

(b) Model comparison for different elements.

Figure 3.1: (a): Ionic form factor of carbon $f_{\mathrm{C}}(k)$ comparing the screened hydrogenic model of Pauling and Sherman (PS) and density-functional theory (DFT) calculations (courtesy of J. Vorberger) for the neutral atom and various ionization states. (b): Comparison for different ions; carbon ($Z^{\mathrm{f}}_{\mathrm{C}} = 2$), aluminium ($Z^{\mathrm{f}}_{\mathrm{Al}} = 3$) and iron ($Z^{\mathrm{f}}_{\mathrm{Fe}} = 6$).

orbital quantum number l; electrons with different magnetic quantum numbers m are assumed to give identical contributions.

This approach is clearly of limited use for many-electron atoms since screening and exchange contribute significantly to the total potential experienced by the electrons. A simple solution follows by modifying the potential experienced by an electron in a given orbit with an effective screened nuclear charge. The strength of the shielding effect is determined by the number of electrons present in lower-energy states. For an bound state with quantum numbers n and l, the general result is

$$f_{n,l}(k) \overset{\mathrm{PS}}{=} \frac{f_{n,n-1}(k)}{(n-l-1)!} \sum_{j=1}^{n-l} (-1)^{j-1} C_j^{n-l-1} \frac{(n+l+j-1)!}{(n+l)!} (1+x_{n,l}^2)^{n-l-j}\, x_{n,l}^{2(j-1)}, \quad (3.29)$$

$$f_{n,n-1}(k) = \frac{1}{2n(1+x_{n,l}^2)^{2n}} \sum_{j=1}^{n} (-1)^{j-1} \frac{(2n)!}{(2(n-j)+1)!(2j-1)!}\, x_{n,l}^{2(j-1)}, \quad (3.30)$$

$$C_j^{n-l-1} = \left[\frac{(n-l-1)!}{(j-1)!}\right]^2 \frac{1}{(n-l-j-1)!}, \quad (3.31)$$

where $x_{n,l} = nka_B/Z^{\mathrm{eff}}_{n,l}$ and $Z^{\mathrm{eff}}_{n,l}$ is the effective nuclear charge.

In light elements, the analytic results of the Pauling-Sherman (PS) model accurately reproduce the contributions of different subshells based on first principles, as shown by Fig. 3.1(a). The deviation relative to the DFT results becomes larger as the nuclear charge and number of bound states increases, and is most pronounced near the transition between shells (Fig. 3.1(b)). Nevertheless, the PS model gives a very reasonable description of $f_i(k)$ for the application of XRTS to low- and mid-Z targets.

3.4 Screening cloud

The second term in $W_{\mathrm{R}}(\mathbf{k})$ is the screening cloud $q_i(\mathbf{k})$ due to the electrons. In the chemical picture this term represents the response of kinematically free electrons to the low-frequency fluctuations of the ions. Following the multicomponent approach of Wünsch [Wünsch, 2011], a general definition of the screening cloud can be established in terms of the partial SSFs. This enables first principles results to be used (e.g. MC or DFT-MD simulations) and, thus, fully accounts for strong correlations between all particle species.

On the other hand, Eqs. (3.19) and (3.21) give an explicit form of the screening cloud

$$q_i(\mathbf{k}) = \frac{\Pi^{\mathrm{R}}_{ee}(\mathbf{k},0)V_{ei}(k)}{1-\Pi^{\mathrm{R}}_{ee}(\mathbf{k},0)V_{ee}(k)} \equiv \frac{\Pi^{\mathrm{R}}_{ee}(\mathbf{k},0)V_{ei}(k)}{\varepsilon_{ee}(\mathbf{k},0)}. \tag{3.32}$$

In this approximation, the electron response to the ions is clearly linear since the interaction is via the bare Coulomb potential. Non-linear contributions arising from, e.g., bound states and strong electron-ion coupling, can be considered by re-writing the Bethe-Salpeter equation Eq. (2.69) in terms of non-interacting (OCP) density response functions and introducing generalised dynamic potentials [Vorberger and Gericke, 2015]. The result is a quantum statistical analogue of using classical direct correlation functions [Chihara, 2000; Wünsch, 2011]. However, such an approach is currently only well-understood under the restriction of equilibrium and will not be pursued here.

For Coulomb-like electron-ion interactions, the electron-ion potential can be expressed as $V_{ei}(k) = Z_i^{\mathrm{f}} V_{ee}(k)$ and Eq. (3.32) can be re-written in the general form

$$q_i(\mathbf{k}) = Z_i^{\mathrm{f}} \frac{\zeta_e^2(\mathbf{k})}{k^2+\zeta_e^2(\mathbf{k})}, \tag{3.33}$$

where $\zeta_e^2(\mathbf{k}) = k^2\left[\varepsilon_{ee}(\mathbf{k},0)-1\right]$. Eq. (3.33) is valid for arbitrary $\mathbf{k}$ and contains strong coupling effects in the electron subsystem via the polarisation function. Moreover, it is also valid under non-equilibrium conditions.

Since the most important effect of screening is the modification of long-range interactions between particles, the long-wavelength ($k \to 0$) limit is often of interest. In this limit, Eq. (3.33) can be significantly simplified. In RPA, one may derive from Eq. (2.99)

$$\zeta_e^2(\mathbf{k}) \overset{k\to 0}{=} \kappa_e^2 = \frac{2m_e}{\varepsilon_0}\int \frac{\mathrm{d}\mathbf{p}}{(2\pi\hbar)^3}\frac{\mathbf{k}\cdot\partial f_e(\mathbf{p})/\partial\mathbf{p}}{\mathbf{k}\cdot\mathbf{p}}. \tag{3.34}$$

For isotropic systems, i.e. $f_e(\mathbf{p}) \to f_e(p)$, Eq. (3.34) reduces to the result derived by Gericke et al. [Gericke et al., 2010] given in Eq. (1.20), which is independent of the as wave number k. In this case, the screening cloud follows as

$$q_i(k) \overset{k\to 0}{=} Z_i^{\mathrm{f}} \frac{\kappa_e^2}{k^2+\kappa_e^2}. \tag{3.35}$$

In thermal equilibrium the screening length is given by Eq. (1.9). In the long-wavelength limit, the general result for the screening cloud Eq. (3.35) is referred to as the Debye-Hückel (DH) model. Static correlations beyond the RPA are known to be important at intermediate wave numbers, but are not expected to constitute a significant source of error to estimates of screening properties for $k \to 0$.

In contrast to the DH result Eq. (3.35), which is valid strictly in the long-wavelength limit $\lambda = 2\pi/k \to \infty$, the fully k-dependent RPA expression Eq. (3.33) is referred to as the finite-wavelength screening (FWS) model [Chapman et al., 2015]. Comparing the results of the FWS and DH models under equilibrium WDM conditions shows the expected agreement for small k (Fig. 3.2(a)). However, at large k the decay of the FWS result is significantly stronger compared to the $1/k^2$ scaling predicted by the DH model.

The scaling of the decaying tail for $k \to \infty$, i.e. the short-wavelength limit, can be obtained by straightforwardly transforming Eq. (2.104) and considering the static limit

$$\Pi_{ee}^{\mathrm{R0}}(k,0) = -\frac{n_e\beta_e}{2\sqrt{\pi}D_e}\frac{1}{\varkappa_e^2}\,\mathcal{P}\int_{-\infty}^{\infty}\frac{\mathrm{d}x}{1-x/\varkappa_e}\ln\!\left(1+e^{\eta_e-x^2}\right). \tag{3.36}$$

Expanding Eq. (3.36) around $x/\varkappa_e = 0$ (which is valid for large k), one finds

$$\Pi_{ee}^{\mathrm{R0}}(k,0) \overset{k\to\infty}{=} -\frac{n_e\beta_e}{2\varkappa_e^2}\left[1+\frac{1}{\sqrt{\pi}}\sum_{j=2}^{\infty}\varkappa_e^{-j}\,\Gamma(j-1/2)\frac{\mathcal{F}_{j-1/2}(\eta_e)}{D_e}\right] \tag{3.37}$$

The asymptotic behaviour of $q_i(k)$ for large k is described by the leading order term, giving

$$q_i(k) \overset{k\to\infty}{=} Z_i^{\mathrm{f}}\frac{\gamma_e^4}{k^4+\gamma_e^4}, \tag{3.38}$$

where $\gamma_e = (16\pi n_e/a_{\mathrm{B}})^{1/4}$. Thus, the scale length characterising the behaviour of the screening in this regime is temperature independent (see the upper curves in Fig. 3.2(a)).

Eq. (3.38) can be used to study the free electron density distribution in the immediate vicinity of a test ion due to the effective screened potential

$$n_e(r) \overset{r\to 0}{=} \frac{(\gamma_e/\sqrt{2})^3}{2\pi}\mathrm{sinc}\left(\frac{\gamma_e r}{\sqrt{2}}\right)e^{-\frac{\gamma_e r}{\sqrt{2}}}. \tag{3.39}$$

The electron density around an ion therefore decays exponentially and also fluctuates around the mean number density far from the ion. This effect is well-known from solid state theory as the Friedel oscillations [Friedel, 1954] and has recently been directly observed experimentally [Ono et al., 2006]. Note that although the long-ranged behaviour of the density distribution is qualitatively similar to that predicted by the DH result, the scale length of the decay is different.

The characteristic radius of the degenerate bulk of electrons near the ion is set by the chemical potential [Resta, 1977]. One may therefore expect that for non-degenerate

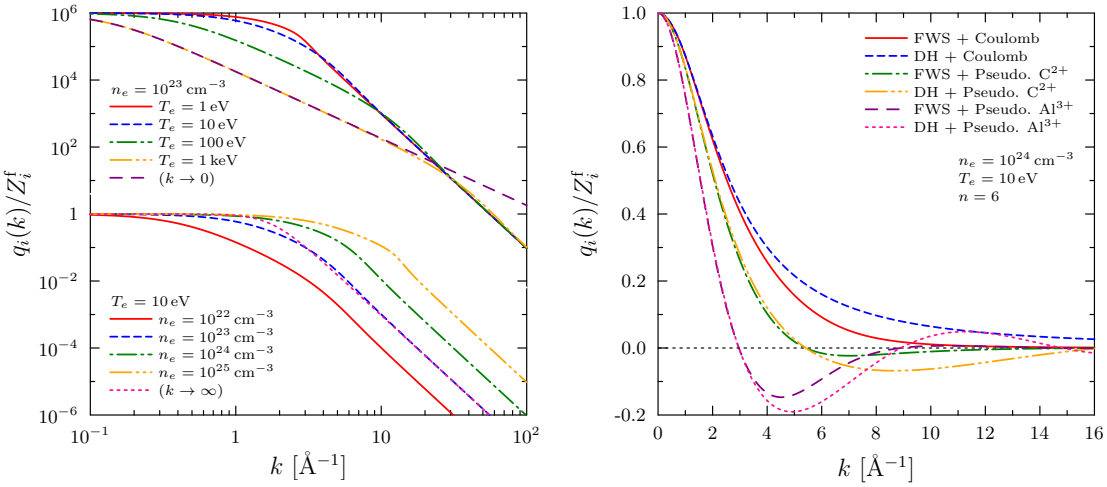

(a) Limiting cases of the screening cloud.

(b) Effect of pseudo-potentials.

Figure 3.2: (a): Charge-normalised FWS screening cloud $q_i(k)/Z_i^{\mathrm{f}}$ for different electron densities (lower set of curves) and temperatures (upper set of curves); the upper set of curves have been artificially offset on the y-axis. The DH result, valid in the $k \to 0$ limit, is shown to reproduce FWS calculations under low degeneracies up to large k (long-dashed purple curve). The short-wavelength $k \to \infty$ behaviour is important in the WDM regime for intermediate k. (b): Comparison of models for $n_e = 10^{24}\,\mathrm{cm}^{-3}$ and $T_e = 10\,\mathrm{eV}$ using different screening and electron-ion potentials. Effective core radii of $r_{\mathrm{core}} = 29$ (C^{4+}) and $r_{\mathrm{core}} = 53\,\mathrm{pm}$ (Al^{3+}) are considered for the soft-core pseudo-potential.

conditions that deviations from the $1/k^2$ scaling of the DH model sufficiently close to the ion, i.e. at large k, to be readily accessible using XRTS. Indeed, such behaviour is shown in Fig. 3.2(a). For the WDM regime, however, the transition occurs for intermediate wave numbers, making large-angle XRTS the ideal tool with which to probe the structure of the screening cloud [Chapman et al., 2015]. The effect of finite-wavelength screening and its impact on interpretation of XRTS data will be addressed in the last chapter.

Beyond the linear response approximation, strong electron-ion correlations such as bound states are expected to influence the screening cloud. For partially ionized plasmas treated in the chemical picture, a well-known alternative to evaluating the direct polarisation terms is to use a pseudo-potential to describe the modification of the interaction between the free electrons and ions due to bound electrons. As simple estimate of this effect can be implemented using a soft empty core (EC) potential similar to a well-known approximation used in solids [Ashcroft, 1966]

$$V_{ei}(r) \overset{\mathrm{EC}}{=} V_{ei}^{\mathrm{C}}(r)\left[1 - \exp\left(-\frac{r^n}{r_{\mathrm{core}}^n}\right)\right]. \tag{3.40}$$

In Eq. (3.40), r_c is the empty core radius and the parameter n determines the slope of the transition from the Coulomb-like behaviour at large distances. In the limit $n \to \infty$, the transition term tends to a step function, which yields the well-known result $V_{ei}(k) = V_{ei}^{\mathrm{C}}(k)\cos(kr_{\mathrm{core}})$. The oscillating behaviour, which results in reduced contributions to

screening (Fig. 3.2(b)), is due to the exclusion of free electrons from the vicinity of bound states [Gericke et al., 2010].

The exact behaviour of the screening function is currently one of the most uncertain aspects of modelling XRTS in dense matter. High-precision, all-electron numerical studies of the elastic scattering has recently demonstrated both the important of the FWS model at large k and also supports the need for pseudo-potentials such as the EC model discussed here [Vorberger and Gericke, 2015]. Nevertheless, appropriate values of r_{cut} for different elements and conditions remains an issue which can only be reliably constrained using expensive numerical methods.

3.5 Static ion structure factors

In WDM, the ions may be ubiquitously treated as non-degenerate (see Fig. 1.1), such that their dynamic and static properties may be evaluated using the techniques of classical statistical mechanics. In the classical framework, the microscopic spatial correlations between pairs of ions is defined as the ensemble average over the two-particle Klimontovich density [Hansen and McDonald, 1990]

$$g_{ab}(\mathbf{r}) = \frac{1}{n_a n_b} \left\langle \sum_{\alpha=1}^{N_a} \sum_{\beta=1}^{N_b} \delta(\mathbf{r}_1 - \mathbf{r}_\alpha)\delta(\mathbf{r}_2 - \mathbf{r}_\beta) \right\rangle_{\alpha\neq\beta\,\forall\, a=b}. \tag{3.41}$$

In this form, the precise time-dependent orbits of the ions makes fully numerical discrete particle approaches such as molecular dynamics (MD) feasible, thereby enabling a robust treatment of strong inter-particle forces in non-equilibrium systems. The partial SSFs needed to describe multicomponent systems are defined from the general relationship

$$S_{ab}(\mathbf{k}) = \delta_{ab} + \sqrt{n_a n_b} \int \mathrm{d}\mathbf{r}\, e^{-i\mathbf{k}\cdot\mathbf{r}}\, [g_{ab}(\mathbf{r}) - 1]. \tag{3.42}$$

Simulations of classical Coulomb and Yukawa systems are extensively used to investigate microphysical phenomena such as charged-particle transport and energy relaxation processes and macroscopic thermodynamics such as plasma phase transitions and Wigner crystallisation. For simple systems such as fully-ionized one-component plasmas, the ionic properties are expected to be quite accurate. However, explicit consideration of the electrons within a classical framework is elusive even if their interactions with the ions can be described using pseudo-potentials.

Coupling classical MD simulations to DFT calculations [Gonze et al., 2002; 2005; 2009] has now enabled the effective inter-particle potentials to be informed by the self-consistent field produced by the electrons, thereby circumventing the need to construct pseudo-potentials to model complex electron-ion systems. Although these techniques have become the standard tools for investigating the static correlations of dense matter, alternatives to such numerically intensive simulations are generally desirable.

3.5.1 Fluid theory approach

For the conditions of interest the ions can often be treated in thermal equilibrium since non-equilibrium effects tend to be restricted to the electrons. Considering an isotropic, homogeneous fluid in which static correlations between strongly-interacting charged ions are contained in the potential of mean force $W_{ab}(r)$, Eq. (3.41) may be expressed as

$$g_{ab}(r) = \exp\left[-\beta W_{ab}(r)\right]. \tag{3.43}$$

This quantity can be interpreted as the probability of locating an ion of species b at a radius r from an ion of species a. The total number of ions of species b within a shell of thickness $r + \mathrm{d}r$ centred on the central ion is then $4\pi r^2 g_{ab}(r)\mathrm{d}r$.

In the low density limit, $W_{ab}(r)$ must of course reduce to the direct interaction $V_{ab}(r)$, which is Coulomb-like for charged particles. Correlation and screening effects then become important as the density increases. The mean potential can be considered via a virial expansion in powers of the density and products of rapidly decaying Mayer functions, thereby limiting strong correlations to short distances [Hansen and McDonald, 1990]. Subsequently, the deviation from the bare interaction may be decomposed into $\beta W_{ab}(r) - \beta V_{ab}(r) = N_{ab}(r) + B_{ab}(r)$; the first term is known as the *nodal* contribution and the second is the non-nodal or *bridge* term. Thus, it follows from Eq. (3.43)

$$g_{ab}(r) = \exp\left[-\beta V_{ab}(r) + N_{ab}(r) + B_{ab}(r)\right]. \tag{3.44}$$

The fully correlated system can also be expressed in terms of the direct and indirect interactions via the famous Ornstein-Zernicke equation

$$h_{ab}(r) = c_{ab}(r) + N_{ab}(r) \tag{3.45}$$

$$N_{ab}(r) = \sum_c n_c \int \mathrm{d}\mathbf{r}'\, c_{ac}(r')\, h_{ab}(\left|\mathbf{r} - \mathbf{r}'\right|), \tag{3.46}$$

where $c_{ab}(r)$ and $h_{ab}(r) = g_{ab}(r) - 1$ are the direct and total correlation functions, respectively [Ornstein and Zernike, 1914]. In the context of the cluster expansion for the mean potential Eq. (3.44), the second term $N_{ab}(r)$ is identified as the nodal contribution [van Leeuwen et al., 1959]. The Fourier transforms of Eqs. (3.45) and (3.46) give

$$h_{ab}(k) = c_{ab}(k) + N_{ab}(k), \tag{3.47}$$

$$N_{ab}(k) = \sum_c n_c\, c_{ac}(k) h_{cb}(k) \tag{3.48}$$

which form a linear set of algebraic equations that can be solved by matrix inversion, thereby directly relating $c_{ab}(k)$ and $N_{ab}(k)$. Without further approximation, however, the system remains unclosed since the bridge term is unknown.

Thus far, the ion-ion interaction has not been specified beyond that it is Coulomb-like.

In general, considering a bare Coulomb potential is not useful since the electrons modify ion interactions by screening; this was recognised in Eqs. (3.19) and (3.21). As discussed in section 3.4, static screening can be evaluated in RPA to yield the Debye potential

$$V_{ab}^{\mathrm{D}}(r) = V_{ab}^{\mathrm{C}}(r)\, e^{-\kappa_e r}, \quad V_{ab}^{\mathrm{D}}(k) = \frac{V_{ab}^{\mathrm{C}}(k)}{1 + (\kappa_e/k)^2}, \tag{3.49}$$

in which κ_e can be calculated from Eq. (1.21) under degenerate conditions.

Analytic results can be obtained for weakly coupled ions by neglecting the bridge term and linearising Eq. (3.44), such that $h_{ab}(r) \approx -\beta V_{ab}(r) + N_{ab}(r)$ and subsequently $c_{ab}(r) \approx -\beta V_{ab}(r)$ for the total and direct correlation functions, respectively. In the important case of a screened OCP, Eq. (3.47) can be solved directly and yields

$$S_{ii}(k) \overset{\mathrm{DH}}{=} \frac{k^2 + \kappa_e^2}{k^2 + \kappa_e^2 + \kappa_{\mathrm{D}i}^2}. \tag{3.50}$$

The pair distribution function follows as

$$g_{ii}(r) \overset{\mathrm{DH}}{=} 1 - \beta V_{ii}^{\mathrm{C}}(r)\, e^{-\kappa_{\mathrm{scr}}\, r}. \tag{3.51}$$

where $\kappa_{\mathrm{scr}}^2 = \kappa_e^2 + \kappa_{\mathrm{D}i}^2$. Considering Eq. (3.51) as the linearisation of Eq. (3.42) identifies the mean potential as $W_{ii}(r) = V_{ii}^{\mathrm{C}}(r) e^{-\kappa_{\mathrm{scr}} r}$. Thus, the indirect binary interactions lead to screening of the bare Coulomb potential, even for OCP-like systems in which $\kappa_e \to 0$.

3.5.2 Hypernetted-chain approximation

In the strongly coupled regime, the non-linear character of the total correlation function must be preserved. Neglecting the bridge term, the Ornstein-Zernicke equation is formally closed by the relations connecting the direct correlation function and nodal term in real and Fourier space; this is known as the *hypernetted-chain* (HNC) closure relation [van Leeuwen et al., 1959]. Unfortunately, it cannot be solved analytically.

Based on an initial guess for $c_{ab}(r)$, the two equations can be solved by iteratively transforming between Fourier and real space using numerical FFT [Press et al., 2007] to compute nodal corrections until convergence is reached. However, this process can only be performed numerically providing that the potential decays faster than $1/k^2$, which is incompatible with Coulomb-like systems. This problem can be solved by defining short- and long-ranged auxiliary functions [Springer et al., 1973]

$$V_{ab}(r) = V_{ab}^{\mathrm{s}}(r) + V_{ab}^{\mathrm{l}}(r) = V_{ab}(r) e^{-\alpha r} + V_{ab}(r)[1 - e^{-\alpha r}], \tag{3.52}$$

$$c_{ab}(r) = c_{ab}^{\mathrm{s}}(r) - \beta V_{ab}^{\mathrm{l}}(r), \tag{3.53}$$

$$N_{ab}(r) = N_{ab}^{\mathrm{s}}(r) + \beta V_{ab}^{\mathrm{l}}(r), \tag{3.54}$$

where α is constrained by the requirement $V_{ab}(r_{\max}) \to 0$. The long-ranged behaviours of $c_{ab}(r)$ and $N_{ab}(r)$ result from the known limiting behaviour $h_{ab}(r) \overset{r\to\infty}{=} 0$.

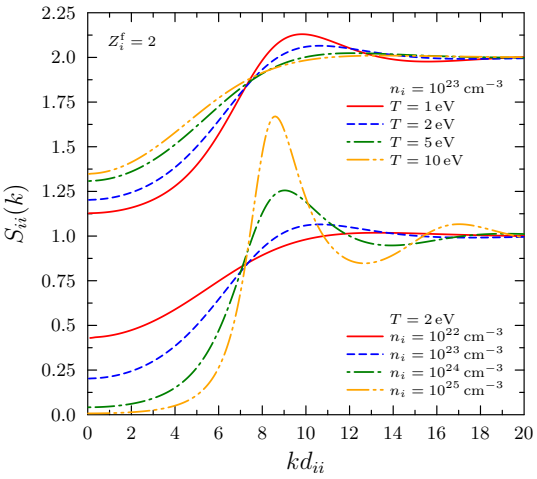

Figure 3.3: Static ion-ion structure factor of He-like beryllium in the WDM regime using a Debye potential (3.49) in the HNC approximation, as a function of the mean ion separation $d_{ii} = (6/\pi n_i)^{1/3}$. The lower set of curves show the density dependence at a fixed temperature and the upper set of curves show the temperature dependence for a constant density; the latter have been artificially offset in the y-axis for clarity.

Applying Eqs. (3.52 - 3.54) allows the relevant equations to be reformulated in terms of the unknown short-ranged components and the long-ranged interactions in Fourier space. For example, one finds in the case of an OCP

$$c_{ii}^{\mathrm{s}}(r) \overset{\mathrm{HNC}}{=} \exp\left[-\beta V_{ii}^{\mathrm{s}}(r) + N_{ii}^{\mathrm{s}}(r)\right] - N_{ii}^{\mathrm{s}}(r) - 1, \tag{3.55}$$

$$N_{ii}^{\mathrm{s}}(k) \overset{\mathrm{HNC}}{=} \frac{n_i\, c_{ii}^{\mathrm{s}}(k)\left[c_{ii}^{\mathrm{s}}(k) - \beta V_{ii}^{\mathrm{l}}(k)\right] - \beta V_{ii}^{\mathrm{l}}(k)}{1 - n_i\left[c_{ii}^{\mathrm{s}}(k) - \beta V_{ii}^{\mathrm{l}}(k)\right]}. \tag{3.56}$$

Thus, potentials which are analytic in Fourier space enable numerical solution of the HNC scheme for an appropriate value of α. For the Debye potential (3.49), one has

$$V_{ii}^{\mathrm{s}}(r) \overset{\mathrm{D}}{=} V_{ii}^{\mathrm{D}}(r)\, e^{-\alpha r}, \tag{3.57}$$

$$V_{ii}^{\mathrm{l}}(k) \overset{\mathrm{D}}{=} V_{ii}^{\mathrm{D}}(k)\, \frac{\alpha^2 + 2\alpha\kappa_e}{k^2 + (\alpha + \kappa_e)^2}. \tag{3.58}$$

Naturally, one recovers the expected results for a Coulomb plasma in the limit $\kappa_e \to 0$. The initial guess for $c_{ii}^{\mathrm{s}}(r)$ is provided by initialising the iterative loop with $N_{ii}^{\mathrm{s}}(r)|_{j=0} = 0$ and proceeding until $N_{ii}^{\mathrm{s}}(r)|_{j+1} - N_{ii}^{\mathrm{s}}(r)|_j$ satisfies some definition of convergence, whereafter $h_{ii}(r)$ and $S_{ii}(k)$ can be found. The generalisation of the HNC scheme to multicomponent systems has recently been examined in detail [Wünsch, 2011] for various effective ion-ion interaction models, and will therefore not be further elaborated upon in this work. Note that all HNC calculations presented in this thesis are calculated using an independent multicomponent code written by the author.

The temperature and density dependence of the SSF given by the HNC scheme using a Debye potential is shown in Fig. 3.3 for one ion species under WDM conditions. The spatial distribution of the ions becomes more lattice-like as the coupling in the plasma increases (via increasing the density and/or decreasing the temperature) and develops substantial short-range order due to strong correlations. The development of a strong correlation hole at small k results from the exclusion of ions from the immediate vicinity of the central ion in

real space due to the strong Coulomb repulsion. Increasing the temperature both broadens the peaks as thermal excitations weaken correlations and also increases the screening of the potential, partially filling the correlation hole.

3.5.3 Ion-ion pseudo-potentials for warm dense matter

As discussed in Section 3.4, the screening of Coulomb interactions can strongly depart from the Debye potential (3.49) in the WDM regime. In particular, in dense plasmas the mean ion separation may be sufficiently small for the ion-ion interaction to be modified by the oscillating short-range component of the screening cloud. However, for arbitrary k the screened potential is no longer analytic in Fourier space. To be compatible with the Springer form of the potentials one can use numerical FFT to evaluate

$$V_{ii}^{\mathrm{s}}(r) \overset{\mathrm{FWS}}{=} \mathcal{F}\left\{\frac{V_{ii}^{\mathrm{C}}(k)}{\varepsilon_{ee}^{0}(k,0)}\right\} e^{-\alpha r}, \tag{3.59}$$

$$V_{ii}^{\mathrm{l}}(k) \overset{\mathrm{FWS}}{=} \frac{V_{ii}^{\mathrm{C}}(k)}{\varepsilon_{ee}^{0}(k,0)} - \mathcal{F}^{-1}\left\{V_{ii}^{\mathrm{s}}(r)\right\}. \tag{3.60}$$

Surprisingly, the results do not differ greatly from the usual Debye potential, even in the intermediate degeneracy regime where the FWS form of the screening departs significantly from the DH limit.

In partially-ionized matter, the influence of bound states on the ion-ion interactions is also potentially significant. A simple model pseudo-potential has recently been introduced for modelling the effect of the increased *short-range repulsion* (SRR) due to overlapping bound states [Wünsch et al., 2009]

$$V_{ii}(r) \overset{\mathrm{SRR}}{=} V_{ii}^{\mathrm{D}}(r) + k_B T_i \left(\frac{\sigma_{ii}}{r}\right)^4. \tag{3.61}$$

The effective core radius σ_{ii} must be calibrated against the sources such as experiments or DFT-MD results, and generally depends on the plasma conditions.

The form of Eq. (3.61) has the disadvantage that it cannot be Fourier transformed, and the long-ranged Springer potential $V_{ii}^{\mathrm{l}}(k)$ must be estimated by neglecting the $1/r^4$ term. An alternative model potential which avoids this issue is the *charge-switching Debye* (CSD) model [Vorberger and Gericke, 2013], which transitions between the unscreened nuclear charge Z_a^{A} and the effective ionic charge Z_i^{f}

$$V_{ii}^{\mathrm{s}}(r) \overset{\mathrm{CSD}}{=} V_{ii}^{\mathrm{D}}(r)\left[1 + \zeta e^{-\gamma_{ii} r}\right] e^{-\alpha r}, \tag{3.62}$$

$$V_{ii}^{\mathrm{l}}(k) \overset{\mathrm{CSD}}{=} V_{ii}^{\mathrm{D}}(k)\left\{\frac{\zeta[\alpha^2 + 2\alpha(\gamma_{ii} + \kappa_e)](k^2 + \kappa_e^2)}{[k^2 + (\gamma_{ii} + \kappa_e)^2][k^2 + (\alpha + \gamma_{ii} + \kappa_e)^2]} - \frac{\alpha^2 + 2\alpha\kappa_e}{k^2 + (\alpha + \kappa_e)^2}\right\}, \tag{3.63}$$

in which $\zeta = (Z_i^{\mathrm{A}}/Z_i^{\mathrm{f}})^2 - 1$. In the limit $\gamma_{ii} \to 0$, interactions between fully stripped ions rise to the strong repulsion, while the usual Debye-like interaction between effective ionic charge states is recovered for $\gamma_{ii} \to \infty$.

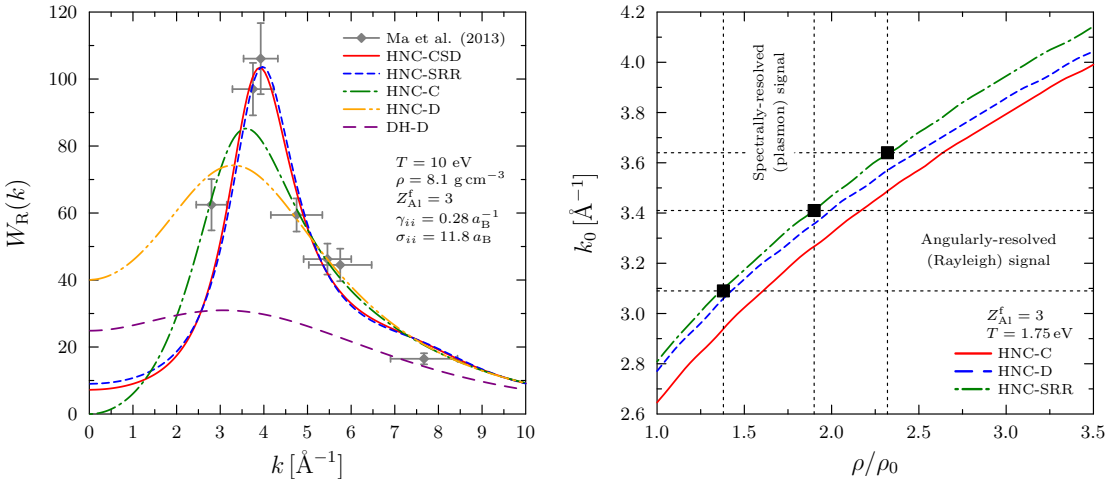

(a) Rayleigh scattering in shock-compressed Al. (b) Correlation peak position vs. Al compression.

Figure 3.4: (a): Experimental total elastic scattering data in shock-compressed aluminium (courtesy of T. Ma) also supports the presence of strong repulsion between ion cores. Here, $f_i(k)$ is given by the screened hydrogenic approach of Pauling and Sherman Eq. (3.29), and $q_i(k)$ is given by Eq. (3.33) and uses a Coulomb electron-ion interaction. (b): Comparison of predictions of the correlation peak position as a function of target compression using different ion pseudo-potentials in HNC, compared to experimental data in shock-compressed aluminium (courtesy of L. Fletcher).

Both the SRR and CSD models can be used to accurately reproduce DFT-MD calculations of partially-ionized WDM, as shown by Fig. 3.4(a), in which recent experimental results of elastic scattering strength in shock-compressed aluminium [Ma et al., 2013; 2014] are compared with theory. Here, $W_{\rm R}(k)$ was calculated according to Eq. (3.27). As expected, the weakly coupled DH results fail to explain the data other than at large k, where the SSF approaches the ideal plasma limit and the decay of the Rayleigh signal is mostly determined by $f_i(k)$ alone. A pure Coulomb system gives a reasonably good estimate of the scatter at both small and large k values, but fails to describe the scattering amplitude near the correlation peak ($k_0 \sim 3.5$–$4.5\,$Å^{-1}). Applying models which account for short-range repulsion can also reproduce the observed height of this feature, although in these cases the leading edge of the peak is less accurate.

The width of the error bars represent the significant uncertainties associated with gradients in the sample and the large divergence of the laser-driven x-ray source. To address these issues, experiments are presently being conducted using FEL x-rays [Gauthier et al., 2014; Fletcher et al., 2015] to enable angularly-resolved measurements with significantly improved signal-to-noise levels and vastly reduced source divergence. A further example of the utility of the SRR and CSD models is shown in Fig. 3.4(b). This demonstrates that the measured correlation peak position in shock-compressed aluminium gives results which are only consistent with spectrally-resolved data if strong repulsion is accounted for.

3.6 Inelastic free-free feature

As implied by Eq. (3.19), the free-free component of Eq. (3.26) can be considered as the structure of an interacting one-component electron plasma (electron gas) in which the ions are considered as a static neutralising background; the *jellium* model [Chihara, 2000]. Neglecting all ion contributions to the dynamic structure Eq. (3.13) reduces to

$$S_{ee}(\mathbf{k},\omega) = \frac{\hbar}{2\pi n_e}\frac{i\Pi^{>}_{ee}(\mathbf{k},\omega)}{\left|\varepsilon_{ee}(\mathbf{k},\omega)\right|^2} \overset{\text{RPA}}{=} \frac{S^0_e(\mathbf{k},\omega)}{\left|\varepsilon^0_{ee}(\mathbf{k},\omega)\right|^2}, \tag{3.64}$$

which is again valid for non-equilibrium and equilibrium systems [Chapman and Gericke, 2011]. In thermal equilibrium the KMS condition (2.95) relates the imaginary part of the dielectric function to the greater correlation function in the numerator, yielding

$$S_{ee}(\mathbf{k},\omega) \overset{\text{equil.}}{=} \frac{2\omega_{\mathrm{C}e}}{\pi\omega^2_{\mathrm{pe}}}\frac{1}{e^{-\beta\hbar\omega}-1}\operatorname{Im}\varepsilon^{-1}_{ee}(\mathbf{k},\omega). \tag{3.65}$$

Eq. (3.65) is valid for arbitrary electron coupling beyond RPA. By extension, Eq. (3.64) can be thought of as a generalisation of the FDT to the non-equilibrium electron gas, which will be studied extensively in the next chapter.

3.6.1 Collective excitations

From Eq. (3.65), the shape of the excitation spectrum of the free electrons is entirely determined by the spectral function $\operatorname{Im}\varepsilon^{-1}_{ee}(\mathbf{k},\omega)$. Examining this function in terms of its real and imaginary parts reveals a Lorentzian-like structure

$$\operatorname{Im}\varepsilon^{-1}_{ee}(\mathbf{k},\omega) = \frac{-\operatorname{Im}\varepsilon_{ee}(\mathbf{k},\omega)}{\left[\operatorname{Re}\varepsilon_{ee}(\mathbf{k},\omega)\right]^2+\left[\operatorname{Im}\varepsilon_{ee}(\mathbf{k},\omega)\right]^2}, \tag{3.66}$$

which fully characterises the mode spectrum of the electron density fluctuations. It is straightforward to see that Eq. (3.66) is analogous to the mode spectrum of a simple damped harmonic oscillator and, thus, the resonant frequency and damping rate of the fluctuations are determined by $\operatorname{Re}\varepsilon_{ee}(\mathbf{k},\omega)$ and $\operatorname{Im}\varepsilon_{ee}(\mathbf{k},\omega)$, respectively.

The structure of Eq. (3.66) exhibits maxima (resonances) when the denominator is minimised, i.e. when $\operatorname{Re}\varepsilon_{ee}(\mathbf{k},\omega) \ll \operatorname{Im}\varepsilon_{ee}(\mathbf{k},\omega)$. Moreover, from the definition $\varepsilon_{ee}(\mathbf{k},\omega) = 1-V_{ee}(k)\Pi^{\mathrm{R}}_{ee}(\mathbf{k},\omega)$, one notes that if a frequency range exists for which $V_{ee}(k)\Pi^{\mathrm{R}}_{ee}(\mathbf{k},\omega) > 1$ then the real part of the dielectric function has a pair of roots

$$\operatorname{Re}\varepsilon_{ee}(\mathbf{k},\omega_j) = 0, \tag{3.67}$$

corresponding to the characteristic excitation frequencies of the free electrons ω_j. Eq. (3.67) is known as the *dispersion relation* of the collective modes. In the general non-equilibrium case (3.64), the collective excitations are still determined by Eq. (3.67), but the amplitudes and widths of the resonances are no longer straightforwardly correlated.

3.6.2 Collective and non-collective scattering

Fig. 3.5(a) shows dispersion curves resulting from numerically solving Eq. (3.67) in RPA for a range of equilibrium conditions in the WDM regime. Each curve shows two distinct branches with different frequency-scales (dispersions); the upper branch is referred to as the *plasmon* branch and the lower is known as the *acoustic branch* [Kremp et al., 2005]. The plasmon branch is of particular interest as it invariably experiences less damping than the acoustic branch, and is therefore far more accessible to experiments.

The two branches merge for a critical wave number that is some fraction of the inverse screening length κ_e, after which $\mathrm{Re}\,\varepsilon_{ee}(\mathbf{k},\omega)$ ceases to have roots. This feature corresponds to the transition from the collective regime $\alpha = \kappa_e/k > 1$, where the length scale interrogated by the probe is larger than the characteristic scale length for correlations between electrons (the screening length), and the non-collective regime $\alpha < 1$, in which the probe is scattered by the motions of individual particles. Thus, in the collective scattering regime the free electron response is dominated by the dispersion and damping of the plasmons, whereas under non-collective conditions it reflects the shape of the momentum distribution. The transition from collective- to non-collective scattering is shown in Fig. 3.5(b).

The sensitivity of the equilibrium DSF to the free electron density and temperature is shown in Fig. 3.5 for fixed k. Here, the transition from non-collective to collective scattering occurs due to the changes κ_e. In the collective regime, the plasmon resonance position provides a sensitive diagnostic of the electron density (Fig. 3.5(a)). On the other hand, the damping of the plasmons strongly increases with the electron temperature once the thermal contribution to the screening becomes important. Note that in panel (d) the plasmon is so weakly damped for $T_e = 1\,\mathrm{eV}$ that the acoustic mode can be clearly distinguished; this is completely obscured by the broadened plasmon when the temperature is increased.

3.6.3 Plasmon dispersion relation

Under strongly collective conditions the dispersion relation can be expanded in the long-wavelength $k \to 0$ limit to provide a simple relationship between the observed resonance position and the plasma conditions. In RPA, one may expand Eq. (2.99) up to order $(k/\omega)^2$ for an arbitrary distribution function and find [Kremp et al., 2005]

$$\mathrm{Re}\,\varepsilon^0_{ee}(\mathbf{k},\omega) \overset{k\to 0}{=} 1 - \frac{\omega_{\mathrm{pe}}^2}{\omega^2}\left[1 + 2\frac{k^2\langle K_e\rangle}{m_e\omega^2}\right], \tag{3.68}$$

in which the mean kinetic energy of the electrons $\langle K_e\rangle$ is defined in Eq. (1.8). Relation (3.68) can be solved iteratively to give a closed form expression for the resonance frequency

$$\omega_{\mathrm{pl}}(k) = \omega_{\mathrm{pe}}\left[1 + \frac{k^2\langle K_e\rangle}{m_e\omega_{\mathrm{pe}}^2}\right]. \tag{3.69}$$

Despite this derivation being limited to the RPA, the general form of Eq. (3.69) is also

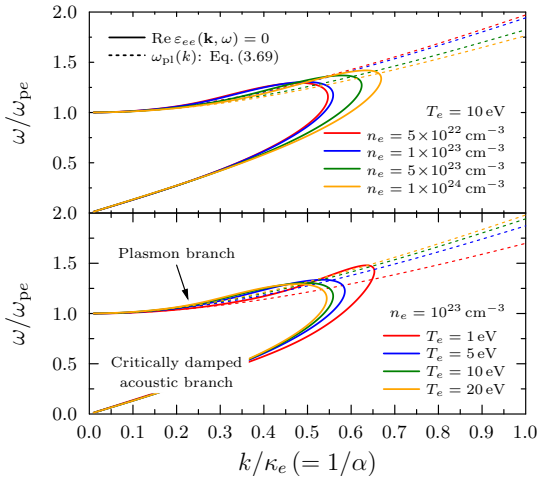

(a) Plasmon dispersion curves.

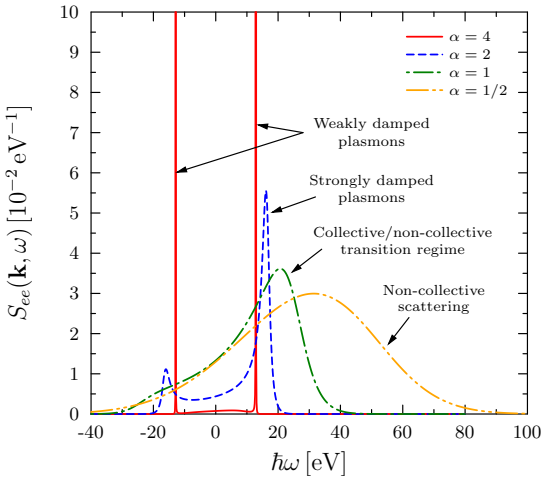

(b) Collective-non-collective transition.

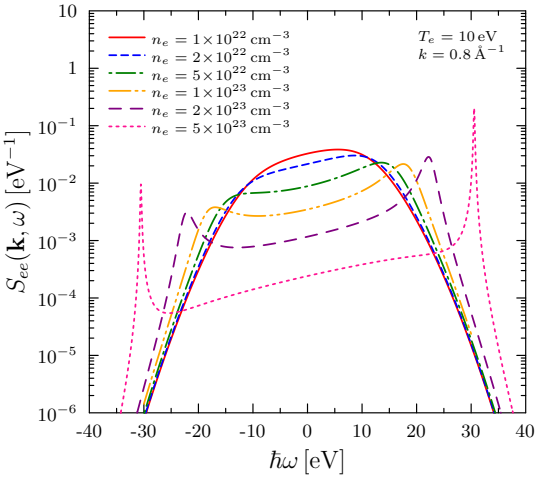

(c) Density dependence of $S_{ee}(\mathbf{k},\omega)$.

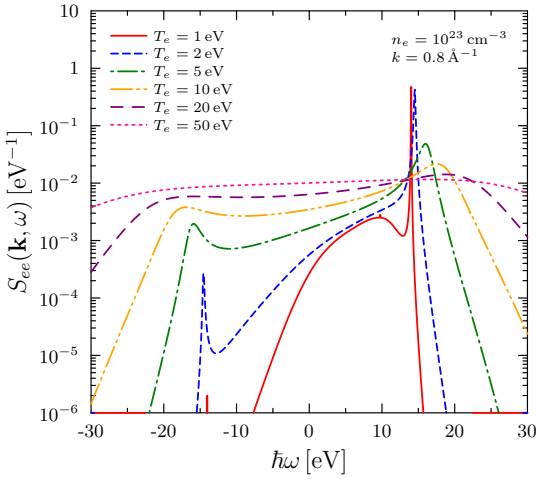

(d) Temperature dependence of $S_{ee}(\mathbf{k},\omega)$.

Figure 3.5: (a): Plasmon dispersion curves in RPA, given by the contour $\mathrm{Re}\,\varepsilon_{ee}(\mathbf{k},\omega) = 0$, for varying electron density at a fixed temperature (upper panel) and for different temperatures for a constant density (lower panel). In each case, the small k limit of the dispersion relation Eq. (3.69) is shown by the thin dashed (colour-coordinated) curves for comparison. (b): Evolution of the DSF for $T_e = 10$ eV and $n_e = 10^{23}$ cm^{-3} from strongly collective- to non-collective scattering due to increasing the wave number k. (c): Sensitivity of the DSF to the number density for a fixed temperature and wave number. (d) Temperature sensitivity for a constant density and wave number.

expected to hold for non-ideal conditions. Specifically, the plasmons are expected to be excited close to the fundamental harmonic oscillations (plasma frequency) of the electrons [Tonks and Langmuir, 1929], yielding a strong dependence on the free electron density. For non-ideal states, however, the additional dispersion due to the force resulting from the plasma pressure is reduced by the correlation energy.

In the case of thermal equilibrium it is straightforward to show that Eq. (3.69) gives the famous Bohm-Gross dispersion relation under non-degenerate conditions [Bohm and Gross,

1949], and the Klimontovich-Silin dispersion relation for degenerate conditions [Klimontovich and Silin, 1952]. The results provide good estimates of the plasmon dispersion for strongly collective conditions (see thin dashed curves in Fig. 3.5(a)), but fails to capture the stronger dispersion shown by the numerical solution of Eq. (3.67) at intermediate k.

3.6.4 Detailed balance relation in thermal equilibrium

Another notable feature of the free electron DSF shown by Fig. 3.5 is the asymmetric shape of the spectrum with respect to positive and negative energy shifts. This is particularly obvious in the collective regime from the amplitudes of the red- and blue-shifted plasmon peaks. Noting that the inverse dielectric function is an odd function of ω, the origin of this asymmetry must be due to the Bose-like term. Considering scattering events resulting in opposite energy and momentum shifts, i.e. $\{\mathbf{k}, \omega\}$ and $\{-\mathbf{k}, -\omega\}$, one finds the simple relationship

$$\frac{S_{ee}(\mathbf{k}, \omega)}{S_{ee}(-\mathbf{k}, -\omega)} \overset{\text{equil.}}{=} e^{\beta\hbar\omega}, \tag{3.70}$$

which is known as the principle of *detailed balance* [Thomsen, 1953]. This result reflects the greater availability (lower occupation) of final states for electrons that gain energy during the scattering process. The ratio of the availability of states is represented by the temperature-dependent Boltzmann factor. Naturally, the detailed balance becomes more important under degenerate conditions as the FD distribution approaches higher levels of occupation at low energy/momentum relative to the MB distribution.

Since Eq. (3.70) is independent of the approximation of the dielectric function, measurement of the detailed balance using XRTS offers a model-independent mechanism for determining the temperature of degenerate matter. Although this technique has been used in experiments [Döppner et al., 2009], such measurements are generally considered difficult to realise with laser-driven x-ray sources due to limited range of conditions under which plasmons can be observed and the high level of signal-to-noise typically required. It should also be noted that the detailed balance relation is strictly valid for equilibrium only. Indeed, this relationship is shown to break down for non-equilibrium electron distributions in the next chapter.

3.6.5 Strong coupling corrections to the RPA

It is well-known that the RPA does not accurately describe the properties of electrons in strongly coupled states. In particular, the (negative) correlation contribution reduces the second (pressure) term in Eq. (3.69), shifting the plasmon resonance to lower frequencies. Consequently, the plasmon is also expected to reduce in amplitude and increase in width due to heavier damping. Indeed, XRTS measurements in solid aluminium [Batson et al., 1976], beryllium [Mazzone et al., 1983], and more recently laser-driven shock-compressed

warm dense boron [Neumayer et al., 2010], have all observed the expected enhancement of the width of the plasmon peak and the down-shift of the dispersion relation.

One may attempt to go beyond the RPA by evaluating higher-order terms in the perturbation expansion of the polarisation function, as discussed in Section 2.4. Despite the physically rigorous basis of such an approach, which is also appealing due its generalisation to non-equilibrium electrons, it is extremely challenging to evaluate the resulting multi-dimensional integral expressions. Furthermore, it is not presently clear how to handle the time-ordering of terms of second order on the Keldysh contour at all, thereby restricting improvements on the RPA to either equilibrium conditions or the first-order correction to the electron gas.

As first suggested by Hubbard, correlations beyond RPA may be considered in equilibrium via a renormalised dynamic electron-electron interaction [Hubbard, 1957]. This is expressed via a local field correction (LFC) to the bare Coulomb interaction $V_{ee}(k) \rightarrow [1 - G_{ee}(\mathbf{k},\omega)]V_{ee}(k)$, which formally contains all terms beyond RPA

$$G_{ee}(\mathbf{k},\omega) = \frac{1}{V_{ee}(k)\Pi^{\mathrm{R}}_{ee}(\mathbf{k},\omega)} - \frac{1}{V_{ee}(k)\Pi^{\mathrm{R0}}_{ee}(\mathbf{k},\omega)}. \tag{3.71}$$

Eq. (3.71) is not useful in itself as it still requires the form of the fully coupled polarisation function $\Pi^{\mathrm{R}}_{ee}(\mathbf{k},\omega)$ to be given and, thus, alternative methods of assessing the LFC are necessary. A similar scheme may be considered for non-equilibrium systems, although in this case one additionally requires an unknown correlation term.

The study of equilibrium LFCs for the electron gas has been the subject of intensive study by many authors. In particular, theoretical approaches of note include self-consistent schemes [Singwi et al., 1968; 1970], the use of recurrence relations [Hong and Kim, 1991], and sum rule fulfilment [Dabrowski, 1986; Farid et al., 1993]. Furthermore, numerical studies using quantum Monte Carlo codes [Utsumi and Ichimaru, 1982; Gori-Giorgi et al., 2000; Dharma-wardana and Perrot, 2000] have yielded accurate results for the static LFC from which the dynamic behaviour may be constructed by interpolation [Utsumi and Ichimaru, 1981; Ichimaru et al., 1985].

In this work, only static LFCs are considered due to the large uncertainties and differences between the various dynamic approaches. Specifically, parametrised forms [Farid et al., 1993; Geldart and Vosko, 1966] which are valid only for $T = 0$ and $T > 0$, respectively, are combined by a simple Padé interpolation [Gregori et al., 2007]

$$G_{ee}(\mathbf{k},0) \equiv G_{ee}(k) \approx \frac{G^{T=0}_{ee}(k) + \Theta_e G^{T>0}_{ee}(k)}{1+\Theta_e}. \tag{3.72}$$

where $\Theta_e = k_{\mathrm{B}}T_e/E_{\mathrm{F}e} = (3D_e/4\sqrt{\pi})^{-2/3}$ provides a measure of the degeneracy.

For a fully coupled two-component plasma, i.e. $\Pi_{ab} \neq 0$, it is not possible to completely separate the electrons and ions in the high-frequency response; the direct electron-ion coupling appears as a quadratic (second order) contribution. Thus, the shape of the plasmon

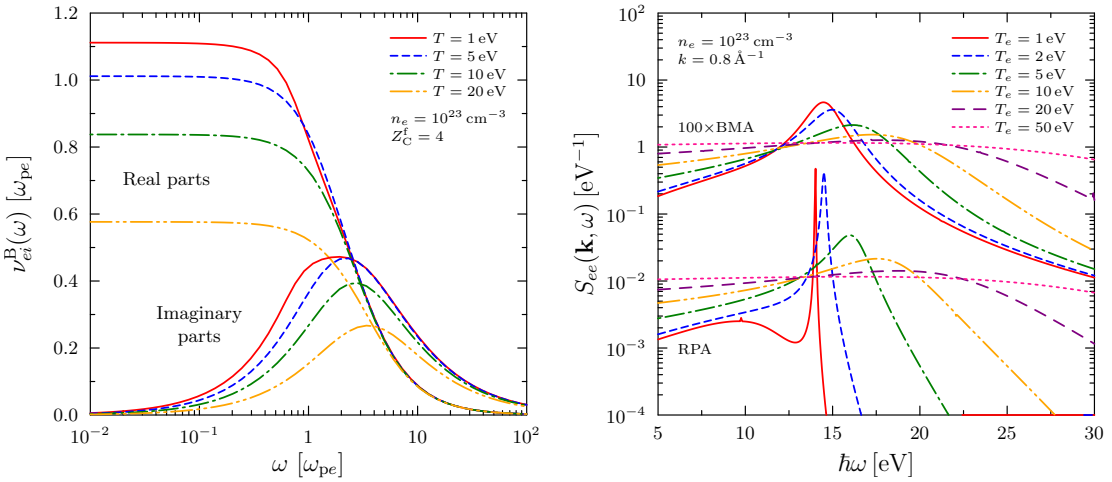

(a) Collision frequency in Born approximation.

(b) Plasmon resonance in RPA and BMA.

Figure 3.6: (a): Real and imaginary parts of the dynamic electron-ion collision frequency in first Born approximation for He-like carbon at $n_e = 10^{23}$ cm^{-3} for various temperatures in the WDM regime. (b): Comparison of the RPA and BMA plasmon resonance for the same conditions in Fig. 3.5(d).

resonance is expected to be modified due to direct interactions between electrons and ions, e.g. via screened binary Coulomb collisions.

The collision frequency can be calculated within a generalised linear response model based on equilibrium Green's functions [Röpke and Wierling, 1998; Röpke et al., 1999; Reinholz et al., 2000]. In the first Born approximation, the result is

$$\nu_{ei}(\omega) \overset{\text{1st Born}}{=} -4\pi i \frac{\omega_{\mathrm{pi}}^2}{\omega} \frac{m_i}{3m_e} \frac{1}{n_e} \int \frac{\mathrm{d}\mathbf{k}}{(2\pi)^3} \frac{S_{ii}(k)}{|\varepsilon_{ee}^0(k,0)|^2} \left[\varepsilon_{ee}^0(k,\omega) - \varepsilon_{ee}^0(k,0)\right] . \tag{3.73}$$

The static correlations between the ions are represented by the SSF. Note that $\nu_{ei}(\omega)$ has both real and imaginary parts, which are related to one another by a Kramers-Kronig relation. The well-known Ziman limit is recovered in the static limit $\omega \to 0$ if the screening is Debye-like [Ziman, 1967], whereupon the imaginary part vanishes.

Going beyond the first Born approximation, one may treat dynamic screening of the electron-ion interaction via the Lenard-Balescu formula and strong (large-angle) collisions using the T-matrix, which may be combined in the Gould-De Witt scheme [Gould and De Witt, 1967]. Only the first Born approximation is considered in this work.

Eq. (3.73) depends strongly on the effective charge and mass of the ions and generally increases with density and decreases with temperature (Fig. 3.6(a)). As discussed by Fortmann et al. [Fortmann et al., 2010], the collision rate decays rapidly under increasingly degenerate conditions as scattering channels are Pauli blocked, if the ion structure is neglected. Conversely, including the SSF partially compensates for the lack of available final states as the ion distribution becomes strongly peaked in Fourier space. Here, the HNC

approximation is used with a Debye potential. As shown by Fig. 3.6(b), collisions are expected to be important in determining the shape of the plasmons in the collective regime. The collision frequency (3.73) can be incorporated into the plasma response phenomenologically by deriving the polarisation function in the relaxation time approximation. Under the additional restriction of particle conservation to ensure fulfilment of the f-sum rule. The result is the famous expression of Mermin [Mermin, 1970; Das, 1975]

$$\Pi_{ee}^{\mathrm{R}}\left(\mathbf{k},\omega;\nu_{ei}(\omega)\right) \overset{\mathrm{BMA}}{=} \frac{\left[\omega+i\nu_{ei}(\omega)\right]\Pi_{ee}^{\mathrm{R0}}(\mathbf{k},0)\,\Pi_{ee}^{\mathrm{R0}}(\mathbf{k},\omega+i\nu_{ei}(\omega))}{\omega\,\Pi_{ee}^{\mathrm{R0}}(\mathbf{k},0)+i\nu_{ei}(\omega)\,\Pi_{ee}^{\mathrm{R0}}(\mathbf{k},\omega+i\nu_{ei}(\omega))}. \tag{3.74}$$

The label BMA stands for Born-Mermin approximation. Note that one recovers the RPA for $\nu_{ei}\to 0$ and that the static response is not affected by the collisions; consequently, the screening cloud $q_i(k)$ is identical in BMA and RPA. Further generalisation of the BMA for multicomponent plasmas [Morawetz et al., 1998] and to momentum and energy conserving forms [Morawetz and Fuhrmann, 2000] have also been previously considered.

The shape of the plasmon in BMA is shown in Fig. 3.6(b) for warm dense beryllium [Glenzer et al., 2007]. The enhanced damping of the peak due to collisions relative to RPA is clear in this regime. One can see that the peak is less sensitive to the temperature in BMA due to the additional temperature-dependence of the collision frequency. Thus, under conditions where the BMA is expected to hold the additional broadening of the plasmons can be used as a measure of collisional phenomena such as electrical and thermal conductivity in WDM [Döppner et al., 2010].

3.7 Inelastic bound-free feature

The last term in Eq. (3.26) corresponds to scattering due to Raman-like transitions, i.e. excitations from tightly bound core states to the continuum induced by the incident x-rays. In general, this contribution follows from evaluating all possible matrix elements corresponding to transitions between the initial and final many-particle states [Eisenberger and Platzmann, 1970; Schumacher et al., 1975]. Since there is little scope of collective scattering from a system of bound electrons near the ground state, one may treat the scattering as non-resonant and treat individual single-particle states independently

$$S_{ea}^{\mathrm{core}}(\mathbf{k},\omega)=\sum_{\mathrm{i}} f_{\mathrm{i}}\sum_{\mathrm{s}}(1-f_{\mathrm{s}})\left|\langle \mathrm{s}|e^{-i\mathbf{k}\cdot\mathbf{r}}|\mathrm{i}\rangle\right|^2\delta\left(\hbar\omega-(E_{\mathrm{s}}-E_{\mathrm{i}})\right). \tag{3.75}$$

Here the initial and scattered single-particle states are denoted $|\mathrm{i}\rangle$ and $|\mathrm{s}\rangle$, with eigen energies E_{i} and E_{s}, respectively. Note that the occupation of the initial states f_{i} and the Pauli blocking factor on occupied scattered states $(1-f_{\mathrm{s}})$ are present and, thus, Eq. (3.75) is suitably general to be applied under non-equilibrium conditions.

It therefore remains to suitably express the initial and final states and evaluate the matrix elements in order to calculate the bound-free scattering. For transitions to the

continuum the final state is strictly the asymptotic limit of the electron energy approaching $E > 0$ at $r \to \infty$, but may often be well-represented by a simple plane wave, i.e. $\langle \mathbf{r}|\mathrm{s}\rangle \sim e^{-i\mathbf{k}\cdot\mathbf{r}}$. The accuracy of this approximation depends on the energy of the photo-electron, and is therefore expected to be reasonable for high energy x-rays. On the other hand, the initial states are strongly sensitive to the potential, which includes the contributions of the central nucleus and other bound electrons via screening of the nuclear charge.

3.7.1 Hydrogenic form factor approximation

An obvious starting point for simplifying the calculation of the bound-free term is to assume hydrogenic wavefunctions with respect to an effective nuclear charge [Wentzel, 1929; Bloch, 1934], similarly to the calculation of the ionic form factor presented in Section 3.3. In this case, the projection of the initial states onto the coordinate space yields the familiar family of wavefunctions $\langle \mathbf{r}|n,l,m\rangle \equiv \Psi_{n,l,m}(\mathbf{r}) = R_{n,l}(r)Y_{l,m}(\theta,\phi)$ and the final states are represented by the continuum limit $\Psi_k(\mathbf{r})$ [Eisenberger and Platzmann, 1970]. Transitions from the K-shell to the continuum have an analytic result which compares well to synchrotron data [Mattern and Seidler, 2013].

The continuum hydrogenic wavefunctions are tabulated [Green et al., 1958], showing that for high energy electrons the solution approaches a plane wave, as expected. Assuming a plane wave for the final state, the matrix elements depend only on the Fourier transform of the radial part of the initial wavefunction [Bloch and Mendelsohn, 1974; Schumacher et al., 1975], leading to analytic results for all subshells. Due to its close connection with the ionic form factors, this approach is referred to as the form factor approximation (FFA).

Without further elaboration the result can be succinctly written in terms of the dimensionless Compton profile functions $J_{n,l}(k,\omega)$ which describe the density distribution of the bound electrons along the direction of the scattering wave vector $\mathbf{k}$

$$S_{ea}^{\mathrm{core}}(k,\omega) = \frac{1}{ck}\sum_{n,l} J_{n,l}(k,\omega), \tag{3.76}$$

$$\begin{aligned} J_{n,l}(k,\omega) \overset{\mathrm{FFA}}{=}\ & \left(1+q^2\right)^{1/2} \frac{2^{4l+3}\Gamma(n-l)\left[n\Gamma(l+1)\right]^2}{\pi\alpha_0(Z_a^{\mathrm{A}}-s_{n,l})\Gamma(n+l+1)} \\ & \times\left[\phi_{n,l}\left(1+(1/x_{n,l}^{-})^2\right)-\phi_{n,l}\left(1+(1/x_{n,l}^{+})^2\right)\right], \end{aligned} \tag{3.77}$$

where $x_{n,l}^{\pm} = n(q \pm \hbar k/m_e c)/\alpha_0 Z_{n,l}^{\mathrm{eff}}$, $q^2 = (\hbar\omega/m_e c^2 - E_{n,l}^{\mathrm{bind}}/m_e c^2 + 1)^2 - 1$ with $Z_{n,l}^{\mathrm{eff}}$ being the effective nuclear charge previously discussed for the ionic form factor and α_0 is the fine structure constant. The functions $\phi_{n,l}(x)$ are polynomials related to the integrals of Gegenbauer polynomials [Schumacher et al., 1975]. As discussed in the latter work, significant discrepancies are found for high-Z elements if the plane wave approximation is used for the final state, especially for the inner shell electrons. This is due to the violation fo energy conservation relsulting from the use of different Hamiltions for the initial and final states [Mattern and Seidler, 2013].

The binding energy of the state determines the location of the edge of the bound-free profiles in energy space. In dense plasmas, this is reduced due to screening of the ion charge, known as *continuum lowering* [Ciricosta et al., 2012; Hoarty et al., 2013a]. In this work, the famous model of Stewart and Pyatt is used

$$\Delta E = -\frac{3}{2}\frac{Z_i^{\mathrm{f}} e^2 \kappa_{\mathrm{D}}}{4\pi\varepsilon_0}\frac{\left[1+(\kappa_{\mathrm{D}} d_{ii}/2)^3\right]^{2/3}-1}{(\kappa_{\mathrm{D}} d_{ii}/2)^3}, \tag{3.78}$$

where $\kappa_{\mathrm{D}}^2 = \kappa_{\mathrm{D}e}^2 + \kappa_{\mathrm{D}i}^2$ is the square of the total screening length in the plasma and d_{ii} is the usual mean ion separation [Stewart and Pyatt Jr., 1966]. The excitation energies of the bound states now become $E_{n,l}^{\mathrm{bind}} + \Delta E$. The contributions of K- and L-shell states in FFA, including the shifted excitation edge due to continuum lowering, are shown in Fig. 3.7(a) for carbon for $k = 8.4$ Å^{-1} and the conditions of Ref. [Fletcher et al., 2014].

3.7.2 Impulse approximation

Although the FFA makes use of realistic wavefunctions for the initial states, detailed investigation of the bound-free scattering of compressed He-like carbon using non-collective XRTS by Fletcher et al. have shown that the FFA gives a poor description of the K-shell [Fletcher et al., 2014]. Alternative approaches which are better suited to such states are therefore required. Following the derivation given by Eisenberger and Platzman a exact representation of the DSF can be given using the Fourier transform of the δ-function

$$S_{ea}^{\mathrm{core}}(\mathbf{k},\omega) = \sum_{\mathrm{i}} f_{\mathrm{i}} \int_{-\infty}^{\infty} \mathrm{d}\tau\, e^{i\omega\tau}\, \langle \mathrm{i}| e^{i\hat{H}_e t} e^{-i\mathbf{k}\cdot\mathbf{r}} e^{-i\hat{H}_e t} e^{i\mathbf{k}\cdot\mathbf{r}} |\mathrm{i}\rangle. \tag{3.79}$$

In Eq. (3.79), the Pauling blocking term has been neglected on the basis that the photoelectron is ejected into a final state with negligible occupation.

The time evolution operators are expanded as a power series in the time over which the state changes; this can be thought of as the reciprocal of the interaction energy, i.e. $\tau \sim \omega^{-1}$. Thus, if $\hbar\omega \gg E_{n,l}^{\mathrm{bind}}$, one may truncate the series are the first term and the single-particle Hamiltonian retain only the zeroth-order contribution $\hat{H}_e \approx \hat{H}_e^0 + \hat{V}_{ei}$. Since the potential terms commute with the position operator, the latter cancel from the initial and final states leaving the DSF fully described in terms of free-particle wavefunctions; this simple approach is known as the impulse approximation (IA) [Chew and Wick, 1952; Eisenberger and Platzmann, 1970]. This can be physically interpreted as the interaction with the probe occurring sufficiently quickly for the potential in which the electron moves to be static. In the IA, the expressions of Schumacher et al. for the FFA are modified by neglecting the change in the initial momentum, leading to the simple expressions

$$J_{n,l}(k,\omega) \overset{\mathrm{IA}}{=} \frac{2^{4l+3}\Gamma(n-l)\left[n\Gamma(l+1)\right]^2}{\pi\alpha_0(Z_a^{\mathrm{A}} - s_{n,l})\Gamma(n+l+1)}\phi_{n,l}(1+1/x_{n,l}^2), \tag{3.80}$$

where in IA the dimensionless frequency shift is $x_{n,l} = nq/\alpha_0 Z_{n,l}^{\mathrm{eff}}$.

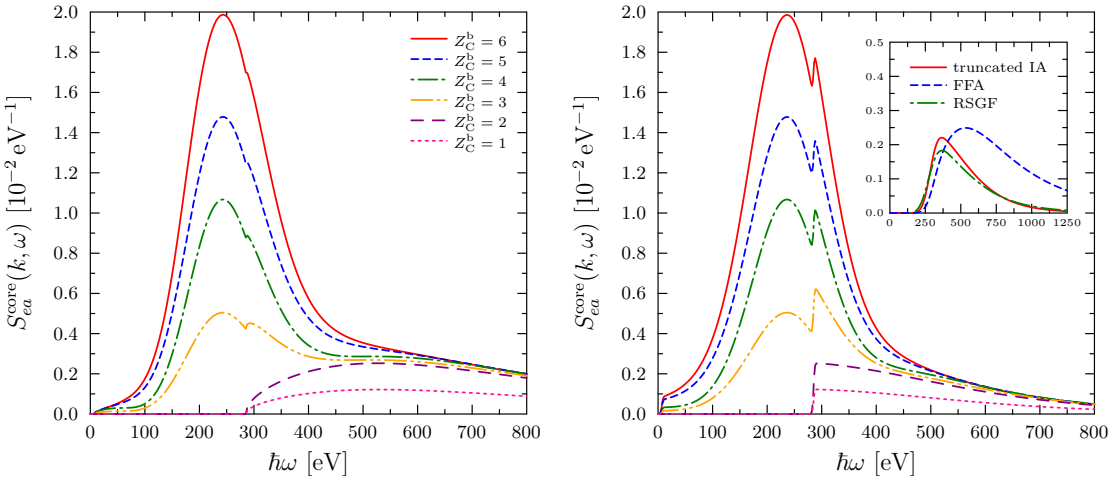

(a) Bound-free DSF for carbon in FFA

(b) Bound-free DSF for carbon in IA

Figure 3.7: (a): Dynamic structure contributions due to bound-free scattering for various different ionization states of solid-density carbon in the FFA for $k = 8.4$ Å^{-1}. (b): Similar calculations as in panel (a), but using the truncated IA model. The inset compares the K-shell contributions for He-like warm dense carbon for FFA and IA against the RSGF approach, supplied courtesy of B. Mattern. Here, all curves have been convolved with a Gaussian instrument function with a FWHM of 100 eV.

In treating the electrons as free-particles, the binding energy is neglected in the IA. Thus, the Compton profiles inevitably extend over a range of energy transfers which are inaccessible to the probe. As suggested by Mattern and Seidler, the profiles can be truncated artificially to emulate the natural cut-off at the binding energy. The results are shown to compare well to detailed calculations based on the real-space Greens function (RSGF) representation [Mattern et al., 2012] for large momentum transfers, as expected, but break down as k decreases.

Finally, it is worth mentioning that corrections to the IA based on the higher-order terms of the Hamiltonian result in corrections to the Compton profile. The first-order corrections were investigated by [Holm and Ribberfors, 1989] for K- and L-shell electrons and applied to modelling low-density carbon foam targets by [Gregori et al., 2004]. In fact, the impact of these corrections are minimal for large k and, thus, may typically be neglected since the IA itself breaks down at small k.

The truncated IA predictions for various ionization states of carbon are shown in Fig. 3.7(b). As expected, the largest differences to the FFA are seen in the structure of the K-shell contributions and demonstrate that the truncated IA gives better agreement with the RSGF approach. This is a very useful result since the latter is extremely numerically intensive and cannot currently include continuum lowering. For the L-shell states, the IA and FFA yield very similar results. The truncated IA is therefore used for modelling the bound-free scattering component of the XRTS spectrum throughout this thesis. This completes the last part of the model required to model XRTS in dense plasmas.

Chapter 4

X-ray Thomson scattering for systems with non-equilibrium electrons

In this chapter, the contribution of the free electrons to the total DSF is studied in the context of non-equilibrium distributions. This is of fundamental interest to the modelling and development of XRTS diagnostics for dense plasmas as both recent and ongoing experiments in this field may be conducive to creating non-equilibrium conditions. Firstly, a simple analytic model is used to represent quasi-thermal, high-energy perturbations to the tail of the low-energy equilibrium distribution. This is further generalised to incorporate populations of non-thermal particles concentrated around a characteristic excitation energy. The resulting excitation spectra are evaluated in comparison to the usual equilibrium theory in the context of collective XRTS. The plasmon structure shows the importance of high-energy electrons in determining the dispersion and damping of the resonances. The formation of beam acoustic modes is shown to emerge from non-thermal populations.

The second half of chapter applies the non-equilibrium framework to modelling recent data from strongly-driven cryogenic liquid hydrogen at the FLASH free electron laser. The results demonstrate the importance of the time-evolution of the non-equilibrium distribution to accurately modelling the scattered power spectrum. The formation of a non-equilibrium state is also shown to explain the lack of Rayleigh scattering in the data. Finally, a fully numerical approach is applied to Monte Carlo simulations of FEL-matter interactions in solid density targets, thereby demonstrating the versatility of the non-equilibrium model.

4.1 Sources of non-equilibrium electrons in dense matter

It is well known that non-equilibrium electron distributions are often produced in both laboratory and astrophysical plasmas. For example, simulations using particle-in-cell [Estabrook et al., 1975; Kemp et al., 2014] and Vlasov-Fokker-Planck [Bell et al., 2006; Sircombe and Arber, 2009] codes have consistently shown that the distribution function of laser-heated underdense targets develops a tail of high-energy non-thermal electrons with an approximately Maxwell-Boltzmann (MB) shape. This hot tail may often be characterised by an effective temperature T_h, which can be significantly higher than the temperature of the background plasma. Furthermore, solid targets irradiated with ultra-high intensity short-pulse lasers (with intensities of $I \gtrsim 10^{20}\,\mathrm{W\,cm^{-2}}$) gives rise to several distinct quasi-equilibrium tail populations characteised by hot temperatures ranging from $10\,\mathrm{keV} \lesssim T_\mathrm{h} \sim 1\,\mathrm{MeV}$ [Sherlock, 2009; Sircombe et al., 2013]. The presence of large numbers of hot electrons is known to modify transport and heating processes, and also influences the large-scale hydrodynamics. Consequently, such considerations constitute a potentially significant source uncertainty in the study of dense matter.

Non-equilibrium effects in the ions have also been considered in targets heated by strong shocks or charged-particle deposition [Tsallis, 1988; Garbett, 2013]. Furthermore, the ions may also be in a state of non-equilibrium with respect to the mean potential in the plasma, e.g. resulting from ultra-fast ionization by a high-energy x-ray pulse. On such short time scales, the shape of the pre-excitation equilibrium distribution may still be appropriate for describing the thermodynamics of the ions. The high collision rate amongst the ions ensures that the subsequent relaxation may often be adequately described using an equilibrium form with a time-dependent temperature.

4.1.1 Impact of non-equilibrium electrons on XRTS

The description of DSF given in Chapter 3 suggests that non-equilibrium electron distributions may strongly affect the interpretation of experimental XRTS data. In particular, the contributions of the free electrons to both the elastic (via the screening cloud) and inelastic scattering have been shown to depend directly on the distribution function.

An important example of the impact of non-equilibrium electrons on the interpretation of scattering experiments is the well-known super-Gaussian form [Langdon, 1980; Matte et al., 1988]. This model is of particular relevance to optical Thomson scattering (OTS) experiments using high-power probe lasers, since inverse Bremsstrahlung absorption of the probe strongly perturbs the electrons in the scattering volume. Specifically, depletion of high-energy states leads to an exponential reduction in the Landau damping of the high-frequency plasmon modes, resulting in significantly sharper resonances [Zheng et al., 1997; Liu et al., 2002]. Plasmon scattering experiments performed in diffuse, high-temperature gold plasmas [Glenzer et al., 1999a;b] could only be self-consistently described using a modified Langdon-Matte distribution [Fourkal et al., 2001].

For dense plasmas probed with XRTS, the coupling of the probing x-rays to the plasma by means of electron-ion collisions is negligible, such that distributions similar to the Langdon-Matte type are not expected to be an important consideration. On the other hand, heating solid density targets by means of laser-driven x-rays [Glenzer et al., 2003; 2007; Gregori et al., 2008] and shocks [García Saiz et al., 2008; Kritcher et al., 2009; Kraus et al., 2013], and high-energy charged particle beams [Pelka et al., 2010] produce significant numbers of hot electrons. In the cases of shock-compression and heating by x-ray absorption, the energy of the drive laser is absorbed in the coronal plasma via resonance absorption [Forslund et al., 1977], whereas direct illumination of solid targets with short-pulse lasers couples energy into hot electrons via vacuum heating [Brunel, 1987] and ponderomotive acceleration [Kruer and Estabrook, 1985; Wilks et al., 1992].

4.1.2 Isotropic approximation

In the general case of arbitrary non-equilibrium distribution functions, one must consider not only distortions from the usual equilibrium shape, but also anisotropy with respect to the components of the momentum. Anisotropic distributions may be encountered for scattering from quasi-monoenergetic charged-particle beams or strongly magnetised plasmas, in which steady states can exist with distinct temperatures parallel and perpendicular to the B-field [Watt and Pietrzyk, 1979; Yatsuka et al., 2011]. Without further simplification the DSF must be calculated entirely numerically [see, e.g., Pastor et al., 2012].

In dense matter, frequent elastic collisions, which randomise the momenta of the particles but do not affect their energies, ensure rapid isotropisation of the distribution function. Whilst this inexorably leads to thermalisation over sufficiently long time scales, an evolving isotropic non-equilibrium distribution may persist throughout scattering measurements. Indeed, simulations based on spherical harmonics expansion of the distribution function [Bochkarev et al., 2004] have demonstrated the importance of long-lived (quasi-steady-state) isotropic non-equilibrium distributions in the regime of interest to this work.

4.2 Two-temperature electron distributions

Appealing to the simple idea of a two-temperature distribution function enables many of the important dynamic processes studied by XRTS to be investigated without the need for expensive numerical calculations. The form of a distribution function with a hot tail is

$$f_e(p) = x_\mathrm{c}\,\frac{n_e\Lambda_\mathrm{c}^3}{2\mathcal{F}_{1/2}(\eta_\mathrm{c})}\left[1+\exp\left(\frac{p^2}{2p_\mathrm{c}^2}-\eta_\mathrm{c}\right)\right]^{-1} + x_\mathrm{h}\,\frac{n_e\Lambda_\mathrm{h}^3}{2}\,\exp\left(-\frac{p^2}{2p_\mathrm{h}^2}\right). \tag{4.1}$$

In Eq. (4.1), $x_a = n_a/n_e$ are the fractional densities of the components $a = \mathrm{c},\mathrm{h}$ (see Appendix A). Naturally, all the parameters are time-dependent in order to capture the evolution of the system. Examples of the distribution (4.1) for typical WDM conditions are shown in Fig. 4.1.

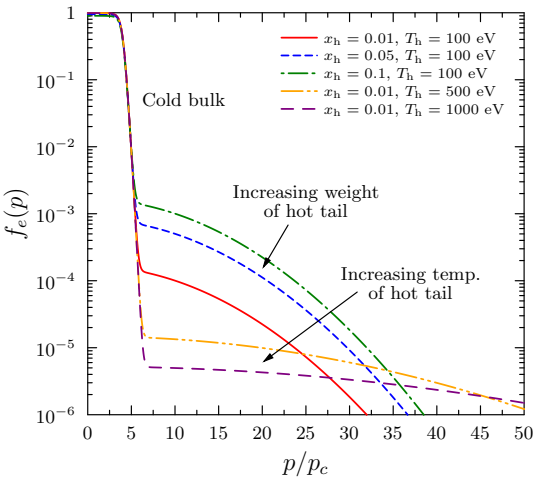

Figure 4.1: The two-temperature electron distribution function for various values of the hot fraction x_h and temperature T_h for typical WDM conditions of $n_e = 10^{23}$ cm^{-3} and $T_\mathrm{c} = 1$ eV. The momentum scale is normalised to the thermal speed of the cold component, $p_\mathrm{c} = (m_e/\beta_\mathrm{c})^{1/2}$.

Using non-collective XRTS, the high-frequency (free electron) part of the power spectrum of the scattered radiation yields a direct measure of the shape of the electron distribution function along the direction of the probed wave vector $\mathbf{k}$. Thus, in principle, fitting the modified high-energy wings of the free electron feature due to hot electrons could be used to determine T_h and x_h. On the other hand, for typical hot fractions $x_\mathrm{h} = 0.01$–0.1, the deviation from the shape of the equilibrium signal may be difficult to distinguish. Accurately measuring the shape of the wings of the Compton feature is also experimentally challenging. For example, the low-amplitude wings are, naturally, particularly susceptible to poor signal-to-noise levels, and in WDM one must also consider that the blue-shifted wing of the Compton feature typically overlaps with the elastic feature, and that scattering from bound-free transitions may overlap the red-shifted wing. Such factors complicate the interpretation of the features of interest and obscure the signature of the hot component.

4.2.1 Two-temperature plasmon dispersion

Significant numbers of hot electrons are expected to distort the equilibrium shape of the dielectric function, leading to observable shifts of the plasmons in the collective scattering regime. Substituting Eq. (4.1) into the plasmon dispersion relation (3.69), one finds

$$\omega_\mathrm{pl}(k) \approx \omega_{pe} + \frac{3k^2}{2\omega_{pe}} \left[x_\mathrm{c} v_\mathrm{c}^2 \frac{\mathcal{F}_{3/2}(\eta_\mathrm{c})}{\mathcal{F}_{1/2}(\eta_\mathrm{c})} + x_\mathrm{h} v_\mathrm{h}^2 \right] . \tag{4.2}$$

The leading order term in Eq. (4.2) is the usual plasma frequency determined by the total electron density. The hot tail contribution has the effect of increasing the mean kinetic energy so that significant deviations to the plasmon dispersion occur for $x_\mathrm{c}/x_\mathrm{h} \lesssim T_\mathrm{h}/T_\mathrm{c}$. The high energy of x-rays required to probe dense matter makes accessing the strongly collective limit challenging. Moreover, the $k \to 0$ limit is less well-fulfilled for the hot electrons, irrespective of the probe energy. Subsequently, the shifts predicted by Eq. (4.2) quickly become inaccurate as one probes larger wave numbers and, thus, are of limited use for predicting the modification of the plasmon position.

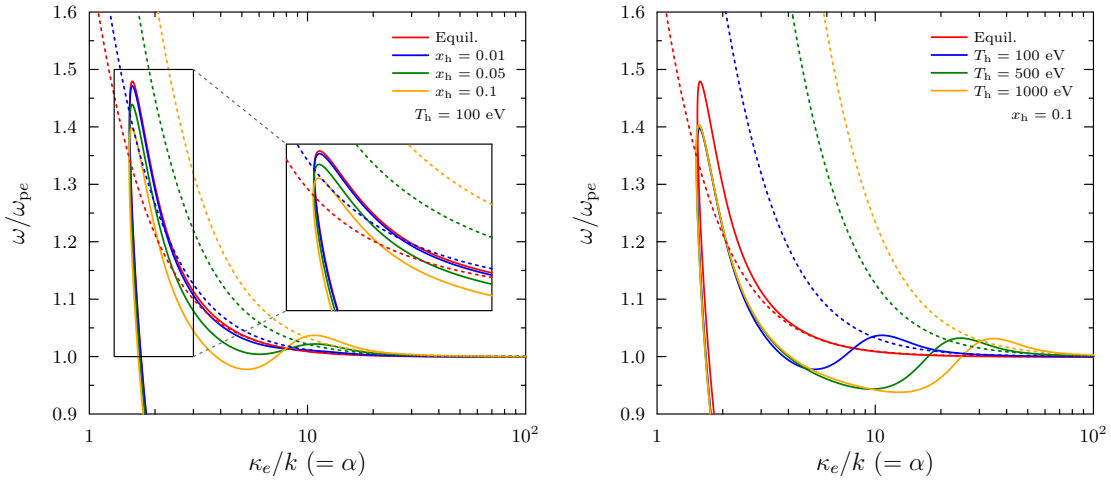

(a) Varying hot fraction x_h.

(b) Varying hot temperature T_h.

Figure 4.2: Dispersion curves for a two-temperature (TT) distribution at for the same bulk conditions as Fig. 4.1. The fraction (a) and temperature (b) of the hot component are varied between $x_\mathrm{h} = 0.01 - 0.2$ and $T_\mathrm{h} = 100 - 1000$ eV, respectively. In each case, the long wavelength expansion of the dispersion relation is given by the colour-coordinated dotted curves. The inset in panel (a) shows the weakly collective end of the plasmon branch in greater detail for clarity.

As per Eq. (3.67), a more robust prediction of the dispersion relation is given by solving for $\mathrm{Re}\,\varepsilon_{ee}(\mathbf{k},\omega) = 0$. Given the simple form of Eq. (4.1), the dielectric function of the electron subsystem is given by a weighted sum of the cold and hot components

$$\varepsilon_{ee}(\mathbf{k},\omega) = 1 - V_{ee}(k)\left[x_\mathrm{c}\,\Pi^\mathrm{R}_{ee}(\mathbf{k},\omega;n_e,T_\mathrm{c}) + x_\mathrm{h}\,\Pi^\mathrm{R}_{ee}(\mathbf{k},\omega;n_e,T_\mathrm{h})\right]. \tag{4.3}$$

The cold and hot contributions are calculated from the usual equilibrium form of the polarisation function in RPA at the appropriate temperature and using the total electron density n_e. The cold component additionally depends on an effective chemical potential η_c, although this must simply be thought of as an additional free parameter which controls the width of the bulk at low temperatures.

Fig. 4.2 shows the dispersion curves given by $\mathrm{Re}\,\varepsilon_{ee}(\mathbf{k},\omega) = 0$ for the example two-temperature distributions in Fig. 4.1. The thin curves with quasi-quadratic k-scaling are the long-wavelength dispersion relations predicted by Eq. (4.2). As expected, for strongly collective states the latter agree well with the full dispersion function but break down for larger wave numbers. The addition of a hot component upshifts the dispersion for small wave numbers as the mean kinetic energy is increased. However, at a critical wave number the hot component ceases to yield a root, effectively becoming non-collective, such that the dispersion curve smoothly transitions to a purely cold solution scaled by the relative fraction x_c. The plasmon is then sharply downshifted from the long-wavelength approximation.

The transition wave number strongly depends on T_h, moving to smaller k for hotter tail components. Since plasmon frequency is further upshifted with both the fraction and temperature of the hot electrons, the deviation from the true plasmon position gets larger. This reflects the fact that distribution functions with hotter, more strongly weighted hot tails contain many electrons in states with momenta above the phase speed of the plasmon.

4.2.2 Ratio of plasmon amplitudes

Substituting Eq. (4.1) into the general form of the non-interacting DSF Eq. (3.14) yields a solution of the form

$$S_e^0(\mathbf{k},\omega) = x_\mathrm{c} S_\mathrm{c}^0(\mathbf{k},\omega) + x_\mathrm{h} S_\mathrm{h}^0(\mathbf{k},\omega) + x_\mathrm{c} x_\mathrm{h} S_\times^0(\mathbf{k},\omega). \tag{4.4}$$

The first two terms are the *pure* cold and hot contributions, which can respectively be shown to give

$$\begin{aligned} S_\mathrm{c}^0(\mathbf{k},\omega) = \frac{1}{\sqrt{2\pi} v_\mathrm{c} k} \frac{2}{n_e \Lambda_\mathrm{c}^3} \frac{1}{1-e^{-\beta_\mathrm{c}\hbar\omega}} \Big\{ \Big[1-(1-x_\mathrm{c})\, e^{-\beta_\mathrm{c}\hbar\omega}\Big] \ln\left(1+e^{\eta_\mathrm{c}-(w_\mathrm{c}-\varkappa_\mathrm{c})^2}\right) \\ -x_\mathrm{c} \ln\left(1+e^{\eta_\mathrm{c}-(w_\mathrm{c}+\varkappa_\mathrm{c})^2}\right)\Big\}, \end{aligned} \tag{4.5}$$

$$S_\mathrm{h}^0(\mathbf{k},\omega) = \frac{1}{\sqrt{2\pi} v_\mathrm{h} k} e^{-(w_\mathrm{c}-\varkappa_\mathrm{c})^2/\mathcal{T}_\mathrm{hc}} \left[1 - x_\mathrm{h} \frac{n_e \Lambda_\mathrm{h}^3}{4} e^{-(w_\mathrm{c}+\varkappa_\mathrm{c})^2/\mathcal{T}_\mathrm{hc}}\right]. \tag{4.6}$$

Here, $w_\mathrm{c} = \omega/\sqrt{2}kv_\mathrm{c}$ and $\varkappa_\mathrm{c} = \hbar k/\sqrt{8}p_\mathrm{c}$, as usual, and the ratio of the hot and cold temperatures is $\mathcal{T}_\mathrm{hc} = T_\mathrm{h}/T_\mathrm{c}$. Since the hot electrons are invariably highly non-degenerate, the second term in square brackets in Eq. (4.6) can be neglected; the Gaussian-shaped correction to the structure of the high-energy wings of the free electron feature is then readily identifiable. Note that the expected result for an equilibrium system is obtained for $x_\mathrm{h} = 0$.

The third (cross) term results from the Pauli blocking factor and, thus, is only important for hard x-rays for which $\varkappa_{c,h} \sim 1$. The analytic result for this term is

$$\begin{aligned} S_\times^0(\mathbf{k},\omega) = \frac{1}{\sqrt{2\pi} v_\mathrm{h} k} \Bigg[\frac{B\, e^{-w_1}}{A}\, {}_2F_1\left(\begin{matrix}1, A\\ 1+A\end{matrix}; -e^{-w_1}\right) \frac{B\, e^{-w_2}}{A}\, {}_2F_1\left(\begin{matrix}1, A\\ 1+A\end{matrix}; -e^{-w_2}\right) \\ -e^{-B\,w_3}\, {}_2F_1\left(\begin{matrix}1, B\\ 1+B\end{matrix}; -e^{w_3}\right) - e^{-B\,w_4}\, {}_2F_1\left(\begin{matrix}1, B\\ 1+B\end{matrix}; -e^{w_4}\right) \\ + {}_2F_1\left(\begin{matrix}1, B\\ 1+B\end{matrix}; -e^{w_1}\right) + {}_2F_1\left(\begin{matrix}1, B\\ 1+B\end{matrix}; -e^{w_2}\right)\Bigg], \end{aligned} \tag{4.7}$$

in terms of the Gauss hypergeometric function ${}_2F_1$ [Abramowitz and Stegun, 1970]. The following dimensionless parameters have also been defined: $A = 1 - B$, $B = -1/\mathcal{T}_\mathrm{hc}$, $w_1 = -(\eta_\mathrm{c} - 4\varkappa_c w_c)$, $w_2 = -(\eta_\mathrm{c} + 4\varkappa_c w_c)$, $w_3 = -(w_\mathrm{c} + \varkappa_\mathrm{c})^2$ and $w_4 = -(w_\mathrm{c} - \varkappa_\mathrm{c})^2$. Given the complexity of Eq. (4.7), it is actually more expedient to evaluate it numerically.

The effect of the hot electrons on DSF is demonstrated in Fig. 4.3 for collective scat-

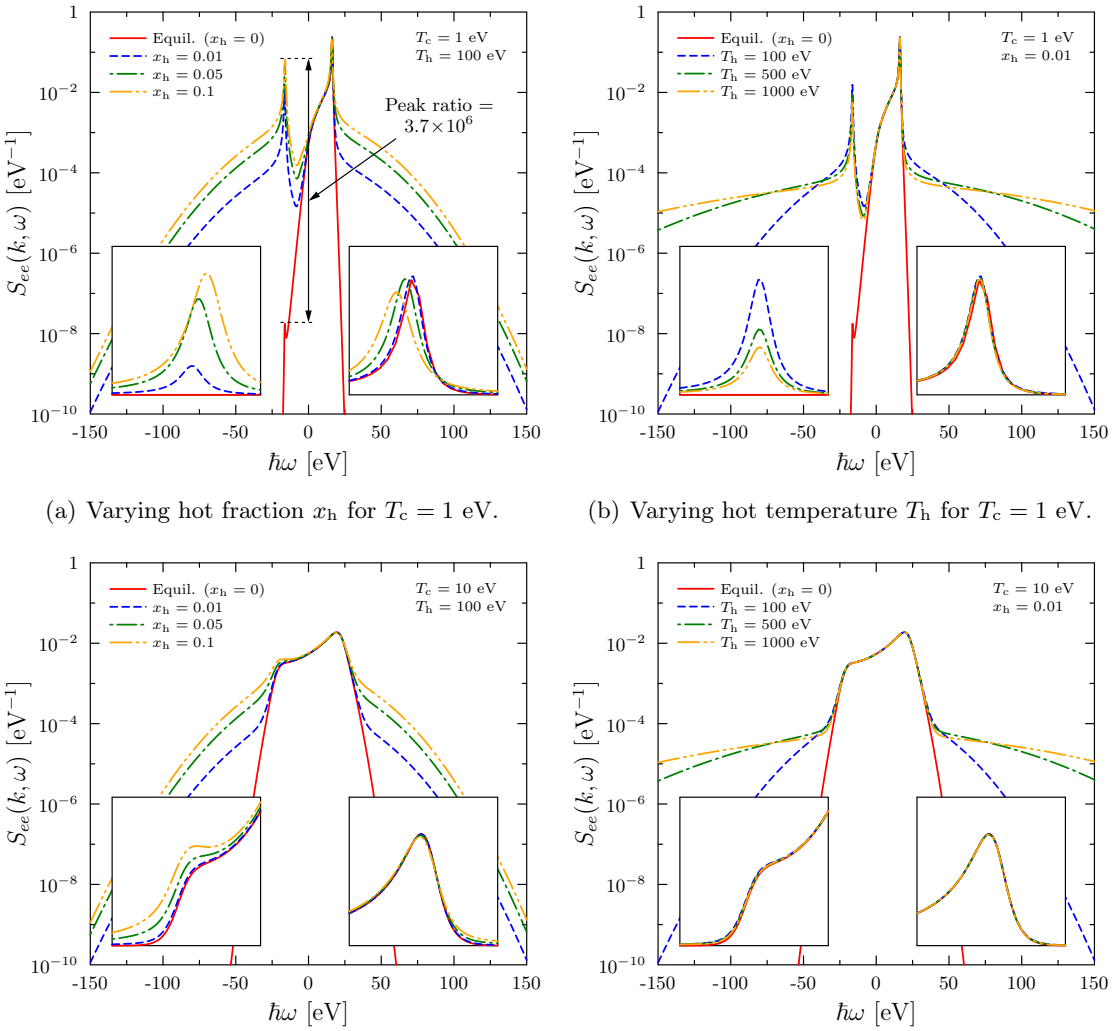

(a) Varying hot fraction x_h for $T_c = 1$ eV.

(b) Varying hot temperature T_h for $T_c = 1$ eV.

(c) Varying hot fraction x_h for $T_c = 10$ eV.

(d) Varying hot temperature T_h for $T_c = 10$ eV.

Figure 4.3: Logarithmic plots of the DSF for the distirbution (4.1) for the same conditions as Fig. 4.2 (a) and (b). The cold bulk temperature is increased to $T_c = 10$ eV with all other parameters held constant in (c) and (d). In each panel the insets show zoomed views of the down- (left) and upshifted (right) plasmon peak structures with linear y-axes.

tering. Here, the wave number of the fluctuations is $k = 0.28$ Å^{-1}, yielding $\alpha = 1.67$–1.78. The shape of the high-energy wings resulting from the hot tail is determined by T_h, as expected. Increasing T_h leads to larger wings with decreasing amplitude at lower energy shifts. Moreover, even for low weighting fractions, $x_h \leq 0.01$, the downshifted peak, which is effectively absent for the equilibrium calculation at $T_c = 1$ eV due to detailed balance, is enhanced by a factor of $> 10^6$. Conversely, the damping on the upshifted peak is only weakly affected. Increasing x_h further amplifies the downshifted peak as well as the amplitude of the high energy wings and the shift of the plasmon position. Raising the temperature of the colder bulk component reduces these effects, although significant modification of the downshifted plasmon damping can be observed for larger hot populations.

The modification of the downshifted plasmon amplitude for low temperatures can be understood by considering the physical interpretation of detailed balance in the context of a non-equilibrium plasma. This is a manifestation of the fact that scattering processes resulting in electrons/plasmons loosing energy (photons gaining energy) become extremely improbable as the distribution function approaches full occupation, e.g. for degenerate matter. Conversely, processes involving electrons gaining energy (photons loosing energy) are far more probable as free states are more plentiful. Under non-degenerate conditions the occupation of low-energy states is relatively low, such that the scattering rates are almost equal. Excitations corresponding to equal and opposite energy and momentum shifts are then similarly damped.

Shifting weight to the hot tail uniformly reduces the occupation of low energy states by a factor of $x_\mathrm{c} = 1 - x_\mathrm{h}$ and, thus, makes available states for transitions which would otherwise be Pauli blocked. The shape of the hot component is essentially irrelevant here since the hot contribution to the distribution at low-momentum states is insignificant. This explains why increasing T_h does not significantly affect the ratio of the plasmon peaks for a fixed value of x_h. Based on the present result, mitigation or accurate characterisation of hot electron production in WDM diagnosed by XRTS is essential if the detailed balance principle is used to infer the temperature [Döppner et al., 2009].

4.2.3 Evidence of hot electrons in warm dense beryllium

In order to demonstrate the potential difficulties in data analysis resulting from hot electrons, a recent experiment is considered [Glenzer et al., 2007]. Here, solid Be was uniformly heated to around 12 eV by absorption of thermal x-rays produced by a laser-heated Ag tamper. Probe x-rays at 2.96 keV observed through a mean scattering angle $\theta = 40^\circ$ were used to interrogate the collective response of the target. The pump and probe were delayed by 500 ps, ostensibly allowing sufficient time for the sample to be probed under equilibrium conditions.

Despite this experiment being carefully designed to produce a homogeneous equilibrium sample, hot electrons produced by resonance absorption of the heating beams may have sufficiently long ranges to propagate into the scattering volume during probing. Conservatively estimating the intensity of the heater beams as $I \sim 10^{16}\,\mathrm{W\,cm^{-2}}$ and appealing to the well-known scaling for the energies of electrons produced via classical resonance absorption [Forslund et al., 1977], the distribution function in the sample may have a hot tail characterised by a temperature between 0.1–1 keV.

Fig. 4.4 compares the experimental data to theoretical power spectra calculated using Eq. (4.1). The temperature and fractional density of the hot tail are varied within the aforementioned reasonable limits. As expected, the shape of the red-shifted plasmon is only marginally affected by the hot electrons when $x_\mathrm{c}/x_\mathrm{h}$ is varied, with larger hot populations leading to a small enhancement of the wing near the foot of the plasmon near 2962 eV. Since the cold bulk component is rather degenerate, adding a hot tail significantly alters

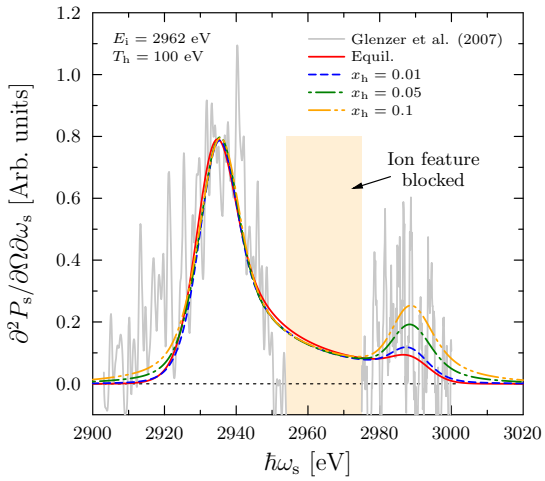

Figure 4.4: Scattered power spectrum for beryllium probed at $\theta = 40°$ with 2.96 keV x-rays at $T_c = 12$ eV and $n_e = 2.7 \times 10^{23}$ cm^{-3}. The fractional density of the hot tail is varied between $x_h = 0.01$–0.1. The spectrum is averaged over a Gaussian distribution of scattering angles (FWHM of 15°) to represent the divergence of the x-ray source, and is convolved with a Gaussian x-ray source function (FWHM of 7.7 eV).

the ratio of the plasmon peaks; the blue-shifted plasmon amplified by a factor of ~ 2 for only $x_h = 0.01$, and increasing the hot fraction to $x_h = 0.1$ roughly doubles its amplitude.

From the scatter in the measured data $x_h = 0.05$ seems to give the best overall fit, although the noise on the data is sufficiently large to make any fit questionable. Varying the hot temperature does not significantly change the shape of the spectrum. The presence of a small population of hot electrons driven by resonance absorption of the heating beams may therefore help to understand the anomalous scatter in this data at the blue-shifted peak. More importantly, the results discussed here suggest that hot electrons introduce significant uncertainty to the determination of T_e via detailed balance.

4.3 Bump-on-hot-tail distributions

A more recent development in the diagnostics of dense matter has been the use of free-electron lasers (FELs) as probes. With FELs, ultra-short (c.a. fs) pulses and peak intensities comparable to modern optical systems are possible, reaching $10^{13} - 10^{17}$ Wcm^{-2}. Combined with higher shot repetition rates than conventional laser facilities and highly collimated beams with small focused spot sizes, FELs are ideally suited to x-ray scattering experiments [Höll et al., 2007; Gauthier et al., 2014; Fletcher et al., 2015]. However, operating at such high photon fluences and short time scales inevitably means that the sample under study is strongly driven and probed during a highly dynamic phase of relaxation.

In contrast with optical probes, FEL radiation does not couple to the free electrons via collective and collisional absorption or parametric instabilities. Instead, high energy x-rays are primarily absorbed by electrons in bound states, which are subsequently ejected through processes such as photoionization and the Auger effect [Medvedev and Rethfeld, 2010; Medvedev et al., 2011]. The liberated electrons occupy a narrow spread of energies around the difference of the probe energy and the appropriate transition energy, e.g. $\hbar\omega - E_{\text{bind}}$.

Naturally, ultra-fast kinetic processes such as collisional ionization, inelastic scattering and radiative recombination rapidly fill lower-energy states. Non-thermal electrons quickly

thermalise into a quasi-thermal hot population and then diffuse energy more gradually into the low-energy bulk of the distribution. Photo-pumping of accessible bound states will continue for as long as the FEL pulse remains active. In the absence of an external energy source, equilibration of the electronic subsystem is achieved on c.a. 100 fs.

Motivated by the utility of Eq. (4.1), a simple and practical extension may be made which adequately captures the relevant physics. By adding a Gaussian 'bump' to describe the non-thermal electrons produced by, e.g. photoionization and Auger decay, Eq. (4.1) is further generalised to (see once more Appendix A)

$$f_e(p) = x_\mathrm{c}\,\frac{n_e\Lambda_\mathrm{c}^3}{2\mathcal{F}_{1/2}(\eta_\mathrm{c})}\left[1+\exp\left(\frac{p^2}{2p_\mathrm{c}^2}-\eta_\mathrm{c}\right)\right]^{-1} + x_\mathrm{h}\,\frac{n_e\Lambda_\mathrm{h}^3}{2}\,\exp\left(-\frac{p^2}{2p_\mathrm{h}^2}\right) + x_\mathrm{b}\,\frac{n_e\Lambda_\mathrm{b}^3}{2\Psi(p_0/\sqrt{2}p_\mathrm{b})}\,\exp\left[-\frac{(p-p_0)^2}{2p_\mathrm{b}^2}\right], \tag{4.8}$$

where $\Psi(x) = xe^{-x^2} + \frac{1}{2}\big(2x^2+1\big)\big(1+\mathrm{erf}(x)\big)$, and $\mathrm{erf}(x)$ is the error function.

In Eq. (4.8), the high-energy bump features are centred on the momentum corresponding to the excitation energy $p_0 = (2m_eE_0)^{1/2}$, with some characteristic width p_b. As with Eq. (4.1), one may consider as many distinct hot tail and bump components as is required in general, although one of each is typically sufficient. Due to the form of (4.8), this model is referred to as the *bump-on-hot-tail* (BOHT) distribution [Chapman and Gericke, 2011].

4.3.1 Development of beam acoustic modes

Based on the results of the previous section, one expects that the dielectric properties of systems described by Eq. (4.8) cannot be reliably investigated using the long-wavelength limit of the dispersion function. Once again, the linear form of the BOHT model admits a straightforward representation of the dielectric function, with the decaying components represented by weighted Fermi-Dirac or Maxwell-Boltzmann-like functions at distinct temperatures as in Eq. (4.3) and a more complicated component describing the bump

$$\varepsilon_{ee}(\mathbf{k},\omega) = 1 - V_{ee}(k)\big[x_\mathrm{c}\,\Pi_\mathrm{c}^\mathrm{R}(\mathbf{k},\omega) + x_\mathrm{h}\,\Pi_\mathrm{h}^\mathrm{R}(\mathbf{k},\omega) + x_\mathrm{b}\,\Pi_\mathrm{b}^\mathrm{R}(\mathbf{k},\omega)\big]\,. \tag{4.9}$$

For the imaginary part of the bump component, one can take the third term of Eq. (4.8) and derive from Eq. (2.101)

$$\mathrm{Im}\,\Pi_\mathrm{b}^\mathrm{R}(\mathbf{k},\omega) = \frac{\sqrt{\pi}n_em_e}{4\varkappa_\mathrm{b}\,p_\mathrm{b}^2\,\Psi(y)}\Big[e^{-(|w_\mathrm{b}+\varkappa_\mathrm{b}|-y)^2} - e^{-(|w_\mathrm{b}-\varkappa_\mathrm{b}|-y)^2} - \sqrt{\pi}y\left(\mathrm{erf}\left(|w_\mathrm{b}+\varkappa_\mathrm{b}|-y\right) - \mathrm{erf}\left(|w_\mathrm{b}-\varkappa_\mathrm{b}|-y\right)\right)\Big], \tag{4.10}$$

where $w_\mathrm{b} = \omega/\sqrt{2}kv_\mathrm{b}$, $\varkappa_\mathrm{b} = \hbar k/\sqrt{8}p_\mathrm{b}$ and, $y = p_0/\sqrt{2}p_\mathrm{b}$. For the limit $k \to 0$, one has

$$\mathrm{Im}\,\Pi_\mathrm{b}^\mathrm{R}(\mathbf{k},\omega) \overset{k\to 0}{=} -\frac{\sqrt{\pi}n_em_e}{p_\mathrm{b}^2\,\Psi(y)}w_\mathrm{b}\,e^{-(w_\mathrm{b}-y)^2}, \tag{4.11}$$

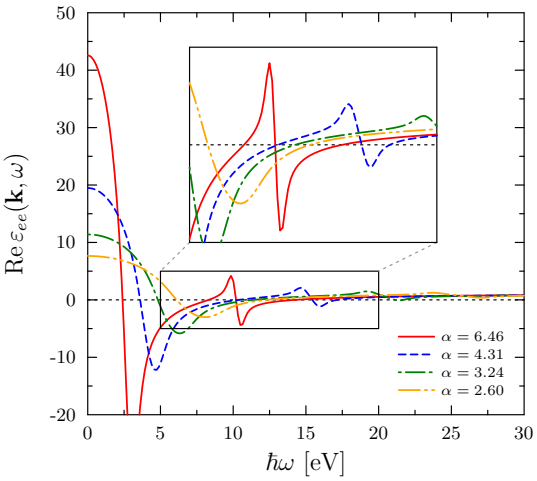

Figure 4.5: Real part of the retarded dielectric function in the WDM regime for various wave numbers (degrees of collectivity). Here, a bump component at $E_0 = 100\,\mathrm{eV}$ with weight $x_\mathrm{b} = 0.1$ and width $E_\mathrm{b} = 10\,\mathrm{eV}$ is considered. The inset panel shows a close-up view of the feature resulting from the addition of the bump.

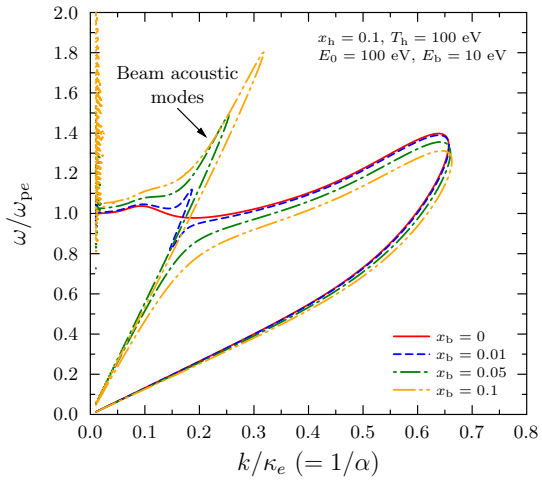

(a) Varying bump fraction x_b.

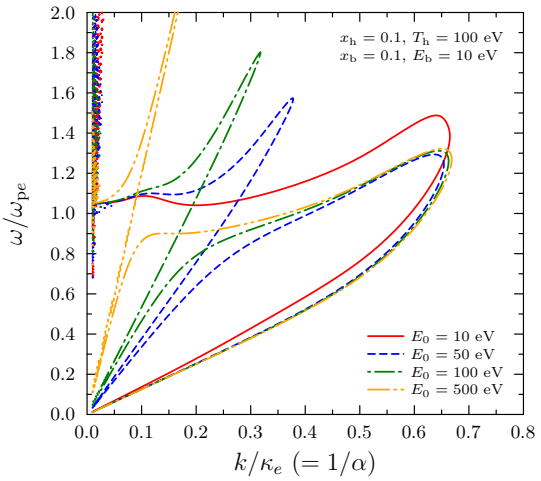

(b) Varying bump energy E_0.

Figure 4.6: Dispersion function from the root of the real part of the dielectric function for the BOHT distribution with varying x_b (a) and E_0 (b). The hot tail component is held constant at x_h and $T_\mathrm{h} = 100$ eV.

$$\begin{aligned}\operatorname{Re}\Pi_\mathrm{b}^\mathrm{R}(\mathbf{k},\omega) &\overset{k\to 0}{=} -\frac{\sqrt{\pi} n_e m_e}{p_\mathrm{b}^2\,\Psi(y)}\mathcal{P}\int_{-\infty}^{\infty}\frac{\mathrm{d}w_\mathrm{b}'}{\pi}\frac{w_\mathrm{b}'\,e^{-\left(w_\mathrm{b}'-y\right)^2}}{w_\mathrm{b}'-w_\mathrm{b}} \\ &= -\frac{n_e m_e}{p_\mathrm{b}^2\,\Psi(y)}\left[1-2w_\mathrm{b}\mathcal{D}(w_\mathrm{b}-y)\right]. \end{aligned} \tag{4.12}$$

The functional forms obtained in Eqs. (4.11) and (4.12) give some useful insight into the features expected to arise in the dielectric function due to the bump. In particular, one notices that the Gaussian term in Eq. (4.11) is shifted by y, which determines the bump location in $f_e(p)$. Adding this contribution to the cold and hot components therefore also results in a distinct asymmetrical bump at $\hbar\omega = \hbar k p_0/m_e$. The corresponding feature in the real part can result in the high-frequency tail yielding multiple roots as x_b increases, or if the distribution is probed in the strongly collective regime (see Fig. 4.5).

Fig. 4.6 shows contours of Re $\varepsilon_{ee}(k,\omega) = 0$ under the same WDM conditions considered previously, with a hot tail characterised by $x_\mathrm{h} = 0.1$ and $T_\mathrm{h} = 100$ eV. Additionally, a bump component is now included in accordance with Eq. (4.8). Considering a small fraction of electrons in the bump, $x_\mathrm{b} = 0.01$, shows that the dispersion is largely unchanged from the the two-temperature case, except for the development of a characteristic discontinuous feature near $k/\kappa_e = 0.15$. This new feature is greatly enhanced as more electrons are moved from the bulk component into the bump.

For a constant k, three roots may now exist instead of the usual single solution at the plasmon frequency. At small k, the plasmon is upshifted and a downshifted pair of resonances develops at low frequencies. The structure changes as k increases, eventually swapping over beyond a critical wave number, and is greatly amplified as x_b is increased. The location of the discontinuity is determined by the bump energy E_0 and shifts to larger wave numbers as $E_0 \to 0$, eventually merging into the solution of the cold component.

The feature which develops from the addition of the bump population has been extensively studied theoretically from the perspective of electron beam-plasma interactions [O'Neill and Malmberg, 1968]. Due to the quasi-linear (acoustic-like) dispersion of this feature, it is described as a *beam acoustic mode* (BAM). Moreover, BAMs have been observed in classical electrodynamics simulations [Vu et al., 2005] and also experimentally [Kline et al., 2005] in which the non-thermal electrons were driven by stimulated Raman scattering. Neither the PIC simulations nor the experimental dispersion traces show strong evidence of the low-frequency slope of the BAM since the damping is stronger, similar to the acoustic branch of the usual electron gas dispersion. One may reasonably expect that observation of collective structures such as BAMs using XRTS should be possible and, moreover, could provide clear evidence of non-equilibrium processes.

4.4 Modelling VUV self-scattering from cryogenic hydrogen

Recently, measurements of FEL scattering from cryogenic hydrogen under WDM conditions have been performed at the FLASH facility in Hamburg [Fäustlin et al., 2010]. In this experiment, liquid droplet targets were simultaneously heated and probed by the same soft x-rays with energy 91.7 eV, in an ultra-short pulse lasting 40 fs at FWHM. The collective scattering regime was accessed by using a scattering angle of $\theta = 90°$, resulting in a very small wave number shift of $k = 0.066$ Å^{-1}.

Due to the small number of scattered photons per FEL pulse, the measured scattered power spectrum was built up statistically over 4500 shots (15 mins integration time at a shot repetition rate of 5 Hz). In this way, high-quality spectra with extremely high signal-to-noise ratios were obtained [Toleikis et al., 2010]. This experiment is particularly well-suited as a benchmark to the present work as the self-scattering configuration used accesses the collective dynamic response of a strongly-driven, rapidly evolving non-equilibrium system.

4.4.1 Numerical simulation of the electron distribution

The evolution of the electron distribution has been studied by B. Ziaja et al. using a Boltzmann approach for atomic clusters [see, e.g., Ziaja et al., 2006; Ziaja and Medvedev, 2012]. The simulation model is based on a Legendre polynomial expansion of $f_e(\mathbf{p})$, thereby accounting for anisotropic contributions arising from electrons being ionized by the linearly polarised FEL. Due to collisions with ions, neutral atoms and other electrons, however, the anisotropic components are negligible.

The results show that at early times $f_e(p)$ is strongly peaked about the energy of photoionized electrons, i.e. $E_i - E_{\text{bind}} = 91.7 - 13.6 \approx 78.1$ eV (see Fig. 4.7(a)). A second, smaller peak downshifted from the probe energy by roughly twice the binding energy quickly develops, corresponding to collisional ionization of secondary electrons. Diffusion of energy from these distinctive non-thermal features via ultra-fast kinetic processes quickly populates an equilibrium-like branch, which gradually thermalises with the cold electron bath. Throughout the probe duration a significant weight remains in the hot, non-thermal populations since the distribution is pumped by the heating/probing x-rays.

Despite the fact that electrons are continually pumped into high-energy free states by the FEL, the free electron density is rather low due the relatively low coupling of photons in the pulse. Accordingly, the plasma remains weakly coupled conditions throughout the measurement (see Fig. 4.7(b)). Near the peak of the FEL pulse, however, the density is high enough for the probe to access the weakly collective response of the plasma. As the intensity of the pulse decreases the distribution evolves towards thermal equilibrium characterised by a temperature of $T_e = 3.4$ eV and electron density of $n_e = 5.8{\times}10^{20}$ cm^{-3}.

4.4.2 Results with fitted BOHT distributions

By fitting the cluster simulation results with the BOHT model (4.8) the important features of the non-equilibrium distribution can be adequately captured (see Fig. 4.8(a)). The fitting parameters are summarised in Tab. 4.1. Clearly, the evolution of $f_e(p)$ is not well-represented at any time by a FD distribution at the density and temperature given by Fäustlin et al. from fitting the measured scattering data with an equilibrium calculation: $T_e^{\text{fit}} = 13$ eV and $n_e^{\text{fit}} = 2.8{\times}10^{20}$ cm^{-3} [Fäustlin et al., 2010].

At early times, the large non-thermal population gives rise to a strong BAM in the dispersion curve (Fig. 4.8(b)) which decreases in strength by the peak of the pulse as the bump is continually broadened and feeds the growth of the quasi-thermal hot tail. As the relaxation progresses, the distinction between the cold and hot components decreases until a single dispersion curve emerges which is dominated by the conditions of the cold bulk. Note the similarity between the late-time non-equilibrium dispersion and that corresponding to the equilibrium best fit estimate. This occurs because the difference between the mean kinetic energies of the systems is balanced by the difference in their respective screening lengths, leading to similar loci being followed as a function of k/κ_e.

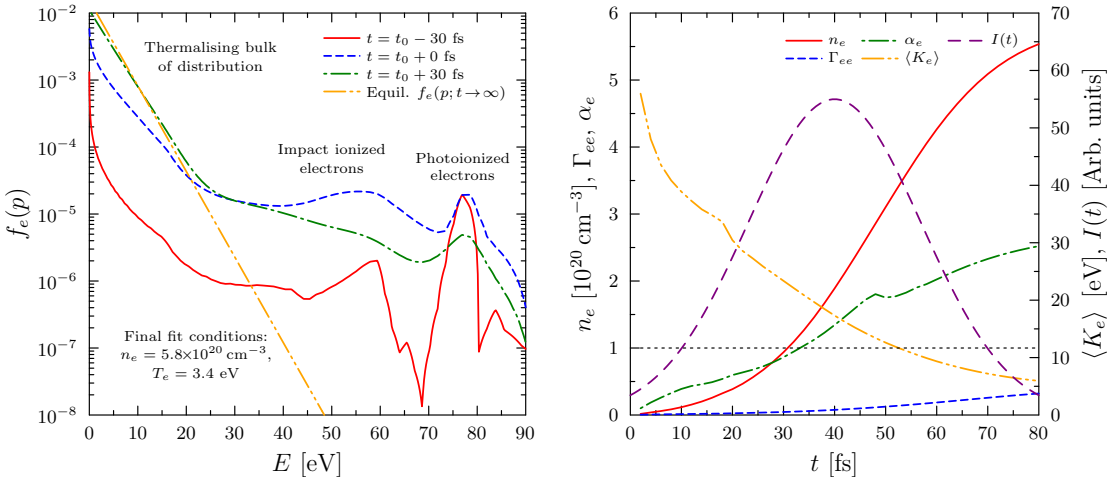

(a) Evolution of the electron distribution.

(b) Evolution of non-equilibrium parameters.

Figure 4.7: (a): Simulations of the electron distribution as function of energy (courtesy of B. Ziaja) during interaction of the FLASH FEL beam with cryogenic liquid hydrogen droplets. (b): Time dependence of the free electron density n_e, mean kinetic energy $\langle K_e \rangle$, coupling parameter $\Gamma_{ee} = \langle V_{ee} \rangle / \langle K_e \rangle$ and scattering parameter $\alpha = \kappa_e / k$ of the non-equilibrium hydrogen plasma. All the dimensionless plasma parameters have been calculated from their generalised non-equilibrium forms in terms of $f_e(p)$ only. The FEL intensity profile is also shown for clarity.

t [fs]	n_e [cm^{-3}]	T_c [eV]	x_h	T_h [eV]	x_b	E_0 [eV]	E_b [eV]
$t_0 - 20$	$3.86{\times}10^{19}$	3.0	0.28	48.0	0.12	74.2	12.0
$t_0 + 0$	$1.89{\times}10^{20}$	3.8	0.43	35.0	0.007	77.9	1.6
$t_0 - 20$	$4.26{\times}10^{20}$	4.1	0.13	20.5	0.0035	77.6	6.0

Table 4.1: Fitting parameters for the BOHT distributions shown in Fig. 4.8(a).

The structure factors of the interacting system (Fig. 4.8(c)) show the expected characteristic features of the non-equilibrium states. Initially, the plasma is probed in the non-collective regime, such that the spectral shape reflects the integrated electron distribution along the direction of k. The large step-like features result from the substantial weight of the bump component and extended high-frequency wings are due to the hot tail. The spectrum then develops and pair of plasmons as the screening length gets shorter with increasing ionization, and a transition to a weakly collective state occurs. The plasmons are also shifted to higher frequencies and less strongly damped as the electron density increases throughout the pulse.

4.4.3 Importance of time-averaging over non-equilibrium states

A more useful comparison to the measured data can be made if the power spectra are calculated from the structure factors shown in Fig. 4.8(c). Weighting by the density and

convolving with a Gaussian source function to represent the various sources of blurring, it is clear that no single time-step accurately reproduces the experimental power spectrum (Fig. 4.8(d)). In fact, such a result is expected since the spectrometer records the total scattered power over the full duration of the probe pulse and, thus, reflects the time-averaged response of the rapidly evolving plasma.

Averaging over the macroscopic time evolution, the inelastically scattered power is

$$\frac{\partial^2 P_\mathrm{s}^\mathrm{in}}{\partial\Omega\partial\omega_\mathrm{s}} \propto \int \mathrm{d}t\, \bar{n}_i\, \bar{Z}_i^\mathrm{f}(t) \Big[(\omega_\mathrm{s}/\omega_\mathrm{i})^2\, S_{ee}(k,\omega;t) * I(\omega;t) \Big] , \tag{4.13}$$

$$I_\mathrm{i}(\omega,t) = \frac{I_\mathrm{i}^0 \ln(16)}{\pi \Delta_\omega \Delta_t} \exp\left[-\ln(16) \left(\frac{\omega}{\Delta_\omega} \right)^2 \right] \exp\left[-\ln(16) \left(\frac{t-t_0}{\Delta_t} \right)^2 \right] . \tag{4.14}$$

In Eq. (4.14), Δ_ω and Δ_t respectively stand for the FWHMs of the FEL intensity profile in the frequency and time domains. The density of the liquid hydrogen, $n_\mathrm{H} = 4.2\times10^{22}$ cm^{-3}, is assumed to be constant as the FEL duration is far shorter than the hydrodynamic response of the target. Spatial gradients are not considered as the energy deposition range of the FEL is tuned to the droplet size, leading to reasonably uniform heating. Note that despite the clear importance of bound-free scattering from photoionization, its contribution can be neglected since the range of the detector is not large enough to see features shifted by the binding energy, i.e. energies less than $\hbar\omega < E_\mathrm{i} - E_\mathrm{bind} \approx 79$ eV.

The time-averaging blurs the contributions from states with very different excitation spectra, with the largest contributions given by states around the peak of the FEL intensity. In Fig. 4.9, the time-resolved spectra corresponding to the cluster simulation data have been estimated using BOHT fits to the cluster simulation results for the evolution of the distribution function. The best fit conditions gives a good match to the experimental data in general, but does not show the same degree of asymmetry in the positions of the two peaks. Taking a time-integrated non-equilibrium approach with only inelastic scattering contributions matches the width of the main part of the spectrum. However, the separation of the peaks is slightly too large, and a significant underestimate of the scattering near the probe energy is present.

A reasonable representation of the experimental data is only possible if a small, but non-negligible elastic contribution is considered, which enhances the signal in between the plasmons. The Rayleigh weight in the fit shown is $W_\mathrm{R}(k) = 0.2$. Conversely, the best fit curve from Fäustlin et al. requires that elastic scattering be practically absent. It is claimed that this results from a temperature-dependent Debye-Waller effect which strongly suppresses elastic scattering. This effect is known to diminish elastic scattering from strongly coupled, regular, lattice-like ion distributions such as metallic crystals [Gregori et al., 2006b]. However, such an explanation seems unreasonable in the present case since the target is in a disordered liquid state prior to irradiation. Moreover, as the pulse is too short for the ions to adjust to the potential created by ionization, an equilibrium plasma-based description is not suitable.

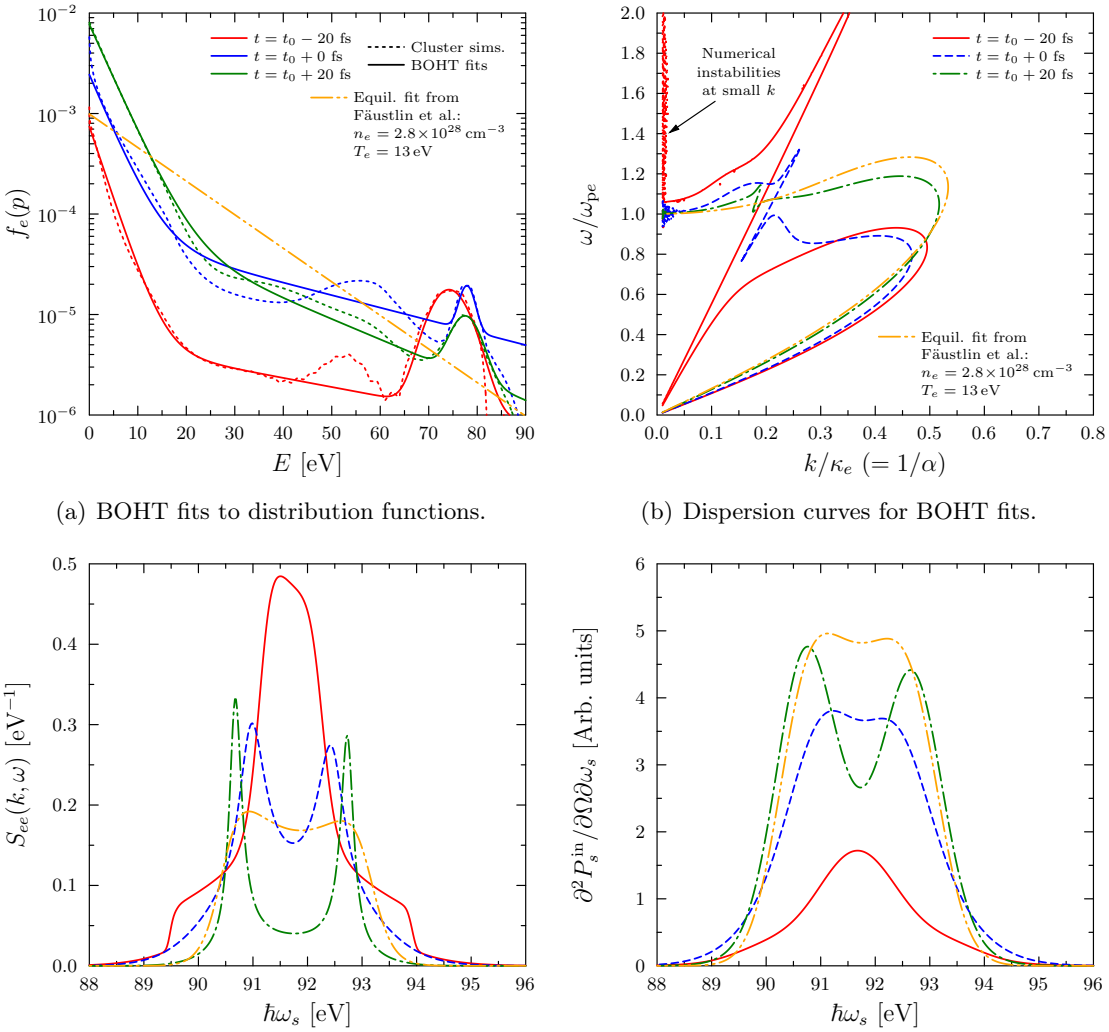

(a) BOHT fits to distribution functions.

(b) Dispersion curves for BOHT fits.

(c) Free electron DSFs for BOHT fits.

(d) Inelastic power spectra for BOHT fits.

Figure 4.8: (a): Fits to the cluster simulation data at the peak of the FEL pulse, $t = t_0$, and the FWHM points, $t = t_0 \pm 20$ fs. These fits are used to calculate the dispersion curves (b), free electron DSF in RPA (c) and total inelastically scattered power spectra (d) of the non-equilibrium system. In all cases, the equilibrium results at the best fit conditions reported by Fäustlin et al. are also shown for comparison. The power spectra are convolved with a Gaussian function (FWHM of 0.79 eV) representing both source broadening and the shape of the FEL spectrum.

Using a multicomponent treatment with neutral hydrogen, free protons and electrons, the Rayleigh amplitude is given by Eq. (3.27). The density of free electrons forming a screening cloud around the neutrals can safely be neglected, such that $q_H(k) = 0$. Similarly, there are no bound states around free protons, $f_H(k) = 0$. The Rayleigh weight is then

$$W_R(k) = x_0 f_0^2(k) S_{00}(k) + 2\sqrt{x_0 x_H} f_0(k) q_H(k) S_{0H}(k) + x_H q_H^2(k) S_{HH}(k). \tag{4.15}$$

For hydrogen the form factor of the bound electrons surrounding the neutrals may be

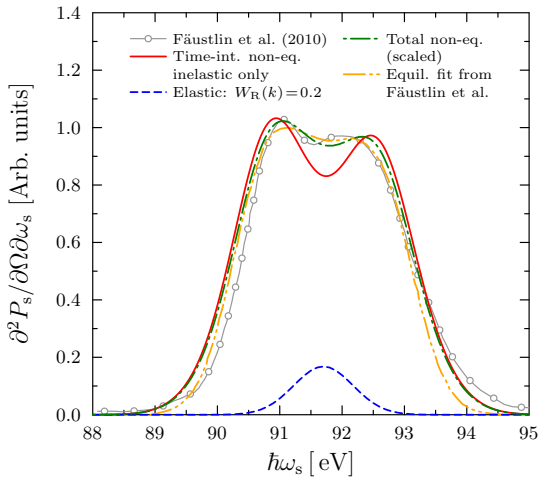

Figure 4.9: Experimental data of [Fäustlin et al., 2010] compared to theoretical fits using a time-integrated non-equilibrium approach informed by the cluster simulations, and an equilibrium calculation at n_e^{fit} and T_e^{fit}. A purely inelastic calculation is not sufficient when considering a non-equilibrium treatment. The necessary elastic feature is shown for clarity.

described exactly with the well-known expression for the 1s states which can be derived from Eqs. (3.29 - 3.31). The latter is roughly constant in time, the only change being the negligibly small change to the x-ray dispersion due to the increasing electron density. For the wave number under investigation one has $f_0(k) = 0.9994$. On the other hand, the screening cloud surrounding the protons evolves substantially as the density steadily increases. Considering the long wavelength Debye-Hückel limit $q_{\text{H}}(k) = \kappa_e^2/(k^2 + \kappa_e^2)$, where the time-dependent inverse screening length κ_e is related to $f_e(p)$ via Eq. (1.20), one finds $q_{\text{H}}(k) = 0.01$–0.8.

4.4.4 Static structure of liquid hydrogen

Eq. (4.15) can be further simplified since the first term dominates by virtue of the low mean ionization produced by the FEL. Furthermore, taking $f_0(k) \approx 1$ and $x_0 \approx 1$, it is clear that the total weight of elastic scattering is effectively given by the structure of the neutrals, $W_{\text{R}}(k) \approx S_{00}(k)$, which is inherited from the undisturbed liquid system. For liquid hydrogen, a number of interaction potentials have been suggested [Silvera and Goldman, 1978; Ross et al., 1983]. In particular, the model of Ross et al. (RRY) includes both the pair interaction and triple dipole contribution to the inter-molecular potential. At cryogenic temperatures the inter-particle coupling is sufficiently strong to make simple perturbative approaches, such as the HNC method described in Chapter 3, unsuitable. Instead, Monte Carlo (MC) simulations [see, e.g., Allen and Tildesley, 1999] have been performed by J. Vorberger.

Fig. 4.10 shows the static structure factor calculated from MC simulations using the RRY potential for a system of 4096 H_2 molecules. The results show a large correlation hole is found for small wave numbers and damped oscillations for larger k. Both features are characteristic of strongly coupled fluid systems. Unfortunately, significant numerical noise is present at small k due to restrictions on the size of the simulation box. However, it is clear that the structure factor at the wave number of interest is very small.

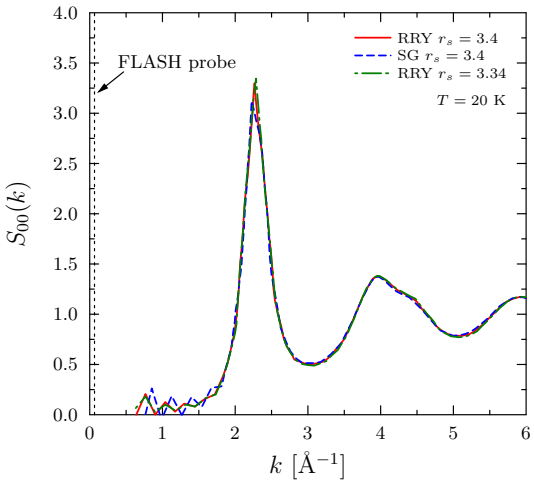

Figure 4.10: Monte Carlo simulations of the SSF of cryogenic liquid hydrogen at $\bar{n}_\mathrm{H} = 4.2 \times 10^{22}$ cm^{-3} and $T = 20$ K (courtesy of J. Vorberger), in which the model potentials of Ross et al. (RRY) [Ross et al., 1983] and Silvera and Goldman (SG) [Silvera and Goldman, 1978] have been used. The two different RRY results demonstrate the insensitivity to small uncertainties in the neutral density due to ionization.

Estimates of the SSF in the $k \to 0$ limit can instead be obtained using the compressibility sum rule Eq. (2.83). In terms of the static structure factor this is

$$\lim_{k\to 0} S(k) = n\, k_\mathrm{B} T \varkappa_T. \tag{4.16}$$

For liquid hydrogen at $T = 20$ K and a pressure of 0.101 MPa, the compressibility is $\varkappa_T \approx 0.0198\,\mathrm{MPa}^{-1}$ [McCarthy et al., 1981], giving $S_{00}(k = 0) = 0.23$. This value is also roughly in agreement with calculations based on empirical data from the NIST database which give a value of 0.165. The small value of the structure factor inherited from the cold liquid state is in excellent agreement with the value of $W_\mathrm{R}(k)$ used in Fig. 4.9. This also explains the small contribution of elastic scattering in the measured scattering data without the need to invoke unphysical correction factors.

In conclusion, it can be stated that the experimental data is well-represented by calculations based on the non-equilibrium framework presented in this section. Although present time-integrated data can also be described with an equilibrium treatment, future experiments may explore the non-equilibrium dynamics more directly and, thus, provide a stringent test of the theoretical formalism applied. Such measurements are highly desirable as they can highlight the microscopic dynamics in dense systems, i.e. the relaxation rates. In the analysis presented here, it was shown that a clear distinction between two different time scales was possible. Namely, a non-equilibrium treatment enables both the ultra-short momentum relaxation in the electron subsystem and the much slower response of the atomic/ionic system to be investigated.

4.5 Fully numerical approach for arbitrary distributions

So far in this chapter, only simple model forms for non-equilibrium electron distributions have been considered. Although it is possible to model increasingly complex distributions with a *multi-bump* generalisation of the BOHT model, the number of free parameters

rapidly increases. The benefit of the semi-analytic results which may be obtained is subsequently diminished. For complicated distribution functions with multiple features, it is often more expedient to solve the requisite equations entirely numerically.

In order to efficiently implement a fully numerical model, a sensible choice of normalisation for the momentum p is required. Since the concept of temperature is not well-defined in non-equilibrium, the natural normalisation of the thermal momentum p_a cannot be used. Instead, the momentum is normalised according to $x = 2p/\hbar k$, from which one obtains

$$S_e^0(k,\omega) = \frac{m_e k}{8\pi^2 \hbar n_e} \int_{|1+z|}^{\infty} \mathrm{d}x\, x\, [1 - f_e(x)]\, f_e\left(\sqrt{x^2 - 4z}\right), \tag{4.17}$$

$$\mathrm{Im}\, \varepsilon_{ee}(k,\omega) = \frac{e^2 m_e}{8\pi\hbar^2 \varepsilon_0 k} \int_{|1-z|}^{|1+z|} \mathrm{d}x\, x\, f_e(x). \tag{4.18}$$

where $z = \omega/\omega_{Ce}$ is the dimensionless frequency shift. The real part of the dielectric function is straightforwardly obtained from the Kramers-Kronig Eq. (2.77). Of course, the free electron density must also be calculated from the distribution function as a function of time. The details of the numerical evaluation of this set of equations is given in Appendix A. It is interesting to note that time-integrating over the structure factors produced by post-processing the full time-evolution of the distribution function supplied by B. Ziaja yields a negligible improvement to the results presented in the previous section. Such a positive result is attributable to the utility of the BOHT model.

4.5.1 Application to strongly-driven solid aluminium

An example of complicated electron distributions for which fitting using the BOHT model is not practical are those presented by Medvedev et al. [Medvedev et al., 2011]. Here, MC calculations were used to model the evolution of $f_e(p)$, which were used to investigate the importance of non-equilibrium physics on the Bremsstrahlung emission and fluorescence of FEL-irradiated solid aluminium targets at FLASH. In this example, the pulse length is $t_{\mathrm{pulse}} = 10\,\mathrm{fs}$. Accordingly, a strong departure from equilibrium may be expected over the pumping period. The physical processes included in this model are well-documented [Ziaja and Medvedev, 2012].

Fig. 4.11 shows the results of a fully numerical calculation of the DSF based on the input distribution functions provided by N. Medvedev for an incident x-ray fluence of $5\,\mathrm{J\,cm^{-2}}$. The evolution of $f_e(p)$ from the initial cold Fermi function (shaded region) is clearly demonstrated in Fig. 4.11(a), which shows the rapid development of distinct population of electrons at c.a. 30 eV, corresponding to photoionization of weakly bound L-shell states. Further ionization of L-shell electrons can be seen from the presence of the smaller peak near 25 eV. Moreover, fast inverse Auger decay populates a broader feature peaked around 75 eV, which grows substantially over the duration of the pulse. Unlike the distributions studied in the previous section, where the relaxation time was similar to the

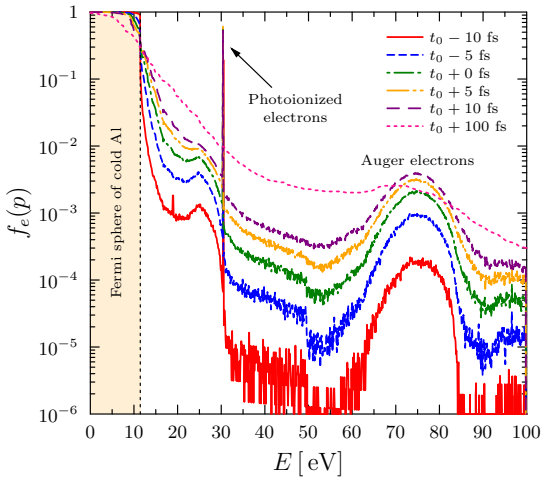

(a) Evolution of the electron distribution.

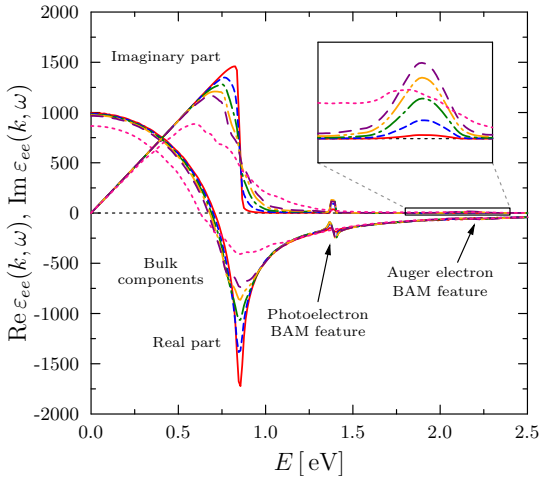

(b) RPA dielectric function components.

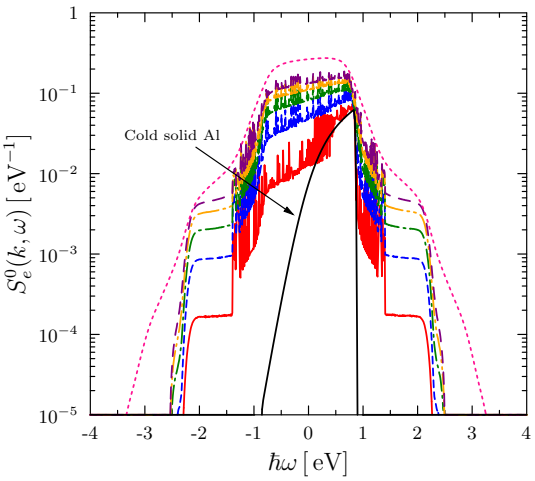

(c) Non-interacting structure factor.

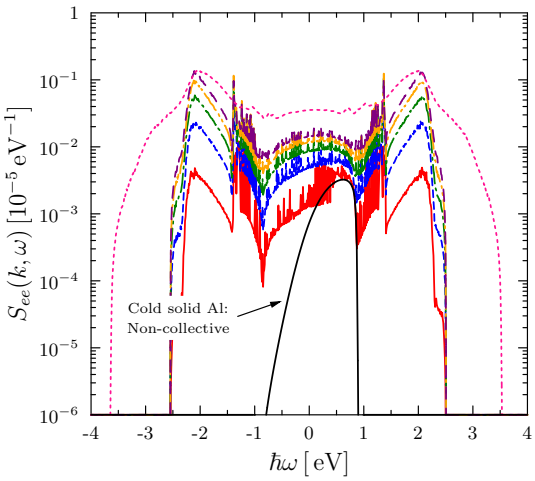

(d) RPA structure factor.

Figure 4.11: (a): Evolution of the distribution function during the FEL excitation pulse as calculated using a Monte Carlo-based model, courtesy of N. Medvedev. (b-d): Real and imaginary parts of the electronic dielectric function, and the non-interacting and interacting dynamic structure factors calculated directly from the distribution function in RPA. The inset in panel (b) shows a close-up view of the Auger electron feature in the imaginary components. Panels (b-d) all follow the colour-coding of the curves shown in panel (a). For all calculations, the probe energy and scattering angle are $E_\mathrm{i} = 91.7\,\mathrm{eV}$ and $\theta = 90°$, respectively, to be consistent with the experiment of Fäustlin et al..

pump/probe duration, here a quasi-thermal high-energy tail persists for several 100 fs after the end of the FLASH pulse.

The components of the dielectric function are shown in Fig. 4.11(b) for the case of 90° scattering at $E_\mathrm{i} = 91.7\,\mathrm{eV}$. It is immediately clear that the highly degenerate cold bulk electrons dominate the response function, although small features due to the photo- and Auger electrons can be seen at higher energies (see, e.g., the feature highlighted in the

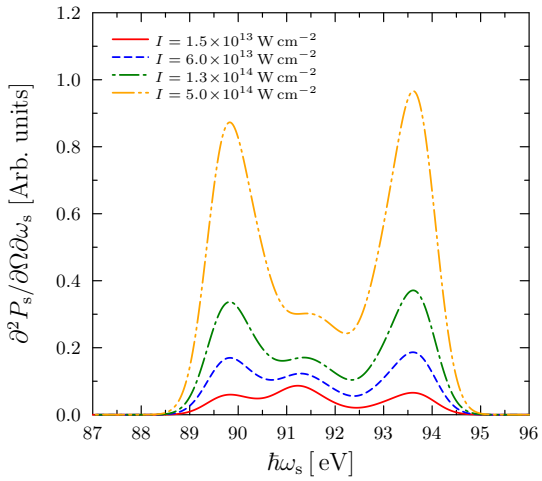

Figure 4.12: Theoretical scattered power spectra due to free electrons for various FEL intensities based on the distribution functions calculated by [Medvedev et al., 2011]. The x-ray source spectrum shape and source broadening effect are unchanged from Fig. 4.9. The pulse is Gaussian in time with a FWHM of $\Delta_t = 10\,\text{fs}$, centred on $t = 15\,\text{fs}$. Strong beam acoustic scattering corresponding due to Auger electrons is clearly visible for the highest intensities.

inset). The gradual heating of the bulk over time is reflected in the smoothing of the sharp edge of the imaginary part, and the broadening of the corresponding inverted peak in the real part. These features are also present in the non-interacting structure (see Fig. 4.11(c)) where the Auger electrons in particular give rise to low-amplitude, step-like wings beyond the bulk states at small energy shifts. These features rapidly grow in amplitude throughout the intensity profile of the pump/probe.

In contrast to the example of liquid hydrogen studied in the previous section, Fig. 4.11(d) shows that non-equilibrium contributions dominate the excitation spectrum of the interacting system. Indeed, the DSF of the cold, undriven solid in RPA shows only a non-collective response. The scattering due to the bulk in particular is strongly suppressed in comparison to the signal due to the non-thermal populations, which is greatly amplified. It should be noted that the real part of the dielectric function does not have a root and, thus, these excitations are not plasmon-like, but instead correspond to the highly transient collective response of excited states.

4.5.2 Possibility of observing transient non-equilibrium modes

Considering these results in the context of a self-scattering experiment similar to that of [Fäustlin et al., 2010] suggests that such a platform may enable the study of transient non-equilibrium collective phenomena. Accordingly, the time-integrated scattered spectrum Eq. (4.13) expected from such an experiment is shown in Fig. 4.12. As with the liquid hydrogen case, no bound-free scatter is present in the energy range of interest. Furthermore, the small k probed is not in the vicinity of the Bragg peaks of solid Al and, thus, the Rayleigh scattering is expected to be negligible. Given that the absolute power contained in the interacting DSF is 10^5 times less than that of the non-interacting system, the absence of Rayleigh scattering would be highly desirable.

The different curves shown in Fig. 4.12 correspond to different incident FEL fluences (the highest intensity corresponds to the results shown in Fig. 4.11). For low intensities, the non-collective scattering from the bulk can be distinguished, although the shifted BAM

resonances are clearly visible. Increasing the intensity drives more electrons into non-thermal states and the BAM features dominate. This result has important ramifications for real experiments with similar setups since the potential to confuse BAM scattering with plasmons is clear. Misidentifying these features would lead to incorrect interpretations of data, resulting in erroneous plasma conditions being inferred. This may have significant implications for measurements of any subsequently derived properties of the plasma.

Chapter 5

Investigating temperature relaxation in dense matter using x-ray Thomson scattering

Following excitation with either a heating laser or probe, the electron distribution inexorably relaxes into an equilibrium shape characterised by a well-defined, time-dependent temperature. For dense matter driven with FEL x-rays, relaxation occurs within c.a. 10–100 fs following the peak of the pulse, depending on the collision and excitation rates. Over longer time scales, the electron and ion distributions relax toward full thermodynamic equilibrium by means of both collisions and interactions between collective excitations. Given the strong influence of both the electron and ion temperatures on the dynamic and static structural properties of plasmas, XRTS may be an ideal diagnostic tool with which to characterise such processes.

In this chapter, the feasibility of using XRTS to measure temperature relaxation in dense plasmas is considered. The relaxation rates are derived within the same general quantum statistical framework used to describe the DSF in order to apply to non-ideal states. Low-density metal foams and solid targets driven to low and high temperatures are investigated to access different degeneracy regimes. It is shown that foam targets driven to c.a. $T \sim 20$–$30\,\mathrm{eV}$ yield conditions conducive to such measurements. Calculations of complementary spectrally- and angularly-resolved XRTS show clear features from which the time-dependent electron and ion temperature could be determined. Moreover, it is shown that such measurements may enable distinctions between energy relaxation models to be made.

5.1 Modelling temperature relaxation in dense plasmas

The accurate characterisation of temperature relaxation is of fundamental importance to experiments involving matter under extreme conditions in which energy is preferentially absorbed into a particular subsystem (the electrons or ions). For example, experiments have been performed using strong shocks [Ng et al., 1995], VUV-FEL irradiation [Inogamov et al., 2011] and charged particle beam stopping [White et al., 2012; 2014], resulting with non-equilibrium states with respect to the temperature.

The subsequent relaxation to local thermodynamic equilibrium is coupled to both the energy transfer rate and partial equation of state, neither of which are presently well-understood under such challenging conditions. Moreover, temperature relaxation is a critically important component of the microphysical models which underpin the large-scale simulation tools ubiquitously used to design, optimise and analyse such experiments, e.g. radiation-hydrodynamics.

For the dilute, high-temperature plasmas typically created in laboratory astrophysics experiments and high-power laser-plasma interactions, temperature relaxation occurs over relatively long time scales (100 ps–1 ns). High-resolution time-streaked data on the temporal evolution of such states may be obtained using a variety of diagnostics techniques, including emission and absorption spectroscopy, optical pyrometry and optical Thomson scattering (OTS). In this regime, the theoretical description of energy and temperature exchange is mostly described by simple models based on binary collisions in the weakly coupled limit, which are expected to be robust. Furthermore, uncertainties in the equation of state properties of near-ideal plasmas are known to be minimal. Nevertheless, no experiments have yet been performed which can claim to have made a direct measurement of temperature equilibration and, thus, even simple models remain unvalidated under WDM conditions.

In the case of dense plasmas, equilibration experiments are hampered practically by significantly faster relaxation rates (1–10 ps), inhibiting high-resolution time-resolved measurements, and theoretically due to uncertainties in the treatment of correlations, partial ionization, band structure, phase transitions and material properties. In particular, the contributions of collective excitations to the energy relaxation rate in WDM has recently been the subject of much research and debate [see, e.g., Dharma-wardana and Perrot, 1998; Hazak et al., 2001; Daligault and Mozyrsky, 2008; Daligault and Dimonte, 2009]. As XRTS provides in situ measurements of the thermodynamics of dense plasmas, and static and dynamic information across a wide range of conditions, its potential as a diagnostic for temperature relaxation is certainly worth assessing.

5.1.1 Governing equations for temperature relaxation calculations

In general, the temporal evolution of the electron and ion temperatures obeys a matrix equation which couples together the partial equations of state and the energy exchange

and dissipation mechanisms in the plasma [Vorberger and Gericke, 2012]

$$\begin{pmatrix} C_{ee}(T_e,T_i) & C_{ei}(T_e,T_i) \\ C_{ie}(T_e,T_i) & C_{ii}(T_e,T_i) \end{pmatrix} \begin{pmatrix} \dfrac{\partial T_e}{\partial t} \\ \dfrac{\partial T_i}{\partial t} \end{pmatrix} = \begin{pmatrix} \mathcal{Z}_{ei}(T_e,T_i) + \nabla\cdot\mathbf{Q}_e(T_e,T_i) + W_e^{\mathrm{rad}}(T_e) + \mathcal{S}_e^{\mathrm{ext}} \\ \mathcal{Z}_{ie}(T_e,T_i) + \nabla\cdot\mathbf{Q}_i(T_e,T_i) + \mathcal{S}_i^{\mathrm{ext}} \end{pmatrix}. \tag{5.1}$$

The time-dependence of each term has been suppressed for brevity. In Eq. (5.1), C_{ab} are the contributions to the specific heat capacities, $\mathcal{Z}_{ab}$ are the energy exchange rates between particles and $\mathbf{Q}_a$ are the heat fluxes characterising heating/cooling by means of thermal diffusion. For high-temperatures one expects the electrons to also radiate energy via thermal and line emission, which is accounted for by the radiated power per unit volume W_e^{rad}. The radiation from the ions can always be neglected. Furthermore, external energy sources $\mathcal{S}_a^{\mathrm{ext}}$ are included to model heating mechanism which specifically couple to the electrons or ions. Note that the nature of the absorption mechanisms themselves will not be addressed as this is beyond the scope of the present work.

A significant simplification to the governing equation Eq. (5.1) can be made if cross contributions to the heat capacity are dropped, such that $C_{a\neq b} = 0$. The cross terms may be important in strongly screened systems where the electrons modify the structural properties of the ions, but are usually still small relative to pure electron and ion terms. In this case, one obtains the two-temperature model of Lin et al. [Lin et al., 2008]. Furthermore, if the sample is relatively homogeneously heated, e.g. using proton stopping, the thermal diffusion terms can typically also be neglected. The result is a pair of coupled equations

$$\frac{\partial T_e}{\partial t} = \frac{\mathcal{Z}_{ei}(T_e,T_i) + W_e^{\mathrm{rad}}(T_e) + \mathcal{S}_e^{\mathrm{ext}}}{C_{ee}(T_e,T_i)}, \tag{5.2}$$

$$\frac{\partial T_i}{\partial t} = \frac{\mathcal{Z}_{ie}(T_e,T_i) + \mathcal{S}_i^{\mathrm{ext}}}{C_{ii}(T_e,T_i)}. \tag{5.3}$$

A similar set of equations has recently been used to study the electron-phonon coupling strength in warm dense tantalum using Bragg diffraction [Hartley et al., 2015].

5.2 Energy relaxation rates

5.2.1 Binary collision approximations

The most commonly-used model of energy exchange in plasmas is due to Landau and Spitzer [Landau, 1936; Spitzer, 1962], which is described in terms of long-range, i.e. small angle, binary Coulomb interactions between electrons and ions. Starting from a highly simplified Fokker-Planck collision operator, and considering hyperbolic trajectories, the energy exchange rate per unit volume between electrons and ions is straightforwardly

derived to be

$$\mathcal{Z}_{ei}^{\mathrm{LS}} = \frac{\omega_{\mathrm{pe}}^2 \omega_{\mathrm{pi}}^2 k_{\mathrm{B}}(T_i - T_e)}{\left[2\pi(v_e^2 + v_i^2)\right]^{3/2}} \ln \Lambda^{\mathrm{H}}, \tag{5.4}$$

Here, $\omega_{\mathrm{p}a} = ((Z_a^{\mathrm{f}} e)^2 n_a/\varepsilon_0 m_a)^{1/2}$ and $v_a = (k_{\mathrm{B}} T_a/m_a)^{1/2}$ are the usual plasma frequencies and thermal speeds of species a, respectively. The factor $\ln \Lambda^{\mathrm{H}} = \frac{1}{2}\ln(1 + b_{\max}^2/b_{\min}^2)$ is the famous Coulomb logarithm written here for hyperbolic orbits [Gericke et al., 2002a].

For higher densities, where degeneracy is important, Eq. (5.4) can be re-derived considering a FD distribution [Brysk, 1974]. The result is a correction to Eq. (5.4)

$$\mathcal{Z}_{ei}^{\mathrm{B}} = \frac{\mathcal{F}_{-1}(\eta_e)}{D_e} \mathcal{Z}_{ei}^{\mathrm{LS}}, \tag{5.5}$$

where $\mathcal{F}_{-1}(x) = [1 + \exp(-x)]^{-1}$. Further extensions of the Landau-Spitzer (LS) theory to moderately- and strongly coupled states have been also been performed by considering higher-order terms in the collision operator [Li and Petrasso, 1993], quantum mechanical corrections to classical Coulomb collisions [Brown and Singleton, Jr., 2009], parametrisations of empirical data [Bannasch et al., 2012] and effective potentials extracted from strongly coupled fluid calculations [Baalrud and Daligault, 2013].

A more consistent approach which enables treatment of large-angle scattering is based on the quantum Boltzmann equation [Klimontovich and Kremp, 1981]. The ensemble averaged energy change due to electron-ion collisions for a homogeneous, isotropic and non-degenerate plasma can be shown to give

$$\begin{aligned}\mathcal{Z}_{ei}^{\mathrm{TM}} = \frac{2\pi}{n_e \hbar} \int \frac{\mathrm{d}\mathbf{p}\,\mathrm{d}\mathbf{p}'\,\mathrm{d}\mathbf{q}\,\mathrm{d}\mathbf{q}'}{(2\pi\hbar)^{12}} E_e(\mathbf{p}) \left| \langle \mathbf{p}, \mathbf{p}' | \hat{T}_{ei}^{\mathrm{R}} | \mathbf{q}, \mathbf{q}' \rangle \right|^2 \\ \times \delta(\mathcal{E}_{ei}(\mathbf{p}) - \mathcal{E}_{ei}(\mathbf{q})) \left[f_e(\mathbf{q}) f_e(\mathbf{q}') - f_e(\mathbf{p}) f_e(\mathbf{p}') \right],\end{aligned} \tag{5.6}$$

where $\mathcal{E}_{ei}(\mathbf{p}) = E_e(\mathbf{p}) + E_i(\mathbf{p})$ and $\hat{T}_{ei}^{\mathrm{R}}$ is the operator for the retarded electron-ion interaction defined by the Lipmann-Schwinger equation. Eq. (5.6) is accordingly known as the T-matrix relaxation rate [Gericke et al., 1996; 2002b].

If the matrix element is interpreted as a generalised scattering cross section then, upon substitution of the Maxwell-Boltzmann (MB) distribution, one arrives at a multi-dimensional integral expression which depends on the phases shifts of the electron propagator following scattering in the screened potential of the ion. Numerical solutions for a Debye potential are fitted to high accuracy using

$$b_{\max}^{\mathrm{TM}} = \lambda_{\mathrm{D}e} \exp\left[\frac{1.65 - 0.4 \ln[\ln \Lambda^{\mathrm{H}}]}{1 + (\ln \Lambda^{\mathrm{H}})^{0.64}} \right], \tag{5.7}$$

where the above replaces the maximum impact parameter used in $\ln \Lambda^{\mathrm{H}}$ [Gericke et al., 2002a]. The T-matrix formula has proved to be extremely effective at reproducing sim-

ulations of the stopping power of dense, high-temperature plasmas of interest to ICF. However, a full solution of Eq. (5.6) under degenerate conditions is extremely challenging. Furthermore, the fit given by Eq. (5.7) is inappropriate for $D_e \lesssim 1$, restricting its usefulness for WDM.

Temperature relaxation can also be studied numerically using classical molecular dynamics [see, e.g., Benedict et al., 2009; 2012]. For dense plasmas with degenerate electrons, the electron-ion interaction can be approximately described using pseudo-potentials [Hau-Riege et al., 2013; Graziani et al., 2014b]. Naturally, such first-principles simulations are computationally expensive; a problem only exacerbated if small time resolution is required to capture dynamic processes such as screening. Thus, in order to adequately capture physics beyond simple models in large scale simulations it is important to investigate models which are robust over a large range of degeneracies and coupling strengths, and can be evaluated with relatively little numerical effort.

5.2.2 Contributions from collective modes

A rigorous approach to the exchange of energy between species with well-established but different temperatures can be constructed in terms of real-time non-equilibrium Green's functions, thereby robustly incorporating strong coupling and degeneracy. One can write the energy exchange rate via the general definition

$$\frac{\partial U_a}{\partial t} \equiv \frac{\partial}{\partial t}\Big[\langle K_a\rangle + \langle V_{aa}\rangle\Big] = \sum_b \mathcal{Z}_{ab}\,. \tag{5.8}$$

Note that although the summation is over all other species in the plasma ($b = e, i$), the electron and ions are assumed to be fully thermalised and one therefore has $\mathcal{Z}_{ee} = \mathcal{Z}_{ii} = 0$ and consequently $\mathcal{Z}_{ei} = -\mathcal{Z}_{ie}$. Starting from this completely general definition carries the strong advantage over alternative approaches as the total energy is conserved rather than just the kinetic energy, the latter requiring potential energy contributions to be added through higher-order effects or correction terms.

Following Vorberger et al. [Vorberger et al., 2010], the energy transfer rate is

$$\mathcal{Z}_{ei} = -\,2\int \frac{\mathrm{d}\mathbf{k}}{(2\pi)^3}\int_0^\infty \frac{\mathrm{d}\omega}{2\pi}\,\omega\, V_{ei}(k)\,\mathrm{Im}\big\{i\hbar L_{ei}^{<}(\mathbf{k},\omega)\big\}\,, \tag{5.9}$$

where the form of the lesser density fluctuation correlation function $L_{ei}^{<}(\mathbf{k},\omega)$ is identical to Eq. (3.20). It is worth restating that this expression is derived in a local approximation and, thus, is strictly accurate for energy transfers which occur over far longer time scales than the correlation time. The latter is expected to be well-fulfilled in dense matter, in which equilibration occurs over 1–10 ps.

The limitation of this approach lies in the difficulties involved with approximating the polarisation functions, in particular the cross terms $\Pi_{ei}(\mathbf{k},\omega)$ and $\Pi_{ie}(\mathbf{k},\omega)$. As discussed

in Chapter 3, the direct correlations between different species arise at second order in the interaction and, thus, are less important than strong correlations within the electron and ion subsystems. The latter can be treated within RPA, with strong coupling corrections accounted for by using LFCs (see Section 3.6.5). Considering equilibrium statistics, and using the KMS condition (2.95), one can derive from Eq. (3.20)

$$L_{ei}^{<}(\mathbf{k},\omega) = \frac{2\,\Delta n_{\mathrm{B}}(\omega)\,V_{ei}(k)\,\mathrm{Im}\,\mathcal{L}_{ee}^{\mathrm{R}}(\mathbf{k},\omega)\,\mathrm{Im}\,\mathcal{L}_{ii}^{\mathrm{R}}(\mathbf{k},\omega)}{\left|1-\mathcal{L}_{ee}^{\mathrm{R}}(\mathbf{k},\omega)\,V_{ei}(k)\,\mathcal{L}_{ii}^{\mathrm{R}}(\mathbf{k},\omega)\,V_{ie}(k)\right|^2}\,, \tag{5.10}$$

where the difference between the two Bose functions is $\Delta n_{\mathrm{B}}(\omega) = n_{\mathrm{B}i}(\omega) - n_{\mathrm{B}e}(\omega)$ and $n_{\mathrm{B}a}(\omega) = [\exp(\beta_a\hbar\omega) - 1]^{-1}$.

Substituting Eq. (5.10) into Eq. (5.9), straightforwardly gives [Dharma-wardana and Perrot, 1998; Vorberger et al., 2010]

$$\mathcal{Z}_{ei} = -4\hbar \int \frac{\mathrm{d}\mathbf{k}}{(2\pi)^3} \int_0^\infty \frac{\mathrm{d}\omega}{2\pi}\,\omega\,\frac{\Delta n_{\mathrm{B}}(\omega) V_{ei}^2(k)\,\mathrm{Im}\,\mathcal{L}_{ee}^{\mathrm{R}}(\mathbf{k},\omega)\mathrm{Im}\,\mathcal{L}_{ii}^{\mathrm{R}}(\mathbf{k},\omega)}{\left|1-\mathcal{L}_{ee}^{\mathrm{R}}(\mathbf{k},\omega)\,V_{ei}(k)\,\mathcal{L}_{ii}^{\mathrm{R}}(\mathbf{k},\omega)\,V_{ie}(k)\right|^2}\,. \tag{5.11}$$

The only potentially restrictive approximation applied in deriving Eq. (5.11) is the diagonalisation of the polarisation functions. This expression can therefore be treated as exact for systems in which the direct electron-ion coupling is not important.

For plasmas in which the electron-ion interaction is sufficiently weak, i.e. $V_{ei}(k) \to 0$, the renormalisation term in the denominator of Eq. (5.11) which couples the subsystems together can be dispensed with, giving the *Fermi golden rule* (FGR) expression

$$\mathcal{Z}_{ei} = -4\hbar \int \frac{\mathrm{d}\mathbf{k}}{(2\pi)^3} \int_0^\infty \frac{\mathrm{d}\omega}{2\pi}\,\omega\,\Delta n_{\mathrm{B}}(\omega) V_{ei}^2(k)\,\mathrm{Im}\,\mathcal{L}_{ee}^{\mathrm{R}}(\mathbf{k},\omega)\mathrm{Im}\,\mathcal{L}_{ii}^{\mathrm{R}}(\mathbf{k},\omega). \tag{5.12}$$

If the electron-ion interaction is Coulomb-like then one can make the usual transformation to the product of potentials $V_{ei}^2(k) = V_{ee}(k)V_{ii}(k)$ and write the two screened polarisation functions in terms of one-component dielectric functions (which dependent only on k due to the homogeneous and isotropic conditions)

$$\mathcal{Z}_{ei} \overset{\mathrm{FGR}}{=} -\frac{\hbar}{\pi^3} \int_0^\infty \mathrm{d}k\,k^2 \int_0^\infty \mathrm{d}\omega\,\omega\,\Delta n_{\mathrm{B}}(\omega)\,\frac{\mathrm{Im}\,\varepsilon_{ee}(k,\omega)}{|\varepsilon_{ee}(k,\omega)|^2}\frac{\mathrm{Im}\,\varepsilon_{ii}(k,\omega)}{|\varepsilon_{ii}(k,\omega)|^2}. \tag{5.13}$$

The dynamic response properties of the plasma in this approximation are now clear; both the electrons and ions subsystems support separate, fully self-screening collective modes, which interact to exchange energy via the direct electron-ion interaction $V_{ei}(k)$.

If the denominator in Eq. (5.11) is retained, one finds the *coupled modes* (CM) formula

$$\mathcal{Z}_{ei} \overset{\mathrm{CM}}{=} -\frac{\hbar}{\pi^3} \int_0^\infty \mathrm{d}k\,k^2 \int_0^\infty \mathrm{d}\omega\,\omega\,\Delta n_{\mathrm{B}}(\omega)\,\frac{\mathrm{Im}\,\varepsilon_{ee}(k,\omega)\mathrm{Im}\,\varepsilon_{ii}(k,\omega)}{|\varepsilon(k,\omega)|^2}. \tag{5.14}$$

The CM expression (5.14) differs from the FGR result (5.13) in that the screening for both

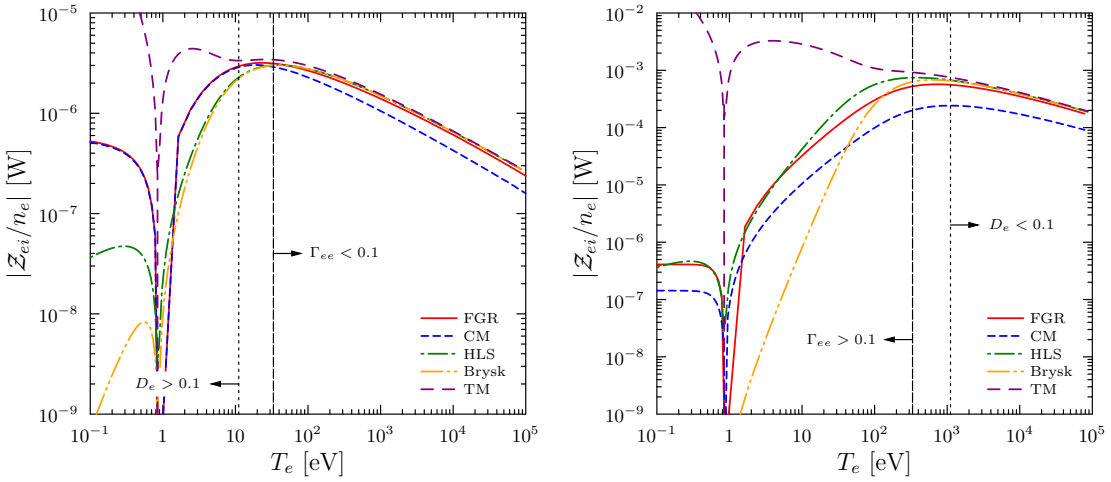

(a) Comparison of models for $n_e = 10^{22}\,\mathrm{cm}^{-3}$. (b) Comparison of models for $n_e = 10^{25}\,\mathrm{cm}^{-3}$.

Figure 5.1: (a): Comparison of various models for the energy transfer rate commonly used in radiation-hydrodynamics codes compared to the reduced models explored in this work at low- (a) and high (b) densities at $T_i = 0.86\,\mathrm{eV}$. The T-matrix fit curves are not appropriate under degenerate conditions, here arbitrarily delineated by $D_e = n_e\Lambda_e^3/2 > 0.1$.

the electronic and ionic subsystems is provided the two-component dielectric function. In the case of the electrons, the screening due to the ions does not greatly affect the plasmon mode structure as the ion density response is negligible at high frequencies. On the other hand, the ion excitations are significantly modified due to screening. The physics is identical to that underpinning the development of the ion acoustic mode from the bare ion plasmon [Vorberger and Gericke, 2009].

5.2.3 Comparison of energy transfer models

A comparison of the energy transfer models discussed so far is presented in Fig. 5.1 for the simple case of fully-ionized hydrogen at densities relevant to WDM and highly-compressed ICF plasmas. The FGR and CM calculations have been provided courtesy of J. Vorberger, and are based on full numerical solution of Eqs. (5.13) and (5.14) for $T_i = 0.86\,\mathrm{eV}$ ($10^4\,\mathrm{K}$). For simplicity, the electron and ion polarisation functions have been calculated in RPA.

Under weakly coupled conditions (marked by the vertical dashed lines) one expects the binary collision-type models to be valid. Indeed, good agreement with the FGR curves is seen for both densities in the limit $T_e \to \infty$, where the energy transfer rate scales as $\sim n_e^2 \ln(T_e/n_e)/T_e^{1/2}$. However, none of the models which neglect electron-ion mode coupling reproduce the results of the CM results in this limit, where the CM rate is around half as fast as all others [Vorberger and Gericke, 2009].

As the electron and ion temperatures becomes comparable, the binary collision models yield slower rates at low densities. Conversely, for higher densities the rates are significantly overestimated, before peaking and falling sharply. Note that large-angle scattering correc-

tions do not significantly affect any of the results in the weakly degenerate regime where the fitted form of the Coulomb logarithm (5.7) is valid, even for moderately coupled states. It is also interesting to note that the Brysk model gives extremely slow relaxation rates under strongly degenerate conditions where it would be expected to be a better estimate than the LS model.

5.3 Heat capacities

The thermalisation of energy into heat is governed by the heat capacities of the electron and ion subsystems, which are also functions of the thermodynamic state. For a system of constant volume, $\mathcal{V}$, these are determined by

$$C_{ab} = \left.\frac{\partial U_a}{\partial T_b}\right|_{\mathcal{V}} . \tag{5.15}$$

The determination of the internal energy contributions of electrons and ions in dense plasmas is important to many areas of current interest, such as first-principles calculations of the equation of state [Morales et al., 2012; Vorberger et al., 2013].

5.3.1 Electronic heat capacity

The pure electronic contribution C_{ee} may be determined from first principles simulations in terms of the density of states $g(E)$ [see, e.g., Lin et al., 2008; Hartley et al., 2015]. If strong electron-ion correlations, e.g. bound states, can be neglected one may instead attempt to calculate the internal energy using a quantum statistical perturbation approach. This level of approximation is applicable to the present work since the DSF is considered in linear response (see discussion in Chapter 3), in which the electrons and ions interact only indirectly via screening.

Within a quantum statistical approach, the mean energy of a strongly coupled electron gas can be developed via a series expansion in terms of the interaction strength. Terms up to second order have previously been considered [Kremp et al., 2005; Vorberger et al., 2013], but are numerically expensive to evaluate and will therefore not be considered in this work. In terms of the specific heat capacity, the leading order term is the ideal contribution

$$C_{ee}^{\mathrm{id}}(T_e;\eta_e) = \frac{\partial}{\partial T_e}\left[\frac{3}{2} n_e k_{\mathrm{B}} T_e \frac{\mathcal{F}_{3/2}(\eta_e)}{D_e}\right] . \tag{5.16}$$

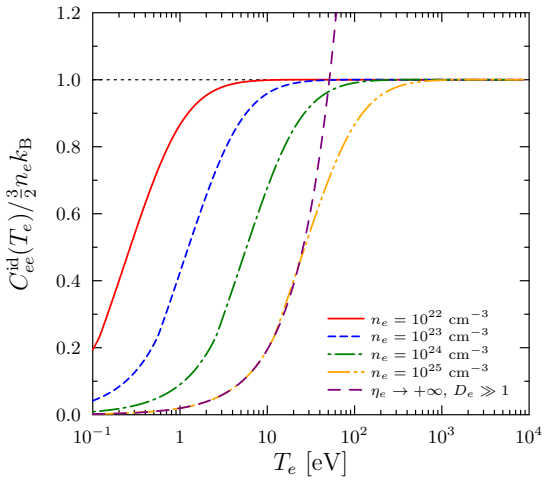

Figure 5.2: (a): Behaviour of the ideal component of the pure electronic heat capacity for different densities and temperatures. The curves are all normalised to the ideal value for a non-degenerate electron gas, i.e. $\frac{3}{2}n_e k_{\mathrm{B}}$.

In general, Eq. (5.16) must be calculated numerically but has the well-known limiting cases

$$C_{ee}^{\mathrm{id}}(T_e;\eta_e) = \begin{cases} \dfrac{3}{2}n_e k_{\mathrm{B}} & : \eta_e \to -\infty \ (D_e \ll 1) \\ \dfrac{\pi^2 n_e k_{\mathrm{B}}}{2}\left(\dfrac{4\sqrt{\pi}}{3D_e}\right)^{2/3} & : \eta_e \to +\infty \ (D_e \gg 1) \end{cases} . \tag{5.17}$$

Fig. 5.2 shows the ideal contributions to Eq. (5.17) as a function of electron density and temperature. Clearly, the most important behaviour to capture in the context of temperature relaxation is the transition from a low-heat capacity state in the initial cold target to the non-degenerate limit as the electrons are heated.

5.3.2 Ionic heat capacity

For the ions, one may assume non-degenerate statistics as usual, such that the ideal part of the pure ionic contribution C_{ii} is simply

$$C_{ii}^{\mathrm{id}} = \frac{3}{2}n_i k_{\mathrm{B}}. \tag{5.18}$$

The excess ion energy contribution due to screened correlations in a two-component plasma can then be calculated within the classical fluid description [Hansen and McDonald, 1990; Ichimaru, 1982]. The total ionic heat capacity is

$$\begin{aligned} C_{ii}(T_e,T_i) &= C_{ii}^{\mathrm{id}} + C_{ii}^{\mathrm{corr}}(T_e,T_i) \\ &= \frac{3}{2}n_i k_{\mathrm{B}}\left\{1 + \frac{1}{6\pi^2 k_{\mathrm{B}}}\frac{\partial}{\partial T_i}\int_0^\infty \mathrm{d}k\, k^2\left[S_{ii}(k;T_e,T_i)-1\right]\frac{V_{ii}^{\mathrm{C}}(k)}{\varepsilon_{ee}(k,0;T_e)}\right\}. \end{aligned} \tag{5.19}$$

Electronic screening influences both the effective ion-ion potential and subsequently the ion structure, thereby introducing dependence on the electron temperature. This is one of the sources of the cross contributions to the heat capacity. The nature of the screening is particularly important since the decay of the the ion-ion interactions limits contributions

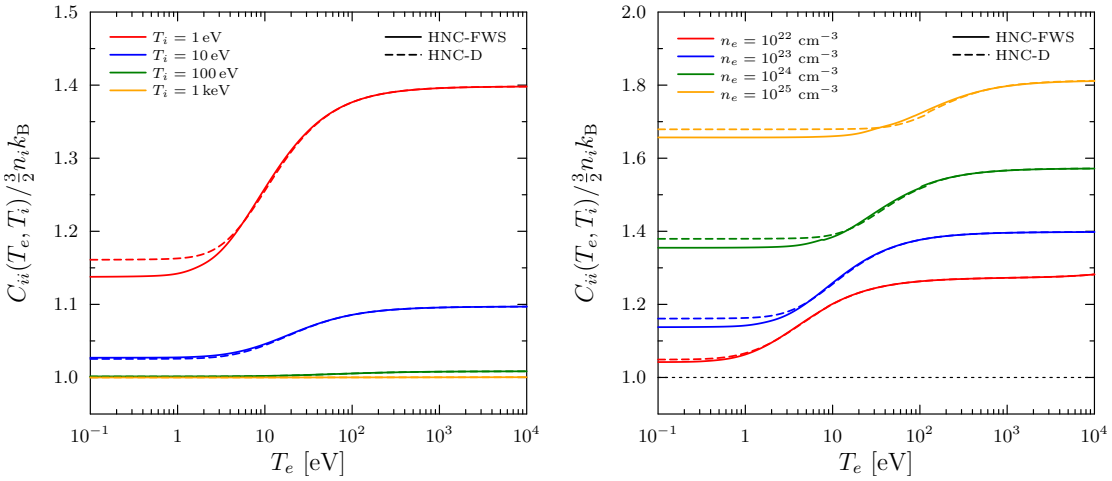

(a) Varying ion temperature.

(b) Varying ion density.

Figure 5.3: (a): Normalised ionic heat capacity $C_{ii}/\frac{3}{2}n_i k_\mathrm{B}$ of fully ionized hydrogen for various ion temperatures at a density of $n_i = 10^{23}\,\mathrm{cm}^{-3}$. (b): Effect of varying the ion density with $T_i = 1\,\mathrm{eV}$. The static structure factor is calculated in the HNC approximation using both the FWS and Debye potentials to include electronic screening.

from short range correlations in strongly coupled states at large k. Thus, one expects the heat capacity of ions screened by the FWS and DH static dielectric functions to differ significantly for degenerate conditions. The static correlations between the ions can be accurately accounted for using the HNC approximation.

To evaluate Eq. (5.19), the derivative of the ion structure with respect to the ion temperature must be taken. Here, this is approximated by computing the SSF at three temperatures $\{(1-\delta_T), 1, (1+\delta_T)\} \times T_i$, where T_i is the ion temperture of interest and $\delta_T \ll 1$, fitting a quadratic $AT_i^2 + BT_i + C$ to the results and setting $C_{ii}^{\mathrm{corr}} = 2AT_i + B$.

As a simple example, Fig. 5.3 shows the normalised ionic heat capacity $C_{ii}/\frac{3}{2}n_i k_\mathrm{B}$ of fully-ionized hydrogen at $T_i = 1\,\mathrm{eV}$ for a wide range of dense, non-equilibrium states. For all cases, the screening of the ion-ion interactions resulting from the Debye and FWS potentials are compared; the ion structure is calculated from the HNC method with the corresponding potentials for consistency. As expected, the results show that the correlation contribution is small for lower densities and higher ion temperatures, but gives a significant correction to the ideal term under strongly coupled conditions. Given the strong dependence of the excess contribution (5.19) on the effective ion charge, both directly from the interaction potential and indirectly via the SSF, significantly stronger deviation from the ideal case is expected for more highly charged ions.

The largest deviations from the ideal heat capacity arise for strongly coupled and strongly non-equilibrium states. In particular, if the ions are fixed at low temperature and high density, the correlation term increases as the electrons are strongly heated since the screening becomes weaker and the ion structure tends to a more strongly coupled pure Coulomb system. In the low temperature limit the screening tends to the Thomas-Fermi

model and ceases to be temperature-sensitive. The transition between these limits occurs at higher electrons temperatures as the Fermi energy (electron density) increases. Considering the full k-dependence of the screening via the FWS dielectric function decreases the heat capacity further in this regime as ion correlations at large k are more effectively shielded. Nevertheless, the simple Debye-like screening cloud provides a reasonable estimate of the correlation contribution over the full range of conditions.

5.4 Results for the temperature evolution

A series of relaxation calculations are now performed in order to assess the suitability of XRTS for measuring temperature equilibration. Volumetrically and isochorically heated targets are considered in order to eliminate the complications associated with thermal diffusion and hydrodynamic motion. Accordingly, energy absorption into the ions can also be neglected. The target material is taken to be pure aluminium since this is a well-characterised standard material which is likely to be used to realise such experiments. Different degeneracy regimes are accessed by considering a low density foam ($\rho = 0.2\,\mathrm{g\,cm^{-3}}$) and a typical solid target ($\rho = 2.7\,\mathrm{g\,cm^{-3}}$).

Within the limited scope of this chapter, the energy relaxation can be investigated numerically by solving Eq. (5.2) using finite-difference integration

$$T_e(t_{j+1}) \approx T_e(t_0) + \sum_{j=1}^{N_t-1} \delta t\, C_{ee}^{-1}(t_j)\big[\mathcal{Z}_{ei}(t_j) + W_e^{\mathrm{rad}}(t_j) + \mathcal{S}_e^{\mathrm{ext}}(t_j)\big]\,, \tag{5.20}$$

$$T_i(t_{j+1}) \approx T_i(t_0) - \sum_{j=1}^{N_t-1} \delta t\, C_{ii}^{-1}(t_j)\, \mathcal{Z}_{ei}(t_j), \tag{5.21}$$

where N_t is the number of time steps. Whilst relatively crude, this method of solution converges provided that $\delta t = t_{j+1} - t_j \ll T_a(\partial T_a/\partial t)^{-1}$. Note that the energy exchange is assumed to be perfectly thermalised between subsequent time steps. This may be inaccurate for strongly driven targets, e.g. using FELs, or for the very small time steps required to adequately resolve periods of rapid temperature change such as heating.

In these calculations, the temperature and density dependence of the ionization of the target is estimated using a simple model

$$\bar{Z}_i^{\mathrm{f}}(\rho, T_e) = \Big\{\big[\bar{Z}_i^{\mathrm{f}}(T=0)\big]^4 + \big[\bar{Z}_{\mathrm{TF}}^{\mathrm{f}}(\rho, T_e)\big]^4\Big\}^{1/4}, \tag{5.22}$$

in which $\bar{Z}_i^{\mathrm{f}}(T=0) = 3$ is the mean ionization of cold aluminium, and $\bar{Z}_{\mathrm{TF}}^{\mathrm{f}}(\rho, T_e)$ is given by the well-known parametrisation of Thomas-Fermi theory [Saltzmann, 1998]. Furthermore, due to the numerical intensity of the FGR and CM models, accurate reduced approaches [Chapman et al., 2013a] have been implemented. The details of these reduced models (referred to as RCM and RFGR) are covered in appendix B.

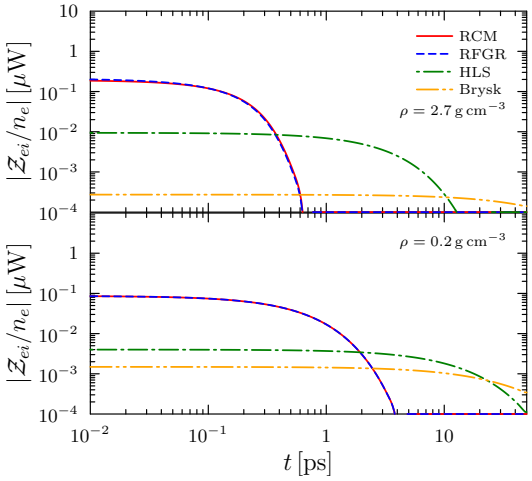

(a) Energy transfer evolution for $T_e(t_0) = 1$ eV.

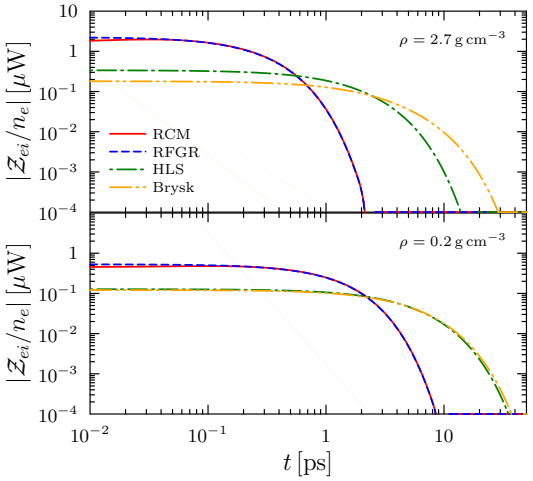

(b) Energy transfer evolution for $T_e(t_0) = 10$ eV.

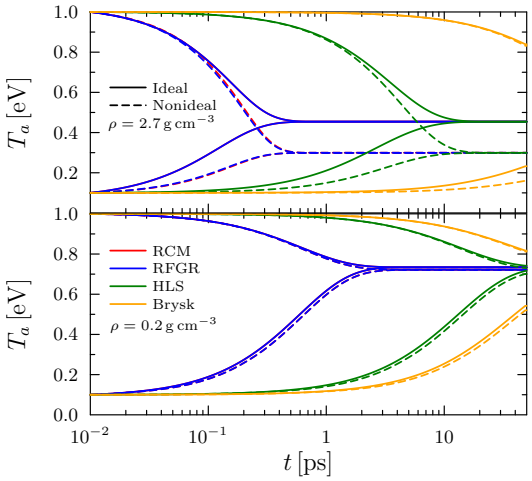

(c) Temperature evolution for $T_e(t_0) = 1$ eV.

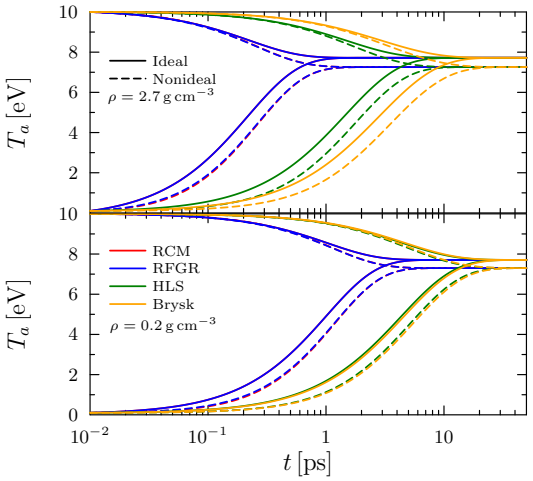

(d) Temperature evolution for $T_e(t_0) = 10$ eV.

Figure 5.4: Time evolution of temperature relaxation in foam (bottom panels) and solid (top panels) aluminium. (a,b): Energy transfer rates. (c,d): Electron and ion temperatures. In both cases, the electrons at are initially at $T_e(t_0) = 1\,\mathrm{eV}$ (left) and $T_e(t_0) = 10\,\mathrm{eV}$ (right). No energy absorption from an external source or radiation losses are considered.

5.4.1 Pure equilibration dynamics

The importance of the various components of Eqs. (5.20) and (5.21) the to relaxation dynamics can be studied with a simple test case. For this purpose, a two-component system of electrons and ions at well-defined and initially clearly separated temperatures is considered. Energy absorption and radiative losses are both neglected in this case. The initial temperature of the electrons is set at $T_e(t_0) = 1\,\mathrm{eV}$ and $T_e(t_0) = 10\,\mathrm{eV}$; these conditions are readily achievable using short-pulse laser-driven protons. In both cases, the initial temperature of the ions is set at $T_i(t_0) = 0.1\,\mathrm{eV} > T_{\mathrm{Al}}^{\mathrm{melt}}$ in order for a fluid-based description to be valid.

Of particular interest are the predictions of the different classes of the energy transfer rate, i.e. theories based on binary collisions and collective modes, and the contributions of non-ideal corrections. Fig. 5.4 shows that similar trends can be seen for all cases studied. In particular, the binary collision energy transfer rates are significantly slower, leading to longer equilibration of the system. Interestingly, no readily discernible coupled mode effect can be seen between the calculations using the RFGR and RCM models, except at extremely early times (see shaded regions in Figs. 5.4(a) and 5.4(b)) which affect neither the equilibration time nor the final equilibrium temperature.

The small coupled mode effects are most pronounced and persistent in the case of low density and large initial temperature separation as the electronic screening of the acoustic modes is largest and the frequency of the interactions decreases with decreasing density. From these results, it is reasonable to conclude that the RFGR gives a reliable estimate of the energy transfer rate over the range of conditions of interest this work. Furthermore, the Brysk model gives the least reasonable equilibration times for all cases.

The contributions of strong correlations to the partial equation of state, i.e. the ionic heat capacity, show a significant deviation from the ideal contribution in all cases. As expected, the largest effects occurs for the most strongly coupled conditions, where the increased heat capacity results in a lower final equilibrium temperature. The coupling to the electrons also feeds into the evolution of the ionic subsystem by screening the correlations; states with higher ionic heat capacity slow the cooling of the electrons, which leads to weaker screening and therefore stronger correlations. The results demonstrate that the equilibration time is strongly affected by the rate at which energy is exchanged but is largely independent of how efficiently it is thermalised. In general, it is clear that non-ideal physics is crucial to understanding the time-evolution of dense plasmas.

5.4.2 Laser-driven targets

The simple model considered thus far demonstrates that relaxation in dense plasmas is likely to be challenging to measure experimentally, and that the equilibration is expected to occur on similar time scales to typical heating mechanisms. The scenario of clearly separated initial electrons and ion temperatures is therefore rather artificial and, thus, the heating of the electrons is now also treated.

As discussed, the external energy source is assumed to be driven by a laser pulse. The power profile is taken to be of Gaussian shape

$$P_{\mathrm{laser}}(t) = P_0 \exp\left[-\ln(16)\,\frac{(t-t_{\mathrm{peak}})^2}{\Delta_t^2}\right], \tag{5.23}$$

where $P_0 \sim 1\,\mathrm{PW}$ is the peak laser power and $\Delta_t \sim 0.5\,\mathrm{ps}$ is the FWHM; these are reasonable values for modern high-power laser facilities such as Orion or Vulcan. Of course, only a small fraction of the energy of the driver is typically absorbed and, moreover, the absorption efficiency varies with the plasma conditions. Here, the absorption is assumed to

be constant $f_{\text{abs}} = 0.1$, which is consistent with simulations of short-pulse laser irradiated solids [Gibbon, 2005]. The source term in Eq. (5.20) can therefore be written as

$$\mathcal{S}_e^{\text{ext}}(t) = f_{\text{abs}} n_e(t) P_{\text{laser}}(t). \tag{5.24}$$

Finally, the power density term due to radiation losses is estimated from a simple analytic expression for Bremsstrahlung emission [Atzeni and Meyer-ter-Vehn, 2004]. Additional radiation losses via line emission are difficult to calculate, requiring solution of the rate equations for the full range of atomic configurations [Chung et al., 2005], and are beyond the scope of this work.

The results of initially cold, laser-driven calculations for low density aluminium foam are shown in Fig. 5.5. The sharp rises in the energy exchange rate and electron temperature coincides with the onset of the heating pulse (shown at the bottom of Fig. 5.5(a)). The peaks in the latter coincide with the trailing wing of the pulse, around $t = 1.5\,\text{ps}$, after which the energy exchange overtakes the heating. Once again, the relaxation rates based on binary collision approximations and collective modes give very different results whilst models within the two classes of approximation are very similar. This is not surprising for the LS and Brysk models since the plasma is rapidly heated into a non-degenerate state and the correction term in Eq. (5.5) tends to unity.

In the case of the RFGR and RCM models, a very small coupled mode effect occurs during the electron heating phase, as shown by the shaded region between the two curves in the inset of Fig. 5.5(a). This difference arises due to the screening of the ion density fluctuations by free electrons, shifting the positions of the peaks in the ion mode spectrum and increasing the damping. Nevertheless, the effect is too small to produce any discernible impact on the evolution of either the rates or temperatures.

In terms of the temperature evolution, the slower rates predicted by the LS and Brysk models allow a slightly higher maximum electron temperature to be reached, although the initial heating profile is indistinguishable from that produced by the RCM and RFGR models. On the other hand, the heating of the ions is far slower if collective mode contributions are ignored, taking over twice as long to equilibrate with the electrons.

Considering a solid density target increases the electron density of the calculations by a factor of ten, greatly accelerating the equilibration of the system and increasing the importance of electron degeneracy. This is evident in the slower energy exchange rate predicted by the Brysk model. On the other hand, the degeneracy is not high enough to affect the collective mode models since the ion temperature rapidly exceeds the Fermi energy. In contrast to the foam case, no difference between the two curves can be seen for the solid target, despite the fact that the coupled mode effect is known to increase with the electron density. This behaviour is due to the significantly smaller temperature separation resulting from the more rapid equilibration; this is an example of the importance of the coupling and feedback between the relaxation rates and the temperature evolution.

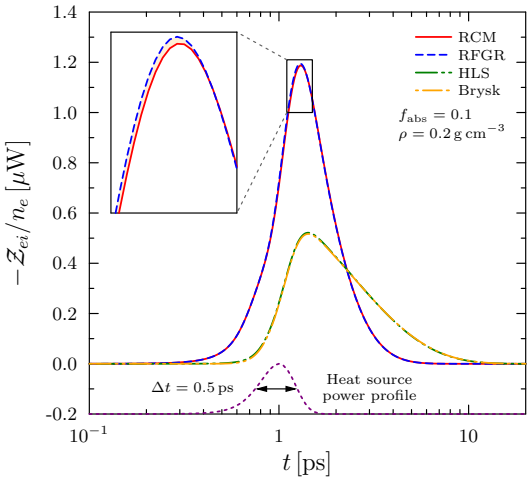

(a) Energy exchange rate for Al foam.

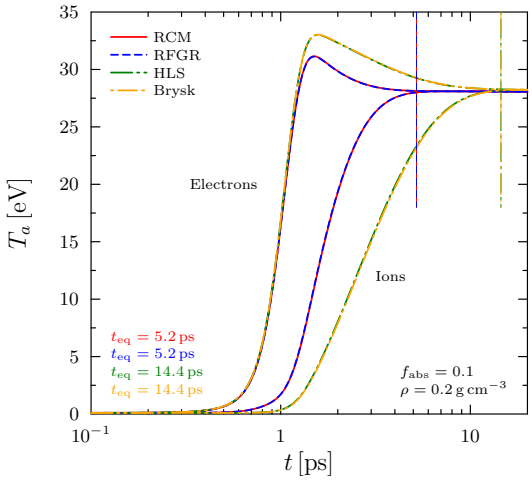

(b) Temperature relaxation for Al foam.

Figure 5.5: (a): Evolution of the electron-ion energy relaxation rates in isochorically heated aluminium foam ($\rho = 0.2\,{\rm g\,cm^{-3}}$), initially at $T_e(t_0) = T_i(t_0) = 0.1$eV. (b): Corresponding temperature relaxation. In both panels, the energy relaxation rates are calculated in the hyperbolic Landau-Spitzer (LS), Brysk, reduced Fermi golden rule (RFGR) and reduced coupled modes (RCM) approximations. The inset in panel (a) shows a small coupled mode effect can be seen near the peak of the heating pulse. In panel (b), the equilibration times for each model are shown by the colour-coded vertical lines.

In terms of the electron and ion temperatures, the solid target achieves a slightly lower peak electron temperature and a slightly higher equilibrium temperature than the foam target. As before, no significant differences between the initial heating profile of the electrons can be distinguished, although the relative difference between binary collision-based and collective mode-based energy exchange rates is larger during the cooling phase.

Due to the shorter equilibration time in the solid target, as well as the necessity of accounting for non-ideal physics in the heat capacities and relaxation rates, one may conclude that a foam target would be more conducive to making viable XRTS measurements.

5.5 Diagnosing temperature relaxation using x-ray scattering

It is straightforward to post-process the temperature relaxation calculations using the MCSS code outlined in Chapter 3 to produce a synthetic, time-dependent scattered power spectrum. However, it is not immediately clear how to maximise sensitivity of the XRTS diagnostic to both the electron and ion temperatures, e.g. using geometries conducive to collective or non-collective scattering, and, thus, a brief review of previous work to implement such techniques is warranted.

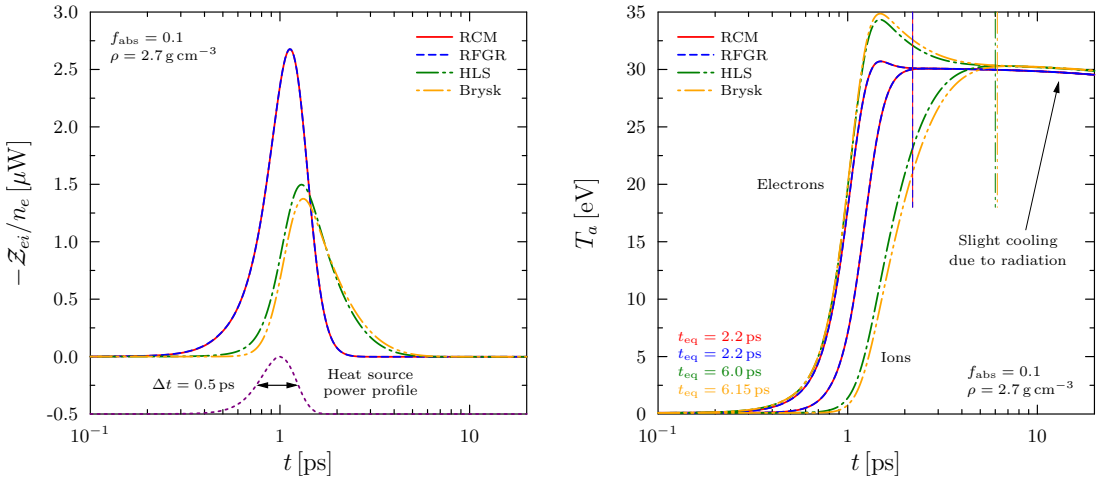

(a) Energy exchange rate for solid Al.

(b) Temperature relaxation for solid Al.

Figure 5.6: Energy relaxation rate and temperature evolution calculations for solid aluminium ($\rho = 2.7\,\mathrm{g\,cm^{-3}}$), as described in Fig. 5.5.

5.5.1 Previous attempts at relaxation measurements using scattering

In pioneering work by Froula et al. [Froula et al., 2002; 2006b; 2007], a scheme for simultaneous measurements of electron and ion temperatures using collective OTS was developed for low-density, high-temperature laser-ablated plasmas. Here, beryllium foil targets were doped with low concentrations of gold impurities and the scattered spectrum was recorded around the low-frequency (acoustic) and high-frequency (plasmon) resonances simultaneously. Electron density and temperature information obtained from fitting to the resonance position and damping of the plasmons was used in combination with similar measurements of the acoustic spectra to constrain the ionization state of the gold and the ion temperature (the beryllium and gold ions are assumed to be in equilibrium with each other). In particular, the ion temperature measurement is enabled by fitting the relative damping of the distinct acoustic modes of two species of ions.

In principle, this scheme could be applied to XRTS, enabling access to relaxation measurements within the range of densities of interest to this work. Unfortunately, this is not currently feasible due to a number of practical considerations: Firstly, spectrally-resolved x-ray measurements of the acoustic modes are extremely difficult to resolve using crystal-based spectrometers, although recent advances using seeded x-ray FELs are showing promising results. Secondly, time-resolving the scattering over sub-picosecond time scales is not currently possible, even using state-of-the-art streak cameras. Finally, the theoretical description of dynamic ion correlations on which analysis of such data would crucially rely is not yet sufficiently well-developed.

With respect to the experimental restrictions of making time-resolved measurements, a more practical approach might be to take multiple shots of properly metrologised targets

and vary the pump-probe delay in order to build up a picture of the relaxation. Indeed, time-dependent measurements of evolving WDM systems have been successfully performed [Kritcher et al., 2011a;b; Fletcher et al., 2013; 2014], albeit over far longer time scales than those presently of interest.

5.5.2 Practical considerations for XRTS measurements

A novel platform for x-ray FEL scattering on laser-driven shock-heated matter has recently been described [Gauthier et al., 2014]. This platform enables angularly- (wave number) and spectrally-resolved scattering spectra to be taken simultaneously, thus combining aspects of alternative XRTS-based proposals [Riley et al., 2000; Gregori et al., 2006b]. Similarly to the OTS-based scheme of Froula et al., the setup uses fitting of the high-frequency dynamic structure to estimate the properties of the electrons, i.e. number density and temperature. This information is subsequently used to constrain the ion temperature from the low-frequency scattering. The main difference to the scheme of Froula et al. is that here the ion mode spectrum cannot be resolved and, thus, the k-dependent elastic scattering strength is used instead.

Although utilising FEL probes is attractive for the present application due to the extremely short pulse lengths that can be produced such high-intensity x-ray sources may also significantly perturb the plasma, as discussed in chapter 4. Since the detailed dynamics of the creation and relaxation of non-equilibrium electrons distributions cannot easily be incorporated into the present model, the probe is assumed to be ideal and non-perturbative.

X-ray scattering data from foam targets with similar densities to those of interest here have previously been used [Gregori et al., 2008] using He-α emission at $E_i = 4.75\,\mathrm{keV}$ from laser-driven Ti foil. In those experiments, the scattering was viewed through $\theta = 95°$ to access the non-collective regime. Presently, the collective scattering regime is preferable as it potentially yields more simultaneous information on the plasma. The decreased total signal strength associated with small scattering angles is adequately compensated by the high brilliance of the proposed FEL probe. For the conditions predicted for the relaxation shown in Fig. 5.5, collective scattering can be accessed for $E_i = 3\,\mathrm{keV}$ and $\theta = 10°$.

Finally, one must consider the restrictions associated with the widths of the spectral features. Using the probe energy and scattering angle discussed, the plasmon shift is expected to be near $\hbar\omega_{\mathrm{pl}}(k) \sim 10\,\mathrm{eV}$ with widths close to $\Delta_{\mathrm{pl}}(k) \sim 5\,\mathrm{eV}$. Thus, the x-ray source function $\Sigma(\omega)$ (including the width of the FEL source, resolution of the detector and any source broadening effect) must be around 1 eV to clearly resolve the spectral features.

5.5.3 Spectrally resolved inelastic scattering

The time evolution of the spectrally resolved inelastic scattering corresponding to the relaxation of heated aluminium foam are shown in Fig. 5.7. The temporal range shown corresponds to the equilibration time for the RCM energy relaxation model. For the

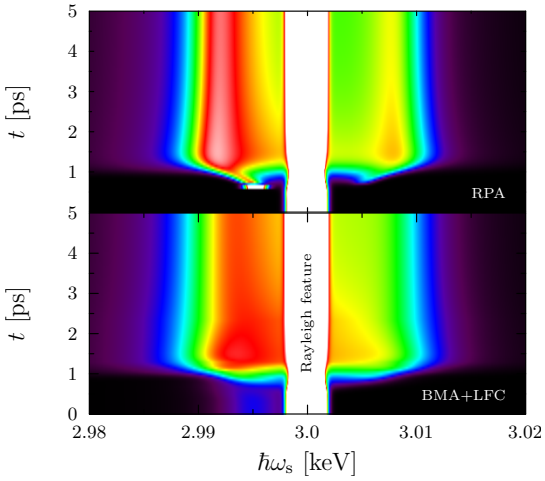

(a) XRTS evolution for RCM relaxation.

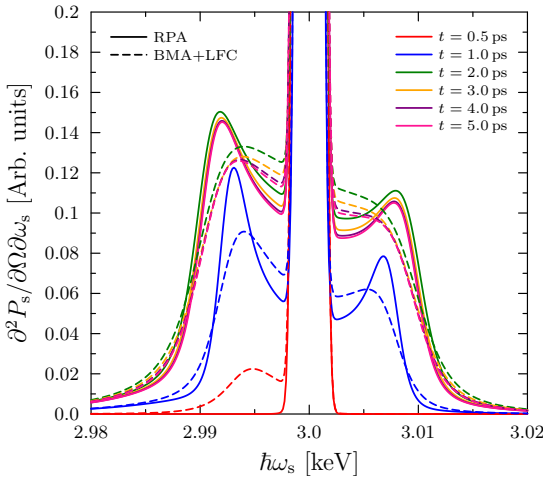

(b) Lineouts for RCM relaxation.

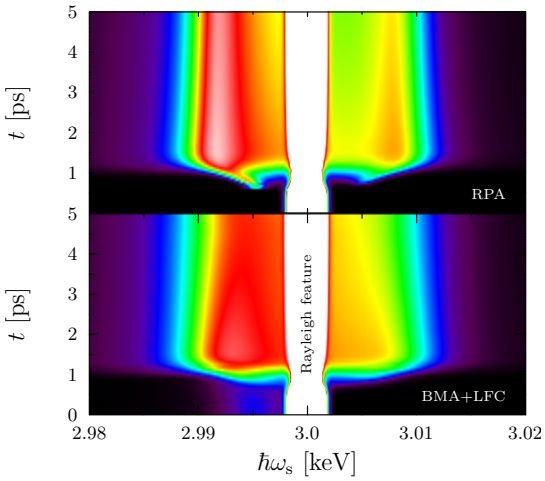

(c) XRTS evolution for LS relaxation

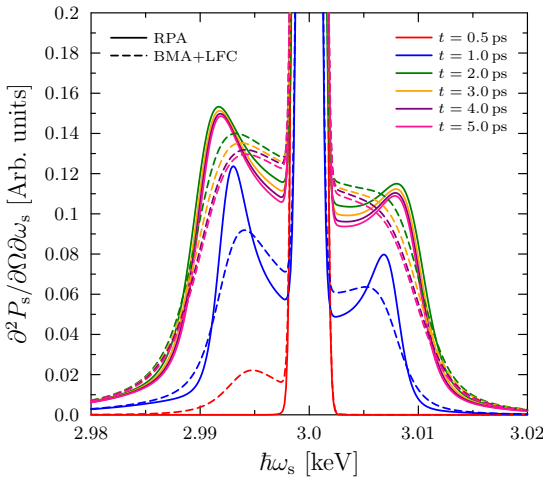

(d) Lineouts for LS relaxation.

Figure 5.7: Calculations of the time-dependent XRTS spectra and lineouts for the evolution of aluminium foam predicted by electron-ion relaxation rates according to the RCM model, panels (a) and (b), and the LS approach, panels (c) and (d), models. In each case, the free-free contribution to the total inelastic scattering are calculated within a weakly coupled approach (RPA) and including screened electron-ion collisions and local field corrections (BMA+LFC). In panels (a) and (c), the vertical white strip corresponds to the elastic scattering (Rayleigh feature), which is c.a. 20 times more intense than the plasmons on this scale and is therefore saturated. The bound-free inelastic scattering is treated via the impulse approximation.

spectrally resolved spectra, the inelastic scattering resulting from weakly coupled RPA calculations is compared to the BMA model Eqs. (3.73) and (3.74) to account for electron-ion collisions and further includes static local field corrections via Eq. (3.71). The impulse approximation Eq. (3.80) is used to describe the bound-free transitions.

An immediate and clear feature of the inelastic scattering spectra is the importance of collisions on the shape of the plasmons. Most notably, the BMA yields plasmons which

are significantly broadened and slightly downshifted relative to RPA results. Moreover, at very early times the plasmon is undamped in RPA (no Landau damping), whereas collisional damping yields a clear (although low amplitude) downshifted peak (Figs. 5.7(b) and 5.7(d)). The electron temperature around this time is sufficiently low that no upshifted peak can be seen on this scale. For these calculations, the electron-ion collision frequency is based on an average atom approach according to Eq. (5.22).

During the heating phase, the increasing temperature and ionization (electron density) of the target can be seen from the rapidly increasing plasmon dispersion and damping and via the detailed balance between the downshifted and upshifted peaks. The spectra relating to the RCM and LS relaxation calculations are very similar during this phase, reflecting the similar heating profiles. Following the peak of the laser pulse the two sets of spectra begin to subtly diverge as the LS model yields a higher peak temperature and longer equilibration time. In particular, the difference in the equilibration times is evident from the observation that the plasmon shape effectively ceases to evolve beyond 3 ps in the RCM case, whereas a steady evolution toward the final equilibrium state can be seen in the LS case. Nevertheless, the differences are small and are not likely to be differentiable from experimental data. These results further highlight the insensitivity of inelastic scattering to the ion temperature since the RCM and LS models predict very different ion heating.

5.5.4 Angularly resolved elastic scattering

The sensitivity of the XRTS diagnostic to the ion temperature required to make an equilibration measurement is based on the evolution of the angularly-resolved elastic scattering, primarily via the static structure of the ions. Measurements of the ion heating are expected to be manifest as a clear broadening of the peaks in the SSF. Moreover, the electron temperature may also be measured from this feature by the variation of screening at small k, further constraining estimates from fitting the inelastic spectra.

Presently, only the mean ionization state of the target is given by Eq. (5.22). This presents a problem for calculation of the Rayleigh amplitude $W_{\mathrm{R}}(k)$ in the MCSS code since the precise partitioning of different charge states can affect correlations between ions, and the strengths of contributions due to the bound electrons and screening cloud. One could determine a realistic charge state distribution for the plasma by solving a degeneracy-corrected Saha-Boltzmann equation for each time step. However, since more significant uncertainties in the precise shape of the Rayleigh feature are expected to arise due to, e.g., the ion-ion potential and screening cloud, such details are neglected here for simplicity.

Instead, a straightforward mechanism of coupling the average atom-like relaxation calculations to Eq. (3.27) is given by considering contributions from ions with integer charge states adjacent to the mean value. This is similar to the approach used in the well-known XRS modelling code [Gregori et al., 2003]. The closest integer charge states,

$$Z_i^{\mathrm{f0}} = \mathrm{floor}(\bar{Z}_i^{\mathrm{f}}), \quad Z_i^{\mathrm{f1}} = Z_i^{\mathrm{f0}} + 1 \tag{5.25}$$

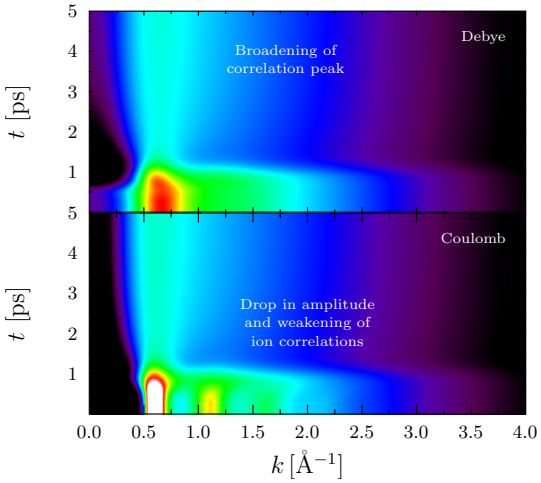

(a) XRTS spectrum for RCM relaxation.

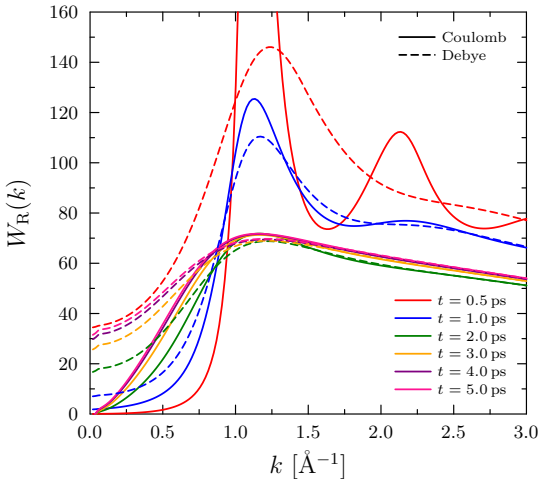

(b) Rayleigh feature for RCM relaxation.

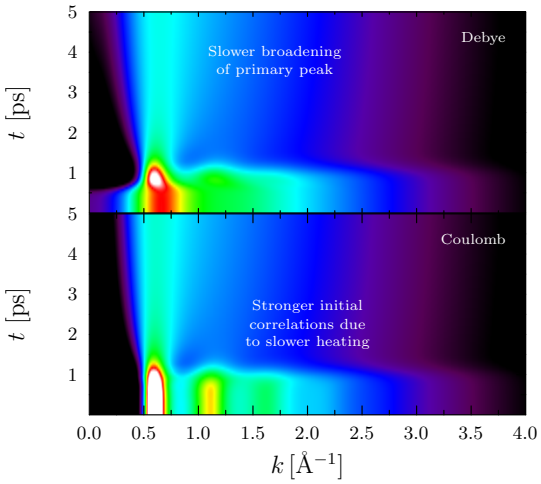

(c) XRTS spectrum for LS relaxation

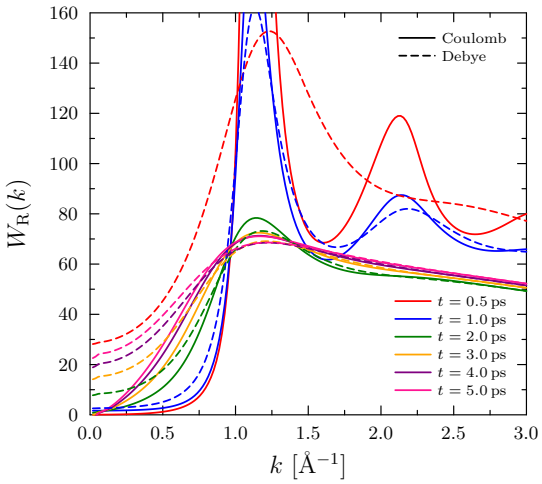

(d) Rayleigh feature for LS relaxation.

Figure 5.8: Calculations of the time-dependent elastic Rayleigh scattering for the evolution of aluminium foam predicted by RCM, panels (a) and (b), and LS, panels (c) and (d), energy relaxation models. Weakly screened systems are considered using a Coulomb potential, whereas the importance of screening is demonstrated using a Debye potential. The initial correlations are sufficiently strong that the primary correlation peak is significantly larger than the scattering throughout the relaxation phase.

are used, which are treated as distinct species within the multicomponent formalism of the DSF. The number densities of these states are then given by

$$n_i^0 = (1 - \delta Z)\bar{n}_i, \quad n_i^1 = \delta Z \bar{n}_i \tag{5.26}$$

in order to fulfil quasi-neutrality, i.e. $n_e = Z_i^{\mathrm{f0}} n_i^0 + Z_i^{\mathrm{f1}} n_i^1 = \bar{Z}_i^{\mathrm{f}} \bar{n}_i$, where $\delta Z = \bar{Z}_i^{\mathrm{f}} - Z_i^{\mathrm{f0}}$.

For the angularly resolved scattering, the electron-ion interaction in the screening cloud is taken to be a Coulomb potential screened by the FWS dielectric function, Eqs. (3.33) and

(3.35). Since the dependence of the short-range correlation part of the ion-ion interactions on the density and temperature is not well understood, here only bare Coulomb and Debye potentials are considered in the HNC approximation. The importance of screening is clearly shown in Fig. 5.8 for both energy transfer models. The Thomas-Fermi screening of the initially cold state leads to filling of the correlation hole present in a weakly-screened Coulomb-like system.

During the heating phase, the screening length in the Debye system decreases in the transition from degenerate to non-degenerate states, leading to the formation of a correlation hole. This gradually refills following the laser pulse as the electrons cool and the ions are heated. The difference between the RCM and LS models is also clearly evident during this phase as the structure remains significantly more strongly coupled for the latter (see Figs. 5.8(b) and 5.8(d)).

From these results, the ion temperature can be determined from the changing strength of the ion correlations. Moreover, such measurements may also serve to distinguish between different energy transfer models. Note that an important deficiency of these conclusions is that the ion-ion interaction is likely to be stronger than the Debye potential, e.g. similar to the SRR or CSD potentials discussed in Section 3.5.3. Nevertheless, the ion temperature can still be determined if the ion interactions are weakly screened.

Chapter 6

Spatial inhomogeneity effects for large-scale plasmas

Thus far, the (time-dependent) plasma conditions have been assumed to be uniform throughout the sample under study. Due to limitations on the energy of laser-driven x-ray sources that have, until recently, been available, the volume of material which can be studied using XRTS has been restricted to a few hundred cubic microns. The plasma can then often be treated as homogeneous. With the advent of megajoule-energy laser facilities, such as the National Ignition Facility, significantly brighter x-rays sources capable of probing large (millimetre-scale) targets can be produced. Spatial gradients in locally equilibrium conditions may therefore be present throughout the sampled volume.

In this Chapter, the detailed modelling of a series of recent experiments performed at the NIF is presented. In these experiments, a series of convergent shocks are driven by hohlraum radiation into millimetre-scale plastic spheres, creating pressures exceeding 1 Gbar in the core region upon shock stagnation. The passage of such strong shocks leads to highly inhomogeneous plasma conditions throughout the volume illuminated by the x-ray probe. In addition to complicating the spatially integrated signal, the gradients in temperature and density lead to a non-uniform opacity profile. The transport of the x-ray probe through this dense, partially opaque matter is also expected to influence the shape of the spectrum. The importance of plasma gradients to the interpretation of the expected spectrum is quantified by statistical analysis.

6.1 Experimental platform for EOS measurements at the NIF

The development of an experimental platform for the NIF to study the EOS of polyα-methylstyrene plastic (CH) at ultra-high pressures along the principal Hugoniot has recently been presented by Kritcher et al. [Kritcher et al., 2014]. A schematic representation of the experimental configuration is shown in Fig. 6.1(a). The experiments use a platform based on the well-characterised 1D convergent ablator (1D ConA) design developed during the National Ignition Campaign (NIC). The hohlraum is driven by 184 beams in 46 quads with a total energy of 1.3 MJ at a wavelength of 351 nm, yielding radiation temperatures of up to 280 eV. The resulting radiation drive launches a series of four shocks which coalesce at a radius of 750 μm to produce a single strong converging shock wave. The remaining 8 beams are directed to a 5 μm thick Zn backlighter foil mounted 7.5 mm from the centre of the plastic sphere, producing a high-energy source of He-α radiation peaked around 9 keV (see example spectrum in Fig. 6.1(b)). The divergence of the x-ray source illuminating the target is primarily controlled by the large backlighter stand off, and is further collimated by a 200 μm tall slit in the hohlraum wall (2.4 mm wide in the equatorial plane).

The implosions are diagnosed using streaked x-ray radiography, emission spectroscopy, penumbral imaging and also scattering of the backlighter probe. The radiography is used to determine shock speed, mass density and opacity profiles in the target [Swift et al., 2012], whereas the size and temperature of the central hot spot created upon stagnation are obtained by penumbral imaging [Bachmann et al., 2014] and self emission [Kraus et al., 2014], respectively. The XRTS measurements are made using a gated, high-efficiency, mono-angle crystal spectrometer [Döppner et al., 2014] under a small range of scattering angles $\theta = 84.5° \pm 6.0°$. These independent measurements will provide the complementary data needed to self-consistently constrain the uncertainties of the experiment. The work presented in this chapter is focussed on the development of the theoretical capability required to robustly analyse the XRTS data.

6.1.1 Expected properties of scattering measurements

The experiments have been modelled by A. Kritcher using experimentally-informed radiation drive models in the NIC design code HYDRA [Marinak et al., 1998; 2001]. The simulations suggest that pressures in excess of 1 Gbar are reached upon shock stagnation, as shown by the cell trajectories plotted in Fig. 6.2(a). The XRTS measurements are made after shock stagnation, t_{stag} (all times quoted in this chapter are relative to the stagnation time), at which the conditions throughout the target range between $0.1-40\,\mathrm{g\,cm^{-3}}$ and $10-2000\,\mathrm{eV}$, respectively. The wave number of density fluctuations probed by the x-rays is $k \approx 2k_i \sin(\theta/2) = 5.9-6.4\,\mathrm{\AA}^{-1}$, yielding scattering parameters in the range $\alpha \approx 0.02-0.5$. Accordingly, the scattering is expected to be non-collective throughout the whole target, directly sampling the electron distribution from the width of the inelastic scattering feature and, thus, enabling measurement of the temperature of the target.

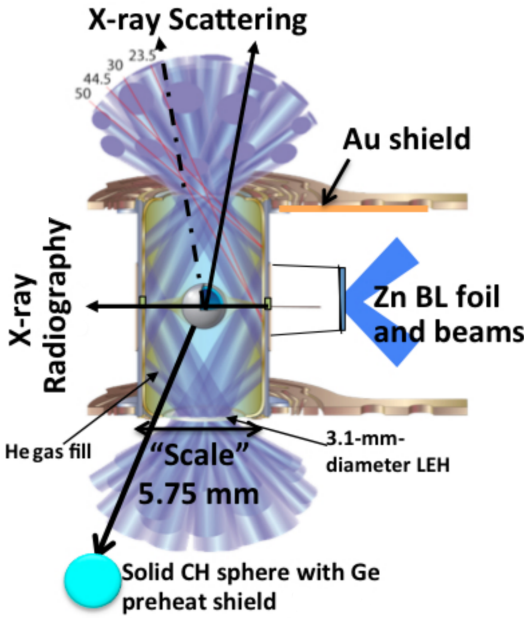

(a) NIF hohlraum for Gbar EOS experiments.

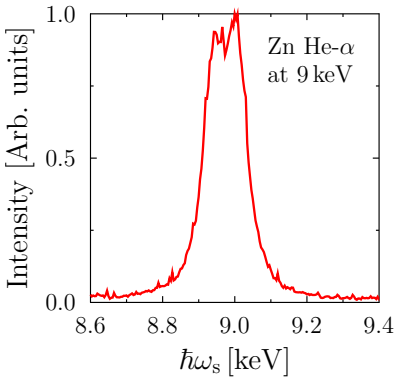

(b) Zn He-α spectrum.

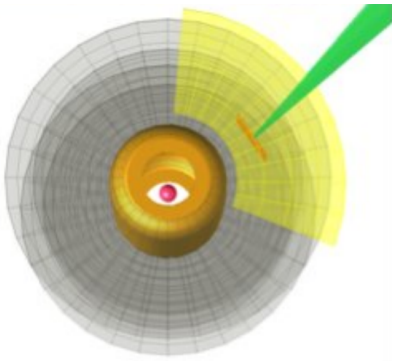

(c) CAD rendering of the view of the target from the detector.

Figure 6.1: (a): Schematic representation of the hohlraum configuration showing the relative positions of the radiography and XRTS diagnostics with respect to the x-ray source. (b): Example of the 9 keV Zn He-α source used to probe the imploding sphere. (c): VISRAD rendering of the experimental platform from the perspective of the MACS detector. The CH target (pink sphere) is visible through the upper laser entrance hole (LEH) of the hohlraum. Elements of this figure have been reproduced with permission from High Energy Density Physics © 2014 Elsevier Publishing and Journal of Physics: Conference Series © 2014 IoP Publishing.

In the previous chapter, it was shown that electron-ion equilibration in dense, highly ionized and strongly coupled plasmas is extremely rapid, occurring on time scales $\lesssim 1$ ps. Relative to the hydrodynamic evolution of the target, which generally occurs on time scales many order orders of magnitude slower, the plasma can therefore be treated in local thermodynamic equilibrium. Nevertheless, the bulk evolution may still be fast enough for significant spatial gradients to be present on scale lengths of $10-100\,\mu$m. Indeed, Fig. 6.2(b) shows several distinct regions in the target which are produced by the passage of the shock. Moreover, the strongly inhomogeneous state persists throughout the duration of backlighter probe and, thus, must be accounted for in modelling and analysis of XRTS measurements.

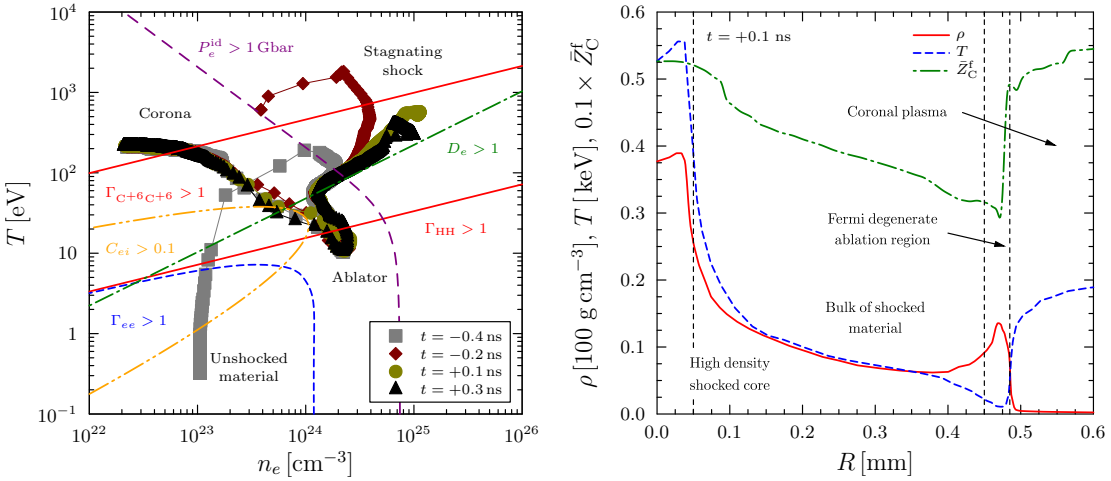

(a) Cell trajectories on the $n-T$ plane.

(b) Radial profiles of plasma parameters.

Figure 6.2: Output from 1D HYDRA simulations courtesy of A. Kritcher. The cell trajectories (a) for several times before and after shock stagnation show the plasma is expected to mostly be in the non-degenerate regime except in the ablator region at the time of measurement. Radial profiles (b) of the temperature, mass density and mean ionization vary strongly throughout the target due to convergence of the shocks.

The simulations suggest that a hot, high-density core of radius $\lesssim 50\,\mu$m is formed at the centre of the imploding target following shock stagnation. This region reaches the extreme pressures $\sim 1\,$Gbar of interest to the experiment. This core is surrounded by a larger bulk of shocked plasma at 8-fold compression and around $100-200\,$eV. In the ablator shell, the density profile peak exceeds 12-fold compression whilst remaining at low ($\sim$10 eV) temperature, and is therefore strongly coupled and partially degenerate. Further outward, the target is enveloped by a quasi-isothermally expanding corona of high-temperature, low-density blow-off plasma. As shown by Fig. 6.1(c) the detector views the a large portion of the hohlraum interior through the upper laser entrance hole of the hohlraum, such that the total XRTS signal observed must fully account for spatial inhomogeneity of the target.

Finally, the blurring due to the finite time resolution of the detector should also be included in a rigorous simulation of the expected spectrum. This is currently limited by the micro-channel plate response of the applied gated x-ray detector to 100 ps. On this time scale the rebounding shock front moves roughly $20\,\mu$m, expanding the volume of the hot high-density core. However, the conditions in the surrounding bulk of shocked plasma, from which the majority of the XRTS signal is expected to originate, do not significantly evolve. The temporal blurring of the signal is therefore negligible.

6.2 Description of XRTS from inhomogeneous plasmas

Scattering from inhomogeneous plasmas has previously been considered in high-temperature laser-produced plasmas probed with optical [Wang et al., 2005; Glenzer et al., 1999a] and

UV [La Fontaine et al., 1993] lasers, optically-pumped XUV sources [Baldis et al., 2002], and WDM probed with soft x-ray free electron lasers [Thiele et al., 2010; Sperling et al., 2013] and laser-driven hard x-ray sources [Falk et al., 2013]. In all cases, significant effects on the shape of the excitation spectrum for both ion acoustic and plasmon modes have been shown to result from gradients in the plasma conditions.

Primarily, the effect of gradients is due to different regions of the target having different scattering powers. This effect becomes further complicated if the sampled volume is large since widely separated regions scatter the probe toward the detector with different scattering angles; this is known as *source divergence* or *k-blurring* [Glenzer et al., 2007]. Finally, for high-density targets the opacity may be sufficiently high that the probe is significantly attenuated as it propagates [Chapman et al., 2014]. This means that regions of the target corresponding to longer total transit path lengths, i.e. the total distance the probe must travel in order to penetrate the target to the point of interest and subsequently leave the target in the direction of the detector, experience a reduced probe intensity and therefore contribute less to the total scattered signal. Furthermore, the spectral profile of the probe may also change as it propagates if the spectral variation of the opacity over the frequency range of the detector is significant.

It is straightforward to generalise the form of the scattered power spectrum at the core of the MCSS code Eqs. (1.33 - 1.35) to accommodate the additional effects that must be considered for inhomogeneous targets

$$\frac{\partial^2 P_\mathrm{s}}{\partial\Omega\partial\omega_\mathrm{s}} \propto \int_{\mathcal{V}} \mathrm{d}\mathbf{R}\, \bar{n}_i(\mathbf{R}) \left\{ I_\mathrm{i}(\omega,\mathbf{R}) * \int_{\theta_\mathrm{min}}^{\theta_\mathrm{max}} \mathrm{d}\theta\, F(\theta)\, \frac{\partial^2\sigma(\omega,\theta;\mathbf{R})}{\partial\Omega\partial\omega_\mathrm{s}} \right\}, \tag{6.1}$$

$$\frac{\partial^2\sigma(\omega,\theta;\mathbf{R})}{\partial\Omega\partial\omega_\mathrm{s}} = \sigma_\mathrm{T} \left(\frac{\omega_\mathrm{s}}{\omega_\mathrm{i}}\right)^2 \Big[W_\mathrm{R}(k(\theta);\mathbf{R})\delta(\omega) + W_\mathrm{C}(\mathbf{k}(\theta),\omega;\mathbf{R}) \Big], \tag{6.2}$$

where the Rayleigh and Compton contributions are as discussed in Chapter 3. In Eq. (6.1), the integration over the macroscopic spatial coordinate $\mathbf{R}$ accounts for the variation of the plasma conditions throughout the volume sampled by the detector $\mathcal{V}$. In particular, the mean ion density profile $\bar{n}_i(\mathbf{R})$ and incident intensity distribution of the probe $I_\mathrm{i}(\omega,\mathbf{R}) = I_\mathrm{i}(\mathbf{R})\,\Sigma(\omega;\mathbf{R})$ must be specifically included. In the latter, the spatial profile of the emission from the backlighter is given by $I_\mathrm{i}(\mathbf{R})$, whereas the spectral shape of the probe profile throughout the target is represented by the spatially varying source function $\Sigma(\omega;\mathbf{R})$. Finally, the integration over the range of scattering angles is performed to account for k-blurring. Each angle is weighted according to the angular distribution $F(\theta)$, which can be determined using ray tracing software.

6.3 Coupling to radiation-hydrodynamics simulations

By directly post-processing the HYDRA simulations of the target evolution with the MCSS code, it is possible to produce high-fidelity predictions of the XRTS signal expected from

these experiments. In particular, the spatial gradients may be rigorously incorporated instead of relying on parametrisations of the plasma profiles. The model developed in this section is referred to as VIXEN: Volume-Integrated X-ray scattering for Experiments with Non-uniform plasmas [Chapman et al., 2014].

For the target used in the experiment under consideration a composition of CH plasma in thermal equilibrium is assumed, with electrons and equal number densities of hydrogen and carbon ions. The Ge doping of the preheat shielding layer (1% by number density) is not expected to significantly contribute and is therefore neglected. The hydrogen is assumed to be fully ionized, i.e. $Z_{\mathrm{H}}^{\mathrm{f}} = 1$, whereas the mean carbon charge state is $\bar{Z}_{\mathrm{C}}^{\mathrm{f}} = 2\bar{Z}_i^{\mathrm{f}} - 1$. Here, $\bar{Z}_i^{\mathrm{f}}$ is the mean ionization of CH as given by the OPAL opacity tables used in HYDRA [Rogers et al., 1996; Iglesias and Rogers, 1996]. In order to couple the output of HYDRA to the XRTS calculations, the mean carbon ionization is split into adjacent integer charge states, as discussed in Section 5.5.4.

6.3.1 Radial profile of dynamic cross section

From the trajectories shown in Fig. 6.2(a) the target generally remains in a weakly coupled ($\Gamma_{ee} \ll 1$), near collisionless ($C_{ei} = \nu_{ei}(0)/\omega_{\mathrm{pe}} < 0.1$) state through the entire volume following shock stagnation. The free electron response is therefore expected to be well-described in RPA. Furthermore, the shape of the inelastic contribution due to bound electrons is only weakly dependent on the plasma conditions via the screening length, which determines the continuum lowering of the K- and L-shell edges. Here, the large k probed makes the impulse approximation reasonable [Mattern and Seidler, 2013] and, thus, the description of the total inelastic scattering is expected to be robust. The sensitivity of the inelastic scattering to model uncertainties is demonstrated in Fig. 6.3(a) for the main regions of the target identified in Fig. 6.2(b).

For the states of interest, the hydrogen ions are weakly coupled whereas the carbon ions are strongly coupled ($\Gamma_{\mathrm{CC}} \gtrsim 1$) due to the high density and moderate ionization. In general, the different correlations between ions of different species and charge state is a potentially significant uncertainty in the description of the elastic scattering strength. This is an important consideration for the determination of the mean ionization from experimental XRTS data since the latter principally relies on the frequency-integrated ratio of the elastic and inelastic signals. Although rigorous comparison of the static structure factors to ab initio simulations is not feasible for such highly-compressed, high-temperature states, multi-component HNC calculations are expected to be robust. Moreover, probing at large k again reduces the model-based uncertainty since the correlations rapidly decay and screening primarily influences the small k behaviour (see Fig. 6.3(b)).

The total dynamic cross section is shown as a function of scattered energy and radial position in Fig. 6.4(a). As previously mentioned, the peak (coloured white) corresponding to the strongest contribution occurs in the degenerate, low-temperature material in the ablator region. Significant contributions to the cross section also come from the bulk of

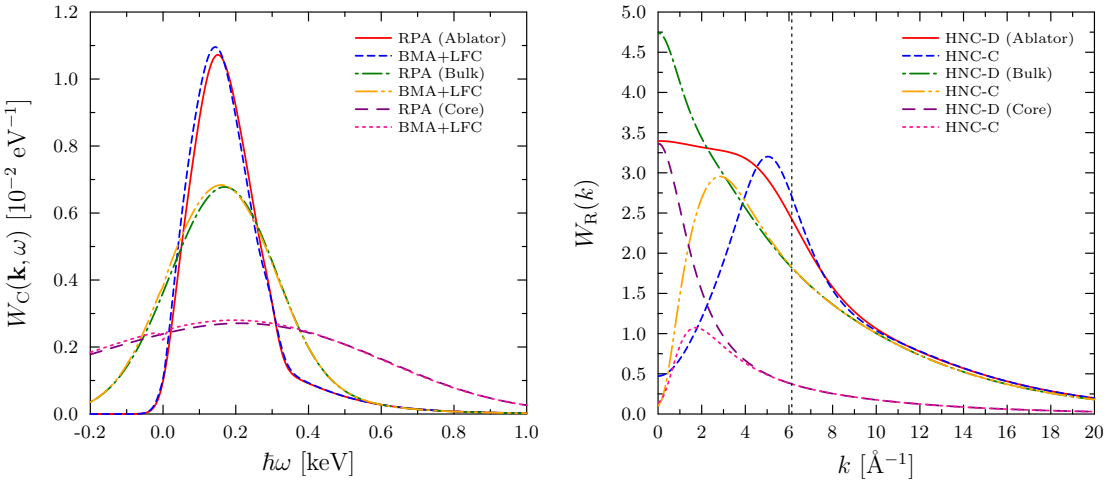

(a) Inelastic Compton scattering terms.

(b) Elastic Rayleigh scattering terms.

Figure 6.3: Comparison of different models for the total inelastic Compton scattering profiles (a) and elastic Rayleigh scattering amplitudes (b) in each of the three distinct regions of the dense part of the target at $t = +0.1$ ns. In panel (a), the weakly coupled (RPA) free electron response is compared to the extended Born-Mermin form to account for electron-ion collisions and static correlations beyond RPA. The bound-free transitions are taken in impulse approximation, without continuum lowering. In panel (b), the partial SSFs are calculated within the HNC scheme, with both Coulomb and Debye-like ion-ion interactions. The wave number probed in the experiment is shown by the vertical dashed line.

the plasma at smaller radii beyond the shocked core. This region is sufficiently hot for the electrons to be non-degenerate and, thus, the scattering is more strongly temperature-sensitive. Note that the scattering from the core is only a small contribution due to thermal broadening despite its high density-weighting. The contribution from the coronal plasma is negligible as it is both hot and diffuse.

Lineouts from Fig. 6.4(a) representative of the four important regions of the target (see Fig. 6.2(b)) are shown in Fig. 6.4(b). Here, the spectral shape of the x-ray source, which controls the shape of the elastic feature and broadens the inelastic feature, is approximated using a fit to the Zn He-α emission spectrum (Fig. 6.1(b)). Clear differences in the total scattering signal from each region can be seen. The stagnation of the shock in the core ($r \lesssim 0.05$ mm) yields high densities and temperatures and near full ionization, resulting in a broad Compton feature due mostly to scattering from free electrons. The strong Rayleigh signal from the core is attributable to the large scale length of the screening cloud around the near-fully ionized carbon ions.

In the bulk of the shocked material surrounding the compressed core ($r \sim 0.05$–0.45 mm) the steady decay of the temperature profile is reflected by the significantly less broadened Compton peak. Moreover, for much of the bulk region the K-shell of the carbon remains fully bound, leading to a small red-shifted tail on the Compton peak due to bound-free transitions and also a strong enhancement of the Rayleigh scattering.

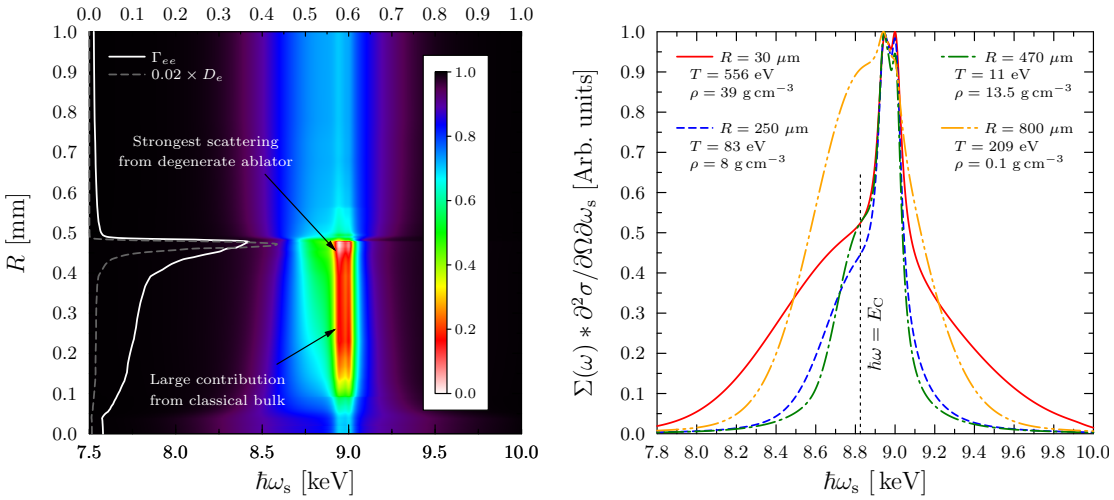

(a) Spectrally and radially resolved scattering.

(b) Lineouts from different regions.

Figure 6.4: Intensity of the dynamic cross section Eq. (6.2) as a function of scattered energy and radius at $t = +0.1$ ns (a), and lineouts from the four distinct regions of the target (b). In both panels, the cross section has been convolved with a fitted lineshape representing the x-ray source function. In panel (a), the scale on the upper x-axis refers to the coupling and degeneracy parameters, which are overplotted. In panel (b), all curves are normalised to the Rayleigh amplitude for each region. The vertical line marks the Compton energy $E_C = \hbar^2 k^2 / 2m_e \approx 190$ eV.

In contrast, the degenerate ablator region ($r \sim 0.47\,\mathrm{mm}$) yields a Compton feature whose shape is more sensitive to the free electron density rather than the temperature, reflecting the transition from Maxwell-Boltzmann to Fermi-Dirac statistics. Moreover, in addition to a pronounced K-shell bound-free feature, a significant contribution due to scattering from bound L-shell states is also present around the Compton energy, E_C. Relative to the bulk of the plasma, the elastic scattering intensity of the ablator material decreases since there are fewer free electrons screening the ions and also due to the shorter screening length of the degenerate system.

Lastly, the shape of the spectrum from the hot, diffuse coronal blow-off plasma ($r \gtrsim 0.5\,\mathrm{mm}$) shows a strong temperature dependent Compton peak, dominated by free-free scattering, as expected. Conversely to the core region, here the total elastic contribution is significantly weaker since the screening cloud contribution falls off with the exponential decay of the density profile.

6.3.2 X-ray attenuation

In addition to the dynamic x-ray scattering cross section, the density and intensity profiles also contribute to the spatial dependence of the scattered power spectrum Eq. (6.1). In particular, the spatial variation of the intensity $I_i(\omega, \mathbf{R})$ accounts for both the source profile and also the dependence of the plasma opacity on the temperature and density profiles. Thus, the photon flux at a given point in the target is affected by the transport of the

x-rays. Such considerations have recently been considered by Golovkin et al., in which XRTS calculations were integrated into the multi-dimensional collisional-radiative spectral analysis code SPECT3D [Golovkin et al., 2013].

In the experiment under consideration in this chapter, the large stand off of the x-ray source (in addition to the collimation provided by the slit in the hohlraum wall) limits the illumination of the imploding target to a weakly divergent elliptical cone characterised by half-angles of $\theta_{1/2} \lesssim 5^\circ$ in the collimated dimension and $\theta_{1/2} \lesssim 10^\circ$ in the equatorial plane. In the context of calculating the radiation transport, it is reasonable to assume parallel incident and scattered x-rays for all points in the scattering volume. Note that this does not necessarily mean that a single uniform scattering angle is appropriate for the XRTS calculations, however.

Following shock stagnation the opacity predicted by the OPAL model for 9 keV photons is around $\kappa \approx 0.8\,\mathrm{cm^2\,g^{-1}}$ in the hot, high-density core region, rapidly rising to between $1.7-3.0\,\mathrm{cm^2\,g^{-1}}$ in the bulk plasma. The opacity profile also varies over the spectral range of the scattered signal, showing a uniform change of around $\pm 15\%$ relative to that of the probe energy for all radii. A single spectral channel centred on 9 keV is therefore likely to be adequate for the scope of this investigation, although considering multi-channel opacity effects would be an important part of future development of the current model.

Restricting the opacity to a single frequency also serves to greatly simplify the VIXEN model. If the source spectrum does not attenuate at different rates in frequency space, the shape does not need to be modified as it propagates through the target. The convolution of the source spectrum and dynamic cross section therefore needs to be applied once, rather than at each point in accordance with the local source profile. Thus, $I_\mathrm{i}(\omega, \mathbf{R})$ can be decomposed according to

$$I_\mathrm{i}(\omega, \mathbf{R}) = I_\mathrm{i}\, \Sigma(\omega)\, \mathcal{P}(\mathbf{R})\, \mathcal{A}(\mathbf{R}), \tag{6.3}$$

where I_i is the peak incident intensity and $\Sigma(\omega)$ and $\mathcal{P}(\mathbf{R})$ represent the spectral and spatial profiles of the emission from the backlighter foil, respectively. The last term $\mathcal{A}(\mathbf{R})$ represents the weight of a given point in the target due to the attenuation of both the incident and scattered photons, as seen by the detector.

Due to the spherical symmetry of the simulations it is convenient to rotate into a frame of reference orthogonal to the scattering plane, which is taken to be the x-y plane. In this coordinate system, the calculation of the integrand of Eq. (6.1) over the full 3D volume of the simulation may be constructed tomographically, i.e. by iterating 2D calculations in the scattering plane over z. Combining Eqs. (6.1 - 6.3) the total scattered power is

$$\begin{aligned}\frac{\partial^2 P_\mathrm{s}^\mathrm{3D}}{\partial\Omega\partial\omega_\mathrm{s}} \propto \sigma_\mathrm{T} I_\mathrm{i} \int_{-R_\mathrm{sim}}^{R_\mathrm{sim}} \mathrm{d}z \int_{-R_\mathrm{sim}}^{R_\mathrm{sim}} \mathrm{d}y \int_{-R_\mathrm{sim}}^{R_\mathrm{sim}} \mathrm{d}x\, \mathcal{W}(x,y,z) \\ \times \Big[\mathcal{S}_\mathrm{R}(\omega; R(x,y,z)) + \mathcal{S}_\mathrm{C}(\omega; R(x,y,z))\Big],\end{aligned} \tag{6.4}$$

where $R(x,y,z) = (x^2+y^2+z^2)^{1/2}$. In Eq. (6.4), $R_{\mathrm{sim}} = 1\,\mathrm{mm}$ is the radius of the outermost cell in the HYDRA simulation considered. It is convenient to define elastic and inelastic scattering contributions

$$\mathcal{S}_{\mathrm{R}}(\omega) = \Sigma(\omega) \int_{\theta_{\min}}^{\theta_{\max}} \mathrm{d}\theta\, F(\theta)\, W_{\mathrm{R}}(k(\theta))\,, \tag{6.5}$$

$$\mathcal{S}_{\mathrm{C}}(\omega) = \Sigma(\omega) * \left[\left(\frac{\omega_{\mathrm{s}}}{\omega_{\mathrm{i}}}\right)^2 \int_{\theta_{\min}}^{\theta_{\max}} \mathrm{d}\theta\, F(\theta)\, W_{\mathrm{C}}(\mathbf{k}(\theta),\omega) \right], \tag{6.6}$$

which include the angular averaging, convolution with the x-ray source spectrum and the momentum change factor $(\omega_{\mathrm{s}}/\omega_{\mathrm{i}})^2$.

The total weight of the scattering signal from a point in the target is made up of contributions from the density, spatial profile of the x-ray source and attenuation factor

$$\mathcal{W}(x,y,z) = \rho(R(x,y,z))\, \mathcal{P}(x,z)\, \mathcal{A}(x,y,z). \tag{6.7}$$

The edges of the cube-shaped integration volume are cut off by setting $\mathcal{W}(x,y,z) = 0$ for $R(x,y,z) > R_{\mathrm{sim}}$. Note that in this geometry the source profile does not depend on y since it represents the projection of the backlighter emission profile onto the plane perpendicular to the incident x-rays. In the present case, one may expect a rotated and elongated shape with relatively sharp edges due to being driven by elliptical, super-Gaussian adjacent spots. On the other hand, at the time of measurement the entire sphere is illuminated through the slit in the hohlraum wall, such that $\mathcal{P}(x,z) \approx 1$.

6.3.3 Attenuation factors for incident and scattered rays

Although the radially symmetric density profile and scattering contributions $\mathcal{S}_{\mathrm{R}}$ and $\mathcal{S}_{\mathrm{C}}$ are easily interpolated into the Cartesian simulation space, the attenuation term is in general a complicated function of position in the 3D volume. The total attenuation effect is cumulative (within exponential factors) as the x-rays travel along longer path lengths and can therefore be decomposed into

$$\mathcal{A}(x,y,z) = \mathcal{A}_{\mathrm{in}}(x,y,z)\, \mathcal{A}_{\mathrm{sc}}(x,y,z). \tag{6.8}$$

The first term corresponds to the attenuation of incident parallel rays moving into the target in the scattering $(x-y)$ plane and the second term gives the further attenuation of the scattered rays as seen from the detector.

In general, the weight of every point in the scattering volume should be calculated independently for every possible combination of incident and scattered ray paths, i.e. from every possible point of emission within the plume of plasma blown off the backlighter foil, to every possible point in the target with a non-negligible view factor, to every possible point on the crystal in the detector. Clearly, this would be extremely computationally intensive

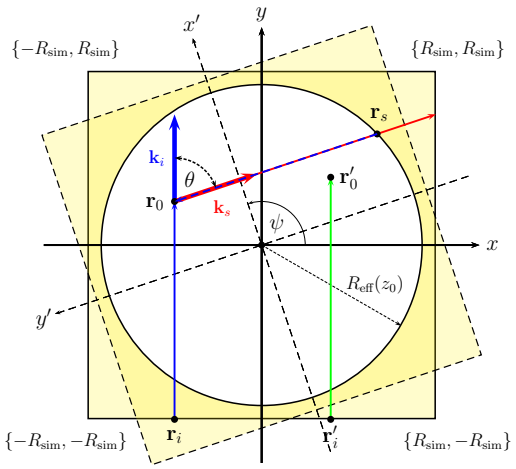

Figure 6.5: Graphical representation of x-ray attenuation calculations performed in VIXEN in the plane with elevation z_0. The paths of incident (thin blue vector) and scattered (thin red vector) rays are shown. The attenuation on the path $\mathbf{r}_0 \rightarrow \mathbf{r}_s$ is identical to that experienced by an incident ray propagating in reverse (dashed thin blue vector). This is also equivalent to the attenuation along the path $\mathbf{r}'_{\rm i} \rightarrow \mathbf{r}'_0$ (thin green vector). Regions outside the simulation space are perfectly transmissive (shaded yellow regions).

to be reasonably well-resolved and amounts to a full ray trace through the simulation mesh in combination with attenuation and dynamic scattering cross section calculations.

Instead, the assumption of parallel incident rays substantially simplifies the current problem, allowing the relevant path integral to be computed on a regular rectilinear Cartesian grid. Figure 6.5 illustrates the simple method by which the transport and propagation of the probe are considered. An incident ray is shown propagating from a point on the rear boundary of the simulation box $\mathbf{r}_{\rm i} = \{x_0, -R_{\rm sim}, z_0\}$ along the y-direction to a point of interest in the target $\mathbf{r}_0 = \{x_0, y_0, z_0\}$. The cumulative attenuation experienced by photons along the path shown is given by the Beer-Lambert law

$$\mathcal{A}_{\rm in}(x_0, y_0, z_0) = \exp\left[-\int_{y_{\rm min}(x_0,z_0)}^{y_0} {\rm d}y\, \rho\left(R(x_0, y, z_0)\right) \kappa\left(\omega_{\rm i}, R(x_0, y, z_0)\right)\right], \tag{6.9}$$

where $y_{\rm min}(x_0, z_0) = -\left(R_{\rm sim}^2 - x_0^2 - z_0^2\right)^{1/2}$ and $\kappa(\omega_{\rm i})$ is the local opacity at the frequency of the incident x-rays. The lower limit of integration is the edge (closest to the x-ray source) of the projection of the spherical simulation onto the scattering plane for the current elevation z (the intersection of the blue vector with the lower circular boundary in Fig. 6.5). For coordinates located outside the spherical region, the opacity and density are assumed to go to zero in the absence of additional data, such that x-rays are perfectly transmitted (see the yellow-shaded regions in Fig. 6.5).

The assumption of parallel rays together with the radial symmetry of the plasma profiles also simplifies the calculation of the attenuation factor for the scattered rays. This is a crucial component of the model since it further decreases the weight of a point in the scattering volume as seen by the spectrometer. For strongly opaque targets, it is possible for the scattered intensity to be significantly asymmetrical, with the total spectrum reflecting the conditions from a small sub-region within the total illuminated volume. Clearly, this constitutes a potentially large source of uncertainty for data analysis.

For the example shown in Fig. 6.5, the intensity of the probe x-rays reaching a given point is decreased by propagating along the path $\mathbf{r}_\mathrm{i} \rightarrow \mathbf{r}_0$. The weight of this point is further decreased since the signal scattered from this point to the detector must propagate along the path $\mathbf{r}_0 \rightarrow \mathbf{r}_\mathrm{s}$. Note that $\mathbf{r}_\mathrm{s}$ does not lie on the edge of the simulation space as the ray is assumed to be perfectly transmitted from this point to the detector, which lies further along the same vector.

It is possible to calculate a new attenuation integral similar to Eq. (6.9) along the path of the scattered ray. However, from the perspective of the detector the weight of the point $\mathbf{r}_0$ is decreased by a fraction which is identical to that of an incident ray propagating in reverse, from a virtual source placed at the detector to $\mathbf{r}_0$ (see Fig. 6.5). Thus, the attenuation of the scattered ray can be found from the application of a simple coordinate rotation in the $x-y$ plane, which is significantly less computationally expensive. The total weighting due to attenuation for the point $\mathbf{r}_0$ can therefore expressed as

$$\mathcal{A}(x,y,z) = \mathcal{A}_\mathrm{in}(x,y,z)\,\mathcal{A}_\mathrm{in}(x',y',z), \tag{6.10}$$

where the transformed coordinates are $x' = x\cos\psi + y\sin\psi$ and $y' = -x\sin\psi + y\cos\psi$, and the angle of rotation is $\psi = \pi - \theta$. The mapping of $\mathcal{A}_\mathrm{in}(x,y,z) \rightarrow \mathcal{A}_\mathrm{in}(x',y',z)$ is performed using bilinear interpolation for each z.

6.3.4 3D weighting distributions

Multiplying the total attenuation factor according to Eq. (6.10) by the density profile and iterating the calculation illustrated in Fig. 6.5 over all z in the simulation space builds a 3D map of the total weighting distribution of points in the target. Fig. 6.6(a) shows a three-slice through $\mathcal{W}(x,y,z)$ at peak compression. In this image the x-ray probe is incident from the right, such that the radiography diagnostic is located to the left. The rays are scattered through a uniform angle of $\theta = 84.5°$ at every point in the target toward the detector, which is located above the simulation space positive x direction). The geometry can be also deduced from the relative orientations of the two *shadows* (purple-black) cast by the high-density ball from the perspective of the two diagnostics.

A contour map of the scattering $(x-y)$ plane for $z = 0$ is shown in Fig. 6.6(b). The thin white region on the detector-facing hemisphere of the illuminated side of the target (upper right quadrant) corresponds to the high-density ablator material. The high weight of this region reflects the short overall path length the x-rays take through low-opacity plasma and also its high density weighting. A region at smaller radii with relatively high weight is also present in the same quadrant, corresponding to scattering from the rebounding high-density shock front. Despite the density in this region being a factor of roughly 5 higher than the ablator, the overall weight is decreased by its strong attenuation factor.

The weighting maps can also be used to assess the importance of k-blurring due to source divergence. As previously noted, the radiation transport can be reliably modelled

by assuming parallel incident and scattered x-rays. On the other hand, the geometry of the x-ray source and target is conducive to the realisation of a small distribution of scattering angle, each of which leads to a slightly different scattering profile. This distribution of contributing angles is itself limited by the density and opacity weighting. Ray tracing calculations have been performed by D. Kraus using the 3D weighting shown in Fig. 6.6(a). The resulting histogrammed angular distributions $F(\theta)$ are presented in Fig. 6.7(a).

Considering the target to be a uniformly dense sphere with $r = 0.5\,\mathrm{mm}$ results in a super-Gaussian shaped distribution with a FWHM of c.a. 20°. Including the 3D weighting distribution halves this range, as only scattering angles realised from the dense parts of the target (approximately half of the simulation radius) will contribute to the total scattering. The effect of the asymmetry introduced by the attenuation factor can be seen when the x-ray source is made larger (by increasing the backlighter spot size) to access a wider distribution of angles. In this case, contributions from the wings increase substantially, although the width does not noticeably change, and the peak is downshifted. This fact reflects the greater weighting of the source- and detector-facing hemisphere of the target.

The total Compton scattering profiles from the dense ablator region for the range of contributing angles found from ray tracing are shown as the lower set of curves in Fig. 6.7(b). Clearly, the range of angles is large enough to access a substantial range of scattering wave numbers k, which yield very different spectral shapes. Averaging these

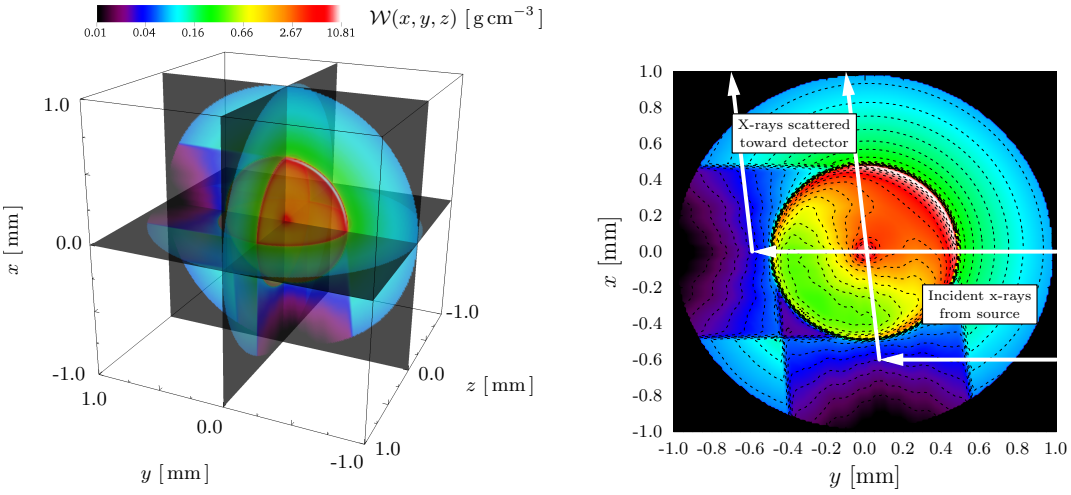

(a) 3D weighting distribution.

(b) Weighting distribution in $z = 0$ plane.

Figure 6.6: (a): 3D view of the total weighting function, $\mathcal{W}(x, y, z)$, of a uniformly illuminated target ($\mathcal{P}(x, z) = 1$) due to both attenuation and density immediately following shock stagnation $t = +0.1\,\mathrm{ns}$. (b): 2D slice through the scattering $(x-y)$ plane at $z = 0$. The colour scale indicates regions contributing low (black-purple) and high (red-white) weight to the Cartesian integration in Eq. (6.4) and is the same in both plots. Scattering from two different locations within the scattering volume with equal total attenuation/path length are shown by the white arrows.

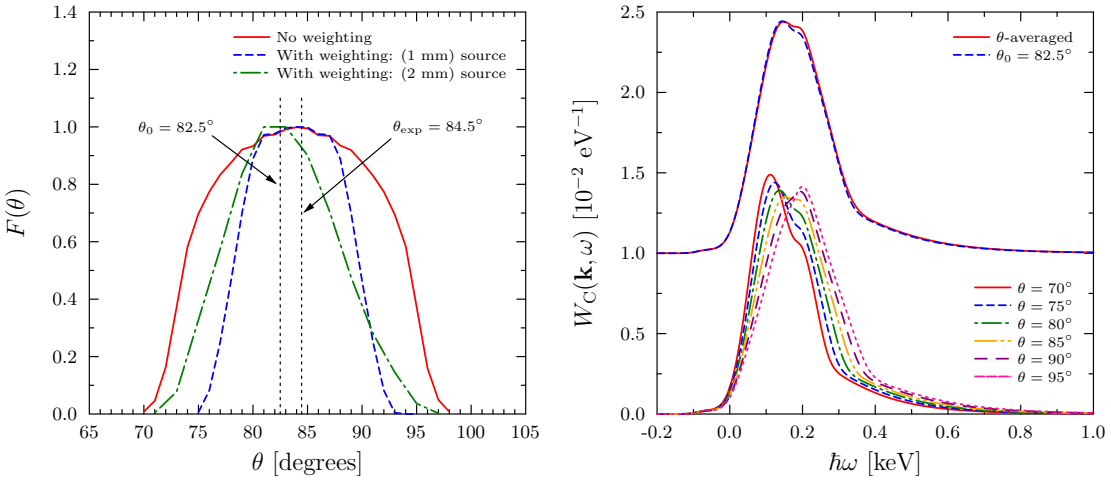

(a) Angular distribution functions $F(\theta)$.

(b) Total Compton profiles for different θ.

Figure 6.7: Histogram of contributing scattering angles (a) and inelastic scattering profile from the dense ablator region (b) resulting from ray tracing calculations by D. Kraus for different weightings and effective source sizes. The mean (peak) scattering angle θ_0 is slightly downshifted due to the attenuation contribution to the 3D weighting. In panel (b), the angular averaging is performed according to Eq. (6.6).

profiles over the weighting distribution $F(\theta)$ yields only a very small broadening effect, and can be accurately reproduced by considering the single-angle spectra corresponding to the peak of the distribution, $\theta_0 = 82.5°$. From here on, the angular integration is ignored by selecting $F(\theta) = \delta(\theta - \theta_0)$ and the XRTS spectra are calculated using θ_0. Finally, note that iterating this process by computing a new weighting map based on θ_0 and again ray tracing to build up a new angular distribution has no impact on these results, suggesting that k-blurring is unimportant for this experiment.

6.4 Results for the spatially integrated scattering spectrum

Having calculated the spatial dependence of the elastic and inelastic scattering profiles Eqs. (6.5) and (6.6) and the weighting function Eq. (6.7), the necessary 3D integration is straightforward to perform. Fig. 6.8(a) shows the spatially integrated power spectrum, calculated according to Eq. (6.4), during the stagnation phase of the implosion. Clearly, the spectral shape does not significantly change during this period. This result simply reflects the findings of the previous sections; the total contribution to the cross section comes from the bulk of the plasma behind the ablation front, in which the conditions are in a near-steady state. The density profile, intensity distribution and the spherical geometry of the target itself (conditions at large radii correspond to a greater number of points/cells in the Cartesian grid) all further amplify the weighting of such states.

Furthermore, in the most strongly-contributing regions of the plasma the carbon is

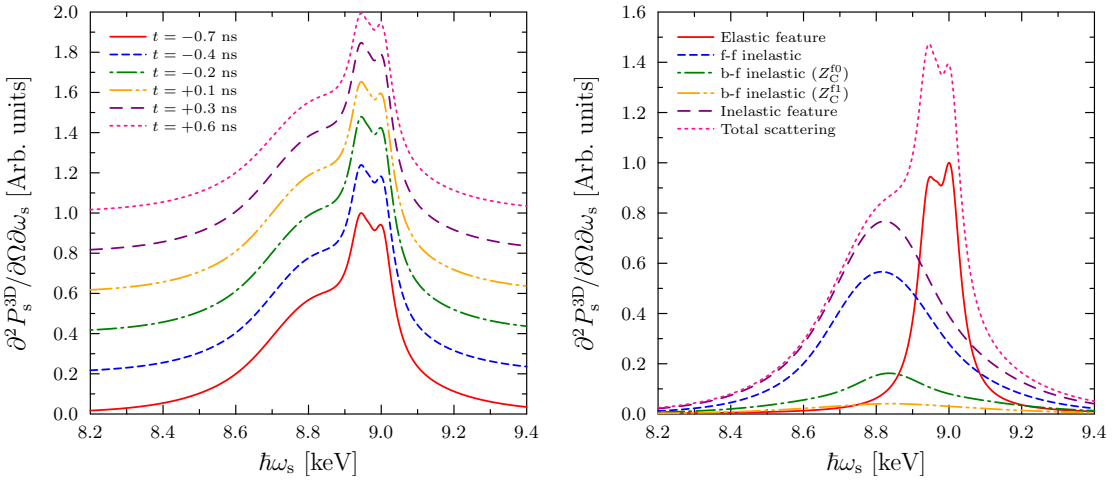

(a) Time evolution of integrated spectrum. (b) Spatially-integrated scattering contributions.

Figure 6.8: (a): The time evolution of the total spatially integrated scattered power spectrum between $t = -0.7\,\mathrm{ns}$ and $t = +0.6\,\mathrm{ns}$ shows no significant changes due to the dominance of the steady state conditions present in the ablator and bulk regions. (b): Contributions to the total scattered signal from inelastic free-free, bound-free and elastic scattering at peak compression. In panel (a), successive times are artificially offset in the y-axis.

relatively weakly ionized, $\bar{Z}_C^f = 3 - 4$. Accordingly, the bound-free scattering contribution around the Compton peak cannot be ignored, which is only weakly sensitive to the plasma conditions. The various components of the spatially integrated result are shown in Fig. 6.8(b). Therein, the relative strengths of the free-free and total bound-free features are emphasised (recall that two distinct carbon charge states are explicitly considered), demonstrating that bound electrons account for a substantial fraction of the inelastic scattering. Note that the inelastic contributions are heavily broadened by the convolution with the x-ray source, which also obscures the asymmetry of the bound-free feature around the x-ray absorption edge. The latter is also thermally blurred [Mattern et al., 2012] and due to the integration over states with different levels of continuum lowering.

6.4.1 Relative importance of x-ray attenuation

The significance of the role played by x-ray attenuation on the total scattered signal can be gauged separately to that of plasma gradients by comparing the 3D-integrated results to calculations in which the opacity is set to zero. In this case, Eq. (6.4) can be written as

$$\frac{\partial^2 P_s^{1D}}{\partial\Omega\partial\omega_s} \propto \sigma_T I_i \int_0^{R_{sim}} \mathrm{d}R\, R^2\, 4\pi\rho(R)\Big[\mathcal{S}_R(\omega;R) + \mathcal{S}_C(\omega;R)\Big]. \tag{6.11}$$

At peak compression, where the mean opacity of the target is highest and attenuation is expected to be most important, the absolute intensity of the full 3D calculation is reduced by a factor of roughly 3.5 compared to the 1D ($\kappa = 0$) completely transparent estimate

(Fig. 6.9(a)). Scaling the 3D-integrated result to reproduce the height of the Compton feature from the 1D calculation shows that the shape of inelastic peak is negligibly affected, whereas the ratio of elastic to inelastic scattering is anomalously reduced by ca. 7.5%. Since the plasma gradients are treated equivalently in both approaches, this reduction can only be a consequence of the opacity of the target.

It was suggested by Gregori et al. that in the non-collective scattering limit the ratio of the integrated strength of the elastic and inelastic features

$$\mathcal{I} = \frac{\int_{-\infty}^{\infty} \mathrm{d}\omega\, \mathcal{S}_{\mathrm{R}}(\omega)}{\int_{-\infty}^{\infty} \mathrm{d}\omega\, \mathcal{S}_{\mathrm{C}}(\omega)}, \tag{6.12}$$

provides a sensitive measurement of the mean ionization state [Gregori et al., 2003]. Clearly, the anomalous reduction of the elastic scattering strength observed here represents a significant source of uncertainty for such measurements. Indeed, the ionization state is one of the key quantities the present experiment aims to investigate with XRTS (in addition to the temperature). Thus, understanding the nature and origin of this observation is important.

Plotting Eq. (6.12) as a function of radius within the target shows a large peak in the ablator ($r = 0.47\,\mathrm{mm}$), where the ionization profile shows a global minimum (Fig. 6.9(b)). A second, broader peak can also be seen between $0.15 \lesssim r \lesssim 0.4\,\mathrm{mm}$. This feature arises due to the scaling of the screening clouds around the carbon ions with the increasing temperature toward the core. Note that the latter is, however, only a small correction to the temperature- and density-independent structure of the K-shell, which is the dominant contribution to the Rayleigh scattering amplitude at large k. Indeed, the peak begins to abruptly drop for $r < 0.22\,\mathrm{mm}$, coincident with the mean carbon ionization increasing above $\bar{Z}_{\mathrm{C}}^{\mathrm{f}} = 4$. The elastic scattering then falls steadily due to the onset of significant K-shell ionization in the core.

The relative contributions of these features to the scattering ratio observed in the spatially integrated signal can be assessed by considering a radial weighting factor, given by integrating the total weighting $\mathcal{W}(x, y, z)$ over all angles θ and ϕ

$$\mathcal{W}_{\mathrm{rad}}^{\mathrm{3D}}(R) = \int_0^{2\pi} \mathrm{d}\phi \int_0^{\pi} \mathrm{d}\theta \sin\theta\, \mathcal{W}(x, y, z). \tag{6.13}$$

Note that for the 1D ($\kappa = 0$) case Eq. (6.13) gives the simple result $\mathcal{W}_{\mathrm{rad}}^{\mathrm{1D}}(R) = 4\pi\rho(R)$, as written in Eq. (6.11). As expected, the radial weighting also peaks strongly in the ablator region since this is where the product of the number of cells and density is maximised. The weighting then decays roughly linearly for the shocked material at smaller radii as the number of cells decreases faster than the density increases toward the compressed core.

In comparison, the result from the 3D-integrated calculation also shows a strong peak in the ablator, although the amplitude is lower by a factor of c.a. 3.5. Again, this reflects the fact that the total scattering is dominated by regions near the edge of the ball. On

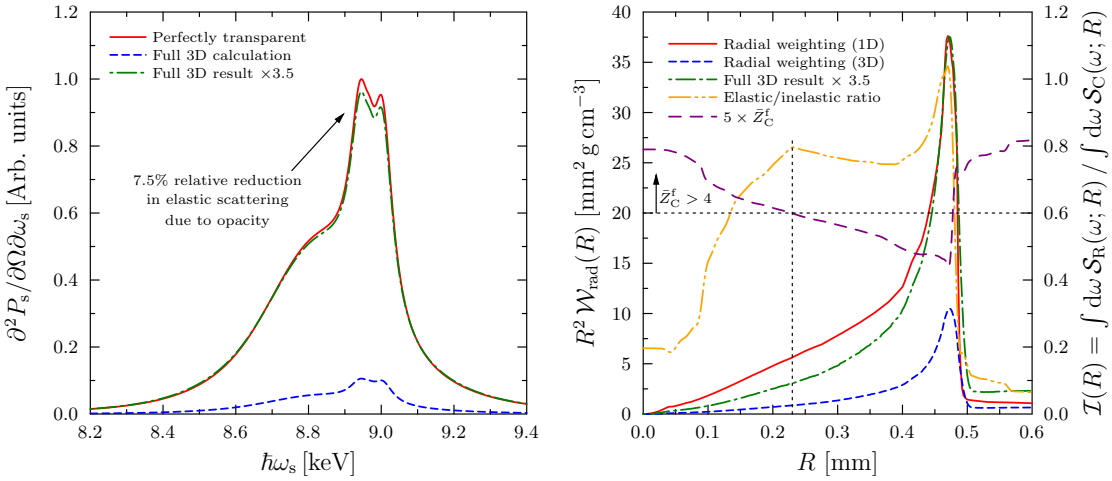

(a) Comparison of 3D and 1D calculations.

(b) Radial weighting profiles.

Figure 6.9: Comparison of VIXEN calculations without (solid red) and with (dashed blue) x-ray attenuation due to the opacity profile of the target (a). Scaling the calculation including opacity (dot-dashed green) reproduces the shape of the Compton feature for the perfectly transparent case, but not the relative amplitudes of the Rayleigh and Compton peaks. The angularly averaged weighting $\mathcal{W}_{rad}(R)$ as a function of radius (b) shows the opacity of the target suppresses the elastic/inelastic scattering ratio (double dot-dashed orange) from the bulk of the plasma ($R = 0.1 - 0.4\,$mm). In panel (b), the mean carbon ionization (long-dashed purple) is also plotted for clarity.

the other hand, the weighting decays faster for deeper regions of the target, in which $\mathcal{I}(r)$ remains large, compared to the 1D case. This relative difference may therefore be identified to be the cause of the weaker Rayleigh signal observed in Fig. 6.9(a).

6.5 Synthetic data fitting using 0D XRTS modelling

Up to this point, robust calculations of the XRTS signal expected from the experiment have been restricted to a forward-modelling role. Whilst providing an important capability for experimental design and qualitative evaluation, such an approach is of limited use for real data analysis due to the importance of knowledge of the plasma gradients. Instead, a more practical consideration is whether meaningful estimates of the mean conditions of such inhomogeneous targets can be extracted by standard fitting techniques. Typically, this involves treating the plasma as a single extended point at a single set of conditions, $\{\bar{Z}_C^f, T, \rho\}$. In this case, the power spectrum is simply the core model of the MCSS code

$$\frac{\partial^2 P_s^{0D}}{\partial\Omega\partial\omega_s} \propto \sigma_T I_i \mathcal{V}_{sim}\, \rho \left[\mathcal{S}_R(\omega) + \mathcal{S}_C(\omega)\right], \tag{6.14}$$

where $\mathcal{V}_{sim} = \frac{4}{3}\pi R_{sim}^3$ is the volume of the simulation. Since no spatial information is contained in this approach, it is referred to here as the 0D approach. Note that similarly

to (6.14) the attenuation of the probe is not accounted for.

A synthetic data set reminiscent of the signal expected to be measured can be constructed using the full 3D VIXEN calculations, thereby incorporating the effects of plasma gradients and the target opacity. Reasonable signal-to-noise levels can be estimated from the statistics of the x-ray source characterisation shots (see Fig. 6.1(b)). The noise is added to each frequency bin of the 3D calculation, with the fluctuations sampled from a normal distribution whose standard deviation scales with the square root of the signal intensity.

The best fit to the synthetic data is performed using χ^2 statistical analysis, with the temperature and mean carbon ionization varied as unknowns. The mass density is treated as an input to the fitting procedure since the radiography diagnostic provides an accurate estimate of the time-dependent density profile independently from XRTS. To be consistent with the density-weighted nature of the diagnostic, the best fit conditions should be compared to mass-weighted average conditions predicted by the HYDRA simulations. Specifically, the density weighting is due to the total electron density.

For the spherical geometry, the appropriate average quantities to compare against are

$$\langle T \rangle_\rho = \frac{\int_0^{R_{\mathrm{sim}}} \mathrm{d}R\, R^2\, \rho(R)\, T(R)}{\int_0^{R_{\mathrm{sim}}} \mathrm{d}R\, R^2\, \rho(R)}, \tag{6.15}$$

$$\langle \bar{Z}_{\mathrm{C}}^{\mathrm{f}} \rangle_\rho = \frac{\int_0^{R_{\mathrm{sim}}} \mathrm{d}R\, R^2\, \rho(R)\, \bar{Z}_{\mathrm{C}}^{\mathrm{f}}(R)}{\int_0^{R_{\mathrm{sim}}} \mathrm{d}R\, R^2\, \rho(R)}. \tag{6.16}$$

Taking the simulated temperature, ionization and density profiles yields a density-weighted average mass density of $\langle \rho \rangle_\rho = 8.0\,\mathrm{g\,cm^{-3}}$ following peak compression, whilst the equivalent density-weighted average temperature and carbon ionization are $\langle T \rangle_\rho = 72\,\mathrm{eV}$ and $\langle \bar{Z}_{\mathrm{C}}^{\mathrm{f}} \rangle_\rho = 3.8$. The density-weighted conditions of the target therefore closely reflect the conditions of the bulk of shocked plasma.

6.5.1 Statistical analysis of synthetic XRTS data

The statistical fitting procedure is performed by calculating the χ^2 parameter [Bevington and Robinson, 2003] with respect to the synthetic experimental data, denoted $\partial P_{\mathrm{s}}^{\mathrm{exp}}(\omega)$, and the expected results of the spectrum based on modelling, denoted $\partial P_{\mathrm{s}}^{\mathrm{mod}}(\omega)$

$$\chi^2 = \sum_j^{N_\omega} \frac{1}{\sigma_j^2} \left[\partial P_{\mathrm{s}}^{\mathrm{exp}}(\omega_j) - \partial P_{\mathrm{s}}^{\mathrm{mod}}(\omega_j) \right]^2. \tag{6.17}$$

In Eq. (6.17), σ_j is the standard deviation of the data in bin j and N_ω is the number of frequency elements in the calculation. Additionally, the *goodness-of-fit* or *reduced-*χ^2 metric is defined as $\chi_\nu^2 = \chi^2/\nu$, where $\nu = N_\omega + D_{\mathrm{fit}} - 1$ gives an estimate of the number of degrees of freedom. A model is unlikely to yield a good fit to the data by chance for $\chi_\nu^2 \sim 1$, whereas a good fit may result by chance if $\chi_\nu^2 \gg 1$; this may equivalently be

interpreted as the definition of a poor fit. Furthermore, it is clear that $\chi^2_\nu < 0$ indicates that the model is over-defined, e.g. there may be too many free parameters.

In the case of real experimental data, the standard deviation of the signal intensity in each bin σ_j must be estimated from the photon intensity distribution averaged over several pixels (corresponding to energy bins) of the detector. Since XRTS experiments using laser-driven x-ray sources are typically photon-starved, such detailed statistical information is often unavailable and, thus, the mean standard deviation of the full range of the signal is used. In future experiments using ultra-bright, high-repetition rate x-rays sources such as FELs, it should be possible to provide much more accurate estimates of such uncertainties.

For the present analysis testing the fitting proceedure, the frequency-dependent standard deviation is precisely known as it has been selected to produce the desired the signal-to-noise ratio in the synthetic data. The χ^2 parameter Eq. (6.17) is then calculated at each point in $\bar{Z}^{\mathrm{f}}_{\mathrm{C}} - T$ space considered, resulting in a distribution of potential fits with different mean accuracies. The location of a unique global minimum is interpreted to yield an estimate of the *best fit* conditions, i.e. the conditions which are least likely to give a good fit to the scattering signal by chance.

In order to mitigate model uncertainties in the description of the Rayleigh weight and any anomalous suppression due to the effect of the target opacity, as seen in Fig. 6.9(a), the energy range over which the fitting is performed is limited to the Compton peak, i.e. $8.3 \leq \hbar\omega_{\mathrm{s}} \leq 8.85\,\mathrm{keV}$. Furthermore, the Rayleigh weight can be constrained to perfectly reproduce the observed ratio of inelastic and elastic scattering of the synthetic data. One may derive the following general expression from Eq. (6.14)

$$W^{\mathrm{id.}}_{\mathrm{R}}(k_0) = \frac{\mathcal{R}\partial P^{\mathrm{in}}_{\mathrm{s}}(\omega_{\mathrm{C}e}) - \partial P^{\mathrm{in}}_{\mathrm{s}}(0)}{\Sigma(0) - \mathcal{R}\Sigma(\omega_{\mathrm{C}e})}, \tag{6.18}$$

where $k_0 = 2k_i \sin(\theta_0/2)$, $\partial P^{\mathrm{in}}_{\mathrm{s}}(\omega)$ is the calculated total inelastic scattering, $\omega_{\mathrm{C}e} = \hbar k^2/2m_e$ is the Compton frequency and $\mathcal{R}$ is a calibration constant determined by the observed ratio of any two spectral features (the Compton and Rayleigh peaks).

6.5.2 Quantifying the fitting errors

Beyond providing estimates of best fit conditions for a given experimental (or synthetic) data set, statistical analysis enables robust estimates of fitting errors [see, e.g., Gregori et al., 2004; Kritcher et al., 2011b; Fortmann et al., 2012]. In this work, the errors are quantified from confidence intervals associated with the probability density function (PDF) related to χ^2 statistics [Bevington and Robinson, 2003]

$$p(\chi^2;\nu) = \frac{(\chi^2/2)^{\frac{\nu}{2}-1}}{2\Gamma(\nu/2)} e^{-\chi^2/2}, \tag{6.19}$$

$$\int \mathrm{d}\chi^2\, p(\chi^2;\nu) = 1. \tag{6.20}$$

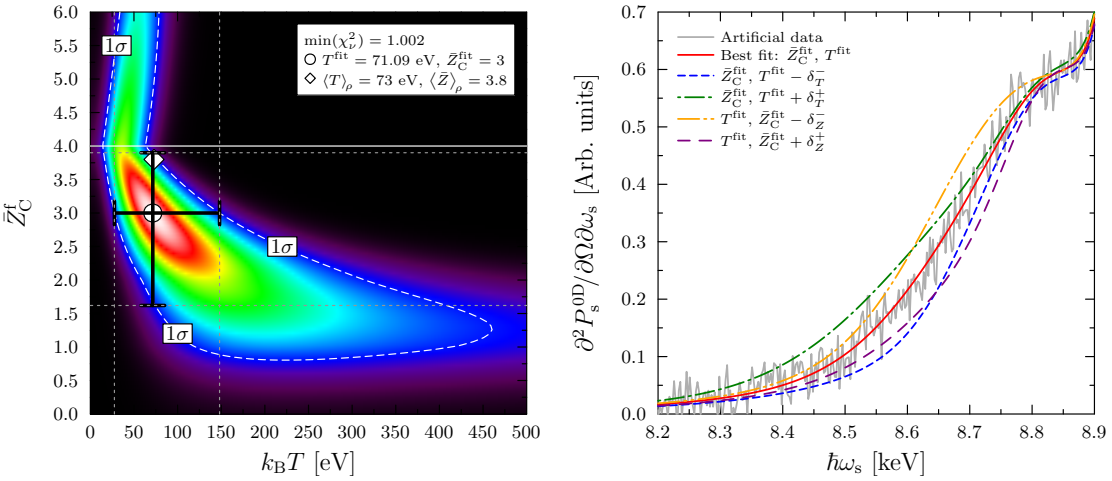

(a) PDF surface for fitting synthetic data.

(b) Compton profile sensitivities.

Figure 6.10: (a): Intensity map of the PDF $p(\chi^2;\nu)$ corresponding to the goodness-of-fit between synthetic XRTS data and simple 0D calculations, as a function of temperature and carbon charge state for an input density of $\rho = 8.0\,\mathrm{g\,cm^{-3}}$. (b) Sensitivity of the Compton profile to changes in temperature and density on the 1σ level of uncertainty.

The contour corresponding to the usual definition of 1σ level of confidence, i.e. where $\int \mathrm{d}\chi^2\, p(\chi^2;\nu) = 68.27\%$, can be found be iteratively integrating an increasing region surrounding the location of the peak in the PDF. Note that this is only strictly meaningful for Gaussian statistics, but nevertheless provides a reasonable estimate by which to robustly quantify the accuracy of the analysis. The error bars are defined by where this contour intersects with a cross-hair centred on the best fit conditions (see the dark grey error bars centred on the peak of the PDF in Fig. 6.10(a)).

6.5.3 Statistical fitting results and conclusions

The statistical analysis results for fitting the synthetic scattering data with 0D calculations are shown in Fig. 6.10. A unique global maximum in the PDF is clearly present, yielding best fit conditions $T^{\rm fit} = 71.6\,\mathrm{eV}$ and $\bar{Z}_{\rm C}^{f\,\rm fit} = 3$. The goodness-of-fit at the peak is $\chi^2_\nu = 1.004$, indicating a good fit to the data. The best fit temperature is in excellent agreement with the density-weighted mean temperature Eq. (6.15), whereas the best fit ionization underestimates the prediction of Eq. (6.16) by 21%.

On the other hand, the uncertainties associated with the best fit conditions are quite large, corresponding to $\delta T = +107\%/-61\%$ and $\delta Z = +30\%/-44\%$, respectively. Within these margins, both parameters agree with their respective density-weighted estimates. The spectra resulting from combinations at the bounds of these errors demonstrate clear departures from the best fit curve (see Fig. 6.10(b)). Note that, on average, each curve for conditions on the 1σ contour do not fit a third of the data points, as expected.

Such large statistical errors are not unsurprising given the constraints of the 0D model. In particular, the spectrum becomes extremely insensitive to the temperature for $\bar{Z}_{\mathrm{C}}^{\mathrm{f}} = 1-2$ since inelastic scattering from bound electrons can adequately describe the location and width of the Compton peak. Increasing the temperature of the free electrons therefore only marginally affects the shapes of the high-energy wings, where the signal amplitude (and therefore the statistical weighting) is low. In this ionization regime, the PDF decays very weakly along the temperature axis, extending out to many tens of keV. Incorporating all probability associated with these states affects the numerical normalisation of the PDF and subsequently the exact location of the 1σ contour. Thus, the precise errors are weakly sensitive to the temperature range considered. The upper limit of the temperature has been capped at $T = 1\,\mathrm{keV}$, which is the maximum temperature achieved in the target predicted by HYDRA. The resulting blurring of the contour location is small relative to the large uncertainties presented.

The behaviour of the probability density close to the K-shell/L-shell boundary (solid white horizontal line in Fig. 6.10(a)) also merits a brief discussion. In this region, the Compton peak mainly contains free-free scattering, since the K-shell bound-free feature is relatively small over this energy range. The sensitivity to the temperature is therefore high, whilst the ionization state is largely unimportant. Indeed, the absence/presence of L-shell bound-free scattering contributions has been successfully used to infer continuum lowering in compressed CH [Fletcher et al., 2014].

Within the accuracy of the radiography analysis an uncertainty in the input density can be conservatively estimated to be ca. 7.5% [Swift, 2014]. The effect of changing the input density on this level results in marginal changes to the best fit conditions. It is therefore reasonable to expect that the main source of uncertainty in temperature and ionization measurements using XRTS will come from the data fitting procedure itself. Since opacity effects have been effectively removed as a source of error from the fitting procedure, the results of this section suggests that the plasma gradients are the source of the discrepancy associated with fitting the mean carbon ionization. This not only illustrates the importance of detailed modelling of XRTS from dense, inhomogeneous plasmas, but also the need for careful target design if XRTS is to be used to make measurements which are correlated with physically meaningful conditions in experiments similar to those discussed in this chapter.

Chapter 7

Observation of finite-wavelength screening in warm dense plastic using x-ray Thomson scattering

Throughout this thesis, it has been shown that different classes of XRTS experiments require significantly different modelling considerations. Primarily, these are driven by the temporal and spatial scales associated with the measurement and target evolution. From the conclusions presented thus far, it is clear that a number of basic criteria must be fulfilled to minimise model-, geometrical- and analysis-based uncertainties and therefore obtain the most accurate measurements possible from experimental data. Near-homogeneous, slowly-evolving, low-Z targets driven into weakly coupled states and probed with laser-driven x-ray sources present the fewest challenges to modelling the scattered spectrum.

In this chapter, the analysis of a recent experiment conducted at the Omega laser facility is presented. In this experiment, a hollow plastic shell target is shock-compressed to a WDM state characterised by moderate coupling, partial degeneracy and partial ionization of the carbon ions. By observing scattering of high-energy x-rays at large angles, the non-collective response of the plasma is accessed, enabling electron density and temperature measurements by fitting the Compton peak. Moreover, the elastic scattering signal in this regime is dominated by the screening cloud. Thus, the platform is uniquely set up to investigate one of the most fundamental aspects of the physics of charged-particle systems. It is found that the commonly-used Debye-Hückel (DH) model of screening cannot describe the experimental data, whereas a more general approach based on the finite-wavelength screening approach yields good agreement.

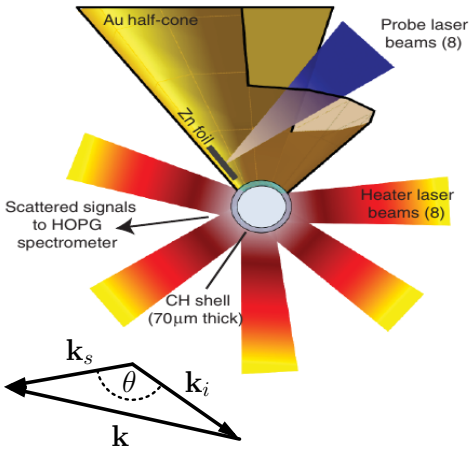

Figure 7.1: Schematic representation of the experimental platform showing the hollow CH shell target mounted on the end of the Au cone shield and the orientation of the spectrometer relative to the Zn foil x-ray source. The vector triangle relating to the scattering is also shown. Elements of this figure have been reproduced with permission from Phys. Rev. Lett. © 2014 American Physical Society.

7.1 Experimental platform

The experiment presented in this chapter was performed at the Omega Laser Facility at the Laboratory for Laser Energetics in Rochester, USA. A total of eight heating beams with a wavelength of 351 nm and a total energy of 13.5 kJ were used to launch multiple shocks into a 70 μm thin plastic (CH) shell. Another eight beams were directed to a Zn foil held in a conical gold shine shield, the end of which served as a mounting point for the CH shell, creating a hot plasma emitting He-α radiation at 9 keV, as used for the NIF experiments described in the previous chapter. Measurements of the conditions created by the coalescent shocks at different stages of the implosion were achieved by introducing controlled time delays between the pump and the probe. The scattered x-rays were recorded using a time-gated ($\lesssim 100$ ps response time) micro-channel plate coupled to a high-resolution HOPG crystal spectrometer with a range of $7.5 \leq \hbar\omega_s \leq 10$ keV, under a range of scattering angles determined by the geometry of both the cone assembly and the size of the imploding shell. This has been characterised using ray tracing as $\theta = 135° \pm 15°$. A schematic representation of the experimental configuration is shown in Fig. 7.1.

Although this experimental platform was originally conceived to study the material- and in-flight properties of spherically-compressed targets in parallel to the National Ignition Campaign [Kritcher et al., 2011b], the low-heating, high-compression adiabat of the implosions yields ideal conditions for validating theoretical models of WDM. For example, the data taken from this experiment has been analysed to investigate continuum lowering [Fletcher et al., 2014], which is currently the subject of intensive debate and research [Ciricosta et al., 2012; Hoarty et al., 2013b]. Furthermore, the large scattering angle used constrains uncertainties associated with the structure of ions and bound electrons, thereby enabling detailed investigation of the screening cloud from the elastic scattering strength. As previously discussed in Chapter 3, the screening cloud constitutes one of the least well-understood aspects of the theoretical description of XRTS in dense matter and is therefore of significant interest to many aspects of this work.

7.2 Motivation for studying charge screening

The well-known theory describing screening in charged-particle systems was first given by Debye and Hückel for electrolyte solutions and diffuse classical plasmas [Debye and Hückel, 1923]. A generalisation for degenerate electrons in cold solids was later given by Thomas and Fermi [Thomas, 1927; Fermi, 1928]. The principal effect involved in charge screening is the exponential reduction of the strength of Coulomb interactions between pairs of particles over long ranges due to polarisation of the background medium. Understanding this effect is of fundamental importance to the study of dense matter as the structural, thermodynamic, transport and relaxation properties are determined by the effective inter-particle potentials. However, since Debye-like screening also builds the basis of a large range of ostensibly unrelated systems, including quark-gluon plasmas and nuclear matter [Braaten and Nieto, 1994; Heinz, 1985], ultra-cold systems in traps [Bannasch et al., 2013] and chemical and biological systems involving charged macro-molecules [Grosberg et al., 2002], significant deviations from the Debye-like (hereafter referred to as simply DH) picture could potentially have a far-reaching impact on other currently active fields of research.

The restrictions of the DH screening model were outlined in Section 3.4 in the context of the Rayleigh scattering contribution to the spectrum of XRTS. Screening of the bare Coulomb interactions between the ions was shown to arise as a consequence of the collective response of the plasma to microscopic charge-density fluctuations, and is principally facilitated by electrons. Specifically, the DH result (3.35) was derived for weakly coupled conditions. It is also, appealing to the long-wavelength, i.e. $\lambda \to \infty$ or $k \to 0$, limit, which is valid for processes involving small momentum transfers (or equivalently large scale lengths) such as small-angle electron-ion scattering in diffuse, high-temperature plasmas. In contrast, processes involving large momentum transfer, such as strong collisions and large-angle scattering of high-energy x-rays, require a more general approach referred to as finite-wavelength screening (FWS). It was shown that the main difference between these descriptions arises under WDM conditions and at wave numbers significantly larger than the usual inverse screening length $\alpha = \kappa_e/k < 1$. Spectrally-resolved non-collective XRTS is therefore an ideal tool with which to study this effect since it simultaneously allows for the determination of the plasma conditions and the study of the screening cloud from a single spectrum [Chapman et al., 2015].

7.3 Theoretical considerations for XRTS modelling

Similarly to the experiment studied in the previous chapter, the slow evolution of the target relative to electron-electron and electron-ion relaxation processes ensures that non-equilibrium considerations can be neglected in modelling this experiment. Since the CH shells used here are very thin and the measurements are made soon after the drive provided

by the heating pulse ends, the plasma profiles can be expected to be relatively uniform. Nevertheless, radiation-hydrodynamics simulations using HYDRA [see, e.g., Fletcher et al., 2013] show a steady decompression of the bulk density of the shell as ablated coronal plasma is allowed to expand outward. Further decompression occurs as the implosion coasts at constant velocity following the final shock, causing decompression of the leading edge of the shell and some filling of the central cavity.

7.3.1 Spatial effects: gradients, x-ray attenuation and source divergence

Based on the VIXEN model developed in the previous chapter, simulated plasma profiles of this experiment yield 3D weighting distributions which confirm the dominance of the relatively uniform shell of dense material (see Fig. 7.2). The attenuation of the x-ray probe is small since the path length through the thin shell is very short, such that a 1D model of the spectrum is sufficient to capture all spatial effects. Moreover, the spatially-integrated results shown in Fig. 7.2(b) clearly indicate that the 1D model is extremely well-described by 0D MCSS calculations based on the mass-weighted average plasma conditions given by expressions with the forms of Eqs. (6.15) and (6.16). Thus, plasma gradients and transport of the x-ray probe are not considered further in this chapter and all XRTS spectra are produced using the MCSS code.

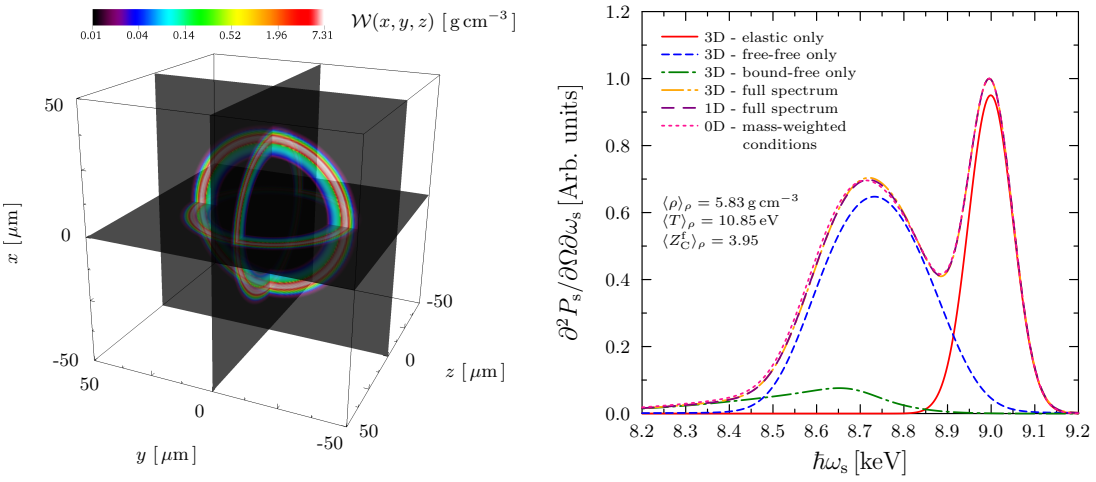

(a) 3D weighting distribution.

(b) Comparison of 3D, 1D and 0D calculations.

Figure 7.2: (a): 3D view of the total weighting function, $\mathcal{W}(x, y, z)$, for a thin CH shell based on a 1D HYDRA simulation (courtesy of L. Divol and A. Kritcher). (b): Contributions to the total spatially integrated XRTS spectrum based on 3D, 1D and 0D models. No difference can be discerned between the 1D and 3D VIXEN calculations since the x-ray attenuation through the thin shell is extremely low. For the 0D model, the mass weighted average plasma conditions of the simulation have been used as inputs. In this example, the scattering angle is $\theta = 135°$ and the x-ray source function is modelled as a Gaussian with a FWHM of 120 eV.

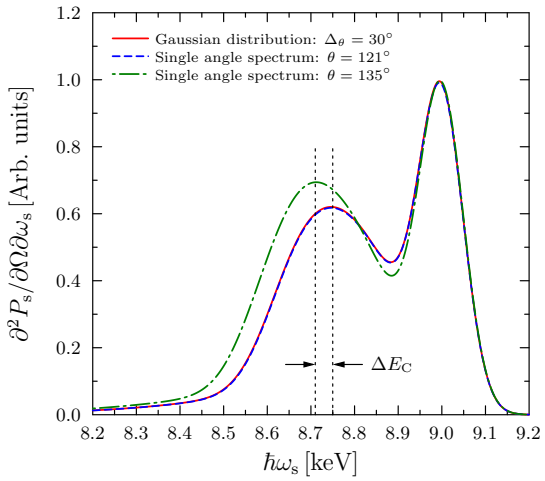

Figure 7.3: Comparison of scattered spectra with and without source divergence. The scattering angle distribution is assumed to be a Gaussian, centred on $\theta = 135°$ and with a FWHM of $\theta = 30°$. The effective scattering angle which reproduces the angularly-integrated result is $\theta = 120°$.

Separately to these considerations, the size of the target at the time of measurement realises a distribution of scattering angles. Since the integrated opacity of the shell is low over all, the peak angle of this distribution is not expected to shift due to asymmetric weighting of different quadrants. It has been previously determined by Fletcher et al. using ray tracing that a Gaussian distribution of angles with a FWHM of 30° is appropriate. The effect of averaging with this weighting on the spectrum is shown in Fig. 7.3. The Compton peak is subsequently shifted closer to the Rayleigh feature by c.a. 40 eV and also reduced in amplitude. Comparison to calculations using a single scattering angle show that an extremely good estimate of the angularly-integrated result is given by choosing $\theta_0 \approx 120°$; the effect on the Rayleigh weight is correspondingly small. Throughout the remainder of this chapter, the appropriate effective scattering angle for each time is determined by the observed location of the Compton peak.

7.3.2 Inelastic scattering contributions

As usual, fitting theoretical calculations to the inelastic contributions to the measured spectra is used to estimate the thermodynamic properties of the free electrons. In the backscattering geometry used, the non-collective response of the plasma is accessed, yielding a pronounced Compton peak containing contributions from bound and free electrons. Under the partially degenerate WDM conditions anticipated from these implosions, the width of the momentum distribution describing the free-free scattering is sensitive to the electron temperature and also the electron density via the chemical potential.

Moreover, in contrast to previous XRTS experiments, the present platform also enables some limited but important additional information of the mean ionization state to be accessed independently of the elastic scattering feature. Specifically, the ionization energy gap between K-shell and L-shell electrons in carbon is sufficiently large for bound-free scattering from L-shell states to significantly overlap with free-free scattering, whereas K-shell contributions overlap with only the red-shifted tail of the free-free feature. Thus, if

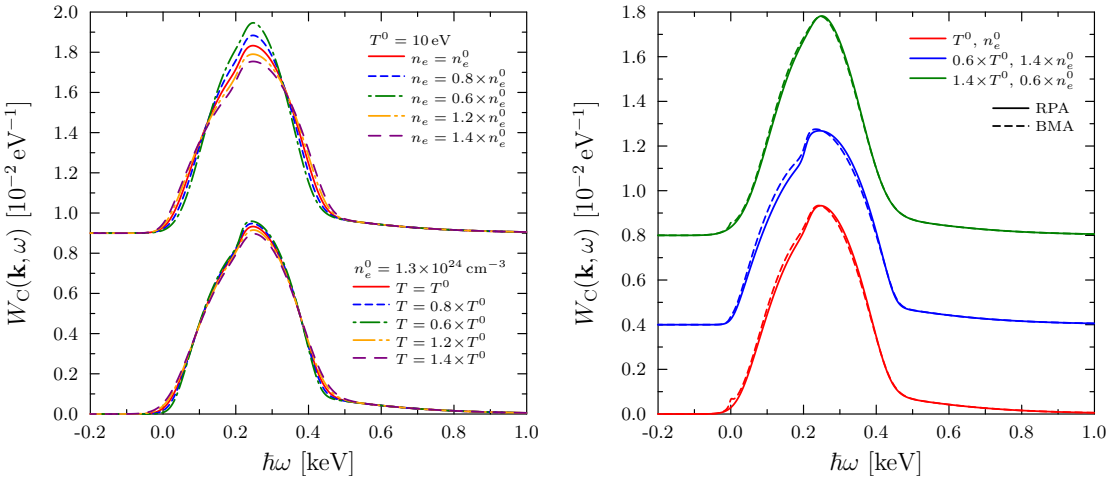

(a) Compton profile sensitivities.

(b) RPA compared to BMA.

Figure 7.4: (a): Comparison of the relative electron temperature and number density sensitivities of the total inelastic scattering for a range of conditions around $T = 10\,\mathrm{eV}$ and $n_e = 1.3 \times 10^{24}\,\mathrm{cm}^{-3}$ for a scattering angle of $\theta = 135°$. The free-free and bound-free contributions are taken in RPA and IA, respectively. (b): Effect of strong coupling and collisions on the profiles for different conditions, as given by the extended BMA model.

bound L-shell electrons are present, such that $\bar{Z}_\mathrm{C}^\mathrm{f} < 4$, a characteristic temperature and density-insensitive distortion to the free-free scattering contribution could be observed. The experimental data, however, shows no sign of such transitions. Conversely, average atom models, such as Thomas-Fermi theory, predict $\bar{Z}_\mathrm{C}^\mathrm{f} \sim 2$, leading to significant discrepancies in the predicted compression of the target; such findings are clearly important to measurements of material properties such as the equation of state.

Note that the ionization potential of carbon K-shell electrons is significantly larger than the mean temperature in the shell and, thus, more strongly ionized states are extremely unlikely. A separate check on the mean charge state has been performed by R. Baggott by solving a set of degeneracy-corrected Saha-Boltzmann equations for the conditions predicted by HYDRA simulations of the implosion. The results for $t = 3.4\,\mathrm{ns}$ (Fig. 7.5) demonstrate the ionization equilibrium of the carbon ions is overwhelmingly dominated by He-like states in the dense part of target which dominates the XRTS signal. As expected, significant contributions from more strongly charged carbon are confined to the high-temperature, low-density corona which do not affect the overall signal. Based on these observations and simulations, it is reasonable to conclude that the temperature and density sensitivity of the free-free and K-shell bound-free scattering profiles allows for the complete characterisation of the electronic subsystem.

The sensitivities of the total Compton scattering profile for a range of conditions around these values (for $\theta = 135°$) are shown in Fig. 7.4(a). As expected, the profile is more sensitive to the electron density than to the temperature since the plasma is moderately degenerate, $D_e \sim 10$. Under these conditions, the inelastic scattering profile is found to

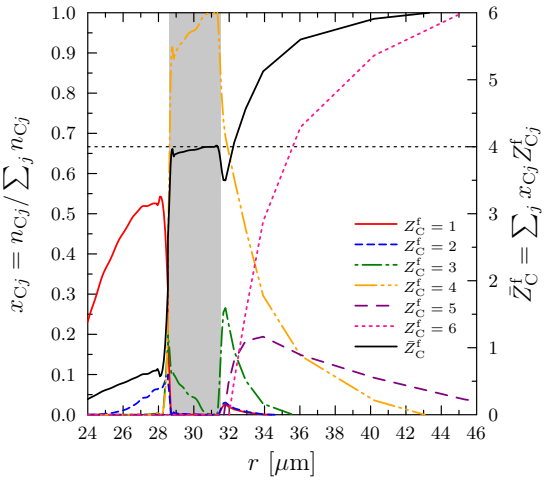

Figure 7.5: Degeneracy-corrected Saha-Boltzmann calculations (courtesy of R. Baggott) based the simulated temperature and density profile at $t = 3.4\,\mathrm{ns}$. The continuum lowering effect is included self-consistently using the Stewart-Pyatt model Eq. (3.78). The results show the dominance of states with $Z^f_C = 4$ in the dense part of the shell which most strongly contributes to the scattering spectrum (grey shaded region).

be quite similar for different theoretical models despite the fact that the electron coupling parameter is relatively large, $\Gamma_{ee} \lesssim 0.5$. In particular, including electron-ion collisions and electron-electron correlations via the extended BMA model discussed in Section 3.6.5 give negligible improvements over weakly coupled RPA calculations (see Fig. 7.4(b)). This result reflects the fact that the free-free correlations are less important for large k and that electron-ion scattering channels are efficiently Pauli blocked in degenerate matter. The inelastic scattering due to free electrons will therefore be treated within RPA throughout the remainder of this chapter. Furthermore, the bound-free feature is treated in IA since it has been shown to most closely reproduce the shape of high-precision calculations based on real-space Green's functions [Fletcher et al., 2014].

7.3.3 Elastic scattering contributions

In contrast to the inelastic scattering, the elastic Rayleigh feature results from electrons which follow the low-frequency density fluctuations of the ions and, thus, is an excellent measure for the static ionic structure and the associated screening properties [Riley et al., 2002; Barbrel et al., 2009; Kritcher et al., 2009; Ma et al., 2013]. The Rayleigh amplitude in partially-ionized multicomponent WDM was given in Eq. (3.27). In the present case of simple CH plastic with a well-defined mean charge state, one need only consider the contributions from fully stripped hydrogen ions (protons) and helium-like carbon ions. The Rayleigh amplitude is therefore

$$W_R(k) = q_H^2(k) S_{HH}(k) + 2q_H(k)\left[f_C(k) + q_C(k)\right] S_{HC}(k) + \left[f_H(k) + q_H(k)\right]^2 S_{CC}(k). \quad (7.1)$$

For these experiments, the potentially large theoretical uncertainty related to the partial SSFs of the ions, e.g. due to screening and short-range repulsion, is heavily mitigated by the large k probed by the x-rays where one has $S_{ab}(k) \approx \delta_{ab}$. Here, high-accuracy DFT-MD simulations can be performed for benchmarking alternative, less computationally expensive methods such as the HNC approach.

The partial SFFs (provided courtesy of J. Vorberger) from DFT-MD simulations of CH are shown in Fig. 7.6(a). The conditions correspond to those reported by Fletcher et al. for a delay of $t = 3.4\,\mathrm{ns}$, based on analysis of the shape of the Compton feature only: $\rho = 5.78\,\mathrm{g\,cm^{-3}}$ and $T = 10\,\mathrm{eV}$. For comparison, multicomponent HNC calculations using screened ion-ion potentials based on both DH and FWS static dielectric functions are also shown. The results clearly demonstrate the robustness of HNC calculations in this regime (especially at the large k of interest). Moreover, a mean carbon ionization of $\bar{Z}_\mathrm{C}^\mathrm{f} = 4$ is appropriate to characterise the ion-ion interactions. Similar agreement is found for all conditions in the range of temperatures and densities of interest to this work. It is interesting to note that no significant differences can be seen between the HNC calculations using different screening models. This simply reflects the fact that the mean ion separation in this density range is too large for finite-wavelength screening to modify the ion-ion interaction potential. Based on these results, the only remaining quantities with significant theoretical uncertainties are the screening clouds around the ions.

Examples of different approaches to the static structures of the screening and bound electrons are shown in Fig. 7.6(b). For the form factors of the bound electrons, the simple approach based on screened hydrogenic wavefunctions (3.29) gives a good description of DFT calculations in general, although a small difference of c.a. 2.5% can be seen in the range of interest. Such discrepancies are mitigated in this work by using a fit to the DFT results with an accuracy of $< 0.1\%$. For the screening cloud, a significant difference

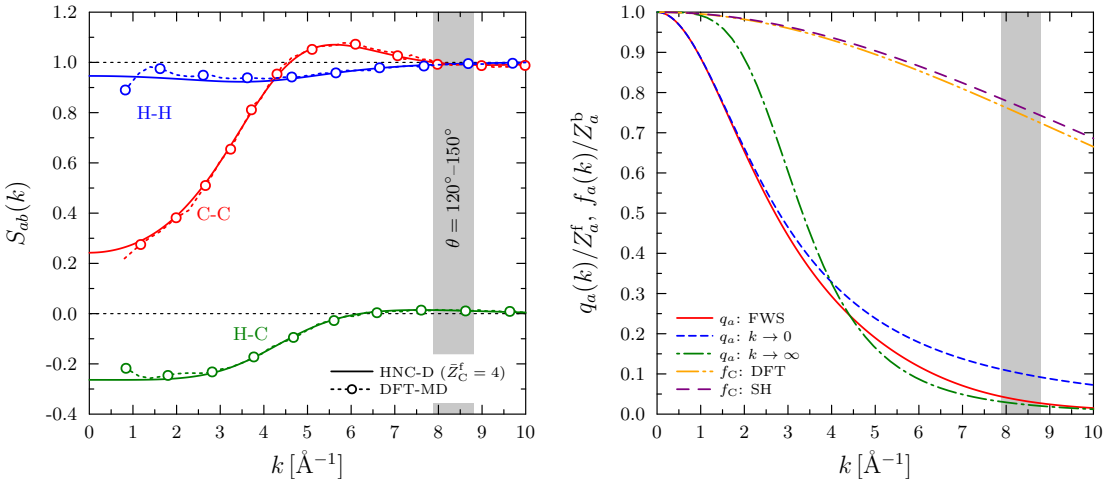

(a) Partial static structure factors.

(b) Screening and bound electron form factors.

Figure 7.6: (a): Comparisons of partial static structure factors for warm dense plastic at $\rho = 5.78\,\mathrm{g\,cm^{-3}}$ and $T = 10\,\mathrm{eV}$ calculated from DFT-MD simulations (courtesy of J. Vorberger) and using the classical multicomponent HNC method. For the HNC calculations the mean carbon ionization is fixed at $\bar{Z}_\mathrm{C}^\mathrm{f} = 4$ and the ion-ion interactions is described by a Debye potential to account for electronic screening. (b): Comparison of different models of screening cloud and bound electron form factors for helium-like carbon under the same conditions as panel (a). In both panels the range of wave numbers of interest are shown by the vertical grey strip.

between the DH and FWS models is clearly present, with the latter approaching the short-wavelength expansion limit and is around 3 times smaller than the prediction of a Debye-like approach. From Eq. (7.1), the most important contribution is that of the carbon ions. Thus, simultaneous analysis of the inelastic and elastic scattering data provide a direct and highly accurate capability for investigating screening.

7.3.4 X-ray source function

In addition to the theoretical description of the scattering profile, extraction of the plasma parameters from experimental data is also sensitive to the shape of the x-ray source function $\Sigma(\omega)$. In particular, convolution of the dynamic scattering cross section with $\Sigma(\omega)$ broadens the inelastic peak, sets the spectral shape of the elastic peak and also contributes to its amplitude. Shifting of the inelastic component may also occur if the source function is strongly asymmetric, e.g. due to depth broadening effects in crystal-based spectrometers [Pak et al., 2004] or the presence of satellite resonance lines. The contribution to the elastic scattering amplitude is of particular interest here as it represents a source of uncertainty on measurements of the static properties of the plasma such as the screening cloud. The amplitude of $\Sigma(\omega)$ is determined by the normalisation condition Eq. (1.36).

Until relatively recently, it has been common practice to assume some analytic form for $\Sigma(\omega)$. In order to determine the most accurate fit to the data possible, it is advantageous to monitor the probe source and take scattering data simultaneously. The resulting shape can then be fitted and normalised numerically to provide an accurate representation of $\Sigma(\omega)$ which includes blurring effects such as instrument resolution and source broadening. Unfortunately, the orientation of the gold cone protecting the scattering spectrometer precludes the possibility of monitoring the x-ray source in this experiment. However, it is possible to extract an estimate of the source shape directly from the experimental data since here the Compton and Rayleigh peaks are clearly separated in frequency space. In this work, the extracted source profiles for each set pump-probe delay used have been provided by L. Fletcher.

7.4 Statistical analysis of experimental data

In order to determine the plasma conditions from the experimental data, a statistical analysis with respect to the probability density corresponding to χ^2 statistics is used, as described in Section 6.5.1. In contrast to the example given in the previous chapter, here the charge state is assumed to be known and the temperature and electron density are allowed to vary independently. As before, the best fit is defined by the location of the global minimum of the χ^2 parameter, whereas the quality and robustness of the fit is estimated by both the goodness-of-fit metric and the shape and amplitude of the probability density function.

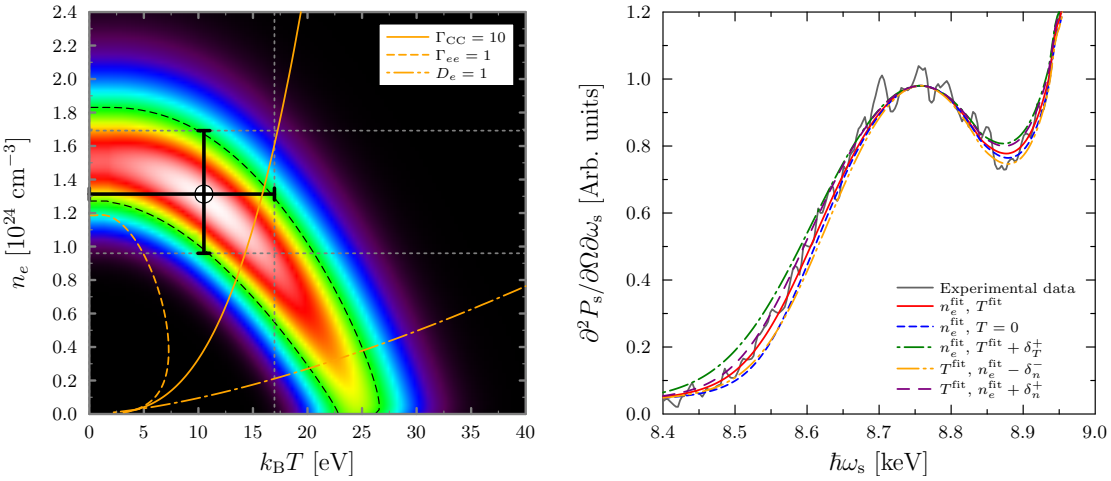

(a) PDF for χ^2 fitting of the Compton peak only. (b) 1σ fitting sensitivity of the Compton peak.

Figure 7.7: (a): Probability distribution function for χ^2 statistics based on fitting the Compton feature only, i.e. using an ideal Rayleigh weight based on Eq. (6.18). The black dashed contour marks the region containing $1\sigma = 68.27\,\%$ of the total probability, giving an estimate of the fitting error. Furthermore, contours denoting the regions of strong coupling for electrons and carbon ions and degeneracy are shown by the orange curves. (b): Comparison of the experimental data and theoretical calculations within the bounds of 1σ certainty. In both panels the pump-probe delay is $t = 3.4\,\text{ns}$.

7.4.1 Modelling inelastic scattering only

Firstly, it is prudent to consider fitting the data based on the Compton feature only. Here, the analysis uses the extracted x-ray source function in conjunction with Eq. (6.18) to reproduce the shape and amplitude of the Rayleigh peak. The values of $W_R(k)$ given by this approach may be taken as experimental measurements of the Rayleigh weight. As demonstrated by Fig. 7.7(a), the fitting procedure results in a well-defined best fit showing a clear peak in the probability density. As expected for the partially degenerate conditions created, the PDF shows a highly elongated shape along the temperature axis indicating much greater sensitivity to the electron density. For example, considering a pump-probe delay of 3.4 ns yields best fit conditions $n_e = 1.31(\pm 0.37) \times 10^{24}\,\text{cm}^{-3}$ and $k_B T = 10.5(+6.5)\,\text{eV}$. Extracted conditions for 3.5 ns and 3.6 ns yield decreasing densities and temperatures consistent with the cooling and decompression of the shell, in agreement with the predictions of the HYDRA simulations.

Once again, the estimated error on these measurements are quantified by finding the contour delineating the region in density-temperature space containing 68.27 % of the total probability, i.e. the 1σ confidence interval. Using the ideal Rayleigh weight, typical error bars of ±20-30 % for the density are found, whereas only an upper limit, typically around 60 %, can be rigorously deduced for the temperature due to the temperature-insensitivity of the theoretical models for colder, strongly degenerate states. The sensitivity of the

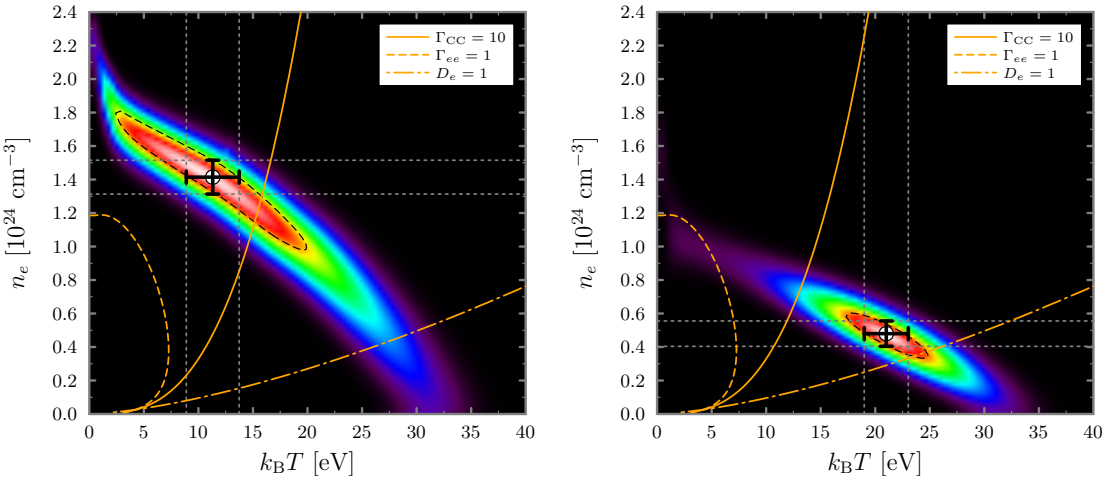

(a) PDF for χ^2 fitting using the FWS model.

(b) PDF for χ^2 fitting using the DH model.

Figure 7.8: (a): Probability distribution function for χ^2 statistics based on simultaneously modelling inelastic and elastic scattering, with screening cloud described by finite-wavelength screening (FWS). (b): Same as panel (a), but using the Debye-Hückel (DH) limit of the screening cloud. In both panels the pump-probe delay is $t = 3.4\,\mathrm{ns}$.

inelastic scattering spectra within the bounds of such errors is shown in Fig. 7.7(b). Note that all the curves shown as normalised to the amplitude of the Compton peak.

7.4.2 Including modelling of elastic scattering

Well-defined conditions are also found when the Rayleigh weight is calculated from theory using the DH and FWS approaches to describe the screening of a the bare Coulomb electron-ion interaction (see Fig. 7.8). Note that in both cases the shape of the contours indicate roughly twice the density sensitivity and substantially improved accuracy with respect to the temperature, compared to using the ideal (experimental) Rayleigh weight. This stems from the additional constraints imposed by the temperature and density dependence of the screening cloud. However, the different screening models yield quite different conditions. For example, at $t = 3.4\,\mathrm{ns}$, the best fit using finite-wavelength screening is found at $n_e = 1.52(\pm 0.1) \times 10^{24}\,\mathrm{cm}^{-3}$ and $k_B T = 9.3(\pm 2.4)\,\mathrm{eV}$, whereas for Debye-like screening the best fit occurs for $n_e = 4.8(\pm 0.76) \times 10^{23}\,\mathrm{cm}^{-3}$ and $k_B T = 20.9(\pm 2.0)\,\mathrm{eV}$. Again, the same trend of cooling and decompression is found for later times.

7.4.3 Results for the Rayleigh weight

Applied to the same conditions, the elastic scattering strength predicted by different screening models significantly differs. In general, the Rayleigh peak is too large if the DH model is applied, whereas the amplitude given by finite-wavelength screening agrees with the measurements within the estimated error bars (see Fig. 7.9(a)). A comparison of the elastic Rayleigh strength obtained using the three approaches presented versus the ideal electron

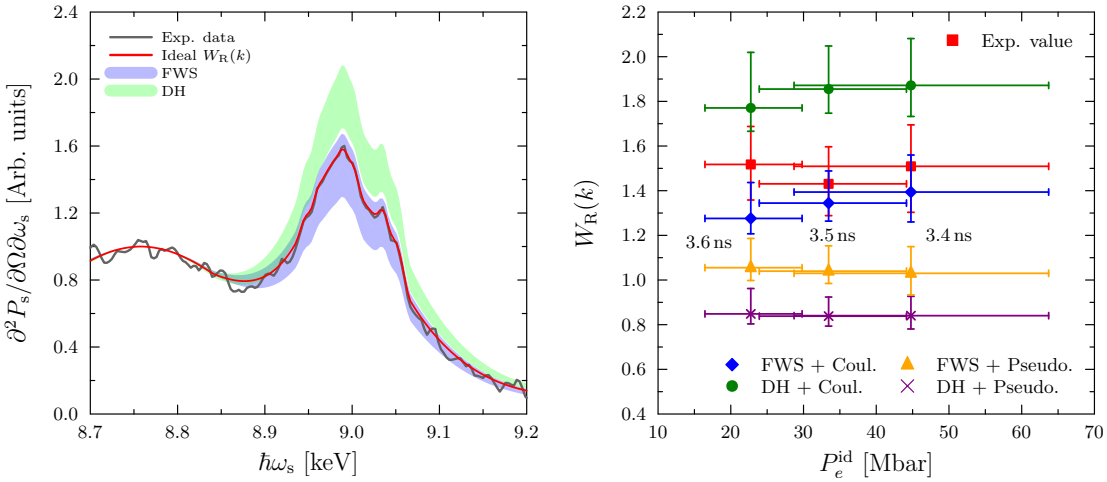

(a) Rayleigh feature using FWS and DH models.

(b) Comparison of Rayleigh weights.

Figure 7.9: (a): Comparison of experimental data for $t = 3.4\,\mathrm{ns}$ in the region around the elastic Rayleigh scattering peak showing the best fit resulting from an ideal fit, i.e. using the observed ratio of elastic to inelastic scattering, and from theoretical calculations based on the DH and FWS models for the screening cloud. The error bands for these calculations show that the FWS model is most suitable, whereas the DH model is clearly ruled out. (b): Results for the Rayleigh weight based on all approaches; ideal W_R and FWS DH models using both Coulomb and empty core pseudo-potential electron-ion interactions. The reference states are based on the best fit conditions determined from the ideal Rayleigh weight, which also determine the large error bars.

pressure $P_e^{\mathrm{id}} = n_e k_B T \mathcal{F}_{3/2}(\eta_e)/D_e$ (thereby combining electron density and temperature into a single parameter) is shown in Fig. 7.9(b). Here, the plasma conditions obtained are taken from fitting with the ideal Rayleigh weight as the reference state. The corresponding errors are subsequently propagated through the calculation of for each model.

For all the time delays studied in this work, significant deviations between the results obtained using Debye-like screening and the extracted (experimental) values are found. On the other hand, finite-wavelength screening is in much better agreement for 3.4 ns and 3.5 ns. For the latest time, $t = 3.6\,\mathrm{ns}$, the cooling and decompression of the imploding shell reaches a state where the electron-electron coupling exceeds unity, such that an RPA description is not likely to be reasonable. This is reflected in the reduction of accuracy found for the FWS model at this time. A more robust model of the free-free inelastic scattering which includes dynamic local field corrections may be required to rigorously analyse the data in this strongly coupled regime.

7.4.4 Pseudo-potential approach to electron-ion interaction

Up to now the free electrons have been assumed to respond to the ions via a screened Coulomb-like potential determined by the effective charge of the ions. Clearly, this is justified for the fully ionized hydrogen component. However, the electrons still bound to

the carbon ions will modify the electron-ion interactions. As shown in Fig. 3.2(b), a pseudo-potential approach based on an empty core model results in an oscillating screening cloud at large k. In the case of helium-like carbon, the cut-off radius of the ionic core can be estimated from the measured effective size of C^{+4} ions, which is given by the web of elements catalogue as $r_c = 29\,\mathrm{pm}$.

Using this simple model in conjunction with the FWS model for the shielding of the interaction potential, the screening cloud is predicted to be small and negative for the wave numbers presently under consideration. This effect is exacerbated by the weaker decay of the DH screening in k-space. Running the fitting code on the experimental data with this form of the electron-ion potential does not result in a well-defined global maximum in the PDF for either the FWS or DH screening approaches. Moreover, comparing the resulting predicted Rayleigh weights against the reference states reveals very poor agreement, with both models yielding substantially lower elastic scattering than observed (see Fig. 7.9(b)).

This unexpected result suggests that significantly more experimental and theoretical effort is required to fully understand screening under extreme conditions. On the other hand, the fact that the FWS model gives generally good agreement with the experimental results constitute the first direct evidence for observation of finite-wavelength screening in WDM using XRTS. As described early in this chapter, the implications of this are potentially far-reaching since understanding screening is of fundamental importance for a wide range of charged-particle systems. In particular, Debye-like screening presently builds the basis for theoretical investigations of, e.g., the phase diagram [Hamaguchi et al., 1996], the ion dynamics [Vorberger et al., 2012], the nucleation times [Daligault, 2006] and relaxation properties [Gericke et al., 2002a] of matter under extreme conditions. Thus, understanding of particle and energy transport in stars or large planets as well as modelling capabilities for ICF experiments may need to be revised with respect to more accurate screening models

Chapter 8

Summary and future work

The principal objective of this thesis was to develop a robust numerical tool for modelling, simulating and analysing experiments applying x-ray Thomson scattering (XRTS) as a diagnostic for dense matter. The features that were identified as particularly important were the combination of a generalised multicomponent framework for the dynamic structure factor (DSF), a generalised non-equilibrium description for the free electrons, and further detailed modelling considerations such as careful averaging over evolving and inhomogeneous targets. The other main objective was to use the resulting modelling capability to design, optimise and analyse current and ongoing experiments. In particular, the different relaxation stages in strongly-driven matter are investigated and their characteristic signatures in the XRTS spectrum are predicted.

8.1 Overview of results

The important results of each chapter are summarised in the following points. Details of where significant published contributions have been made are given where appropriate.

- It was shown that the power spectrum of the radiation scattered by a dense target probed with x-rays is dominated by the electrons. In particular, the dynamic correlations between electron density fluctuations, described by the *dynamic structure factor* (DSF), were shown to be the principal quantities of interest.

- A general quantum statistical description of dense matter was given to provide a robust theoretical basis for investigations of XRTS under conditions in which quantum effects and strong interactions are important. The fundamental objects underpinning the description of the density fluctuations were shown to be the polarisation functions. Successive approximations of the governing equation for these functions were employed in order to make their evaluation tractable. Specifically, the important *random phase approximation* (RPA) was shown to be the most simple treatment which retains dynamic screening and (weak) correlations between particles.

- For partially ionized plasmas, it was shown that the DSF can be decomposed to recover the well-known expression of Chihara. The multicomponent generalisation of this model was adopted as the basic framework in order to correctly represent scattering from realistic (complex) targets. The Rayleigh scattering due to both bound electrons and the screening cloud were treated in the static limit. In particular, it was shown that *finite-wavelength screening* (FWS) at large wave numbers was particularly important for properly describing the screening cloud in the warm dense matter (WDM) regime. The static structure of the ions was taken in the *hypernetted-chain* approximation. It was shown that strong short-ranged repulsion between ions were crucial for describing elastic scattering from WDM. The dynamic inelastic scattering due to free electron was investigated primarily in RPA. Specifically, the dispersion and damping of plasmons were shown to yield a sensitive diagnostic of the free-electron density and mean kinetic energy. For the bound-free contribution the well-known *form factor approximation* and *impulse approximation* were used. These elements were brought together into a multicomponent scattering simulation (MCSS) code. Publications in which calculations using the MCSS code have assisted data analysis include those of Ma et al. [Ma et al., 2014] and Fletcher et al. [Fletcher et al., 2015].

- Under non-equilibrium conditions, the commonly used equilibrium DSF based on the fluctuation-dissipation theorem must be abandoned. Instead, the DSF must be derived from real-time non-equilibrium Green's functions. The results affect both the high-frequency free electron contribution and also the screening cloud which arises in the elastic scattering term. The collective scattering spectrum was shown to be most significantly affected. In particular, the dispersion and damping of plasmons are substantially altered by significant numbers of non-thermal, high-energy electrons. The non-equilibrium model was tested against recent experimental data taken at the FLASH FEL facility. It was shown that time-averaging over rapidly evolving non-equilibrium states is important to interpreting scattering from strongly-driven targets. Here, the important features of the non-equilibrium electron distribution were captured using a simple analytic *bump-on-hot-tail* (BOHT) model. Furthermore, the use of a non-equilibrium, multicomponent framework explained the absence of Rayleigh scattering in the FLASH data. The work presented in this chapter has been documented in publications by Chapman and Gericke [Chapman and Gericke, 2011] and Chapman et al. [Chapman et al., 2012; 2013b].

- Following the generalisation of the MCSS code to non-equilibrium conditions, it was suggested that XRTS could be used as a diagnostic for electron-ion temperature relaxation. To assess its suitability for such experiments, simple simulations of temperature relaxation in isochorically heated targets were performed. The main contributions for these calculations were shown to be the energy exchange rate and the heat capacities of the electrons and ions. Several options for the optimum way to

employ XRTS were subsequently discussed, and it was shown that a combination of spectrally- and angularly-resolved measurements in foam-density targets could potentially be used to simultaneously determine the electron and ion temperatures. Moreover, clearly identifiable differences in the elastic scattering evolution suggested that XRTS could be used to differentiate between energy relaxation models. The reduced approach to the coupled modes model used in this chapter has been documented in the publication of Chapman et al. [Chapman et al., 2013a].

- Next, experiments conducted over longer time scales testing the properties of matter at extreme conditions were considered. Using radiation-hydrodynamics simulations of implosions of millimetre-scale plastic spheres at the National Ignition Facility (NIF), a detailed study of the expected XRTS signal was undertaken. Here, non-equilibrium effects could be neglected, whereas strongly inhomogeneous conditions had to be considered. The MCSS model was used to post-process the hydrodynamics output to produce high-fidelity, time-dependent simulations which fully included plasma gradients. Furthermore, attenuation of the probe beam and source divergence was included using a novel scheme. Statistical analysis was performed on synthetic data created using the calculations to assess the feasibility of using XRTS as a temperature and ionization diagnostic. The results showed that a simple fit based on a single set of plasma conditions gave good agreement to the mass-weighted average temperature predicted by the simulations. However, the fitted ionization was substantially underestimated due to inhomogeneity. The work presented in this chapter has been documented in the publication of Chapman et al. [Chapman et al., 2014].

- The final chapter used the tools and methods developed in the previous chapters to analyse experimental data. The geometry used in the experiment accessed the non-collective scattering regime, enabling measurements of the free electron temperature and density from the inelastic feature. The configuration used also mitigated uncertainty in the ion structure, making possible direct measurements of the screening cloud at large k. It was shown that good agreement with the data could only be obtained using the FWS model. The results constituted the first experimental observation of finite-wavelength screening in WDM using XRTS. The work performed in this chapter has contributed to several publications, e.g. those of Fletcher et al. [Fletcher et al., 2013; 2014] and Chapman et al. [Chapman et al., 2015].

8.2 Future work and conclusions

Throughout this thesis, numerous approximations and limitations of the theoretical description of XRTS have been highlighted. Of particular importance are the limitations of the RPA for descibing the free electrons. Since a robust and consistent methodology for deriving higher-order corrections was given in Chapter 2 using a perturbation expansion in

the screened potential, it would be interesting to evaluate the resulting terms. Initially, one might evaluate only the first-order corrections. However, such an extended model would still be within the linear response approximation since the corrections relate to the one-components subsystems only. To go beyond linear response requires the direct electron-ion coupling be evaluated. Undertaking such work would give a highly robust framework for modelling XRTS from strongly coupled systems with arbitrary distribution functions.

In terms of the ions, the main deficiencies of the MCSS model relate to the restriction of equilibrium in the HNC approximation, and the physics which can be modelled using simple forms for the ion-ion interaction. It would therefore be interesting to undertake a detailed comparison of first-principles simulation results with HNC calculations using suitably flexible pseudo-potentials. Building a comprehensive understanding of the variation of such parametric forms with temperature, density and ionization may shed light on how to construct more effective simple models, which could be used to analyse XRTS data from WDM. An example of this was given in Chapter 5, where the form of the static ion structure had to be estimated using overly-simplistic ion-ion potentials due to lack of understanding of the effect of bound electrons under evolving conditions.

The points highlighted thus far have focussed on deficiencies in theory. Additionally, it is worth stating that best practice methods must be developed and stringently followed when modelling the macroscopic aspects of real experiments. Of particular relevance are time-averaging over evolving states and accounting for inhomogeneous conditions. These issues will become more important as more XRTS experiments are undertaken using FELs and high-energy laser facilities such as NIF. Furthermore, the importance of detailed modelling of the geometry of experiments must be recognised. For example, the integration of the scattering signal over the inhomogeneous plasma in Chapter 6 resulted in a spectrum in which all scattered x-rays are focussed to an infinitely distant detector. In reality, the Bragg reflection condition of the crystals used in x-ray spectrometers requires that only scattering originating from different regions of the target contribute to the intensity of the measured signal in different energy bins. The resulting source broadening effect was therefore not captured in this work and, accordingly, will make direct comparisons between theory and data more difficult. At the time of writing, the next series of shots from the Gbar equation of state NIF experiments is being evaluated using the models developed in this thesis. The initial results show excellent agreement to the measured signal is obtained only when gradients, k-blurring and source broadening are simultaneously considered.

Finally, even for experiments in which such considerations are not anticipated to be significant, detailed modelling may reveal both problems and solutions to the accurate interpretation of experimental data. A good example of this is given by the analysis given in Chapter 7. Here, a novel observation was made possible by using simulations and detailed three-dimensional modelling to eliminate sources of uncertainty on the elastic scattering amplitude, leaving a deficiency in the commonly-used Debye-Hückel description of screening as a viable explanation of the trends in the observed data.

Appendix A

Analytical and numerical methods for modelling the dynamic structure of non-equilibrium plasmas

A.1 Bump-on-hot-tail model distribution function

For the purposes of investigating the dielectric and spectral properties of non-equilibrium plasmas with high-energy quasi-thermal tails and non-thermal populations, one may appeal to a simple model distribution function

$$f_e(p) = A_0 \left[A_{\rm c}\, g_{\rm c}(p) + \sum_i A_{{\rm h}i}\, g_{{\rm h}i}(p) + \sum_j A_{{\rm b}j}\, g_{{\rm b}j}(p) \right]. \tag{A.1}$$

Here, the functions $g_a(p)$, with $a = {\rm c}, {\rm h}, {\rm b}$ describe basis functions which provide the functional forms required to represent the distinct components. Each component is normalised such that $\max(g_a(p)) = 1$. The cold (c) component corresponds to the background population, the hot (h) components to high-energy tail populations and the bump (b) components to non-thermal features driven at specific energies. The coefficients A_a are weighting factors that select the proportion of each basis function. Finally, A_0 is a normalisation pre-factor which is determined by the usual condition

$$n_e = \frac{1}{\pi^2 \hbar^3} \int_0^\infty {\rm d}p\, p^2\, f_e(p). \tag{A.2}$$

Usually, the basis functions used for the cold and hot components are given by normalised equilibrium-like forms, i.e. the Fermi-Dirac or Maxwell-Boltzmann distributions, and the bump components is described by a shifted Gaussian

$$g_{\rm c}(p; p_{\rm c}, \eta_{\rm c}) = \left(1 + e^{-\eta_{\rm c}}\right) \left[1 + e^{p^2/2p_{\rm c}^2 - \eta_{\rm c}}\right]^{-1}, \tag{A.3}$$

$$g_{\mathrm{h}}(p;p_{\mathrm{h}}) = e^{-p^2/2p_{\mathrm{h}}^2}, \tag{A.4}$$

$$g_{\mathrm{b}}(p;p_{\mathrm{b}},p_0) = e^{-(p-p_0)^2 2p_{\mathrm{b}}^2}. \tag{A.5}$$

The widths characterising the exponential decay of the above functions in momentum space can be associated with the effective 'temperatures' of the components via $p_a = (m_e k_{\mathrm{B}} T_a)^{1/2}$. Additionally, the bump components require the locations of the maxima in momentum space p_0. Furthermore, for degenerate matter one must specify the effective chemical potential η_{c}. Note that these parameters, nomenclature notwithstanding, are *not* representative of truly physical quantities such as temperature.

The work presented in Chapter 4 demonstrates that qualitatively accurate representations of the dielectric and spectral properties of non-equilibrium plasmas can be obtained by considering the simple case of (A.1) with one hot and one bump component. Thus, from now on the form of the model distribution is restricted to

$$f_e(p) = A_0 \left\{ A_{\mathrm{c}} \left(1+e^{-\eta_{\mathrm{c}}}\right) \left[1+e^{p^2/2p_{\mathrm{c}}^2-\eta_{\mathrm{c}}}\right]^{-1} + A_{\mathrm{h}}\, e^{-p^2/2p_{\mathrm{h}}^2} + A_{\mathrm{b}}\, e^{-(p-p_0)^2/2p_{\mathrm{b}}^2} \right\}. \tag{A.6}$$

In this case, the overall normalisation is readily found to be

$$A_0 = \frac{n_e \Lambda_{\mathrm{c}}^3}{2A_{\mathrm{c}}} \left[\left(1+e^{-\eta_{\mathrm{c}}}\right) \mathcal{F}_{1/2}(\eta_{\mathrm{c}}) + \mathcal{A}_{\mathrm{hc}} \mathcal{T}_{\mathrm{hc}}^{3/2} + \mathcal{A}_{\mathrm{bc}} \mathcal{T}_{\mathrm{bc}}^{3/2} \Psi(p_0/\sqrt{2}p_{\mathrm{b}}) \right]^{-1}, \tag{A.7}$$

where $\mathcal{A}_{\mathrm{hc}} = A_{\mathrm{h}}/A_{\mathrm{c}}$, $\mathcal{T}_{\mathrm{hc}} = T_{\mathrm{h}}/T_{\mathrm{c}}$ and $\Psi(x) = xe^{-x^2} + \frac{1}{2}(2x^2+1)\big[1+\mathrm{erf}(x)\big]$. The fully normalised distribution function is therefore

$$f_e(p) = \frac{n_e \Lambda_{\mathrm{c}}^3}{2} \left[\frac{\left(1+e^{-\eta_{\mathrm{c}}}\right) \left[1+e^{p^2/2p_{\mathrm{c}}^2-\eta_{\mathrm{c}}}\right]^{-1} + \mathcal{A}_{\mathrm{hc}}\, e^{-p^2 2p_{\mathrm{h}}^2} + \mathcal{A}_{\mathrm{bc}}\, e^{-(p-p_0)^2/2p_{\mathrm{b}}^2}}{\left(1+e^{-\eta_{\mathrm{c}}}\right) \mathcal{F}_{1/2}(\eta_{\mathrm{c}}) + \mathcal{A}_{\mathrm{hc}} \mathcal{T}_{\mathrm{hc}}^{3/2} + \mathcal{A}_{\mathrm{bc}} \mathcal{T}_{\mathrm{bc}}^{3/2} \Psi(p_0/\sqrt{2}p_{\mathrm{b}})} \right]. \tag{A.8}$$

An important distinction which should be made here is that the ratios $\mathcal{A}$ *do not* correspond to the fractions of electrons occupying particular components. Rather, they simply reflect the scalings applied to the basis functions relative to the cold component.

The fraction of electrons in a specific component can be defined as $x_a = n_a/n_e$, where n_a is given by applying (A.2) to the relevant component. It straightforwardly follows that

$$x_{\mathrm{c}} = \frac{\left(1+e^{-\eta_{\mathrm{c}}}\right) \mathcal{F}_{1/2}(\eta_{\mathrm{c}})}{\left(1+e^{-\eta_{\mathrm{c}}}\right) \mathcal{F}_{1/2}(\eta_{\mathrm{c}}) + \mathcal{A}_{\mathrm{hc}} \mathcal{T}_{\mathrm{hc}}^{3/2} + \mathcal{A}_{\mathrm{bc}} \mathcal{T}_{\mathrm{bc}}^{3/2} \Psi(p_0/\sqrt{2}p_{\mathrm{b}})}, \tag{A.9}$$

$$x_{\mathrm{h}} = \frac{\mathcal{A}_{\mathrm{hc}} \mathcal{T}_{\mathrm{hc}}^{3/2}}{\left(1+e^{-\eta_{\mathrm{c}}}\right) \mathcal{F}_{1/2}(\eta_{\mathrm{c}}) + \mathcal{A}_{\mathrm{hc}} \mathcal{T}_{\mathrm{hc}}^{3/2} + \mathcal{A}_{\mathrm{bc}} \mathcal{T}_{\mathrm{bc}}^{3/2} \Psi(p_0/\sqrt{2}p_{\mathrm{b}})}, \tag{A.10}$$

$$x_{\mathrm{b}} = \frac{\mathcal{A}_{\mathrm{bc}} \mathcal{T}_{\mathrm{bc}}^{3/2} \Psi(p_0/\sqrt{2}p_{\mathrm{b}})}{\left(1+e^{-\eta_{\mathrm{c}}}\right) \mathcal{F}_{1/2}(\eta_{\mathrm{c}}) + \mathcal{A}_{\mathrm{hc}} \mathcal{T}_{\mathrm{hc}}^{3/2} + \mathcal{A}_{\mathrm{bc}} \mathcal{T}_{\mathrm{bc}}^{3/2} \Psi(p_0/\sqrt{2}p_{\mathrm{b}})}, \tag{A.11}$$

It is trivial to show that $x_{\mathrm{c}} + x_{\mathrm{h}} + x_{\mathrm{b}} = 1$, as required by particle conservation.

Substituting Eqs. (A.9 - A.11) into Eq. (A.8), one has

$$f_e(p) = \tilde{x_c}\left[1 + e^{p^2/2p_c^2 - \eta_c}\right]^{-1} + x_h \frac{n_e \Lambda_h^3}{2} e^{-p^2/2p_h^2} + x_b \frac{n_e \Lambda_b^3}{2\,\Psi(p_0/\sqrt{2}p_b)}\, e^{-(p-p_0)^2 2p_b^2}, \quad \text{(A.12)}$$

where $\tilde{x}_c = x_c n_e \Lambda_c^3 / 2\mathcal{F}_{1/2}(\eta_c)$. In this form, the model distribution function for a given electron density is fully characterised by seven free parameters; $\{T_c, \eta_c, T_h, p_0, p_b, x_h, x_b\}$, with $x_c = 1 - (x_h + x_b)$. For the more simple case of a cold bulk component and a single hot tail, i.e. $x_b = 0$, only four free parameters are needed; $\{T_c, \eta_c, T_h, x_h\}$, and $x_c = 1 - x_h$. For simplicity, it is also convenient to remove η_c as a free parameter by noting that the shape of the low-momentum portion of the cold component will not be greatly disturbed from it's equilibrium form, provided that $x_h \ll 1$. One can then use the well-known Padé fit [Ichimaru, 1994b] to determine η_c in terms of n_e and T_c. Only under this approximation may one take $\mathcal{F}_{1/2}(\eta_c) = \frac{1}{2} n_e \Lambda_c^3$, such that $\tilde{x}_c = x_c$.

A.2 Implementation of a fully numerical model

Often, a simple analytic form such as Eq. (A.12) may not be appropriate, and instead the DSF must be calculated in a fully numerical framework. In this case, the fundamental equations are given by Eqs. (4.17 - 4.18), in addition to the electron density Eq. (A.2). The evaluation of these equations gives rise to several important criteria, which warrant brief discussion.

A.2.1 Density convergence check

Firstly, due to factor of p^2 in the integrand, the electron density only converges for an arbitrary distribution function providing sufficiently large momenta are considered. For equilibrium-like distributions, convergence to within a suitably small tolerance may be achieved for a few times the normalisation momentum. The accuracy of the estimate then rapidly improves as exponentially less weight is contributed by higher-momentum states. For strongly non-equilibrium distributions with significant structure deep in the tail, the maximum momentum considered to achieve a converged electron density may need to be far larger. Moreover, evaluating Eqs. (4.17) and (4.18) sets limits on the momentum at $|1 \pm z|$, which scale as ω/k^2. Thus, as the wave number of the fluctuations probed by the incident radiation gets smaller, e.g. using a soft x-ray source such as FLASH or going to extremely small scattering angles, then the minimum momentum required to evaluate Eq. (4.18) can potentially exceed the upper limit used to determine the density.

A simple self-consistency check can be used to safeguard against this possibility (see Fig. A.1). The density is first evaluated within a loop which runs until convergence to within a pre-defined accuracy is reached, yielding an estimate for $x_{\max}$. The latter is then compared to the largest value of $\max(|1 - z|, |1 + z|)$ encountered over the frequency

range of interest (both must be considered since ω can be both positive and negative), and repeated until the condition

$$x_{\max} > \max\left(|1-z|, |1+z|\right) \tag{A.13}$$

is satisfied. Note that because k changes non-linearly over the spectral range, in general giving $k(|\omega|) < k(-|\omega|)$, symmetry relations for frequency shifts of equal magnitude but opposite sign cannot be relied upon.

A.2.2 Evaluation of the Kramers-Kronig integral

The fact that the limits of the momentum integration are determined not only by convergence considerations, but also by the range of frequencies of interest, raises another important consideration. Namely, in constructing the real part of the dielectric function using the Kramers-Kronig relation, the imaginary part must be calculated for a sufficiently large range of frequency shifts. In the context of the present problem, this means that the weight added to the total integral by considering larger frequency shifts must decrease below some required tolerance. For example, the constraint can be satisfied by requiring that the magnitude of the imaginary part at the limits of the spectral range is less than some small fraction of the value at the global maximum

$$\left\{|\mathrm{Im}\,\varepsilon_{ee}(k,\omega_{\min})| \text{ and } |\mathrm{Im}\,\varepsilon_{ee}(k,\omega_{\max})|\right\} \leq 10^{-6}\max\left(|\mathrm{Im}\,\varepsilon_{ee}(k,\omega)|\right). \tag{A.14}$$

The absolute values are taken as the imaginary part changes sign with ω. If this test is not passed, $\omega_{\min}$ and $\omega_{\max}$ are increased (with the spectral resolution held constant) and the calculation is re-run from the beginning.

Provided that the final check on the frequency range is passed, the real part can be easily calculated by transforming the usual representation of the Kramers-Kronig relation

$$\begin{aligned}
\mathrm{Re}\,\varepsilon_{ee}(k,\omega) - 1 &= \int_{-\infty}^{\infty} \frac{\mathrm{d}\omega'}{\pi} \frac{\mathrm{Im}\,\varepsilon_{ee}(k,\omega)}{\omega' - \omega} \\
&= \frac{1}{\pi}\left\{\int_0^{\infty} \frac{\mathrm{d}\omega'}{\omega'}\mathrm{Im}\,\varepsilon_{ee}(k,\omega+\omega') + \int_{-\infty}^{0} \frac{\mathrm{d}\omega'}{\omega'}\mathrm{Im}\,\varepsilon_{ee}(k,\omega+\omega')\right\} \\
&= \frac{1}{\pi}\left\{\int_0^{\infty} \frac{\mathrm{d}\omega'}{\omega'}\left[\mathrm{Im}\,\varepsilon_{ee}(k,\omega+\omega') - \mathrm{Im}\,\varepsilon_{ee}(k,\omega-\omega')\right]\right\}.
\end{aligned} \tag{A.15}$$

It is then clear that $\mathrm{Im}\,\varepsilon_{ee}(k,\omega)$ must be indexed into at frequencies outside the spectral range initially supplied; the largest value being $2\omega_{\max}$. However, since the frequency range convergence test guarantees that frequencies beyond $\omega_{\max}$ contribute (normalised) weight on the order of, e.g., $\lesssim 10^{-6}$, then one can safely extend the frequency range as required and simply pad with zeros, such that

$$\mathrm{Im}\,\varepsilon_{ee}(k,|\omega| > |\omega_{\max}|) = 0. \tag{A.16}$$

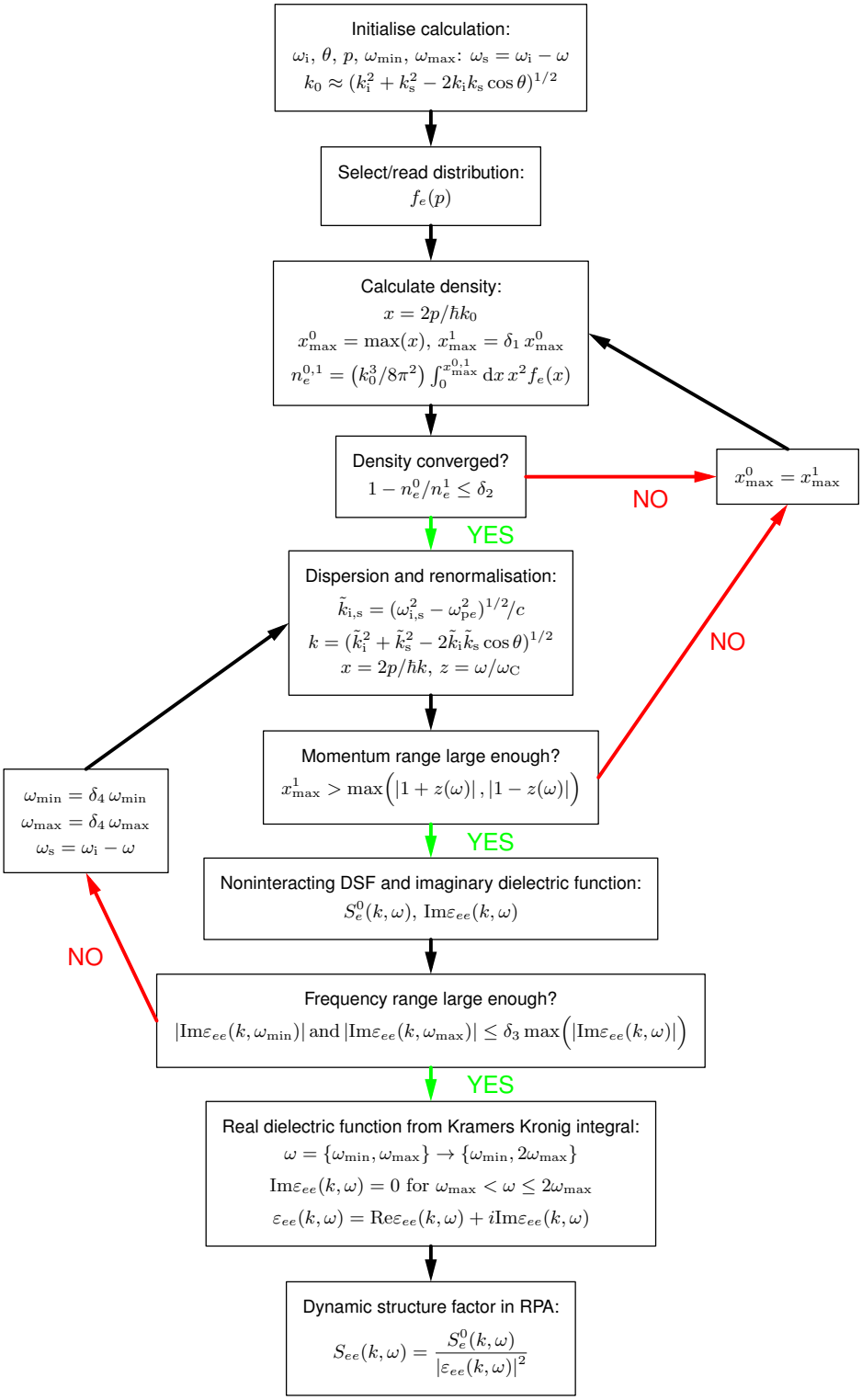

Figure A.1: Flow diagram for evaluating the non-equilibrium dynamic structure model as described by Eqs. (4.17 - 4.18). Typical values of the control constants are $\delta_1 = 1.5$, $\delta_2 = 10^{-3}$, $\delta_3 = 10^{-6}$ and $\delta_4 = 1.5$.

The integration can then be performed without further hindrance by employing a suitable variable transformation and using a general adaptive integration algorithm. Here, an effective transformation is given by *exp-sinh* quadrature, i.e. one write $\omega' = \Omega \exp(\pi \sinh(t))$. The integral then has the form

$$\mathcal{I}(\omega) = \int_{-\infty}^{\infty} \mathrm{d}t \, \cosh(t) \left[f(\omega + \Omega e^{\pi \sinh(t)}) - f(\omega - \Omega e^{\pi \sinh(t)}) \right], \tag{A.17}$$

where Ω is some suitable normalisation frequency, e.g. $\Omega = \omega_{\mathrm{p}e}$. The double-exponential decay of this transformation ensures that the integrand is effectively bounded on a vastly reduced range, such as $-3 \leq t \leq 3$. Subsequently, the complex dielectric function is easily constructed and used to compute the interacting DSF. A flow diagram describing the evaluation of the non-equilibrium model is shown in Fig. A.1.

A.2.3 Additional considerations for dispersion curves

Finally, using the general algorithm described here, one may also compute dynamic response quantities independently resolved in k and ω. An important example is the locus describing the dispersion curves for collective modes, which is given by $\mathrm{Re}\, \varepsilon(\mathbf{k}, \omega) = 0$. This is especially useful for non-equilibrium plasmas since the plasmon resonance location deviates from the modified Bohm-Gross relation at relatively small k. In this case, one performs nested loops over independent frequency and wave number arrays, ignoring the step which refines the momentum normalisation. Moreover, from the fourth moment of the distribution function, i.e. the mean kinetic energy, is also important to the plasmon dispersion. It is therefore also necessary to ensure convergence of $p^4 f_e(p)$ for distributions with significant weight in the high-energy tail. A second convergence test is therefore performed with respect to $\langle K_e \rangle$ before the momentum range is checked.

Appendix B

Reduced approach to the coupled modes model for temperature relaxation

In Chapter 5 it was shown that temperature relaxation in dense plasmas is strongly sensitive to the electron-ion energy transfer rate. Unlike the Landau-Spitzer (LS) model Eq. (5.4), the coupled mode (CM) energy transfer rate Eq. (5.14) must be evaluated numerically. A reduced approach to the coupled modes rate [Chapman et al., 2013a] is therefore required to facilitate highly-resolved relaxation calculations with hundreds of time steps.

B.1 f-sum rule approach

In the case of uncoupled collective modes, i.e. the Fermi golden rule (FGR), a reduced approach which considerably simplifies numerical evaluation has been derived by Hazak et al. [Hazak et al., 2001]. The reduced FGR (RFGR) is based on three approximations which are well-fulfilled under a wide range of conditions. Firstly, the structure of the frequency integral is modulated by the spectral function of the ions, $\mathrm{Im}\,\varepsilon_{ii}^{-1}(k,\omega) = -\mathrm{Im}\,\varepsilon_{ii}(k,\omega)/\left|\varepsilon_{ii}(k,\omega)\right|^2$. This function decays exponentially over significantly smaller frequency scales than the equivalent electronic term due to the large mass difference $m_i \gg m_e$. Taylor expanding the electronic term about $\omega = 0$ is therefore justified

$$\mathrm{Im}\,\varepsilon_{ee}^{-1}(k,\omega) \approx \omega \left[\frac{\partial}{\partial\omega}\mathrm{Im}\,\varepsilon_{ee}^{-1}(k,\omega)\right]_{\omega=0}. \tag{B.1}$$

Secondly, provided that $\beta_a\hbar\omega_{\mathrm{p}a} \ll 1$, one may also Taylor expand the Bose functions

$$n_{\mathrm{B}i}(\omega) - n_{\mathrm{B}e}(\omega) \approx \frac{k_{\mathrm{B}}}{\hbar\omega}(T_i - T_e). \tag{B.2}$$

Eq. (B.2) is valid for non-degenerate states and for small frequencies. Furthermore, this approximation is always expected to hold for the ions since they are ubiquitously non-

degenerate and their mode spectrum is always downshifted due to screening [Vorberger and Gericke, 2014]. Thirdly, assuming only static screening, then the derivative in Eq. (B.1) can be simplified further by approximating $\operatorname{Im}\varepsilon_{ee}^{-1}(k,\omega) \approx -\operatorname{Im}\varepsilon_{ee}(k,\omega)/\left|\varepsilon_{ee}(k,0)\right|^2$. For arbitrary degeneracies one finds

$$\operatorname{Im}\varepsilon_{ee}^{-1}(k,\omega) \approx \frac{\sqrt{\pi}\omega}{\sqrt{2}kv_e}\frac{k^2\kappa_e^2}{\left(k^2+\kappa_e^2\right)^2}\frac{f_e(\hbar k/2)}{D_e}, \tag{B.3}$$

where $f_e(\hbar k/2)$ is the distribution function of the electrons evaluated at $p = \hbar k/2$. Here, the static screening has been taken in the long-wavelength limit $\varepsilon_{ee}(k,0) = 1 + (\kappa_e/k)^2$.

Applying the approximations Eqs. (B.1 - B.3) to Eq. (5.13), and making use of the f-sum rule (2.81), the frequency integration can be performed analytically. The result is

$$\mathcal{Z}_{ei} \overset{\text{RFGR}}{=} \mathcal{V}\frac{\omega_{\text{pe}}^2\omega_{\text{pi}}^2 k_{\text{B}}(T_i - T_e)}{\left(2\pi v_e^2\right)^{3/2}}\int_0^\infty \frac{\mathrm{d}k}{k}\left(\frac{k^2}{k^2+\kappa_e^2}\right)^2\frac{f_e(\hbar k/2)}{D_e}. \tag{B.4}$$

The integration over k is inexpensive to perform numerically, e.g. using the *exp-sinh* transform discussed in Appendix A.

It is tempting to follow a similar approach to the CM energy transfer rate. One then readily derives [Daligault and Mozyrsky, 2008]

$$\begin{aligned}\mathcal{Z}_{ei} \overset{\text{DM}}{=} \mathcal{V}&\frac{\omega_{\text{pe}}^2\omega_{\text{pi}}^2 k_{\text{B}}(T_i - T_e)}{\left(2\pi v_e^2\right)^{3/2}}\int_0^\infty \frac{\mathrm{d}k}{k}\left(\frac{k^2}{k^2+\kappa_e^2}\right)^2\frac{f_e(\hbar k/2)}{D_e}\\ &\times\frac{1}{\pi\omega_{\text{pi}}^2}\int_{-\infty}^{\infty}\mathrm{d}\omega\,\omega\operatorname{Im}\left\{\frac{V_{ii}(k)\Pi_{ii}^{\text{R}}(k,\omega)}{1-V_{ii}^{\text{D}}(k)\Pi_{ii}^{\text{R}}(k,\omega)}\right\}.\end{aligned} \tag{B.5}$$

Since the f-sum rule holds for all systems in which the potential energy commutes with the density operator, i.e. $[\hat{n},\hat{V}] = 0$, the frequency integral term in Eq. (B.5) yields unity, and the RFGR result is recovered exactly. This suggests that a coupled mode effect does not occur when the approximations made here are well-fulfilled, in contradiction to previous numerical results [see, e.g., Dharma-wardana and Perrot, 1998; Vorberger et al., 2010].

B.2 Role of electronic screening

The origin of this contradiction is straightforward to understand. In the derivation of the RFGR rate, the two-component dielectric function $\varepsilon(k,\omega)$ differs from the one-component function for the ions $\varepsilon_{ii}(k,\omega)$ in the real part only; the former retains a static contribution from the electrons. Thus, although the dispersion of the ion excitations is correctly changed from plasmon-like to acoustic, the damping is unchanged from that of the pure ion system.

Of course, the range of the frequency integration is dominated by the decay of the ionic term $\operatorname{Im}\Pi_{ii}^{\text{R}}(k,\omega)$ and, thus, the electrons may always be treated in the low-frequency limit. However, this alone does not justify neglecting the imaginary component of $\varepsilon_{ee}(k,\omega)$. For

small frequencies, the imaginary part scales linearly with ω and becomes more important to the determination of the total mode structure as the peak is shifted to higher frequencies. Retaining the lowest order imaginary contribution, one obtains

$$\varepsilon_{ee}(k,\omega) \overset{\omega\to 0}{\approx} 1 + \frac{\kappa_{\mathrm{D}e}^2}{k^2}\left[\frac{\mathcal{F}_{-1/2}(\eta_e)}{D_e} + i\sqrt{\pi} w_e \frac{f_e(k)}{D_e}\right], \tag{B.6}$$

in which $w_e = \omega/\sqrt{2}kv_e$, as usual. Here, the real part has been taken in the $k \to 0$ limit to be consistent with the RGFR approach.

Using Eq. (B.6), the two-component dielectric function can be written as

$$\begin{aligned}\varepsilon(k,x) \overset{\mathrm{RCM}}{=} 1 + \frac{\kappa_{\mathrm{D}i}^2}{k^2}\Bigg[1 - 2x\mathcal{D}(x) + \mathcal{R}_1\frac{\mathcal{F}_{-1/2}(\eta_e)}{D_e} \\ + i\sqrt{\pi}x\left(e^{-x^2} + \mathcal{R}_1\mathcal{R}_2\frac{f_e(\hbar k/2)}{D_e}\right)\Bigg],\end{aligned} \tag{B.7}$$

where $\mathcal{R}_1 = T_i/Z_i^{\mathrm{f}}T_e$, $\mathcal{R}_2 = (T_i m_e/T_e m_i)^{1/2}$ and $x \equiv w_i$. Substituting Eqs. (B.2) and (B.7) into Eq. (5.14), one obtains a simple reduced CM (RCM) formula

$$\mathcal{Z}_{ei} \overset{\mathrm{RCM}}{=} \mathcal{V}\frac{\omega_{\mathrm{p}e}^2\omega_{\mathrm{p}i}^2 k_{\mathrm{B}}(T_i - T_e)}{(2\pi v_e^2)^{3/2}}\int_0^\infty \mathrm{d}k\, \frac{f_e(\hbar k/2)}{D_e}\,\mathcal{I}_\omega(k), \tag{B.8}$$

$$\mathcal{I}_\omega(k) = \frac{4}{\sqrt{\pi}}\int_0^\infty \mathrm{d}x\, \frac{x^2 e^{-x^2}}{|\varepsilon(k,x)|^2} \equiv \int_0^\infty \mathrm{d}x\, g(k,x). \tag{B.9}$$

Note that by setting $\operatorname{Im}\varepsilon_{ee}(k,\omega) = 0$, one recovers the RFGR rate Eq. (B.4), as expected.

B.3 Numerical evaluation of the RCM model

Although a sharp peak in the integrand in Eq. (B.9) still occurs for some conditions, the additional damping due to screening guarantees that its amplitude increases more slowly than its width, and hence its contribution to the integral decreases. In the case of the full form of the energy transfer rate, the use of adaptive integration over both the k- and ω-spaces leads to unacceptably long evaluation times to be useful for large-scale calculations of energy relaxation.

Instead, it is more expedient approach is to use a fixed grid of points to evaluate the integrand, where the density of points increases close to the peak. The position of the finely-resolved region can be estimated a priori from the dispersion relation, given by the root of the real part of the RCM dielectric function (B.7). The integral term (B.9) can then be split into three regions

$$\mathcal{I}_\omega(k) \approx \left\{\int_0^{(1-\delta_1)x_0} + \int_{(1-\delta_1)x_0}^{(1+\delta_2)x_0} + \int_{(1+\delta_2)x_0}^{x_{\max}}\right\}\mathrm{d}x\, g(k,x), \tag{B.10}$$

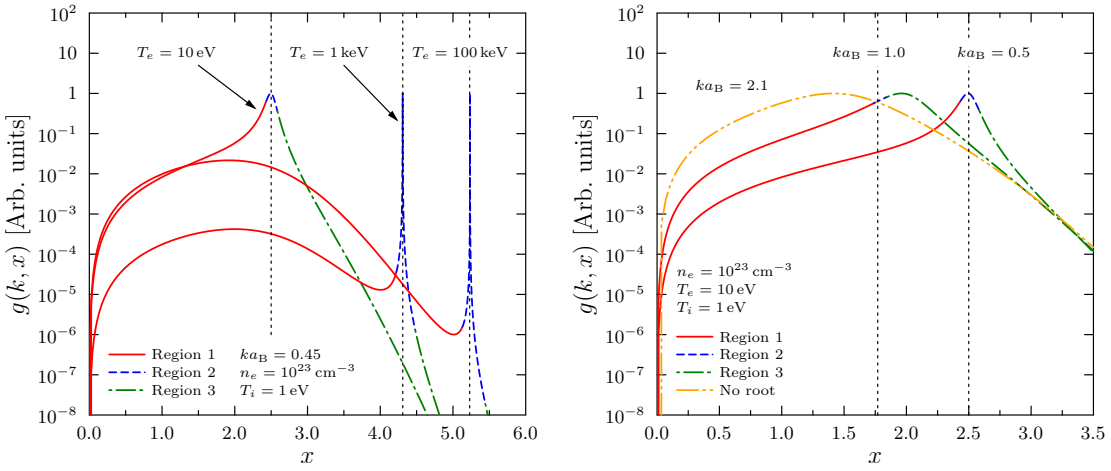

(a) ω integrand for different T_e.

(b) ω integrand for different k.

Figure B.1: Normalised integrand functions of Eq. (B.9) for fixed k and varying T_e (a) and for fixed T_e and varying k (b). The density is $n_e = 10^{23}\,\mathrm{cm}^{-3}$ in all cases. For small k, the collective modes are weakly damped, yielding a strong peak. For the purposes of numerical integration, the function is split into regions around the predicted resonance location (vertical dashed lines). At large k, the dielectric function Eq. (B.7) no longer yields a root, and the function is smooth enough to evaluate on a single grid.

where $x_0 = \omega_0/\sqrt{2}kv_i$ is the high-frequency root solution of $\mathrm{Re}\,\varepsilon(k, x_0) = 0$. The two constants δ_1 and δ_2 determine the size of the integration region surrounding the peak. The latter must be chosen carefully to account for the k-dependence of the asymmetry of $g(k, x)$ close to the peak. If $T_e \gg T_i$ then the additional damping due to screening is negligible and the ion mode is plasmon-like. The peak may then be too sharp to be accurately evaluated (see Fig. B.1(a)). Nevertheless, using the scheme described here the acoustic peak structure can be accurately captured for temperature differences of several orders of magnitude and a wide range of densities.

The assumption that the peak location is given by the root of the dispersion function is valid only for small to moderate wave numbers. For large wave numbers, the dispersion relation ceases to accurately predict the peak position, potentially focusing the finely resolved grid away from the detailed structure (see Fig. B.1(b)). Specifically, the former estimate gives the location of the peak at smaller frequencies than observed. Fortunately, both components of the damping also increase with k and grow fast enough to smooth the peak as it is shifted away from its predicted position.

When the resonance occurs at sufficiently high frequency, the peak is suppressed altogether since the integrand is modulated by the exponential decay of $\mathrm{Im}\,\Pi^\mathrm{R}_{ii}(k, \omega)$. Moreover, if no root exists in the dispersion relation, i.e., $\mathrm{Re}\,\varepsilon(k, \omega) > 0$ for all ω, a sharply peaked structure does not occur at all. Such situations a typical of strongly non-collective states, e.g. for high ion temperatures of large wave numbers. In both of these cases, the entire integrand is smooth and can be evaluated quickly and accurately on a coarse grid.

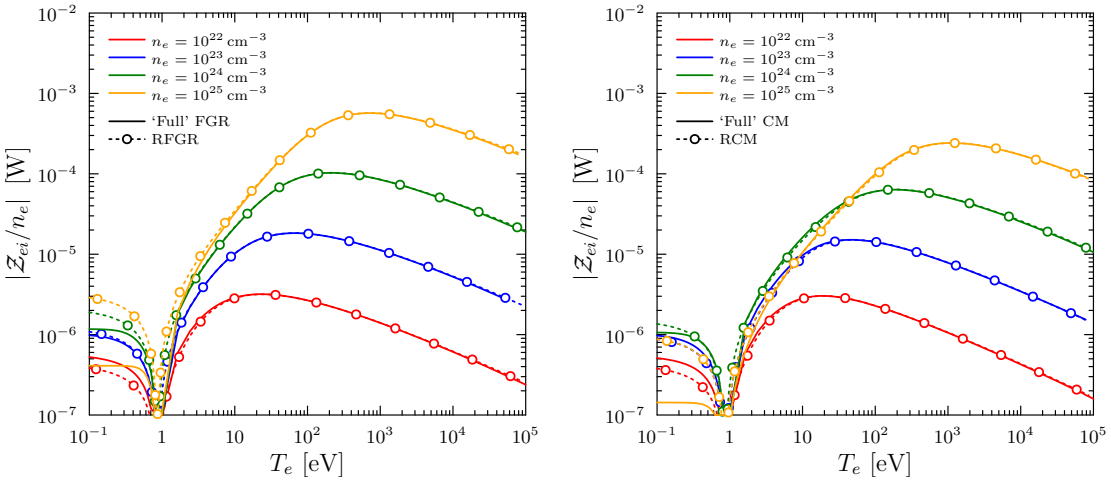

(a) Comparison for FGR relaxation.

(b) Comparison for CM relaxation.

Figure B.2: (a): Comparison of fully numerical and reduced calculations of the Fermi golden rule (FGR) energy transfer rate for $T_i = 0.86\,\mathrm{eV}$ different densities in the WDM regime. (b): Equivalent comparison as panel (a) for the coupled modes (CM) relaxation rate. In both cases, the 'full'calculations are shown by solid curves and the reduced approximations are dashed curves with open circles.

B.4 Comparison to fully numerical calculations

Fig. B.2 shows the RCM model, defined by Eqs. (B.7 - B.9) and the RFGR Eq. (B.4) compared to fully numerical solutions of the full CM and FGR expressions for a fully ionized hydrogen plasma ($Z_i^{\mathrm{f}} = 1$) over a wide range of densities. The fully numerical results are supplied courtesy of by J. Vorberger, which were calculated in RPA using nested adaptive Gaussian integration. In all cases, the ion temperature is fixed at $T_i = 0.86\,\mathrm{eV} = 10^4\,\mathrm{K}$.

As expected, the rates approach zero close to equilibrium and the rate changes sign as the electrons are made colder than the ions. For each density, generally good agreement between the full CM calculations and the results of the RCM model can be seen for $T_e > T_i$. Similarly good agreement is also found with respect to the FGR. For example, for $T_e = 10^5$ K, the maximum relative error between the reduced and full calculations is $< 10\%$ for all densities considered. As T_e tends to T_i, the agreement gets worse, with the higher density results diverging faster. Calculations for higher ion temperatures also show similar agreement and the same trends in the absolute error as a function of T_e/T_i.

The Around thermal equilibrium, i.e. $T_e \approx T_i$, absolute difference between the CM and RCM curve ranges between $< 20\%$ and $> 570\%$ for the highest density. This trend of poor agreement at high degeneracy is consistent with the breakdown of the approximation for the Bose functions Eq. (B.2). Indeed, a similar trend can be seen comparing full and reduced approaches to the FGR [Vorberger and Gericke, 2014]. Contrary to this trend is the observation that the low-temperature error seems to have a minimum for $n_e = 10^{23}\,\mathrm{cm}^{-3}$, with the agreement worsening again for decreasing density.

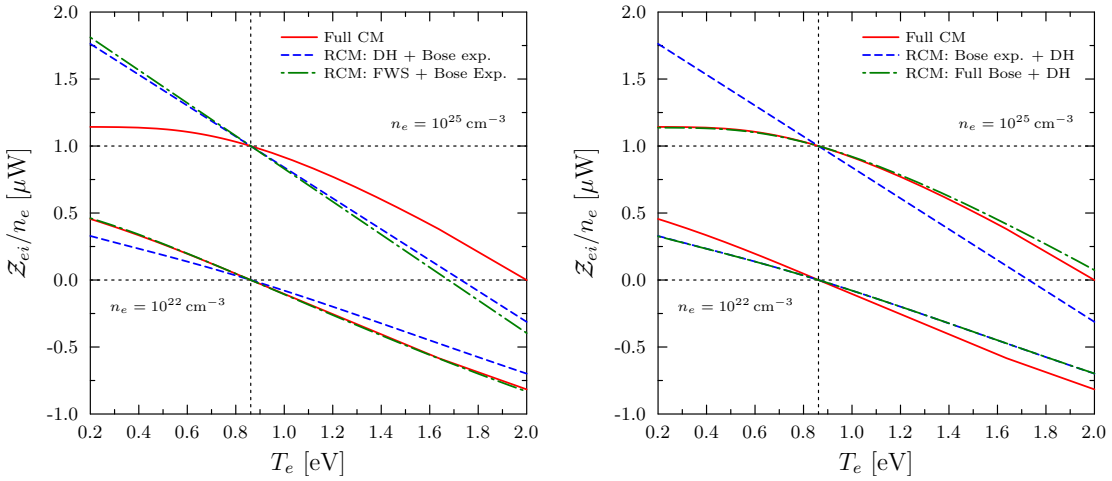

(a) Effect of finite-wavelength screening.

(b) Effect of Bose-like mode occupation.

Figure B.3: (a): Simple and improved RCM relaxation rates near equilibrium at low- and high densities showing the effect of different approximations for static electronic screening of ion acoustic modes; the Debye-Hückel (DH) approximation is compared to the finite-wavelength screening (FWS) approach. (b): Effect of different mode occupation structures; the full Bose function structure for both electrons and ions is compared to the zeroth-order Taylor series expansion. The full structure of the Bose function for the electrons (plasmon occupation) is most important at high density. In contrast, the FWS model makes the greatest improvement at low densities, where the Bose function shape has almost no effect. Note that in both panels the results for $n_e = 10^{25}\,\mathrm{cm}^{-3}$ are offset on the y-axis for clarity.

B.5 Improvements to the RCM model

Whilst the RCM is able to reproduce numerical calculations for $T_e \gg T_i$, the general accuracy for high-density plasmas for $T_i > T_e$ is poor. Improving the accuracy in this regime is potentially important for ICF-relevant calculations. As the model is limited by the necessity of numerical frequency integration, the natural place to begin improving the model is by considering the effect of each of the major approximations made thus far. The desired increase in speed of the code will therefore be made by making the numerics as efficient as possible. In particular, one may consider the full wave number dependence of the screening and the full structure of the Bose functions.

Since the expansion of the Bose functions Eq. (B.2) is appropriate for low degeneracy it is reasonable to conclude that taking the DH approximation for the static screening is responsible for the poor accuracy of the RCM model for $T_e < T_i$ in the low-density case. The overestimation of the rates in this regime occurs because $f_e(\hbar k/2)$ is roughly Gaussian for $D_e \ll 1$ and, thus, has a long tail enabling states with large k to be accessed. As discussed in Chapter 3, the DH screening model is known to be too strong. Instead, the full k-dependence of the static screening can be included with little additional numerical effort using parameterisation of the RPA dielectric function [Dandrea et al., 1986].

In the low-density case, the screening function is most important for $T_e \sim T_i$, giving appreciably larger (in terms of the absolute magnitude) energy transfer rates for $T_e < T_i$ and slightly smaller rates for $T_e > T_i$. Conversely, for higher degeneracies, contributions to the screening from modes with large k are cut off as $f_e(p)$ tends to the a sharp, step-like Fermi distribution (see Fig. B.3(a)); the difference between the DH and FWS screening functions is therefore less unimportant.

Fig. B.3(b) shows that including the full form of the Bose functions has no effect for low-density plasmas, where the low-frequency expansion holds. At higher densities (degeneracies), however, the full structure of the occupation factor of the plasmons decays more strongly than the Taylor expansion in frequency. The result is a significant increase in rate suppression which accounts for nearly all the difference to the full numerical results. One may include the full structure of the Bose functions by multiplying the integrand of Eq. (B.9) by a correction factor to give a modified frequency integral

$$\mathcal{I}_\omega(k) = \int_0^\infty \mathrm{d}x\, g(k,x) \frac{4x\varkappa_i \Delta n_\mathrm{B}(k,x)}{(T_e/T_i - 1)}, \tag{B.11}$$

$$\Delta n_\mathrm{B}(k,x) = \frac{\exp(4\varkappa_i x) - \exp(4\varkappa_e \mathcal{R}_2 x)}{(\exp(4\varkappa_e \mathcal{R}_2 x) - 1)\,(\exp(4\varkappa_i x) - 1)} \tag{B.12}$$

Writing Eq. (B.12) in this form provides numerical stability for small frequency arguments, without the need to set an arbitrary cut-off at which point the Taylor expanded form is used. Nevertheless, for $\omega \to 0$, where the Taylor expansion is suitable, the correction to Eq. (B.11) tends to unity, as expected.

Bibliography

Abdallah Jr, J., Colgan, J., and Rohringer, N. Time-dependent calculations of electron energy distribution functions for neon gas in the presence of intense XFEL radiation. *J. Phys. B: At. Mol. Opt. Phys.*, 46:235004, 2013.

Abramowitz, M. and Stegun, I. A. *Handbook of Mathematical Functions with Formulas, Graphs and Mathematical Tables.* Dover, 1970.

Ackermann, W., Asova, G., Ayvazyan, V., Azima, A., et al. Operation of free-electron laser from the extreme ultra-violet to the water window. *Nat. Photonics*, 1:336, 2007.

Allen, M. P. and Tildesley, D. J. *Computer Simulation on Liquids.* Oxford University Press, 1999.

Aravind, P. K., Holas, A., and Singwi, K. S. Dynamic correlations in an electron gas. II. Kinetic-equation approach. *Phys. Rev. B*, 25:561, 1982.

Arista, N. R. and Brandt, W. Dielectric response of quantum plasmas in thermal equilibrium. *Phys. Rev. A*, 29:1471, 1984.

Arthur, J. Linac Coherent Light Source (LCLS) - Conceptual Design Report., 2002.

Aryasetiawan, F. and Gunnarsson, O. The *GW* Method. *Rep. Prog. Phys.*, 61:237, 1998.

Ashcroft, N. W. Electron-ion pseudopotentials in metals. *Phys. Rev.*, 23:48, 1966.

Atzeni, S. and Meyer-ter-Vehn, J. *The Physics of Inertial Fusion.* Oxford University Press, 2004.

Baalrud, S. D. and Daligault, J. Effective potential theory for transport coefficients across coupling regimes. *Phys. Rev. Lett.*, 110:235001, 2013.

Bachmann, B., Kritcher, A. L., Bendetti, L. R., Falcone, R. W., Glenn, S., Hawreliak, J. A., Izumi, N., Kraus, D., Landen, O. L., Le Pape, S., Ma, T., Perez, F., Swift, D. C., and Döppner, T. Using penumbral imaging to measure micrometer-size plasma hot spots in Gbar EOS experiments on the National Ignition Facility. *Rev. Sci. Instrum.*, 85:11D614, 2014.

Baldis, H. A., Dunn, J., Foord, M. E., and Rozmus, W. Thomson scattering diagnostic of solid density plasmas using x-ray lasers. *Rev. Sci. Instrum.*, 73:4223, 2002.

Bannasch, G., Castro, J., McQuillen, P., Pohl, T., and Killian, T. C. Velocity relaxation in a strongly coupled plasma. *Phys. Rev. Lett.*, 109:185008, 2012.

Bannasch, G., Killian, T. C., and Pohl, T. Strongly coupled plasmas via Rydberg blockade of cold atoms. *Phys. Rev. Lett.*, 110:253003, 2013.

Barbrel, B., Koenig, M., Beunuzzi-Mounaix, A., Brambrink, E., Brown, C. R. D., Gericke, D. O., Nagler, B., Rabec le Gloahec, M., Riley, D., Vinko, C. Spindloe S. M., Vorberger, J., Wark, J.S., Wünsch, K., and Gregori, G. Measurement of short-range correlations in shock-compressed plastic by short-pulse x-ray scattering. *Phys. Rev. Lett.*, 102:165004, 2009.

Batson, P. E., Chen, C. H., and Silcox, J. Plasmon dispersion at large wave vectors. *Phys. Rev. Lett.*, 37:937, 1976.

Bell, A. R., Robinson, A. P. L., Sherlock, M., Kingham, R. J., and Rozmus, W. Fast electron transport in laser-produced plasmas and the KALOS code for solution of the Vlasov-Fokker-Planck equation. *High Energy Density Phys.*, 48:R37, 2006.

Benedict, L. X., Glosli, J. N., Richards, D. F., Streitz, F. H., Hau-Riege, S. P., London, R. A., and Graziani, F. R. Molecular dynamics simulations of electron-ion temperature equilibration in an SF_6 plasma. *Phys. Rev. Lett.*, 102:205004, 2009.

Benedict, L. X., Surh, M. P., Castor, J. I., Khairallah, S. A., Whitley, H. D., Richards, D. F., Glosli, J. N., Murillo, M. S., Scullard, C. R., Grabowski, P. E., Michta, D., and Graziani, F. R. Molecular dynamics simulations and generalised Lenard-Balescu calculations of electron-ion temperature equilibration in plasmas. *Phys. Rev. E*, 86: 046406, 2012.

Bevington, P. R. and Robinson, D. K. *Data Reduction and Error Analysis for the Physical Sciences.* McGraw Hill, New York, NY, 2003.

Bloch, B. J. and Mendelsohn, L. B. Atomic L-shell Compton profiles and incoherent scattering factors: Theory. *Phys. Rev. A*, 9:129, 1974.

Bloch, F. Contribution to the theory of the Compton-line. *Phys. Rev.*, 46:674, 1934.

Bochkarev, S. G., Bychenkov, V. Yu., and Rozmus, W. Nonequilibrium electron distribution functions and nonlinear thermal transport. *Phys. Plasmas*, 11:3997, 2004.

Boehly, T. R., Brown, D. L., Craxton, R. S., Keck, R. L., Knauer, J. P., Kelly, J. H., Kessler, T. J., Kumpan, S. A., Loucks, S. J., Letzring, S. A., Marshall, F. J., McCrory, R. L., Morse, S. F. B., Seka, W., Soures, J. M., and Verdon, C. P. Initial performance results of the OMEGA laser system. *Opt. Commun.*, 133:495, 1997.

Bohm, D. and Gross, E. P. Theory of plasma oscillations. A. Origin of medium-like behaviour. *Phys. Rev.*, 75:1851, 1949.

Bohm, D. and Pines, D. A collective description of electron interactions: III. Coulomb interactions in a degenerate electron gas. *Phys. Rev.*, 92:609, 1953.

Bose, S. N. Plancks Gesetz und Lichtquantenhypothese. *Zeitschr. für Phys.*, 26:78, 1924.

Bourgade, J. L., Villete, B., Borcher, J. L., Boutin, J. Y., Chiche, S., Dague, N., Gontier, D., Jadaud, J. P., Savale, B., Wrobel, R., and Turner, R. E. DMX: An absolutely calibrated time-resolved broadband soft x-ray spectrometer designed for MJ class laser-produced plasmas. *Rev. Sci. Instrum.*, 72:1173, 2001.

Bowles, K. L. Observation of vertical-incidence scatter from the ionosphere at 41 Mc/sec. *Phys. Rev. Lett.*, 1:454, 1958.

Braaten, E. and Nieto, A. Next-to-leading order Debye mass for the quark-gluon plasma. *Phys. Rev. Lett.*, 73:2402, 1994.

Brown, C. R. D., Gericke, D. O., Cammarata, M., Cho, B. I., Döppner, T., Engelhorn, K., Förster, E., Fortmann, C., Fritz, D., Galtier, E., Glenzer, S. H., Harmand, M., Heimann, P., Kugland, N. L., Lamb, D. Q., Lee, H. J., Lee, R. W., Lemke, H., Makita, M., Moinard, A., Murphy, C. D., Nagler, B., Neumayer, P., Plagemann, K. U., Redmer, R., Riley, D., Rosmej, F. B., Sperling, P., Toleikis, S., Vinko, S. M., Vorberger, J., White, S., White, T. G., Wünsch, K., Zastrau, U., Zhu, D., Tschentscher, T., and Gregori, G. Evidence for a glassy state in strongly driven carbon. *Sci. Rep.*, 4:5214, 2014.

Brown, C. R. D., Hoarty, D. J., James, S. F., Swatton, D., Hughes, S. J., Morton, J. W., Guymer, T. M., Hill, M. P., Chapman, D. A., Andrew, J. E., Comley, A. J., Shepherd, R., Dunn, J., Chen, H., Schneider, M., Brown, G., Beiersdorfer, P., and Emig, J. Measurements of electron transport in foils irradiated with a picosecond time scale laser pulse. *Phys. Rev. Lett.*, 106:185003, 2011.

Brown, L. S. and Singleton, Jr., R. L. Temperature equilibration in a fully ionized plasma: Electron-ion mass ratio effects. *Phys. Rev. E*, 79:066407, 2009.

Brunel, F. Not-so-resonant, resonant absorption. *Phys. Rev. Lett.*, 52:59, 1987.

Brush, S. G., Sahlin, H. L., and Teller, E. Monte Carlo study of a one-component plasma. *J. Chem. Phys.*, 45:2102, 1966.

Bruus, H. and Flensberg, K. *Many-Body Quantum Theory in Condensed Matter Physics*. Oxford University Press, Oxford, 2004.

Brysk, H. Electron-ion equilibration in a partially degenerate plasma. *Plasma Phys.*, 16: 927, 1974.

Celliers, P. M., Bradley, D. K., Collins, G. W., Hicks, D. G., Boehly, T. R., and Armstrong, W. J. Line-imaging velocimeter for shock diagnostics at the OMEGA laser facility. *Rev. Sci. Instrum.*, 75:4916, 204.

Chapman, D. A. and Gericke, D. O. Analysis of Thomson scattering from nonequilibrium plasmas. *Phys. Rev. Lett.*, 107:165004, 2011.

Chapman, D. A., Kraus, D., Kritcher, A. L., Bachmann, B., Collins, G. W., Falcone, R. W., Gaffney, J. A., Gericke, D. O., Glenzer, S. H., Guymer, T. M., Hawreliak, J. A., Landen, O. L., Pape, S. Le, Ma, T., Neumayer, P., Nilsen, J., Pak, A., Redmer, R., Swift, D. C., Vorberger, J., and Döppner, T. Simulating x-ray Thomson scattering signals from high-density millimetre-scale plasmas at the National Ignition Facility. *Phys. Plasmas*, 21:082709, 2014.

Chapman, D. A., Vorberger, J., Fletcher, L. B., Baggott, R. A., Divol, L., Döppner, T., Falcone, R. W., Glenzer, S. H., Gregori, G., Guymer, T. M., Kritcher, A. L., Landen, O. L., Ma, T., Pak, A. E., and Gericke, D. O. Observation of finite-wavelength screening in high-energy-density matter. *Nature Comms.*, 6:6839, 2015.

Chapman, D. A., Vorberger, J., and Gericke, D. O. Reduced coupled-mode approach to electron-ion energy relaxation. *Phys. Rev. E*, 88:013102, 2013a.

Chapman, D. A., Vorberger, J., Wünsch, K., and Gericke, D. O. Analysis of Thomson scattering data from strongly-driven hydrogen. *High Energy Density Phys.*, 8:175, 2012.

Chapman, D. A., Vorberger, J., Wünsch, K., and Gericke, D. O. Modelling Thomson scattering for systems with non-equilibrium electron distributions. *Eur. J. Phys.: Web Conf.*, 59:13009, 2013b.

Chew, G. F. and Wick, G. C. The impluse approximation. *Phys. Rev.*, 85:636, 1952.

Chihara, J. Difference in x-ray scattering between metallic and non-metallic liquids due to conduction electrons. *J. Phys. F: Metal Phys.*, 17:295, 1987.

Chihara, J. Interaction of photons with plasmas and liquid metals - photoabsorption and scattering. *J. Phys.: Condens. Matter*, 12:231, 2000.

Chung, H.-K., Chen, M. H., Morgan, W. L., Ralchenko, Yu., and Lee, R. W. FLYCHK: Generalized population kinetics and spectral model for rapid spectroscopic analysis for all elements. *High Energy Density Phys.*, 1:3, 2005.

Ciricosta, O., Vinko, S. M., Chung, H.-K., Cho, B.-I., Brown, C. R. D., Burian, T., Chalupský, J., Engelhorn, J., Falcone, R. W., Graves, C., Hájková, V., Higginbotham, A., Juha, L., Krzywinski, J., Lee, H. J., Messerschmidt, M., Murphy, C. D., Ping, Y., Rackstraw, D. S., Scherz, A., Schlotter, W., Toleikis, S., Turner, J. J., Vysin, L., Wang, T., Wu, B., Zastrau, U., Zhu, D., Lee, R. W., Heimann, P., Nagler, B., and Wark, J. S. Direct measurement of the ionization potential depression in a dense plasma. *Phys. Rev. Lett.*, 109:065002, 2012.

Compton, A. H. A quantum theory of the scattering of x-rays by light elements. *Phys. Rev.*, 21:483, 1923.

Crowley, B. J. B. and Gregori, G. X-ray scattering in many-particle systems. *New J. Phys.*, 15:015014, 2013.

Crowley, B. J. B. and Gregori, G. Quantum theory of Thomson scattering. *High Energy Density Phys.*, 13:55, 2014.

Dabrowski, B. Dynamical local field factor in the response function of an electron gas. *Phys. Rev. B*, 34:4989, 1986.

Daligault, J. Crystal nucleation in the one-component plasma. *Phys. Rev. E*, 73:056407, 2006.

Daligault, J. and Dimonte, G. Correlation effects on the temperature-relaxation in dense plasmas. *Phys. Rev. E*, 79:056403, 2009.

Daligault, J. and Mozyrsky, D. Effect of the liquid-like ionic structure on the electron-ion energy relaxation timescales in dense plasmas. *High Energy Density Phys.*, 4:58, 2008.

Dandrea, R. G., Ashcroft, N. W., and Carlsson, A. E. Electron liquid at any degeneracy. *Phys. Rev. B*, 34:2097, 1986.

Danson, C. N., Collier, J., Neely, D., Barzanti, L. J., Damerell, A., Edwards, C. B., Hutchinson, M. H. R., Key, M. H., Norreys, P. A., Pepler, D. A., Ross, I. N., Taday, P. F., Toner, W. T., Trentelman, M., Walsh, F. N., Winstone, T. B., and Wyatt, R.

W. W. Well characterised 10^{19} Wcm^{-2} operation of VULCAN - an ultra-high power Nd:Glass laser. *J. Mod. Optics*, 45:1653, 1998.

Das, A. K. The relaxation-time approximation in the RPA dielectric formulation. *J. Phys. F: Metal Phys.*, 5:2035, 1975.

De Witt, H. E., Schlanges, M., Sakakura, A. Y., and Kraeft, W. D. Low density expansion of the equation of state for a quantum electron gas. *Phys. Lett. A*, 197:326, 1995.

Debye, P. and Hückel, E. Zur theorie der elektrolyte. I. Gefrierpunktserniedrigung und verwandte erscheinungen. *Phys. Zeitschr.*, 24:185, 1923.

Dharma-wardana, M. W. C. and Perrot, F. Energy relaxation and the quasiequation of state of a dense two-temperature nonequilibrium plasma. *Phys. Rev. E*, 3705:58, 1998.

Dharma-wardana, M. W. C. and Perrot, F. Simple classical mapping of the spin-polarized quantum electron gas: Distribution functions and local field corrections. *Phys. Rev. Lett.*, 84:959, 2000.

Dirac, P. A. M. On the theory of quantum mechanics. *Proc. Roy. Soc. A*, 112:661, 1926.

Dirac, P. A. M. The quantum theory of the emission and absorption of radiation. *Proc. R. Soc. Lond. A: Math. Phys. and Engin. Sci.*, 114:243, 1927.

Dirac, P. A. M. *The Principles of Quantum Mechanics*. Oxford University Press, Oxford, 1930.

Dittrich, T. R., Hurricane, O. A., Callahan, D. A., Dewald, E. L., Döppner, T., Hinkel, D. E., Hopkins, L. F. Berzak, Le Pape, S., Ma, T., Milovich, J. L., Moreno, J. C., Patel, P. K., Park, H. S., Remington, B. A., Salmonson, J. D., and Kline, J. L. Design of a high-foot high-adiabat ICF capsule for the National Ignition Facility. *Phys. Rev. Lett.*, 112:055002, 2014.

Döppner, T., Fortmann, C., Davis, P. F., Kritcher, A. L., Landen, O. L., Lee, H. J., Redmer, R., Regan, S. P., and Glenzer, S. H. X-ray Thomson scattering for measuring dense beryllium plasma collisionality. *J. Phys.: Conf. Series*, 244:032044, 2010.

Döppner, T., Kritcher, A. L., Neumayer, P., Kraus, D., Bachmann, B., Burns, S., Falcone, R. W., Glenzer, S. H., Hawreliak, J., House, A., Landen, O. L., Le Pape, S., Ma, T., Pak, A., and Swift, D. Qualification of a high-efficiency, gated spectrometer for x-ray Thomson scattering on the National Ignition Facility. *Rev. Sci. Instrum.*, 85:11D617, 2014.

Döppner, T., Landen, O. L., Lee, H. J., Neumayer, P., Regan, S. P., and Glenzer, S. H. Temperature measurement through detailed balance in x-ray Thomson scattering. *High Energy Density Phys.*, 5:182, 2009.

Dufour, P., Liebert, J., Fontaine, G., and Behara, N. White dwarf stars with carbon atmospheres. *Nature*, 450:522, 2007.

Einstein, A. Quantentheorie des einatomigen idealen Gases. *Sitzungsber. Kgl. Preuss. Akad. Wiss.*, page 261, 1924.

Eisenberger, P. and Platzmann, P. M. Compton scattering of x-rays from bound electrons. *Phys. Rev. A*, 2:415, 1970.

Engel, E. and Vosko, S. H. Wave-vector dependence of the exchange contribution to the electron-gas response functions: An analytic derivation. *Phys. Rev. B*, 42:4940, 1990.

Estabrook, K. G., Valeo, E. J., and Kruer, W. L. Two dimensional relativistic simulations of resonance absorption. *Phys. Fluids*, 1151:18, 1975.

Evans, D. E. and Katzenstein, J. Laser light scattering in laboratory plasmas. *Rep. Prog. Phys.*, 32:207, 1969.

Falk, K., Collins, L. A., Gamboa, E. J., Kagan, G., Kress, J. D., Montgomery, D. S., Tzeferacos, B. Srinivasan P., and Benage, J. F. Combined x-ray scattering, radiography, and velocity interferometry/streaked optical pyrometry measurements of warm dense carbon using a novel technique of shock-and-release. *Phys. Plasmas*, 21:056309, 2014.

Falk, K., Regan, S. P., Vorberger, J., Crowley, B. J. B., Glenzer, S. H., Hu, S. X., Murphy, C. D., Radha, P. B., Jephcoat, A. P., Wark, J. S., Gericke, D. O., and Gregori, G. Comparison between x-ray scattering and velocity-interferometry measurements from shocked liquid deuterium. *Phys. Rev. E*, 87:043112, 2013.

Farid, B., Heine, V., Engel, G. E., and Robertson, I. J. Extremal properties of the Harris-Foulkes functional and an improved screening calculation for the electron gas. *Phys. Rev. B*, 48:11602, 1993.

Fäustlin, R. R., Bornath, Th., Döppner, T., Düsterer, S., Förster, E., Fortmann, C., Glenzer, S. H., Gölde, S., Gregori, G., Irsig, R., Laarmann, T., Lee, H. J., Li, B., Meiwer-Broer, K. H., Mithen, J., Nagler, B., Przystawik, A., Redlin, H., Redmer, R., Reinholz, H., Röpke, G., Tavella, F., Theile, R., Tiggesbäumker, J., Toleikis, S., Uschmann, L., Vinko, S. M., Whitcher, T., Zastrau, U., Ziaja, B., and Tschentscher, Th. Observation of ultrafast nonequilibrium collective dynamics in warm dense hydrogen plasma. *Phys. Rev. Lett.*, 104:125002, 2010.

Fehske, H., Scheinder, R., and Weiße, A. *Computational many-particle physics*. Springer, Berlin, 2008.

Fermi, E. Zur Quantelung des idealen einatomigen Gases. *Zeitschr. für Phys.*, 36:902, 1926.

Fermi, E. A statistical method for the determination of some atomic properties and the application of this method to the theory of the periodic system of elements. *Zeitschr. für Phys.*, 48:73, 1928.

Fletcher, L. B., Kritcher, A. L., Pak, A., Ma, T., Döppner, T., Fortmann, C., Divol, L., Jones, O. S., Landen, O. L., Scott, H. A., Vorberger, J., Chapman, D. A., Gericke, D. O., Mattern, B. A., Seidler, G. T., Gregori, G., Falcone, R. W., and Glenzer, S. H. Observations of continuum depression in warm dense matter with x-ray Thomson scattering. *Phys. Rev. Lett.*, 112:145004, 2014.

Fletcher, L. B., Kritcher, A. L., Pak, A., Ma, T., Döppner, T., Fortmann, C., Divol, L., Landen, O. L., Vorberger, J., Chapman, D. A., Gericke, D. O., Falcone, R. W., and Glenzer, S. H. X-ray Thomson scattering measurements of temperature and density from multi-shocked CH capsules. *Phys. Plasmas*, 20:056316, 2013.

Fletcher, L. B., Lee, H. J., Döppner, T., Galtier, E., Nagler, B., Heimann, P., Fortmann, C., Le Pape, S., Ma, T., Millot, M. A., Pak, A., Turnbull, D., Chapman, D. A., Gericke, D. O., Vorberger, J., White, T., Gregori, G., Wei, M., Barbrel, B., Falcone, R. W., Cao, C.-C., Nuhn, H., Welch, J., Zastrau, U., Neumayer, P., Hastings, J. B., and Glenzer, S. H. Ultra-bright x-ray laser scattering for dynamic wam dense matter physics. *Nature Photon.*, 9:274, 2015.

Forslund, D. W., Kindel, J. M., and Lee, K. Theory of hot-electron spectra at high laser intensity. *Phys. Rev. Lett.*, 284:39, 1977.

Fortmann, C., Lee, H. J., Döppner, T., Falcone, R. W., Kritcher, A. L., Landen, O. L., and Glenzer, S. H. Measurement of the adiabatic index in Be compressed by counter-propagating shocks. *Phys. Rev. Lett.*, 108:175006, 2012.

Fortmann, C., Redmer, R., Reinholz, H., Röpke, G., Wierling, A., and Rozmus, W. Bremsstrahlung vs. Thomson scattering in VUV-FEL plasma experiments. *High Energy Density Phys.*, 2:57, 2006.

Fortmann, C., Wierling, A., and Röpke, G. Influence of local field corrections on Thomson scattering in collision-dominated two-component plasmas. *Phys. Rev. E*, 81:026405, 2010.

Fourkal, E., Bychenkov, V. Yu, Rozmus, W., Sydora, R., Kirkby, C., Capjack, C. E., Glenzer, S. H., and Baldis, H. A. Electron distribution function in laser heated plasmas. *Phys. Plasmas*, 8:550, 2001.

Friedel, J. Electronic structure of primary solid solutions in metals. *Advanc. Phys.*, 3:446, 1954.

Froula, D. H., Divol, L., Baldis, H. A., Berger, R. L., Braun, D. G., Cohen, B. I., Johnson, R. P., Montgomery, D. S., Williams, E. A., , and Glenzer, S. H. Observation of ion heating by stimulated-Brillouin-scattering-driven ion-acoustic waves using Thomson scattering. *Phys. Plasmas*, 9:4709, 2002.

Froula, D. H., Divol, L., Meezan, N. B., Dixit, S., Neumayer, P., Moody, J. D., Pollock, B. B., Ross, J. S., Suter, L., and Glenzer, S. H. Laser beam propagation through inertial confinement fusion hohlraum plasmas. *Phys. Plasmas*, 14:055705, 2007.

Froula, D. H., Ross, J. S., Divol, L., and Glenzer, S. H. Thomson-scattering techniques to diagnose local electron and ion temperatures, density, and plasma wave amplitudes in laser produced plasmas (invited). *Rev. Sci. Instrum.*, 77:10E522, 2006a.

Froula, D. H., Ross, J. S., Divol, L., Meezan, N. B., MacKinnon, A. J., Wallace, R., and Glenzer, S. H. Thomson scattering measurements of high-electron temperature plasmas for laser-plasma interaction studies. *Phys. Plasmas*, 13:052704, 2006b.

Fünfer, E., Kronast, B., and Kunze, H.-J. Measurement of the spectral distribution of scattered light by a θ-pinch plasma. *Phys. Lett.*, 5:125, 1963.

Gaffney, K. J. and Chapman, H. N. Imaging atomic structure and dynamics with ultrafast x-ray scattering. *Science*, 5830:1444, 2007.

Gamboa, E. J., Fletcher, L. B., Lee, H. J., Zastrau, U., Gauthier, E. Galtier M. J. MacDonald M., Voerberger, J., Gericke, D. O., Grandos, E., Hastings, J. B., and Glenzer, S. H. Single-shot measurements of plasmons in compressed diamond with a x-ray laser. *Phys. Plasmas*, 22:056319, 2015.

Garbett, W. J. Sensitivity of ICF ignition conditions to non-Maxwellian DT fusion reactivity. *Eur. J. Phys.: Web Conf.*, 59:02019, 2013.

García Saiz, E., Gregori, G., Gericke, D. O., Vorberger, J., Barbrel, B., Clarke, R. J., Freeman, R. R., Glenzer, S. H., Khattak, F. Y., Koenig, M., Landen, O. L., Neely, D., Neumayer, P., Notely, M. M., Pelka, A., Price, D., Roth, M., Schollmeier, M., Spindloe, C., Weber, R. L., van Woerkam, L., Wünsch, K., and Riley, D. Probing warm dense lithium by inelastic x-ray scattering. *Nat. Phys.*, 4:940, 2008.

Gauthier, M., Fletcher, L. B., Ravisio, A., Galtier, E., Gamboa, E. J., Granados, E., Hastings, J. B., Heimann, P., Lee, H. J., Nagler, B., Schropp, A., Gleason, A., Döppner, T., Le Pape, S., Ma, T., Pak, A., MacDonald, M. J., Ali, S., Barbrel, B., Falcone, R., Kraus, D., Chen, Z., Mo, M., Wei, M., and Glenzer, S. H. New experimental platform to study high density laser-compressed matter. *Rev. Sci. Instrum.*, 85:11E616, 2014.

Geldart, D. J. W. and Vosko, S. H. The screening function of an interacting electron gas. *Can. J. Phys.*, 44:2137, 1966.

Gericke, D. O., Murillo, M.S., and Schlanges, M. Dense plasma temperature equilibrium in the binary collision approximation. *Phys. Rev. E*, 65:036418, 2002a.

Gericke, D. O. and Schlanges, M. Beam-plasma coupling effects on the stopping power of dense plasmas. *Phys. Rev. E*, 60:904–910, 1999.

Gericke, D. O., Schlanges, M., and Bornath, Th. Stopping power of nonideal, partially ionized plasmas. *Phys. Rev. E*, 65:036406, 2002b.

Gericke, D. O., Schlanges, M., and Kraeft, W. D. Stopping power of a quantum plasma - T-matrix approximation and dynamical screening. *Phys. Lett. A*, 222:241, 1996.

Gericke, D. O., Vorberger, J., Wünsch, K., and Gregori, G. Screening of ionic cores in partially ionized plasmas within linear response. *Phys. Rev. E*, 81:065401(R), 2010.

Gibbon, P. *Short pulse laser interactions with matter.* Imperial College Press, London, 2005.

Glenzer, S. H., Alley, W. E., Estabrook, K. G., de Groot, J. S., Haines, M. G., Hammer, J. H., Jadaud, J. P., MacGowan, B. J., Moody, J. D., Rozmus, W., Suter, L. J., Weiland, T. L., and Williams, E. A. Thomson scattering from laser plasmas. *Phys. Plasmas*, 6: 2117, 1999a.

Glenzer, S. H., Back, C. A., Estabrook, K. G., and MacGowan, B. J. Thomson scattering in the corona of laser-produced gold plasmas. *Rev. Sci. Instrum.*, 68:668, 1997.

Glenzer, S. H., Estabrook, K. G., Lee, R. W., MacGowan, B. J., and Rozmus, W. Detailed characterization of laser plasmas for benchmarking of radiation-hydrodynamics modelling. *J. Quant. Spectrosc. Rad. Trans.*, 65:253, 2000.

Glenzer, S. H., Gregori, G., Lee, R. W., Rogers, F. J., Pollaine, S. W., and Landen, O. L. Demonstration of spectrally resolved x-ray scattering in dense plasmas. *Phys. Rev. Lett.*, 90:175002, 2003.

Glenzer, S. H., Landen, O. L., Neumayer, P., Lee, R. W., Widmann, K., Pollaine, S. W., Wallace, R. J., Gregori, G., Höll, A., Bornath, T., Theile, R., Schwarz, V., Kraeft, W. D., and Redmer, R. Observations of plasmons in warm dense matter. *Phys. Rev. Lett.*, 98: 065002, 2007.

Glenzer, S. H. and Redmer, R. X-ray Thomson scattering in high energy density plasma. *Rev. Mod. Phys.*, 81:001625, 2009.

Glenzer, S. H., Rozmus, W., Bychenkov, V. Yu., Moody, J. D., Albritton, J., Berger, R. L., Brantov, A., Foord, M. E., MacGowan, B. J., Kirkwood, R. K., Baldis, H. A., and Williams, E. A. Anomalous absorption of high-energy green laser light in high-Z plasmas. *Phys. Rev. Lett.*, 88:235002, 2002.

Glenzer, S. H., Rozmus, W., MacGowan, B. J., Estabrook, K. G., De Groot, J. D., Zimmerman, G. B., Baldis, H. A., Harte, J. A., Lee, R. W., Williams, E. A., and Wilson, B. G. Thomson scattering from high-Z laser-produced plasmas. *Phys. Rev. Lett.*, 82:97, 1999b.

Glenzer, S. H., Spears, B. K., Edwards, M. J., Alger, E. T., berger, R. L., Bleuel, D. L., Bradley, D. K., Caggiano, J. A., Callahan, D. A., Castro, C., Casey, D. T., Choate, C., Clark, D. S., Cerjan, C. J., Collins, G. W., Dewald, E. L., J.M. G. Di Nicola, Di Nicola, P., Divol, L., Dixit, S. N., Dylla-Spears, T. Döppner R., Dzenitis, E. G., Fair, J. E., Frenje, L. J. A., Gatu Johnson, M., Giraldez, E., Glebov, V., Glenn, S. M., Haan, S. W., Hammel, B. A., Hatchett, S. P., Haynam, C. A., Heeter, R. F., Heestand, G. M., Herrmann, H. W., Hicks, D. G., Holunga, D. M., Horner, J. B., Huang, H., Izumi, N., Jones, O. S., Kalantar, D. H., Kilkenny, J. D., Kirkwood, R. K., Kline, J. L., Knauer, J. P., Kozioziemski, B., Kricther, A. L., Kroll, J. J., Kyrala, G. A., La Fortune, K. N., Landen, O. L., Larson, D. W., Leeper, R. J., Le Pape, S., Lindl, J. D., Ma, T., Mackinnon, A. J., MacPhee, A. G., Mapoles, E., McKenty, P. W., Meezan, N. B., Michel, P., Milovich, J. L., Moody, J. D., Moore, A. S., Moran, M., Moreno, K. A., Munro, D. H., Nathan, B. R., Nikroo, A., Olson, R. E., Orth, C. D., Park, A., Patel, P. K., Parham, T., Petrasso, R., Ralph, J. E., Rinderknecht, H., Regan, S. P., Robey, H. F., Ross, J. S., Salmonson, J. D., Sangster, C., Sater, J., Scheider, M. B., Seguin, F. H., Shaw, M. J., Shoup, M. J., Springer, P. T., Stoeffl, W., Suter, L. J., Thomas, C. A., Town, R. P. J., Walters, C., Weber, S. V., Wegner, P. J., Widmayer, C., Whitman, P. K., Widmann, K., Wilson, D. C., Van Wonterghem, B. M., MacGowan, B. J., Atherton, L. J., and Moses, E. I. First implosion experiments with cryogenic thermonuclear fuel on the National Ignition Facility. *Plasma Phys. Control. Fusion*, 54:045013, 2012.

Golovkin, I., MacFarlane, J. J., Woodruff, P., Hall, I., Gregori, G., Bailey, J., Harding, E., Ao, T., and Glenzer, S. H. Simulation of x-ray scattering diagnostics in multi-dimensional plasma. *High Energy Density Phys.*, 9:510, 2013.

Gonze, X., Amadon, B., Anglade, P. M., Beuken, J.-M., Bottin, F., Boulanger, P., Bruneval, F., Caliste, D., Caracas, R., Cote, M., Deutsch, T., Genovese, L., Ghosez, Ph., Giantomassi, M., Goedecker, S., Hamann, D., Hermet, P., Jollet, F., Jomard, G., Leroux, S., Mancini, M., Mazevet, S., Oliveira, M. J. T., Onida, G., Pouillon, Y., Rangel,

T., Rignanese, G.-M., Sangalli, D., Shaltaf, R., Torrent, M., Verstraete, M. J., Zérah, G., and Zwanziger, J. W. ABINIT: first-principles approach to material and nanosystem properties. *Comp. Phys. Comms.*, 180:2582, 2009.

Gonze, X., Beuken, J.-M., Caracas, R., Detraux, F., Fuchs, M., Rignanese, G.-M., Sindic, L., Verstraete, M., Zerah, G., Jollet, F., Torrent, M., Roy, A., Mikami, M., Ghosez, Ph., Raty, J.-Y., and Allan., D. C. First-principles computation of material properties: the ABINIT software project. *Comp. Mat. Science*, 25:478, 2002.

Gonze, X., Rignanese, G.-M., Verstraete, M., Beuken, J.-M., Pouillon, Y., Caracas, R., Jollet, F., Torrent, M., Zerah, G., Mikami, M., Ghosez, Ph., Veithen, M., Raty, J.-Y., Olevano, V., Bruneval, F., Reining, L., Godby, R., Onida, G., Hamann, D. R., and Allan., D. C. A brief introduction to the ABINIT software package. *Zeitschr. Kristallogr.*, 220:558, 2005.

Gori-Giorgi, P., Sacchetti, F., and Bachelet, G. B. Analytic static structure factors and pair-correlation functions for the unpolarized homogeneous electron gas. *Phys. Rev. B*, 61:7353, 2000.

Gould, H. A. and De Witt, H. E. Convergent kinetic equation for a classical plasma. *Phys. Rev.*, 155:70, 1967.

Graziani, F., Dejarlais, M. P., Redmer, R., and Trickey, S. B. *Frontiers and Challenges in Warm Dense Matter: Lecture Notes in Computational Science and Engineering*. Springer International Publishing Switzerland, 2014a.

Graziani, F. R., Bauer, J. D., and Murillo, M. S. Kinetic theory molecular dynamics and hot dense matter: Theoretical foundations. *Phys. Rev. E*, 90:033104, 2014b.

Green, L. C., Matsushima, S., and Kolchin, E. K. Tables of the continuum wavefunctions for hydrogen. *Astrophys. J. Suppl. Series*, 3:459, 1958.

Gregori, G. and Gericke, D. O. Low frequency structural dynamics of warm dense matter. *Phys. Plasmas*, 16:056306, 2009.

Gregori, G., Glenzer, S. H., Chung, H. K., Froula, D. H., Lee, R. W., Meezan, N. B., Moody, J. D., Niemann, C., Landen, O. L., Holst, B., Redmer, R., Regan, S. P., and Sawada, H. Measurement of carbon ionization balance in high-temperature plasma mixtures by temporally resolved x-ray scattering. *J. Quant. Spectrosc. Rad. Trans.*, 99:225, 2006a.

Gregori, G., Glenzer, S. H., Fournier, K. B., Campbell, K. M., Dewald, E. L., Jones, O. S., Hammer, J. H., Hansen, S. B., Wallace, R. J., and Landen, O. L. X-ray scattering measurements of radiative heating and cooling dynamics. *Phys. Rev. Lett.*, 101:045003, 2008.

Gregori, G., Glenzer, S. H., and Landen, O. L. Generalized x-ray scattering cross section from nonequilibrium plasmas. *Phys. Rev. E*, 74:026402, 2006b.

Gregori, G., Glenzer, S. H., Rogers, F. J., Pollaine, S. M., Landen, O. L., Blancard, C., Faussurier, G., Renaudin, P., Kuhlbrodt, S., and Redmer, R. Electronic structure measurements in dense plasmas. *Phys. Plasmas*, 11:2754, 2004.

Gregori, G., Glenzer, S. H., Rozmus, W., Lee, R. W., and Landen, O. L. Theoretical model of x-ray scattering as a dense matter probe. *Phys. Rev. E*, 67:026412, 2003.

Gregori, G., Ravisio, A., Höll, A., Glenzer, S. H., and Rose, S. J. Derivation of the static structure factor in strongly coupled non-equilibrium plasmas for x-ray scattering studies. *High Energy Density Phys.*, 3:99, 2007.

Grosberg, A. Yu., Nguyen, T. T., and Shklovskii, B. I. The physics of charge inversion in chemical and biological systems. *Rev. Mod. Phys.*, 74:329–345, 2002.

Guillot, T. Interiors of giant planets inside and outside the solar system. *Science*, 72:286, 1999.

Hamaguchi, S., Farouki, R. T., and Dubin, D. H. E. Phase diagram of Yukawa systems near the one-component-plasma limit revisited. *J. Chem. Phys.*, 105:7641, 1996.

Hansen, J. P. and McDonald, I. R. *Theory of Simple Liquids.* Academic Press, London, 1990.

Hartley, N. J., Belancourt, P., Chapman, D. A., Döppner, T., Drake, R. P., Gericke, D. O., Glenzer, S. H., Le Pape, D. Khaghani S., Ma, T., Neumayer, P., Pak, A., Peters, L., Richardson, S., Vorberger, J., White, T. G., and Gregori, G. Electron-ion temperature equilibration in warm dense tantalum. *High Energy Density Phys.*, 14:1, 2015.

Hau-Riege, S. P., Weisheit, J., Castor, J. I., London, R. A., Scott, H., and Richards, D. F. Modelling quantum processes in classical molecular dynamics simulations of dense plasmas. *New. J. Phys.*, 15:015011, 2013.

Hazak, G., Zinamon, Z., Rosenfeld, Y., and Dharma-wardana, M. W. C. Temperature relaxation in two-temperature states of dense electron-ion systems. *Phys. Rev. E*, 64: 066411, 2001.

Heinz, U. Quark-gluon transport theory: I. The classical theory. *Ann. Phys.*, 161:48, 1985.

Hill, E. G. and Rose, S. J. Thomson scattering in short pulse laser experiments. *Phys. Plasmas*, 19:083302, 2012.

Hoarty, D. J., Allan, P., James, S. F., Brown, C. R. D., Hobbs, L. M. R., Hill, M. P., Harris, J. W. O., Morton, J., Brookes, M. G., Shepherd, R., Dunn, J., Chen, H., Marley, E. Von, Beiersdorfer, P., Chung, H. K., Lee, R. W., Brown, G., and emig, J. The first data from the Orion laser; measurements of the spectrum of hot, dense aluminium. *High Energy Density Phys.*, 9:663, 2013a.

Hoarty, D. J., Allan, P., James, S. F., Brown, C. R. D., Hobbs, L. M. R., Hill, M. P., Morton, J. W. O. Harris J., Brookes, M. G., Shepherd, R., Dunn, J., Chen, H., Von Marley, E., Beiersdorfer, P., Chung, H. K., Lee, R. W., Brown, G., and Emig, J. Observations of the effect of ionization-potential depression in hot dense plasma. *Phys. Rev. Lett.*, 110: 265003, 2013b.

Hoarty, D. J., Guymer, T. M., James, S. F., Gumbrell, E., Brown, C. R. D., Hill, M. P., Morton, J., and Doyle, H. Equation of state studies of warm dense matter samples heated by laser produced proton beams. *High Energy Density Phys.*, 8:50, 2012.

Holas, A., Aravind, P. K., and Singwi, K. S. Dynamic correlations in an electron gas. I. First-order perturbation theory. *Phys. Rev. B*, 20:4912, 1979.

Höll, A., Bornath, Th., Cao, L., Döppner, T., Düsterer, S., Förster, E., Fortmann, C., Glenzer, S. H., Gregori, G., Laarmann, T., Meiwes-Broer, K. H., Przystawik, A., Radcliffe, P., Redmer, R., H. Reinholz and, G. Röpke, Thiele, R., Tiggesbäumker, J., Toleikis, S., Truong, N. X., Tschentscher, T., Uschmann, I., and Zastrau, U. Thomson scattering from near-solid density plasmas using soft x-ray free electron lasers. *High Energy Density Phys.*, 3:120, 2007.

Holm, P. and Ribberfors, R. First correction to the nonrelativistic Compton cross section in the impulse approximation. *Phys. Rev. A*, 40:6251, 1989.

Hong, J. and Kim, C. Dynamic structure of strongly coupled one-component plasmas. *Phys. Rev. A*, 43:1965, 1991.

Hopps, N., Oades, K., Andrew, J., Brown, C. R. D., Cooper, G., Danson, C., Daykin, S., Duffield, S., Edwards, R., Egan, D., Elsmere, S., Gales, S., Girling, M., Gumbrell, E., Harvey, E., Hillier, D., Hoarty, D. J., Horsfield, C., James, S., Leatherland, A., Masoero, S., Meadowcroft, A., Norman, M., Parker, S., Rothman, S., Rubery, M. S., Treadwell, P., Winter, D., and Bett, T. Comprehensive description of the Orion laser facility. *Plasma Phys. Control. Fusion*, 57:064002, 2015.

Hubbard, J. The description of collective motions in terms of many-body perturbation theory. II. The correlation energy of a free-electron gas. *Proc. R. Soc. Lond. A: Math. Phys. and Engin. Sci.*, 352:243, 1957.

Hubbell, J. H., Veigele, W. J., Briggs, E. A., Brown, R. T., Cromer, D. T., and Howerton, R. J. Atomic form factors, incoherent scattering functions, and photon scattering cross sections. *J. Phys. Chem. Ref. Data*, 4:471, 1975.

Hurricane, O. A., Callahan, D. A., Casey, D. T., Celliers, P. M., Cerjan, C., Dewald, E. L., Dittrich, T. R., Döppner, T., Hinkel, D. E., Berzak Hopkins, L. F., Kline, J. L., Le Pape, S., Ma, T., MacPhee, A. G., Milovich, J. L., Pak, A., Park, H.-S., Patel, P. K., Remington, B. A., Salmonson, J. D., Springer, P. T., and Tomassini, R. Fuel gain exceeding unity in an inertially confined fusion implosion. *Nature*, 506:343, 2014.

Ichimaru, S. Strongly coupled plasmas: High-density classical plasmas and degenerate electron liquids. *Rev. Mod. Phys.*, 54:1017, 1982.

Ichimaru, S. *Statistical Plasma Physics Vol. I: Basic Principles*. Westview, 1994a.

Ichimaru, S. *Statistical Plasma Physics Vol. II: Condensed Plasmas*. Westview, 1994b.

Ichimaru, S., Mitake, S., and and. X.-Z. Yan, S. Tanaka. Theory of interparticle correlations in dense, high-temperature plasmas. I. General formalism. *Phys. Rev. A*, 32:1768, 1985.

Iglesias, C. A. and Rogers, F. J. Updated OPAL opacities. *Astrophys. J.*, 464:943, 1996.

Inogamov, N. A., Faenov, A. Ya., Zhakhovsky, V. V., Pikuz, T. A., Skobelev, I. Yu., Petrov, Yu. V., Khokhlov, V. A., Shepelev, V. V., Anisimov, S. I., Fortov, V. E., Fukuda, Y., Kando, M., Kawachi, T., Nagasono, M., Ohashi, H., Yabashi, M., Tono, K., Senda, Y., Togashi, T., and Ishikawa, T. Two-temperature warm dense matter produced by ultrashort extreme ultraviolet free electron laser (EUV-FEL) pulse. *Contrib. Plasma Phys.*, 51:419, 2011.

Jackson, J. D. *Classical Electrodynamics.* John Wiley & Sons, New York, NY, 1962.

Jauho, A. P. Nonequilibrium Green's function techniques applied to hot electron quantum transport. *Solid State Elec.*, 32:1265, 1989.

Keldysh, L. V. Diagram technique for nonequilibrium processes. *Sov. Phys. JETP*, 20: 1018, 1965.

Kemp, A., Fiuza, F., Debayle, A., Johzaki, T., Mori, W. B., Patel, P. K., Sentoku, Y., and Silva, L. O. Laser-plasma interactions for fast ignition. *Nucl. Fusion*, 54:054002, 2014.

Klein, O. and Nishina, Y. Über die Streuung von Strahlung durch freie Elektronen nach der neuen relativistischen Quantendynamik von Dirac. *Zeitschr. für Phys.*, 52:853, 1929.

Klimontovich, Y. L. *Kinetic Theory of Nonideal Gases and Nonideal Plasmas (in Russian).* Nauka, Moskow (Engl. trans. Pergamon Press, 1982), 1975.

Klimontovich, Y. L. and Kremp, D. Quantum kinetic equations in systems with bound states. *Physica A: Stat. Mech. App.*, 109:517, 1981.

Klimontovich, Yu. L. and Silin, V. P. . *Dokl. Akad. Nauk. SSSR*, 82:361, 1952.

Kline, J. L., Montgomery, D. S., Bezzerides, B., Cobble, J. A., DuBois, D. F., Johnson, R. P., Rose, H. A., Yin, L., and Vu, H. X. Observation of a transition from fluid to kinetic nonlinearities for Langmuir waves driven by stimulated Raman backscatter. *Phys. Rev. Lett.*, 94:175003, 2005.

Kohn, W. and Sham, L. J. Self-consistent equations containing exchange and correlation effects. *Phys. Rev.*, 140:A1133, 1965.

Kraus, D., Döppner, T., Kritcher, A. L., Bachmann, B., Chapman, D. A., Collins, G. W., Glenzer, S. H., Hawreliak, J. A., Landen, O. L., Ma, T., Le Pape, S., Neumayer, P., Swift, D. C., and Falcone, R. W. X-ray continuum emission spectroscopy from hot dense matter at Gbar pressures. *Rev. Sci. Instrum.*, 85:11D606, 2014.

Kraus, D., Vorberger, J., Gericke, D. O., Bagnoud, V., Blaževic, A., Cayzac, W., Frank, A., Gregori, G., Ortner, A., Otten, A., Roth, F., Schaumann, G., Schumacher, D., Siegenthaler, K., Wagner, F., Wünsch, K., and Roth, M. Probing the complex ion structure in liquid carbon at 100 GPa. *Phys. Rev. Lett.*, 111:255501, 2013.

Kremp, D., Schlanges, M., and Kraeft, W. D. *Quantum Statistics of Nonideal Plasmas.* Springer Verlag, Berlin, 2005.

Kritcher, A. L., Döppner, T., Fortmann, C., Landen, O. L., Wallace, R., and Glenzer, S. H. Development of x-ray Thomson scattering for implosion target characterization. *High Energy Density Phys.*, 7:271, 2011a.

Kritcher, A. L., Döppner, T., Fortmann, C., Ma, T., Landen, O. L., Wallace, R., and Glenzer, S. H. In-flight measurements of capsule shell adiabats in laser-driven implosions. *Phys. Rev. Lett.*, 107:015002, 2011b.

Kritcher, A. L., Döppner, T., Swift, D., Hawreliak, J., Collins, G., Nilsen, J., Bachmann, B., Dewald, E., Strozzi, D., Felker, S., Landen, O. L., Jones, O., Thomas, C., Hammer, J., Keane, C., Lee, H. J., Glenzer, S. H., Rothman, S., Chapman, D. A., Kraus, D.,

Neumayer, P., and Falcone, R. W. Probing matter at Gbar pressure at the NIF. *High Energy Density Phys.*, 10:27, 2014.

Kritcher, A. L., Neumayer, P., Brown, C. R. D., Davis, P., Döppner, T., Falcone, R. W., Gericke, D. O., Gregori, G., Holst, B., Landen, O. L., Lee, H. J., Morse, E. C., Pelka, A., Redmer, R., Roth, M., Vorberger, J., Wünsch, K., and Glenzer, S. H. Measurements of ionic structure in shock-compressed lithium hydride from ultra-fast Thomson scattering. *Phys. Rev. Lett.*, 103:245004, 2009.

Kruer, W. L. *The Physics of Laser-Plasma Interactions.* Westview, Boulder, CO, 1992.

Kruer, W. L. and Estabrook, K. G. JxB heating by very intense laser light. *Phys. Fluids*, 420:28, 1985.

Kunze, H.-J., Fünfer, E., Kronast, B., and Kegel, W. H. Experimental results on light scattering by a θ-pinch plasma using a ruby laser. *Phys. Lett.*, 11:42, 1963.

La Fontaine, B., Baldis, H. A., Villeneuve, D. M., Dunn, J., Enright, G. D., Kieffer, J. C., Pépin, H., Rosen, M. D., Matthews, D. L., and Maxon, S. Characterization of laser-produced plasmas by ultraviolet Thomson scattering. *Phys. Plasmas*, 1:2329, 1994.

La Fontaine, B., Dunn, J., Baldis, H. A., Enright, G. D., Villeneuve, D. M., Kieffer, J. C., Nantel, M., and Pépin, H. Electron-temperature inhomogeneities along an x-ray laser plasma. *Phys. Rev. E*, 47:583, 1993.

Landau, L. D. *Phys. Z. Sowjetunion*, 10:154, 1936.

Landen, O. L., Edwards, J., Haan, S. W., Robey, H. F., Milovich, J., Spears, B. K., Weber, S. V., Clark, D. S., Lindl, J. D., MacGowan, B. J., Moses, E. I., Atherton, J., Amendt, P. A., Boehly, T. R., Bradley, D. K., Braun, D. G., Callahan, D. A., Celliers, P. M., Collins, G. W., Dewald, E. L., Divol, L., Frenje, J. A., Glenzer, S. H., Hamza, A., Hammel, B. A., Hicks, D. G., Hoffman, N., Izumi, N., Jones, O. S., Kilkenny, J. D., Kirkwood, R. K., Kline, J. L., Kyrala, G. A., Marinak, M. M., Meezman, N., Meyerhofer, D. D., Michel, P., Munro, D. H., Olson, R. E., Nikroo, A., Regan, S. P., Suter, L. J., Thomas, C. A., and Wilson, D. C. Capsule implosion optimization during the indirect-drive National Ignition Campaign. *Phys. Plasmas*, 18:051002, 2011.

Landen, O. L., Glenzer, S. H., Edwards, M. J., Lee, R. W., Collins, G. W., Cauble, R. C., Hsing, W. W., and Hammel, B. A. Dense matter characterization by x-ray Thomson scattering. *J. Quant. Spectrosc. Rad. Trans.*, 71:465, 2001.

Landen, O. L. and Winfield, R. J. Laser scattering from dense cesium plasmas. *Phys. Rev. Lett.*, 54:1660, 1985.

Langdon, A. B. Nonlinear inverse bremsstrahlung and heated-electron distributions. *Phys. Rev. Lett.*, 44:575, 1980.

Langreth, D. C. and Wilkins, J. W. Theory of spin resonances in dilute magnetic alloys. *Phys. Rev. B*, 6:3189, 1972.

Le Pape, S., Neumayer, P., Fortmann, C., Döppner, T., Davis, P., Landen, A. L. Kritcher O. L., and Glenzer, S. H. X-ray radiography and scattering diagnostics of dense shock-compressed matter. *Phys. Plasmas*, 17:053309, 2010.

Lee, H. J., Neumayer, P., Castor, J., Döppner, T., Falcone, R. W., Fortmann, C., Hammer, B. A., Kritcher, A. L., Landen, O. L., Lee, R. W., Meyerhofer, D. D., Munro, D. H., Redmer, R., Regan, S. P., Weber, S., and Glenzer, S. H. X-ray Thomson scattering measurements of density and temperature in shock-compressed beryllium. *Phys. Rev. Lett.*, 102:115001, 2009.

Lee, R. W. and Larsen, J. T. A time-dependent model for plasma spectroscopy of K-shell emitters. *J. Quant. Spectrosc. Rad. Trans.*, 56:535, 1996.

Li, C. -K. and Petrasso, R. D. Fokker-Planck equation for moderately coupled plasmas. *Phys. Rev. Lett.*, 70:3063, 1993.

Lin, Z., Zhigilei, L. V., and Celli, V. Electron-phonon coupling and electron heat capacity of metals under conditions of strong electron-phonon nonequilibrium. *Phys. Rev. B*, 77: 075133, 2008.

Lipavský, P., Špička, V., and Velický, B. Generalized Kadanoff-Baym ansatz for deriving quantum transport equations. *Phys. Rev. B*, 34:6933, 1968.

Liu, Z. J., Zheng, J., and Yu, C. X. Effects of super-Gaussian electron velocity distributions on the ion feature of Thomson scattering off two-ion plasmas. *Phys. Plasmas*, 9:1073, 2002.

Ma, T., Döppner, T., Falcone, R. W., Fletcher, L. B., Fortmann, C., Gericke, D. O., Landen, O. L., Lee, H. J., Pak, A., Vorberger, J., Wünsch, K., and Glenzer, S. H. X-ray scattering measurements of strong ion-ion correlations in shock-compressed aluminium. *Phys. Rev. Lett.*, 110:065001, 2013.

Ma, T., Fletcher, L. B., Pak, A., Chapman, D. A., Falcone, R. W., Fortmann, C., Galtier, E., Gericke, D. O., Gregori, G., Hastings, J., Landen, O. L., Le Pape, S., Lee, H. J., Nagler, B., Neumayer, P., Turnbull, D., Vorberger, J., White, T. G., Wünsch, K., Zastrau, U., Glenzer, S. H., and Döppner, T. Observations of strong ion-ion correlations in dense plasmas. *Phys. Plasmas*, 21:056302, 2014.

MacFarlane, J. J., Golovkin, I. E., Wang, P., Woodruff, P. R., and Pereyra, N. A. SPECT3D - A multi-dimensional collisional-radiative code for generating diagnostic signatures based on hydrodynamics and PIC simulation output. *High Energy Density Phys.*, 3:181, 2007.

Mackinnon, A. J., Kline, J. L., Dixit, S. N., Glenzer, S. H., Edwards, M. J., Callahan, D. A., Meezan, N. B., Haan, S. W., Kilkenny, J. D., Döppner, T., Farley, D. R., Moody, J. D., Ralph, J. E., MacGowan, B. J., Landen, O. L., Robey, H. F., Boehly, T. R., Celliers, P. M., Eggert, J. H., Krauter, K., Frieders, G., Ross, G. F., Hicks, D. G., Olson, R. E., Weber, S. V., Spears, B. K., Salmonsen, J. D., Michel, P., Divol, L., Hammel, B., Thomas, C. A., Clark, D. S., Jones, O. S., Springer, P. T., Cerjan, C. J., Collins, G. W., Glebov, V. Y., Knauer, J. P., Sangster, C., Stoeckl, C., McKenty, P., McNaney, J. M., Leeper, R. J., Ruiz, C. L., Cooper, G. W., Nelson, A. G., Chandler, G. G. A., Hahn, K. D., Moran, M. J., Schneider, M. B., Palmer, N. E., Bionta, R. M., Hartouni, E. P., Le Pape, S., Patel, P. K., Izumi, N., Tommasini, R., Bond, E. J., Caggiano, J. A., Hatarik, R., Grim, G. P., Merrill, F. E., Fittinghoff, D. N., Guler, N., Drury, O., Wilson, D. C., Herrmann, H. W., Stoeffl, W., Casey, D. T., Johnson, M. G., Frenje, J. A., Petrasso, R. D., Zylestra, A., Rinderknecht, H., Kalantar, D. H.,

Dzenitis, J. M., Di Nicola, P., Eder, D. C., Courdin, W. H., Gururangan, G., Burkhart, S. C., Friedrich, S., Blueuel, D. L., Bernstein, I. A., Eckart, M. J., Munro, D. H., Hatchett, S. P., Macphee, A. G., Edgell, D. H., Bradley, D. K., Bell, P. M., Glenn, S. M., Simanovskaia, N., Barrios, M. A., Benedetti, R., Kyrala, G. A., Town, R. P. J., Dewald, E. L., Milovich, J. L., Widmann, K., Moore, A. S., LaCaille, G., Regan, S. P., Suter, L. J., Felker, B., Ashabranner, R. C., Jackson, M. C., Prasad, R., Richardson, M. J., Kohut, T. R., Datte, P. S., Krauter, G. W., Klingman, J. J., Burr, R. F., Land, T. A., Hermann, M. R., Latray, D. A., Saunders, R. L., Weaver, S., Cohen, S. J., Berzins, L., Brass, S. G., Palma, E. S., Lowe-Webb, R. R., McHalle, G. N., Arnold, P. A., Lagin, L. J., Marshall, C. D., Brunton, G. K., Mathisen, D. G., Wood, R. D., Cox, J. R., Ehrlich, R. B., Knittel, K. M., Bowers, M. W., Zacharias, R. A., Young, B. K., Holder, J. P., Kimbrough, J. R., Ma, T., La Fortune, K. N., Widmayer, C. C., Shaw, M. J., Erbert, G. V., Jancaitis, K. S., Di Nicola, J. M., Orth, C., Heestand, G., Kirkwood, R., Haynam, C., Wegner, P. J., Whitman, P. K., Hamza, A., Dzenitis, E. G., Wallace, R. J., Bhandarkar, S. D., Parham, T. G., Dylla-Spears, R., Mapoles, E. R., Kozioziemski, B. J., Sater, J. D., Walters, C. F., Haid, B. J., Fair, J., Nikroo, A., Giraldez, E., Moreno, K., Vanwonterghem, B., Kauffman, R. L., Batha, S., Larson, D. W., Fortner, R. J., Schneider, D. H., Lindl, J. D., Patterson, R. W., Atherton, L. J., and Moses, E. I. Assembly of high-areal-density deuterium-tritium fuel from indirectly driven cryogenic implosions. *Phys. Rev. Lett.*, 108:215005, 2012.

Mancic, A., Robiche, J., Antici, P., Audebert, P., Blancard, C., Combis, P., Dorchies, F., Faussurier, G., Harmand, S. Fourmaux M., Kodema, R., Lancia, L., Mazevet, S., Nakatsutsumi, M., Peyrusse, O., Recoules, V., Renaudin, P., Shepherd, R., and Fuchs, J. Isochoric heating of solids by laser-accelerated protons: Experimental characterization and self-consistent hydrodynamic modeling. *High Energy Density Phys.*, 6:21, 2010.

Marinak, M. M., Haan, S. W., Dittich, T. R., Tipton, R. E., and Zimmerman, G. B. A comparison of three-dimensional multimode hydrodynamic instability growth on various National Ignition Facility capsule designs with HYDRA simulations. *Phys. Plasmas*, 5: 1125, 1998.

Marinak, M. M., Kerbal, G. D., Gentile, N. A., Jones, O., Munro, D., Pollaine, S. W., Dittich, T. R., and Haan, S. W. Three-dimensional HYDRA simulations of National Ignition Facility targets. *Phys. Plasmas*, 8:2275, 2001.

Martin, P. C. Sum rules, Kramers-Kronig relations, and transport coefficients in charged systems. *Phys. Rev.*, 161:143, 1967.

Martin, P. C. and Schwinger, J. Theory of many-particle systems. I. *Phys. Rev.*, 115:1342, 1959.

Matsubara, T. A new approach to quantum-statistical mechanics. *Prog. Theor. Phys.*, 14: 351, 1955.

Matte, J. P., Lamoureux, M., Moller, C., Yin, R. Y., Delettrez, J., Virmont, J., and Johnston, T. W. Non-Maxwellian electron distributions and continuum x-ray emission in inverse bremsstrahlung heated plasmas. *Plasma Phys. Control. Fusion*, 30:1665, 1988.

Mattern, B. A. and Seidler, G. T. Theoretical treatment of the bound-free contribution and experimental best practice in x-ray Thomson scattering from warm dense matter. *Phys. Plasmas*, 20:022706, 2013.

Mattern, B. A., Seidler, G. T., Kas, J. J., Pacold, J. I., and Rehr, J. J. Real-space Green's function calculations of Compton profiles. *Phys. Rev. B*, 85:115135, 2012.

Mattuck, R. D. *A Guide to Feynman Diagrams in the Many-Body Problem.* Dover publications, New York, NY, 1992.

Mazzone, G., Sacchetti, F., and Contini, V. Static structure and electron-electron correlations in Be. A comparison of experiment with electron-gas theory. *Phys. Rev. B*, 28: 1772, 1983.

McCarthy, R. D., Hord, J., and Roder, H. M. *Selected properties of hydrogen (Engineering design data).* U.S. Government Print Office, Washington D.C., 1981.

Medvedev, N., Jeschke, H. O., and Ziaja, B. Nonthermal phase transitions in semiconductors induced by a femtosecond extreme ultraviolet laser pulse. *New J. Phys.*, 15:015016, 2013.

Medvedev, N. and Rethfeld, B. Transient dynamics of the electronic subsystem of semiconductors irradiated with an ultrashort vacuum ultraviolet laser pulse. *New J. Phys.*, 12:073037, 2010.

Medvedev, N., Zastrau, U., Förster, E., Gericke, D. O., and Rethfeld, B. Short-time electron dynamics in aluminum excited by femtosecond extreme ultraviolet radiation. *Phys. Rev. Lett.*, 107:165003, 2011.

Mermin, N. D. Lindhard dielectric function in the relaxation-time approximation. *Phys. Rev. B*, 1:2362, 1970.

Mihara, N. and Puff, R. D. Liquid structure factor of ground-state He^4. *Phys. Rev.*, 174: 221, 1968.

Miliotis, D. M. Bulk-plasmon dispersion spectrum of Be using an x-ray scattering technique. *Phys. Rev. B*, 3:701, 1971.

Morales, M. A., Benedict, L. X., Clark, D. S., Schwegler, E., Tamblyn, I., Bonev, S. A., Correa, A. A., and Haan, S. W. Ab initio calculations of the equation of state of hydrogen in a regime relevant for inertial fusion applications. *High Energy Density Phys.*, 8:5, 2012.

Morawetz, K. and Fuhrmann, U. General response functions for interacting liquids. *Phys. Rev. E*, 61:2272, 2000.

Morawetz, K., Walke, R., and Fuhrmann, U. New collective mode due to collisional damping. *Phys. Rev. C*, 57:R2813, 1998.

Moses, E. and Wuest, C. R. The National Ignition Facility: Laser performance and first experiments. *Fus. Sci. Technol.*, 47:314, 2005.

Nagler, B., Arnold, B., Bouchard, G., Boyce, R. F., Boyce, R. M., Callen, A., Campell, M., Curiel, R., Galtier, E., Garofoli, J., Granados, E., Hastings, J., Hays, G., Heimann, P., Lee, R. W., Milathianaki, D., Plummer, L., Schropp, A., Wallace, A., Welch, M., White, W., Xing, Z., Yin, J., Young, J., Zastrau, U., and Lae, H.-J. The Matter at Extreme Conditions instrument at the Linac Coherent Light Source. *J. Synchrotron Rad.*, 22:520, 2015.

Nardi, E. Scattering of x-rays by the bound and free electrons in dense plasma. *Phys. Rev. A*, 1977:43, 1991.

Neumayer, P., Fortmann, C., Döppner, T., Davis, P., Falcone, R. W., Kritcher, A. L., Landen, O. L., Lee, H. J., Lee, R. W., Niemann, C., Le Pape, S., and Glenzer, S. H. Plasmons in strongly coupled shock-compressed matter. *Phys. Rev. Lett.*, 105:075003, 2010.

Ng, A., Celliers, P., Xu, G., and Forsman, A. Electron-ion equilibration in a strongly coupled plasma. *Phys. Rev. E*, 52:4299, 1995.

O'Neill, T. M. and Malmberg, J. H. Transition of the dispersion roots from beam-type to Landau-type solutions. *Phys. Fluids*, 11:1754, 1968.

Ono, M., Nishigata, Y., Nishio, T., Eguchi, T., and Hasegawa, Y. Electrostatic potential screened by a two-dimensional electron system: A real-space observation by scanning-tunnelling spectroscopy. *Phys. Rev. Lett.*, 96:016801, 2006.

Ornstein, L.S. and Zernike, F. Accidental deviations of density and opalescence at the critical point of a single substance. *Proc. Akad. Sci.*, 1914.

Pak, A., Gregori, G., Knight, J., Campbell, K., Price, D., Hammel, B., Landen, O. L., and Glenzer, S. H. X-ray line measurements with high efficiency Bragg crystals. *Rev. Sci. Instrum.*, 75:3747, 2004.

Palastro, J. P., Ross, J. S., Pollock, B., Divol, L., Froula, D. H., and Glenzer, S. H. Fully relativistic form factor for Thomson scattering. *Phys. Rev. E*, 81:036411, 2010.

Pastor, I., Guasp, J., Álvarez Estrada, R. F., and Castejon, F. Numerical computation of Thomson scattering spectra for non-Maxwellian or anisotropic electron distribution functions. *Nucl. Fusion*, 52:123013, 2012.

Pauli, W. Über den Zusammenhang des Abschlusses der Elektronengruppen im Atom mit der Komplexstruktur der Spektren. *Zeitschr. für Phys.*, 31:765, 1925.

Pauli, W. The connections between spin and statistics. *Phys. Rev.*, 58:716, 1940.

Pauling, L. and Sherman, J. Screening constants for many-electron atoms. The calculation and interpretation of x-ray term values and and the calculation of atomic scattering factors. *Zeitschr. Kristallogr.*, 1:81, 1932.

Peacock, N. J., Robinson, D. C., Forrest, M. J., Wilcock, P. D., and Sanniko, V. V. Measurement of the electron temperature by Thomson scattering in tokamak T3. *Nature*, 224:488, 1969.

Pelka, A., Gregori, G., Gericke, D. O., Vorberger, J., Glenzer, S. H., Günther, M. M., Harres, K., Heathcote, R., Kritcher, A. L., Kugland, N. L, Li, B., Makita, M., Mithen, J., Neely, D., Niemann, C., Otten, A., Riley, D., Schaumann, G., Schollmeier, M., Tauschwitz, An., and Roth, M. Ultra-fast melting of carbon induced by intense proton beams. *Phys. Rev. Lett.*, 105:265701, 2010.

Perrot, F. and Dharma-wardana, M. W. C. Electrical resistivity of hot dense plasmas. *Phys. Rev. A*, 36:238, 1987.

Pines, D. and Bohm, D. A collective description of electron interactions: II. Collective vs individual particle aspects of the interactions. *Phys. Rev.*, 85:338, 1952.

Plagemann, K. U., Sperling, P., Thiele, R., Desjarlais, M. P., Fortmann, C., Döppner, T., Lee, H. J., Glenzer, S. H., and Redmer, R. Dynamic structure factor in warm dense beryllium. *New. J. Phys.*, 14:055020, 2012.

Press, W. H., Teukolsky, S. A., Vetterling, W. T., and Flannery, B. P. *Numerical Recipes Third Edition*. Cambridge University Press, Cambridge, 2007.

Puff, R. D. Application of sum rules to the low-temperature interacting boson system. *Phys. Rev.*, 137:A406, 1965.

Raman, C. V. and Krishnan, K. S. A new type of secondary radiation. *Nature*, 121:501, 1928.

Reinholz, H., Redmer, R., Röpke, G., and Wierling, A. Long-wavelength limit of the dynamical local-field factor and dynamical conductivity of a two-component plasma. *Phys. Rev. E*, 62:5648, 2000.

Resta, R. Thomas-Fermi dielectric screening in semiconductors. *Phys. Rev. B*, 16:2717, 1977.

Richardson, C. F. and Ashcroft, N. W. Dynamic local-field factors and effective interactions in the three-dimensional electron liquid. *Phys. Rev. B*, 50:8170, 1994.

Riley, D., Weaver, I., McSherry, D., Dunne, M., Neely, D., Notley, M., and Nardi, E. Direct observation of strong coupling in a dense plasma. *Phys. Rev. E*, 66:046408, 2002.

Riley, D., Woolsey, N. C., McMSherry, D., Weaver, I., Djaoui, A., and Nardi, E. X-ray diffraction from a dense plasma. *Phys. Rev. Lett.*, 84:1704, 2000.

Riley, K. F., Hobson, M. P., and Bence, S. J. *Mathematical Methods for Physics and Engineering*. Cambridge University Press, 1998.

Robey, H. F., Celliers, P. M., Kline, J. L., Mackinnon, A. J., Boehly, T. R., Landen, O. L., Eggert, J. H., Hicks, D.G., Le Pape, S., Farley, D. R., Bowers, M. W., Krauter, K. G., Munro, D. H., Jones, O. S., Milovich, J. L., Clark, D., Spears, B. K., Town, R. P. J., Haan, S. W., Dixit, S., Schneider, M. B., Dewald, E. L., Widmann, K., Moody, J. D., Döppner, T., Radousky, H. B., Nikroo, A., Kroll, J. J., Hamza, A. V., Horner, J. B., Bhandarkar, S. D., Dzenitis, E., Alger, E., Giraldez, E., Castro, C., Moreno, K., Haynam, C., La Fortune, K. N., Widmayer, C., Shaw, M., Jancaitis, K., Parham, T., Holunga, D. M., Walters, C.F., Haid, B., Malsbury, T., Trummer, D., Coffee, K. R., Burr, B., Berzins, L. V., Choate, C., Brereton, S. J., Azevedo, S., Chandrasekaran, H., Glenzer, S. H., Caggiano, J. A., Knauer, J. P., Frenje, J. A., Casey, D. T., Gatu Johnson, M., Seguin, F. H., Young, B. K., Edwards, M. J., Van Wonterghem, B. M., Kilkenny, J., MacGowan, B. J., Atherton, J., Lindl, J. D., Meyerhofer, D. D., and Moses, E. Precision shock tuning on the National Ignition Facility. *Phys. Rev. Lett.*, 108:215004, 2012.

Rogers, F. J., Swenson, F. J., and Iglesias, C. A. OPAL equation of state tables for astrophysical applications. *Astrophys. J.*, 456:902, 1996.

Röpke, G., Selchow, A., Wierling, A., and Reinholz, H. Lindhard dielectric function in the relaxation-time approximation and generalized linear response theory. *Phys. Lett. A*, 260:365, 1999.

Röpke, G. and Wierling, A. Dielectric function of a two-component plasma including collisions. *Phys. Rev. E*, 57:7075, 1998.

Ross, J. S., Glenzer, S. H., Palastro, J. P., Pollock, B. B., Price, D., Divol, L., Tynan, G. R., and Froula, D. H. Observation of relativistic effects in collective Thomson scattering. *Phys. Rev. Lett.*, 104:105001, 2010.

Ross, M., Ree, F. H., and Young, D. A. The equation of state of molecular hydrogen at very high density. *J. Chem. Phys.*, 79:1487, 1983.

Roth, M., Alber, I., Bagnoud, V., Brown, C. R. D., Clarke, R., Daido, H., Fernandez, J., Flippo, K., Gaillard, S., Gauthier, C., Geissel, M., Glenzer, S. H., Gregori, G., Günther, M., Harres, K., Heathcote, R., Kritcher, A., Kugland, N., Le Pape, S., Li, B., Makita, M., Mithen, J., Niemann, C., Offermann, F. Nürnberg D., Otten, A., Pelka, A., Riley, D., Schaumann, G., Scollmeier, M., Schütrumpf, J., Tampo, M., Tauschwitz, A., and Tauschwitz, An. Proton acceleration experiments and warm dense matter research using high power lasers. *Plasma Phys. Control. Fusion*, 51:124039, 2009.

Salpeter, E. E. Electron density fluctuations in a plasma. *Phys. Rev.*, 120:1528, 1960.

Saltzmann, D. *Atomic Physics in Hot Plasmas*. Oxford University Press, 1998.

Schumacher, M., Smend, F., and Borchert, I. Incoherent scattering of gamma rays by inner-shell electrons. *J. Phys. B.: At. Mol. Opt. Phys.*, 8:1428, 1975.

Schwinger, J. Brownian motion of a quantum oscillator. *J. Math. Phys.*, 2:407, 1961.

Scopigno, T. and Ruocco, G. Microscopic dynamics in liquid metals: The experimental point of view. *Rev. Mod. Phys.*, 77:881, 2005.

Sheffield, J., Froula, D. H., Glenzer, S. H., and Luhmann, Jr., N. C. *Plasma Scattering of Electromagnetic Radiation*. Academic Press, New York, NY, 2011.

Sherlock, M. Universal scaling of the electron distribution function in one-dimensional simulations of relativistic laser-plasma interactions. *Phys. Plasmas*, 16:103101, 2009.

Silvera, I. F. and Goldman, V. V. The isotropic intermolecular potential for H_2 and D_2 in the solid and gas phases. *J. Chem. Phys.*, 69:4209, 1978.

Singwi, K. S., Sjölander, A., Tosi, M. P., and Land, R. H. Electron correlations at metallic densities. IV. *Phys. Rev. B*, 1:1044, 1970.

Singwi, K. S., Tosi, M. P., Land, R. H., and Sjölander, A. Electron correlations at metallic densities. *Phys. Rev.*, 176:589, 1968.

Sinn, H., Sette, F., Bergmann, U., Halcoussis, Ch., Krisch, M., Verbeni, R., and Burkel, E. Coherent dynamic structure factor of liquid lithium by inelastic x-ray scattering. *Phys. Rev. Lett.*, 78:1715, 1997.

Sircombe, N. J. and Arber, T. D. VALIS: A split-conservative scheme for the relativistic 2D Vlasov-Maxwell system. *J. Comput. Phys.*, 228:4773, 2009.

Sircombe, N. J., Hughes, S. J., and Ramsay, M. G. Integrated calculations of short-pulse laser interactions with matter. *New. J. Phys.*, 15:025025, 2013.

Sperling, P., Liseykina, T., Bauer, D., and Redmer, R. Time-resolved Thomson scattering on high-intensity laser-produced hot dense helium plasmas. *New J. Phys.*, 15:025041, 2013.

Spitzer, L. *Physics of Fully Ionized Gases.* Interscience, New York, NY, 1962.

Springer, J. F., Pokrant, M. A., and Stevens, F. A. Integral equation solutions for the classical electron gas. *J. Chem. Phys.*, 58:4863, 1973.

Stewart, J. C. and Pyatt Jr., K. D. Lowering of ionization potentials in plasmas. *Astrophys. J.*, 144:1203, 1966.

Strutt, W. J. On the electromagnetic theory of light. *Phil. Mag.*, 12:81, 1881.

Swift, D., Hawreliak, J., Braun, D., Kritcher, A. L., Glenzer, S. H., Collins, G. W., Rothman, S. D., Chapman, D. A., and Rose, S. Gigabar material properties experiments on NIF and Omega. *AIP Conf. Proc.*, 1426:477, 2012.

Swift, D.C. Private communications, 2014.

Theile, R., Bornath, T., Fortmann, C., Höll, A., Redmer, R., Reinholz, H., Röpke, G., Wierling, A., Glenzer, S. H., and Gregori, G. Plasmon resonance in warm dense matter. *Phys. Rev. E*, 78:026411, 2008.

Thiele, R., Sperling, P., Chen, M., Bornath, Th., Fäustlin, R. R., Fortmann, C., Glenzer, S. H., Kraeft, W. D., Pukhov, A., Toleikis, S., Tschentscher, Th., and Redmer, R. Thomson scattering on inhomogeneous targets. *Phys. Rev. E*, 82:056404, 2010.

Thomas, L. H. The calculation of atomic fields. *Proc. Camb. Philos. Soc.*, 23:542, 1927.

Thomsen, J. S. Logical relations among the principles of statistical mechanics and thermodynamics. *Phys. Rev.*, 91:1263, 1953.

Thomson, J. J. *Conduction of Electricity through Gases.* Cambridge University Press, 1906.

Toleikis, S., Bornath, T., Döppner, T., Dürsterer, S., Fäustlin, R. R., Förster, E., Fortmann, C., Glenzer, S. H., Göde, S., Gregori, G., Irsig, R., Laarmann, T., Lee, H. J., Li, B., Meiwes-Broer, K.-H., Mithen, J., Nagler, B., Przystawick, A., Radcliffe, P., Redlin, H., Redmer, R., Reinholz, H., Röpke, G., Tavella, F., Theile, R., Tiggesbäumker, J., Urschmann, I., Vinko, S. M., Whitcher, T., Zastrau, U., Ziaja, B., and Tschentscher, T. Probing near-solid density plasmas using soft x-ray scattering. *J. Phys. B: At. Mol. Opt. Phys.*, 43:194017, 2010.

Tonks, L. and Langmuir, I. Oscillations in ionized gases. *Phys. Rev.*, 33:195, 1929.

Tsallis, C. Possible generalization of Boltzmann-Gibbs statistics. *J. Stat. Phys.*, 52:479, 1988.

Tyndall, J. On the action of rays of refrangibility upon gaseous matter. *Phil. Trans. R. Soc. Lond.*, 160:333, 1870.

Urry, M. K., Gregori, G., Landen, O. L., Pak, A., and Glenzer, S. H. X-ray probe development for collective scattering measurements in dense plasmas. *J. Quant. Spectrosc. Rad. Trans.*, 99:636, 2006.

Utsumi, K. and Ichimaru, S. Dielectric formulation of strongly coupled electron liquids at metallic densities. III. Dynamic structure factor. *Phys. Rev. B*, 23:3291, 1981.

Utsumi, K. and Ichimaru, S. Dielectric formulation of strongly coupled electron liquids at metallic densities. VI. Analytic expression for the local-field correction. *Phys. Rev. A*, 26:603, 1982.

van Leeuwen, J. M. J., Groeneveld, J., and de Boer, J. New method for the calculation of the pair correlation function. *Physica*, 25:792, 1959.

Vorberger, J., Donko, Z., Tkachenko, I. M., and Gericke, D. O. Dynamic ion structure factor of warm dense matter. *Phys. Rev. Lett.*, 109:225001, 2012.

Vorberger, J. and Gericke, D. O. Coupled mode effects on energy transfer in weakly coupled, two-temperature plasmas. *Phys. Plasmas*, 16:082702, 2009.

Vorberger, J. and Gericke, D. O. Theory of electron-ion energy transfer applied to laser ablation. *AIP Conf. Proc.*, 1462:572, 2012.

Vorberger, J. and Gericke, D. O. Effective ion-ion potentials in warm dense matter. *High Energy Density Phys.*, 9:178, 2013.

Vorberger, J. and Gericke, D. O. Comparison of electron-ion energy transfer in dense plasmas obtained from numerical simulations and quantum kinetic theory. *High Energy Density Phys.*, 10:1, 2014.

Vorberger, J. and Gericke, D. O. *Ab initio* approach to model x-ray diffration in warm dense matter. *Phys. Rev. E*, 91:033112, 2015.

Vorberger, J., Gericke, D. O., Bornath, Th., and Schlanges, M. Energy relaxation in dense, strongly coupled two-temperature plasma. *Phys. Rev. Lett.*, 81:046404, 2010.

Vorberger, J., Gericke, D. O., and Kraeft, W. D. The equation of state for hydrogen at high densities. *High Energy Density Phys.*, 9:448, 2013.

Vorberger, J., Schlanges, M., Gericke, D. O., and Kraeft, W. D. Equation of state of high density plasmas. *J. Phys. A: Math. Gen.*, 39:4707, 2006.

Vu, H. X., Yin, L., DuBois, D. F., Bezzerides, B., and Dodd, E. S. Nonlinear spectral signatures and spatio-temporal behaviour of stimulated Raman scattering from single laser speckles. *Phys. Rev. Lett.*, 95:245003, 2005.

Wang, T., Zhu, D., Wu, B., Graves, C., Schaffert, S., Rander, T., Müller, L., Vodungbo, B., Baumier, C., Bernstein, D. P., Cros, B. Bräuer V., de Jong, S., Delaunay, R., Fognini, A., Kukreja, R., Lee, S., López-Flores, V., Mohanty, J., Pfau, B., Popescu, H., Sacchi, M., Sardinha, A. B., Sirotti, F., Zeitoun, P., Messerschmidt, M., Turner, J. J., Schlotter, W. F., Hellwig, O., Mattana, R., Jaouen, N., Fortuna, F., Acremann, Y., Gutt, C., Dürr, H. A., Beaurepaire, E., Boeglin, C., Eisebitt, S., Grübel, G., Lüning, J., Stöhr, J., and Scherz, A. O. Femtosecond single-shot imaging of nanoscale ferromagnetic order in Co/Pd multilayers using resonant x-ray holography. *Phys. Rev. Lett.*, 108:267403, 2012.

Wang, Z., Zheng, J., Zhao, B., Yu, C. X., Jiang, X., Li, W., Liu, S., Ding, Y., and Zheng, Z. Thomson scattering from laser-produced gold plasmas in radiation conversion layer. *Phys. Plasmas*, 12:082703, 2005.

Watt, R. G. and Pietrzyk, Z. A. Thomson scattering from an anistropic plasma. *Phys. Fluids*, 22:778, 1979.

Wentzel, G. Über den Rückstoß beim Comptoneffekt am Wasserstoffatom. *Zeitschr. für Phys.*, 58:348, 1929.

White, S., Nersisyan, G., Kettle, B., Dzelzainis, T. W. J., McKeever, K., Lewis, C. L. S., Otten, A., Siegenthaler, K., Kraus, D., Roth, M., White, T., Gregori, G., Gericke, D. O., Baggott, R., Chapman, D. A., Wünsch, K., Vorberger, J., and Riley, D. X-ray scattering from warm dense iron. *High Energy Density Phys.*, 9:573, 2013.

White, T. G., Hartley, N. J., Borm, B., Crowley, B. J. B., Harris, J. W. O., Hochhaus, D. C., Kaempfer, T., Li, K., Neumayer, P., Pattison, L. K., Pfeifer, F., Richardson, S., Robinson, A. P. L., Uschmann, I., and Gregori, G. Electron-ion equilibration in ultrafast heated graphite. *Phys. Rev. Lett.*, 112:145005, 2014.

White, T. G., Vorberger, J., Brown, C. R. D., Crowley, B. J. B., Davis, P., Glenzer, S. H., Harris, J. W. O., Hochhaus, D. C., Le Pape, S., Ma, T., Murphy, C. D., Neumayer, P., Pattison, L. K., Richardson, S., Gericke, D. O., and Gregori, G. Observations of inhibited electron-ion coupling in strongly heated graphite. *Sci. Rep.*, 2:889, 2012.

Wilks, S. C., Kruer, W. L., Tabak, M., and Langdon, A. B. Absorption of ultra-intense laser pulses. *Phys. Rev. Lett.*, 1383:69, 1992.

Wünsch, K., Hilse, P., Schlanges, M., and Gericke, D. O. Structure of strongly coupled multicomponent plasmas. *Phys. Rev. E*, 77:056404, 2008.

Wünsch, K., Vorberger, J., and Gericke, D. O. Ion structure in warm dense matter: Benchmarking solutions of hypernetted-chain equations by first-principle simulations. *Phys. Rev. E*, 79:010201(R), 2009.

Wünsch, K., Vorberger, J., Gregori, G., and Gericke, D. O. X-ray scattering as a probe for warm dense mixtures and high-pressure miscibility. *EPL*, 94:25001, 2011.

Wünsch, Kathrin. *Theory of x-ray scattering in warm dense matter*. PhD thesis, University of Warwick, 2011.

Yatsuka, E., Hatae, T., and Kusuma, Y. Principles for local measurement of anisotropic electron temperature of plasmas using incoherent Thomson scattering. *Nucl. Fusion*, 51: 123004, 2011.

Zheng, J., yu, C. X., and Zheng, Z. J. Effects of non-Maxwellian (super-Gaussian) electron velocity distribution on the spectrum of Thomson scattering. *Phys. Plasmas*, 4:2736, 1997.

Ziaja, B., de Castro, A. R. B., Weckert, E., and Möller, T. Modelling dynamics of samples exposed to free-electron-laser radiation with Boltzmann equations. *Eur. Phys. J. D*, 40: 365, 2006.

Ziaja, B. and Medvedev, N. Modelling ultrafast transitions within laser-irradiated solids. *High Energy Density Phys.*, 8:18, 2012.

Ziman, J. M. The electron transport properties of pure liquid metals. *Adv. Phys.*, 16:551, 1967.

Zubarev, D. N. Double-time Green's functions in statistical physics. *Sov. Phys. Usp.*, 3: 320, 1960.

Zylstra, A. B., Frenje, J. A., Grabowski, P. E., Li, C. K., Collins, G. W., Fitzsimmons, P., Glenzer, S. H., Graziani, F., Hansen, S. B., Hu, S. X., Gatu Johnson, M., Keiter, P., Reynolds, H., Rygg, J. R., Séguin, F. H., and Petrasso, R. D. Measurements of charged-particle stopping in warm dense plasma. *Phys. Rev. Lett.*, 114:215002, 2015.